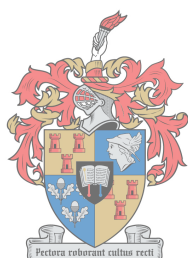


Rationalising the solid-state properties of dithiadiazolyl radicals using a combined theoretical and experimental approach.

by
Alwyn Bernard Dippenaar



UNIVERSITEIT
iYUNIVESITHI
STELLENBOSCH
UNIVERSITY

100
1918 · 2018

*Thesis presented in partial fulfilment of the requirements for
the degree Doctor of Philosophy*

Supervisors: Prof. Catharine Esterhuysen & Prof. Delia Haynes

Department of Chemistry & Polymer Science
Faculty of Science
University of Stellenbosch

March 2018

Declaration

By submitting this thesis/dissertation electronically, I declare that the entirety of the work contained therein is my own, original work, that I am the sole author thereof (save to the extent explicitly otherwise stated), that reproduction and publication thereof by Stellenbosch University will not infringe any third party rights and that I have not previously in its entirety or in part submitted it for obtaining any qualification.

December 2017

This work is dedicated to my parents. For their endless support and encouragement.
Thank you Johanna Wilhelmina & Frederick Christoffel Bernardus Dippenaar.

Acknowledgments

I would like to thank my supervisors, Prof. Delia Haynes and Prof. Catharine Esterhuysen for their patience and guidance during the years of my MSc and PhD studies.

I thank Prof Claude Lecomte, Dr Nicolas Claiser, Dr Javier Campo and Ariste Bolivard Voufack for their valuable contributions to this work. I would also like to thank the members of the Supramolecular Group. In particular, I would like to thank Dr Dominic Castell, Dr Leigh Loots and Bella Claassens.

Finally, I would like to thank the University of Stellenbosch for the providing the necessary facilities and the National Research Foundation for funding.

Abstract

The work describes a series of theoretical and experimental studies carried out to better understand the solid-state properties of 1,2,3,5-dithiadiazolyl (DTDA) radicals.

The attempted co-crystallisation of 4-(4'-cyano-2',3',5',6'-tetrafluorophenyl)-1,2,3,5-dithiadiazolyl (**2**) and 4-(2',6'-difluoro-phenyl)-1,2,3,5-dithiadiazolyl (**7**) yielded the α -phase of **2**, which had previously been shown to only grow on a cold finger at -10 °C. The needle-shaped β -phase crystals of **2** were found to be the first DTDA radical that exhibits flexible properties. The experimental work focussed on the properties of four DTDA radicals. The synthesis of 4-(4'-bromo-2',3',5',6'-tetrafluorophenyl)-1,2,3,5-dithiadiazolyl (**3**) produced a mixture of the desired product and a novel co-crystal (**3-cox**). The crystal structure of **3-cox** was found to contain dimeric pairs of **3** co-crystallised with starting material, 4-bromo-2,3,5,6-tetrafluoro-benzonitrile. The joint refinement of high-resolution X-ray diffraction (HXRD) and polarised neutron diffraction (PND) data was used to determine the spin density of 4-(2',3',5',6'-tetrafluoro-4'-nitrophenyl)-1,2,3,5-dithiadiazolyl (**4**). The spin density values were found to be in good agreement with previously determined experimental values, with the majority of the spin density on the sulfur and nitrogen atoms of the heterocyclic radical ring.

In the computational part of this study, a series of calculations was performed to investigate why specific DTDA radicals prefer monomeric or dimeric modes of association in the solid state. Geometry optimisations and single point energy calculations showed that dimeric radicals yield attractive energies if the geometry optimisation and single point calculations are performed in the singlet or triplet state, whereas monomeric radicals only interact attractively in the triplet state, irrespective of how the geometry optimisation had been undertaken. Radical **3** was found to be the one exception as it exhibits attractive energies for both monomeric and dimeric modes of association. This agreed with the experimental results as the crystal structures of **3** and **3-cox** exhibit monomeric and dimeric modes of association between molecules of **3**, respectively. Geometry and interaction energy calculations on substituted radicals showed that the *ortho* and *para* groups could reduce the tendency of DTDA radicals to dimerise.

Lastly, the results from the first and second sections were used as a basis for a series of calculations to predict the mode of association in radicals that have not yet been synthesised ('unknown radicals'). Geometry optimisation and interaction energy calculations were performed on the unknown radicals arranged in eight monomeric or dimeric modes of

association. The results were used to identify three of the compounds as likely to associate in the dimeric mode, while three were expected to form monomeric radicals. Crystals were obtained for 4-(3'-fluoro-4'-trifluoromethylphenyl)-1,2,3,5-dithiadiazyl (**32**) and 4-(4'-bromophenyl)-1,2,3,5-dithiadiazyl (**33**). The crystal structure of radical **32** shows that the molecules exhibit a *trans-cofacial* mode of association, which was computationally predicted as the most stable mode of association. Similarly, in the crystal structure of radical **33**, the molecules exhibit a *cisoid* mode of association, which was computationally predicted as one of the most stable modes of association. Taken together, the results from the study show that a combination of theoretical and experimental methods provide a powerful tool for studying the properties of DTDAs.

Opsomming

Die werk beskryf 'n reeks teoretiese en eksperimentele studies uitgevoer om die vaste toestand eienskappe van 1,2,3,5-dithiadiazoliel (DTDA) radikale te verstaan.

Die eksperimentele werk het gefokus op die eienskappe van vier gesintetiseerde DTDA radikale. Die poging tot ko-kristallisatie van 4-(4-cyaaan-2',3',5',6'-tetrafluorfeniel)-1,2,3,5-dithiadiazoliel (**2**) en 4-(2',6'-difluor-feniel)-1,2,3,5-dithiadiazoliel (**7**) het radikale geproduseer wat geïdentifiseer was as die α -fase van **2**, waarvoor dit voorheen bepaal was dat dit slegs groei op 'n koue vinger by -10°C . Die naaldvormige β -fase kristalle van **2** was gevind om te wees wat buigsame eienskappe te vertoon. Die sintese van 4-(4'-broom-2',3',5',6'-tetrafluorfeniel)-1,2,3,5-dithiadiazoliel (**3**) radikaal was gevind om 'n mengsel van **3** en 'n nuwe mede-kristal (**3-cox**) te produseer. Die kristalstruktuur van **3-cox** toon 'n dimeriese paar van **3** wat ko-kristalliseer met 4-broom-2,3,5,6-tetrafluor-bensonitriël. Die "joint refinement" van HXRD en PND data was gebruik om die spindigtheid van 4-(2',3',5',6'-tetrafluor-4'-nitrofeniel)-1,2,3,5-dithiadiazoliel (**4**) te bepaal. Die spindigtheid waardes stem goed ooreen met eksperimentele waardes wat voorheen bepaal was, met die meerderheid van die spindigtheid teenwoordig op die stikstof en swael atome van die heterosikliese ring.

In die teoretiese afdeling van hierdie studie was 'n reeks berekeninge uitgevoer om te ondersoek hoekom spesifieke DTDA radikale 'n monomere of dimeriese vorm van assosiasie verkies. Optimalisering en enkelpunt interaksie-energie berekeninge het getoon dimeriese radikale produseer aantreklike energieë indien die optimalisering en interaksie-energie berekening uitgevoer is in die singuletoestand, terwyl monomere radikale reageer slegs in 'n aantreklike wyse indien hulle uitgevoer word in die triplettoestand, ongeag van die toestand waarin die optimalisering uitgevoer word. Radikaal **3** was die een uitsondering aangesien dit aantreklike energie vertoon vir beide monomere en dimeriese vorms van assosiasie. Dit stem goed ooreen met eksperimentele waardes aangesien die kristalstrukture van **3** en **3-cox** beide monomere en dimeriese vorms van assosiasie vir **3** vertoon. Optimalisering en enkelpunt interaksie-energie berekeninge op gesubstitueerde radikale het getoon dat *orto*- en *para*-substituenten die neiging van radikale om te dimeriseer kan verminder.

Laastens is die resultate van die eerste en tweede afdelings gebruik as 'n basis om 'n reeks berekening op te stel, ten einde te kan voorspel watter vorm van assosiasie verkies sal word deur DTDA radikale wat nog nie gesintetiseer is nie ('onbekende radikale'). Optimalisering en enkelpunt interaksie-energie berekeninge was uitgevoer op die onbekende radikale wat

georiënteer was ten opsigte van agt monomeriese en dimeriese vorms van assosiasie. Drie van die verbindings was geïdentifiseer met die potensiaal om die dimeriese vorm van assosiasie te verkies, terwyl drie ander verbindings die monomeriese vorm van assosiasie sal verkies. Kristalstrukture was verkry vir die radikale 4-(3-fluoor-4-trifluormetileen)-1,2,3,5-dithiadiazoliel (**32**) and 4-(4-broom-feniel)-1,2,3,5-dithiadiazoliel (**33**). Die kristalstruktuur van radikaal **32** vertoon molekules in 'n "*trans-cofacial*" vorm van assosiasie. Daar was ook gevind dat hierdie vorm van assosiasie die stabielste vorm is deur middel van berekeninge. Soortgelyk is daar gevind dat die kristalstruktuur van radikaal **33** vertoon molekules in 'n "*cisoid*" vorm van assosiasie, wat ook deur berekeninge geïdentifiseer was as een van die stabielste vorms van assosiasie. Ten einde het die resultate in hierdie studie gewys dat 'n kombinasie van teoretiese en eksperimentele metodes 'n kragtige instrument bied om DTDA's te kan bestudeer.

Conferences

1. **Indaba8**: Serendipity vs Prediction, organised by the South African Crystallographic Society, 16-21 August 2015, held in Skukuza, Kruger National Park, South Africa.

Poster: Rationalising the solid-state properties of dithiadiazolyl radicals using a combined theoretical and experimental approach.

2. **PCCr1**: 1st Pan African Conference on Crystallography by the IUCr, 6 – 11 October 2016, held in in Dschang, Cameroon.

Poster: Rationalising the solid-state properties of dithiadiazolyl radicals using a combined theoretical and experimental approach.

3. **10th CHPC National Conference**: “*The last decade of accomplishment, the next decade of opportunity*“, held by the Centre For High Performance Computing (CHPC), 4 – 9 December 2016, held in East London.

Oral presentation: Rationalising the solid-state properties of dithiadiazolyl radicals using a combined theoretical and experimental approach.

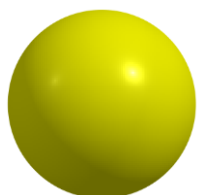
4. **ICOSS XXIII**: 23rd International Conference on the Chemistry of the Organic Solid State in Stellenbosch, South Africa on 2 - 7 April 2017

Oral presentation: Rationalising the solid-state properties of dithiadiazolyl radicals using a combined theoretical and experimental approach.

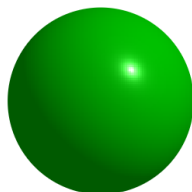
Abbreviations

1D	1-dimensional
2D	2-dimensional
3D	3-dimensional
ADF	Amsterdam Density Functional
AIM	Atoms In Molecules
BCP	Bond Critical Point
BSSE	Basis set superposition error
CSD	Cambridge Structural Database
DCM	Dichloromethane
DTDA	1,2,3,5-dithiadiazolyl
DFT	Density Functional Theory
ECP	Electrostatic Core Potential
EDA	Energy decomposition analysis
EPR	Electron Paramagnetic Resonance
ESP	Electrostatic Surface Potential
EtOAc	Ethyl acetate
GGA	Generalised Gradient Approximation
HF	Hartree-Fock
H-bond	Hydrogen bond
MS	Mass Spectrometry
NaHCO ₃	Sodium bicarbonate
NCI	Non-Covalent Interaction
PES	Potential energy surface
PND	Polarised neutron diffraction
SEM	Scanning electron microscopy
SOMO	Singly Occupied Molecular Orbital
THF	Tetrahydrofuran
TLC	Thin layer chromatography
SQUID	Superconducting Quantum Interference Device
XRD	X-ray diffraction

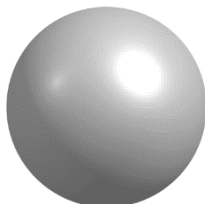
Atomic colour key



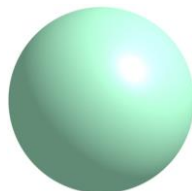
Sulfur



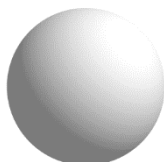
Fluorine



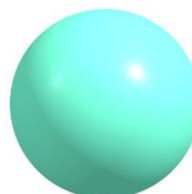
Carbon



Chlorine



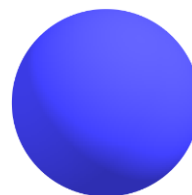
Hydrogen



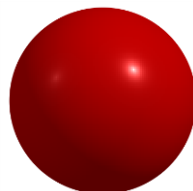
Iodine



Oxygen



Nitrogen



Bromine

Table of contents

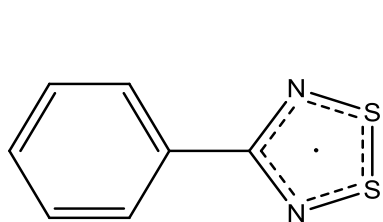
Abstract.....	iv
Opsomming.....	vi
List of DTDA radicals discussed in the text.....	15
CHAPTER 1 Introduction.....	21
General Introduction.....	22
1.1. Organic radicals.....	22
1.1.1. Triphenylmethyl radicals.....	22
1.1.2. α -Nitronyl nitroxide radicals.....	23
1.1.3. Verdazyl radicals.....	24
1.1.4. Thiazyl radicals.....	25
1.2. Dithiadiazolyl radicals.....	27
1.3. Magnetism in organic radicals.....	34
1.3.1. Hysteresis.....	36
1.3.2. Curie temperature (T_c).....	37
1.3.3. Magnetic susceptibility.....	37
1.3.4. Magnetic exchange.....	39
1.3.5. Superconducting Quantum Interference Device (SQUID).....	41
1.3.6. Electron Paramagnetic Resonance.....	42
1.4. Theoretical calculations.....	46
1.4.1. Geometry optimisation calculations on DTDA radicals.....	47
1.4.2. Calculation of intermolecular interaction energies.....	48
1.4.3. Potential energy surface (PES) scans.....	49
1.4.4. Electrostatic Surface Potential.....	50
1.4.5. Atoms in Molecules.....	51
1.4.6. Pancake bonding.....	52
1.5. General aims.....	53
2 Materials and Methods.....	60
Introduction.....	61
2.1. Experimental techniques.....	61
2.1.1. Synthesis of 1,2,3,5-dithiadiazolyl radicals.....	61
2.1.2. Single-Crystal X-ray Diffraction Analysis.....	62

2.1.3. Polarised neutron diffraction.....	63
2.1.4. Joint refinement	64
2.1.5. Crystallographic refinement.....	65
2.1.6. Electron paramagnetic resonance (EPR)	65
2.2. Computational methods	65
2.2.1. Cambridge Structure Database (CSD) searches	65
2.2.2. Geometry optimisation and calculation of intermolecular interaction energies	66
2.2.3. Visualisation of structures.....	67
2.2.4. Atoms in Molecules (AIM) analysis.....	67
2.2.5. Electrostatic potential.....	68
2.2.6 Energy decomposition analysis.....	68
2.2.7 Multifunctional Wavefunction Analyzer (Multiwfn)	69
3 Synthesis and properties of some 1,2,3,5-dithiadiazolyl radicals.....	72
Introduction.....	73
3.1. Properties of the α -and- β -phase 4-(4-cyano-2,3,5,6-tetrafluoro-phenyl)-1,2,3,5-dithiadiazolyl radical (2).....	75
3.2. Flexible properties of the β -phase of 2	75
3.3. Properties of the 4-(2,6-difluorophenyl)-1,2,3,5-dithiadiazolyl radical (7).....	85
3.4. Attempted co-crystallisation of radicals 2 and 7.....	86
3.5. Properties of the 4-(4'-bromo-2',3',5',6'-tetrafluorophenyl)-1,2,3,5-dithiadiazolyl radical (3).....	94
3.6. Properties of the 4-(2,3,5,6-tetrafluoro-4-nitrophenyl)-1,2,3,5-dithiadiazolyl radical (4).....	97
3.7. Joint refinement of experimental charge and spin densities of 4.....	98
3.8. Calculation of spin densities on radical p -NCC ₆ F ₄ CN ₂ SSN (2), p -BrC ₆ F ₄ CN ₂ SSN (3) and p -O ₂ NC ₆ F ₄ CN ₂ SSN (4).....	107
4 A computational study of the modes of association in 1,2,3,5-dithiadiazolyl radicals	115
Introduction.....	116
4.1. 1,2,3,5-Dithiadiazolyl radicals in the CSD	117
4.2. Geometry optimisation of monomeric and dimeric radicals.....	119
4.3. Calculating the strength of intermolecular interactions	122
4.4. The potential energy surface (PES)	130
4.5. Energy decomposition analysis of triplet and singlet radicals.....	134
4.6. Topological analysis of the electron density in DTDA radicals.	138
4.7 Electrostatic surface potential.....	144

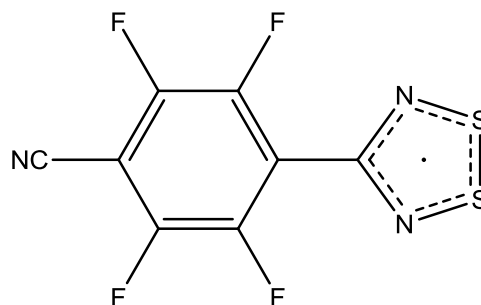
5 The effect of aryl ring substituents on the intermolecular interactions in DTDA radicals.	156
Introduction.....	157
5.1. Geometry optimisation calculations on DTDA radicals with different substituents at the <i>ortho</i> , <i>meta</i> and <i>para</i> positions	157
5.2. Intermolecular interaction energies for substituted radicals	159
5.3. Topological analysis of in substituted radicals	162
5.3.1 Substituted radicals optimised in the singlet state	166
5.3.2 Substituted radicals optimised in the triplet state	168
5.4. EDA analysis of substituted radicals	169
5.5 Halogen substitution on the phenyl ring	171
5.5.1 Radical pairs 2, 22 - 24	173
5.5.2 Radical pairs 3, 25 – 27.....	174
5.5.3 Radical pairs 4, 28 - 30	176
6 Predicting the mode of association in 1,2,3,5-dithiadiazolyl radicals	179
Introduction.....	180
6.1 PES scans on different modes of association.....	181
6.2 Calculations on unknown radicals	186
6.3 Interaction energies of unknown and known monomeric radicals	187
6.3.1 Energies of radicals optimised in the singlet state	187
6.3.2 EDA analysis of unknown radicals optimised in the mode of association of radical 4 (mode g) in the singlet state	194
6.3.3 Energies of radicals optimised in the triplet state	196
6.4. Synthesis of unknown radicals.....	200
6.5. Analysis of synthesised unknown radicals (31 – 34, 36).....	201
6.5.1 Radical 2	201
6.5.2 Radical 31	202
6.5.3 Radical 32	203
6.5.4 Radical 33	206
6.5.5 Radical 34	209
6.5.6 Radical 36	211
7 Summary and concluding remarks.....	214
Addendum A.....	218
A.1. Synthesis of 2,3,5,6-tetrafluoro-4-nitrobenzonitrile	218
A.1.1. Amination of pentafluorobenzonitrile.....	218

A.1.2. Oxidation of aminotetrafluorobenzonitrile	219
A.2. Synthesis of 4-bromo-2,3,5,6-tetrafluorobenzonitrile.....	219
A.3. Synthesis of DTDA radicals.	220
A.4. Synthesis of α -phase of radical 2	221
A.5. Synthesis of novel DTDA radicals.....	222
Appendix.....	224

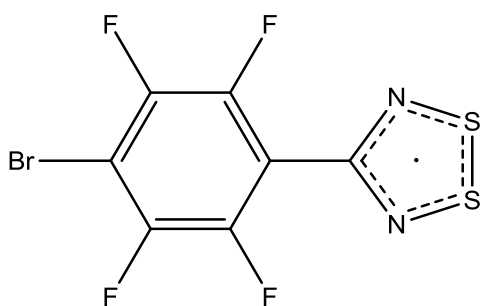
List of DTDA radicals discussed in the text



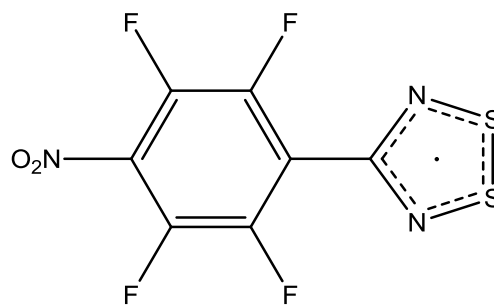
1



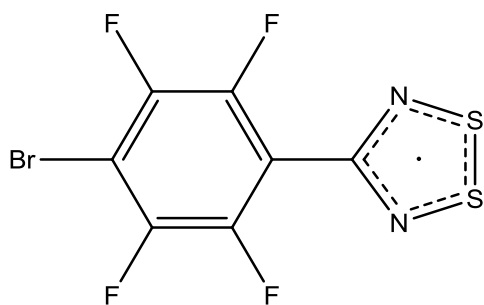
2



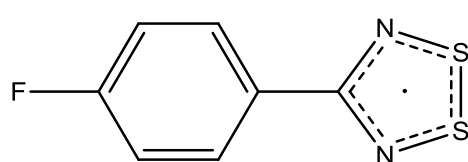
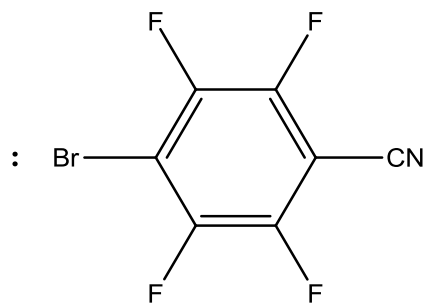
3



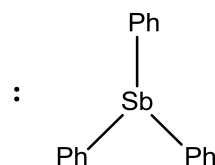
4

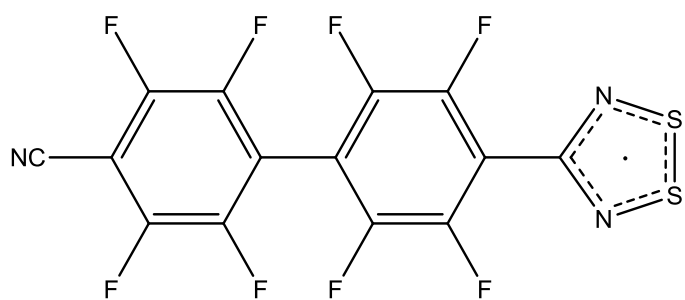


3-cox

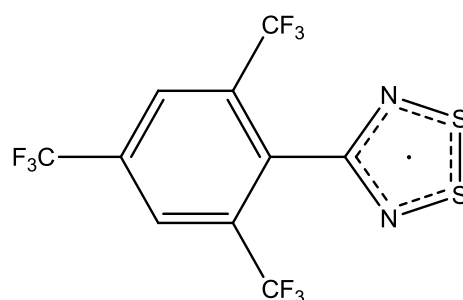


cox-stb

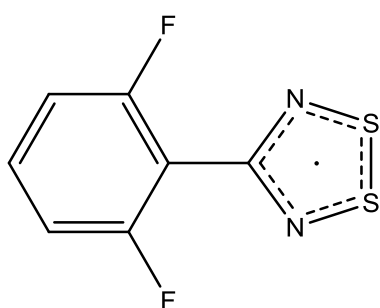




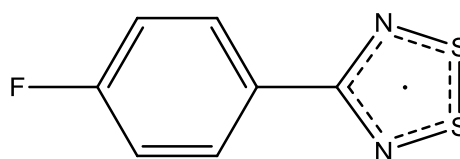
5



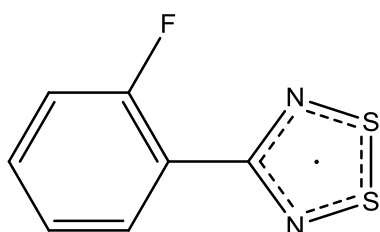
6



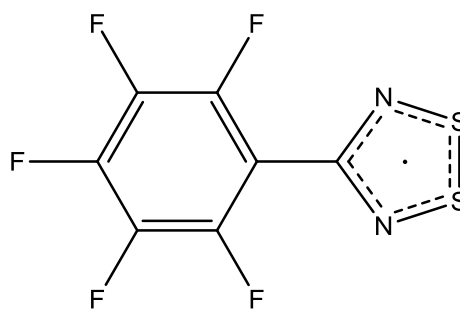
7



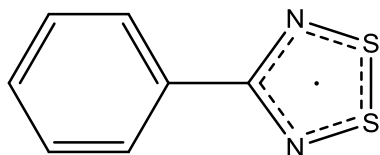
8



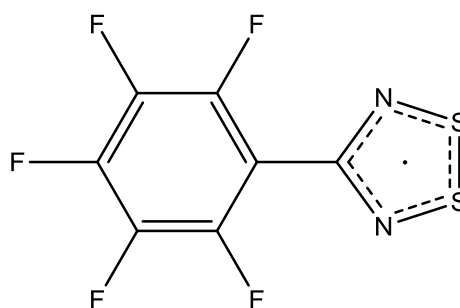
9

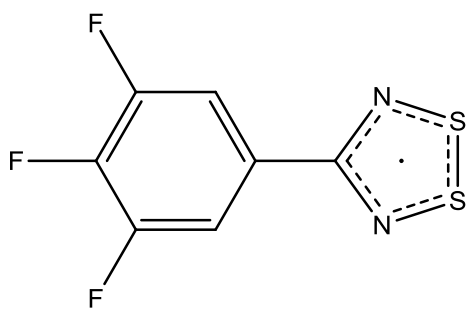


10

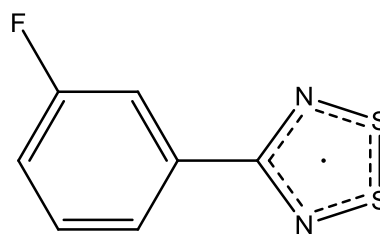


11 (co-crystal)

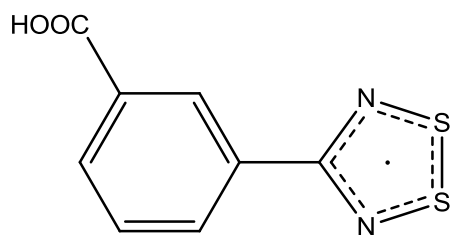




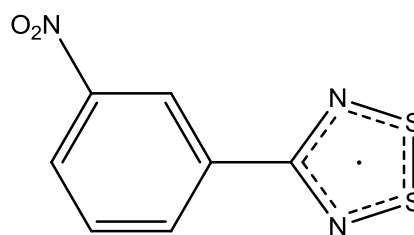
12



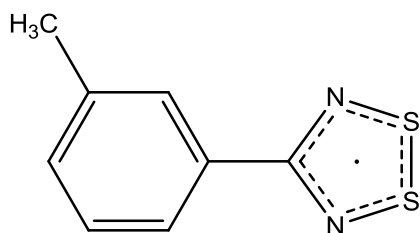
13



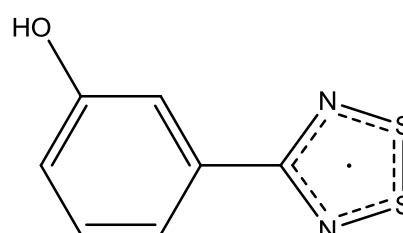
14



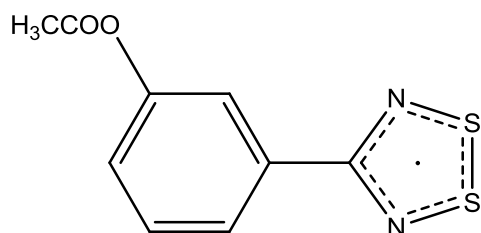
15



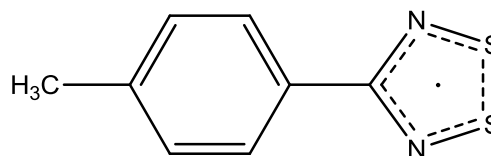
16



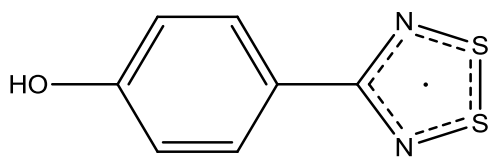
17



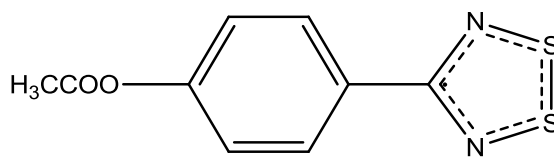
18



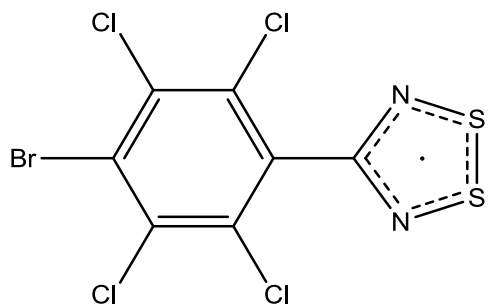
19



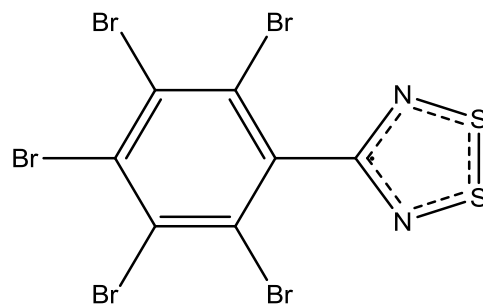
20



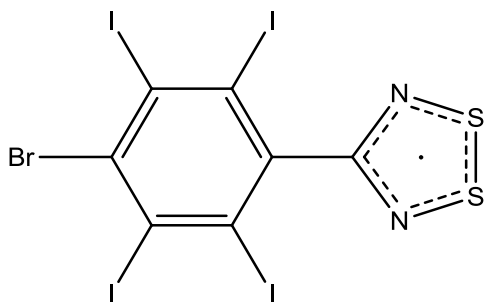
21



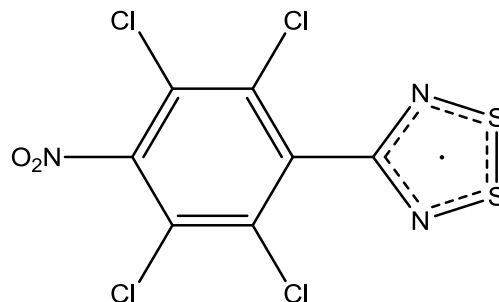
22



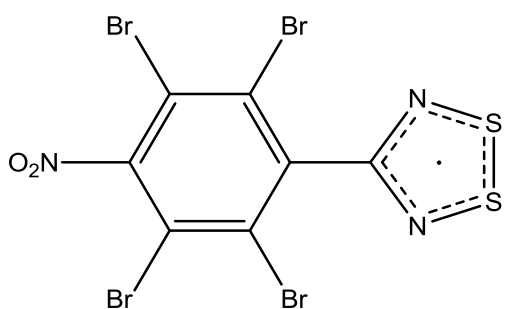
23



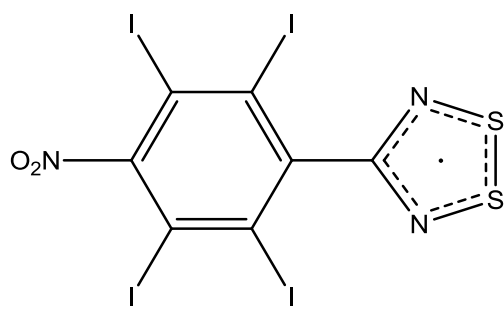
24



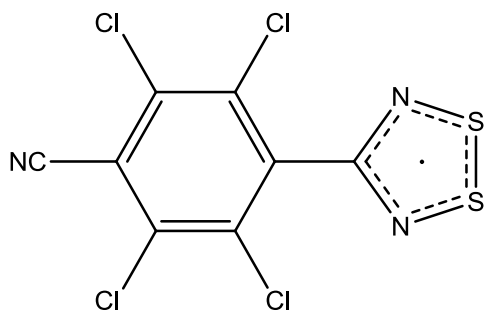
25



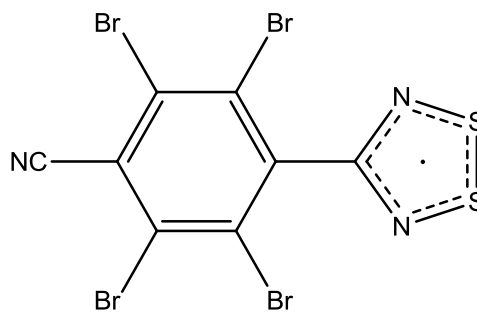
26



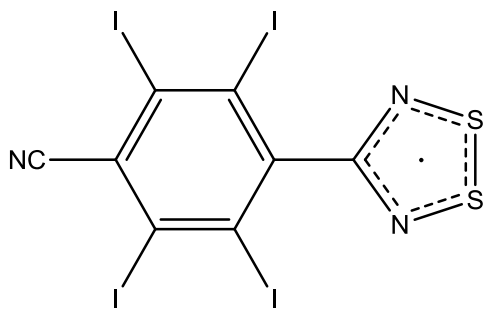
27



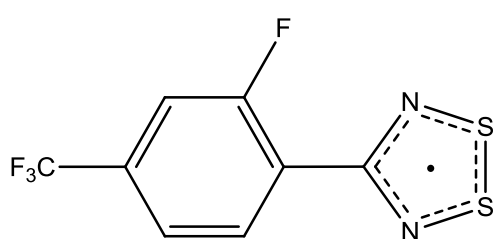
28



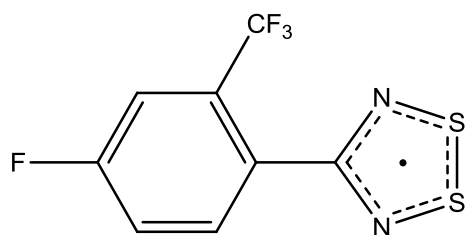
29



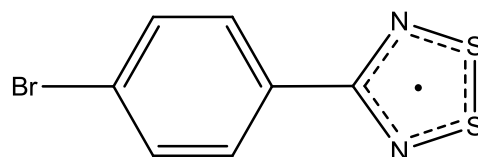
30



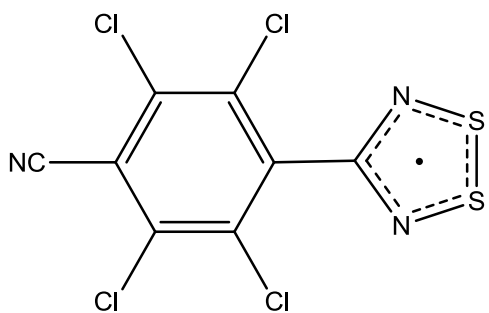
31



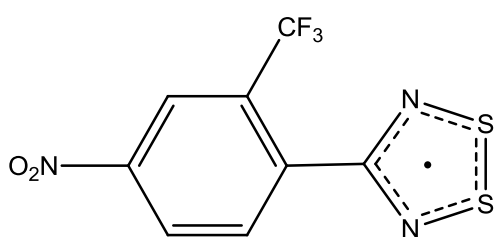
32



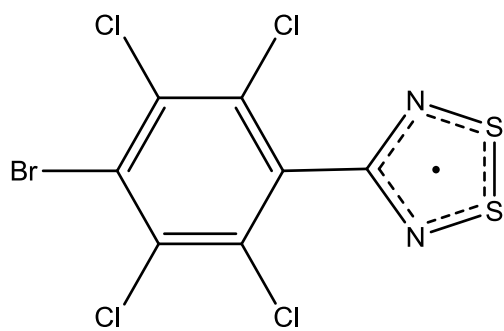
33



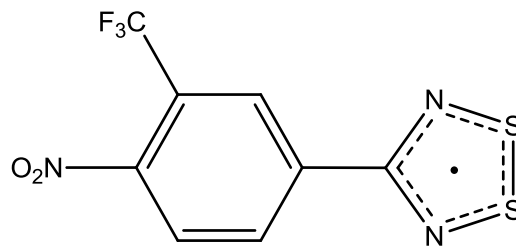
34



35



36



37

CHAPTER 1 Introduction

General Introduction

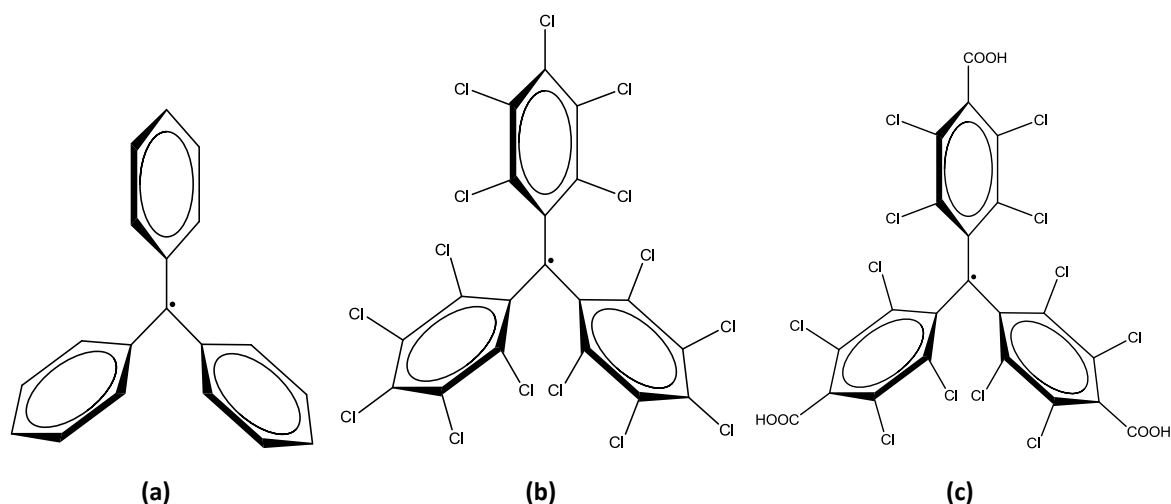
1.1. Organic radicals

The discovery of the triphenylmethyl radical by Moses Gomberg in 1900¹ has led to many researchers identifying him as the founder of the field of free radical organic chemistry. Since this discovery, several studies have shown that organic radical systems are comprised of open-shell electronic structures that often result in materials with applications in magnetochemistry², redox-catalysis³, electron paramagnetic resonance (EPR) imaging⁴, radical polymerisation⁵ and conductive materials^{6,7}. The application of organic radical compounds as magnetic materials has received particular interest, as conventional magnets containing metals (such as Fe, Ni, Co) often require energetically demanding metallurgical processes and the elements are often of low abundance in nature⁸. Organic magnets occur as free radicals and are therefore very reactive species, owing to preferred closed-shell configurations that can form through reduction, oxidation or covalent bond formation. The closed-shell configuration results in a strong interaction owing to the pairing of electrons, which is accompanied by a loss of magnetic properties. However, significant stabilisation of the organic radical can allow for communication between the unpaired electrons, which is propagated through intermolecular interactions present in the solid-state arrangement of molecules in the crystalline material⁹. This has been particularly successful in several classes of radicals, namely triphenylmethyl¹, α -nitronyl nitroxides¹⁰, verdazyls¹¹ and various thiazyl-based compounds¹² that will be discussed in more detail.

1.1.1. Triphenylmethyl radicals

Prior to the discovery of the triphenylmethyl radical¹ (Scheme 1.1a) it was commonly accepted that magnetism was restricted to metallic substances. This discovery played a crucial role in the field of organic radicals and would branch out to several other fields that will be discussed in more detail in the following sections. The triphenylmethyl radical was found to be very reactive as it would readily dimerise or react with oxygen, thus requiring additional substituents to provide the necessary stabilisation¹³. Adding bulky chlorine groups on the phenyl ring (Scheme 1.1b) was found to protect the central radical carbon from unwanted reactions that could result in an overall loss of radical character^{14,15}. The functionalisation of triphenylmethyl

with chlorine and carboxylic groups (Scheme 1.1c) yields a radical that has been shown to exhibit a network of hydrogen bonds (H-bonds) that have the ability to transmit magnetic interactions. The presence of weak interactions between radical molecules in the solid state results in magnetic ordering only occurring at low temperatures⁹. An increase in interaction strength poses a significant challenge, as steric crowding is required to stabilise unpaired electrons, but will in turn result in weak interactions that allow for a magnetic pathway¹⁶. A further advantage of these radicals is that their trigonal symmetry can result in the formation of channels held together by weak intermolecular interactions and they can easily be utilised as coordinating magnetic ligands¹⁷. Recent studies have shown that triphenylmethyl radicals can be grafted onto surfaces, which shows some promising results for the development of non-volatile memory devices⁹.

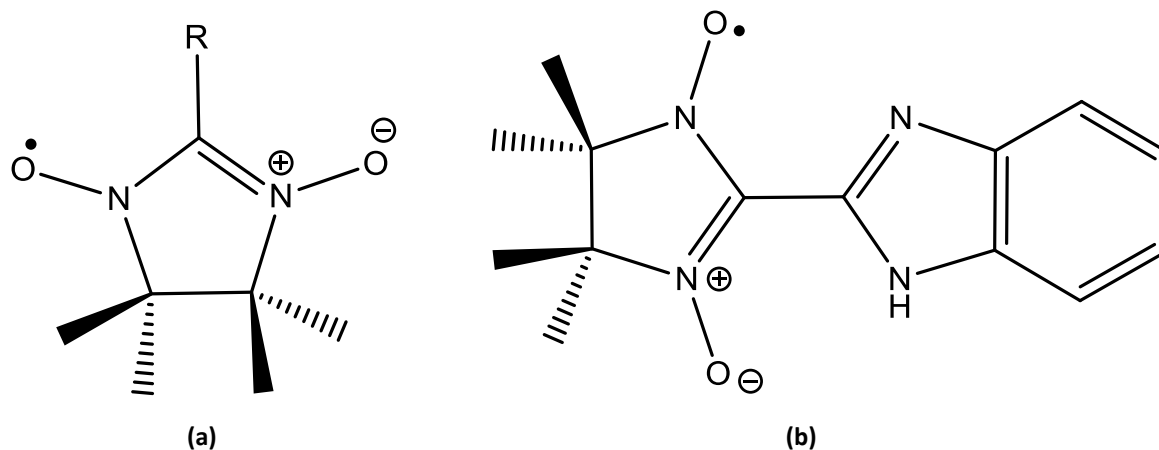


Scheme 1.1 (a) triphenylmethyl, (b) perchlorotriphenylmethyl and (c) 4,4',4''-(2,3,5,6-tetrachlorobenzoic acid)triphenylmethyl

1.1.2. α -Nitronyl nitroxide radicals

The α -nitronyl nitroxides (Scheme 1.2a) are open-shell molecules that have received considerable attention due to their ability to order as ferromagnets¹⁸, where this behaviour originates from its network of intermolecular interactions in the solid state that are primarily directed by H-bonds¹⁰. The α -nitronyl nitroxide radicals are stabilised by the presence of methyl groups that help shield the unpaired electrons from air or water¹⁹. Moreover, these radicals can be easily synthetically modified, which results in a different network of intermolecular interactions that ultimately result in different crystal architectures^{20,21}. This was found to be particularly successful with 2-benzimidazolyl α -nitronyl nitroxide (Scheme 1.2b),

which undergoes a phase transition to a ferromagnetically ordered state below 1 K that has been shown to exhibit a ferromagnetic exchange term (J/k_B) of 22 K. To date, this has been shown to be the largest recorded value of J/k_B for a purely organic species²².



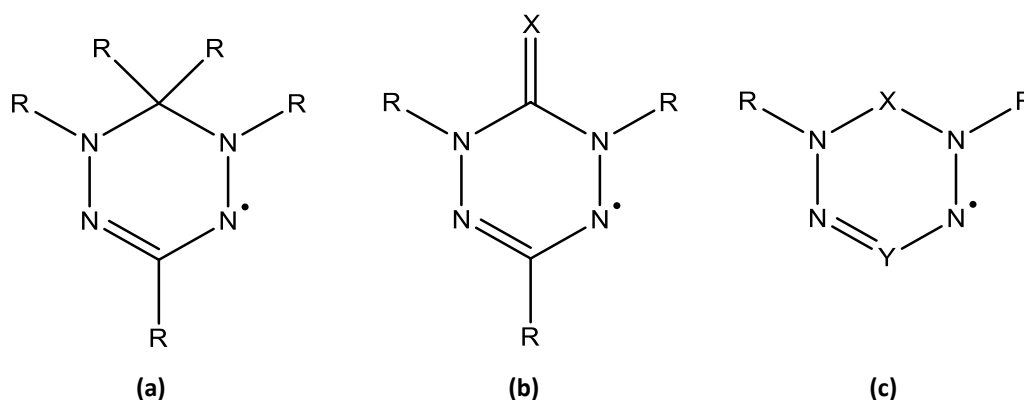
Scheme 1.2 (a) α -nitronyl nitroxide and (b) 2-benzimidazolyl α -nitronyl nitroxide.

1.1.3. Verdazyl radicals

Verdazyls are another class of organic radicals that can be subdivided into three different classes (Scheme 1.3) depending on the nature of the carbon atom between the nitrogen atoms in the 6-membered ring. The first class of verdazyls (Scheme 1.3a) contain saturated carbon atoms, the second class of verdazyls (Scheme 1.3b) contain carbonyl or thiocarbonyl groups, and the third class of verdazyls (Scheme 1.3c) contain a boron or phosphorous atom at positions X and Y, respectively^{23,24}. Verdazyl radicals are among the most stable radicals as their spin density is localised on the nitrogen atoms, and the compounds can be stored for a long time before the onset of decomposition in the presence of air and moisture²⁵. A further result of their chemical stability is that they can easily be synthetically modified and are capable of forming metal complexes²⁶⁻²⁸.

The formation of a metal complex with verdazyls stems from research aimed to use stable free radicals as building blocks in the design of molecular magnetic materials. Furthermore, the use of open-shell ligands can greatly modify the electronic structure of coordination complexes and result in the formation of molecular materials with bistable memory and sensing applications⁹. Magnetic studies of the verdazyl radicals have revealed that their properties originate from through-bond exchange coupling and through-space exchange coupling in

crystals of radical molecules. There are examples where the magnetism is largely unaffected by a strong increase in temperature²⁹⁻³².



Scheme 1.2 The three classes of verdazyl radicals that contain either saturated carbon atoms (a), carbonyl or thiocarbonyl groups (b) or contain a boron or phosphorous atom at position X and Y (c).

1.1.4. Thiazyl radicals

Thiodithiazyl monochloride $[S_3N_2^{+}]Cl^{-}$ was the first thiazyl radical successfully synthesised with its crystal structure exhibiting a spin-paired 4-centre-2-electron bond as illustrated in Figure 1.1^{33,34}. The aforementioned light heteroatom (N,O) radicals triphenylmethyl, α -nitronyl nitroxide and verdazyl radicals contain localised spin density, which can often result in suppressed unpaired electrons.

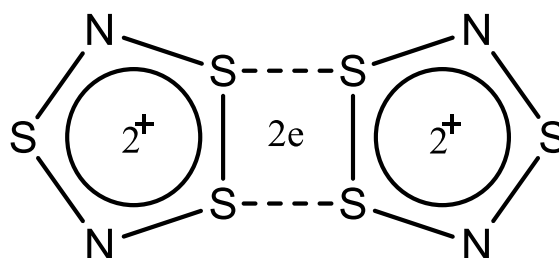


Figure 1.1: $S_6N_4^{2+}$ cation consisting of two aromatic 1,2-dithiolium cations linked by sulfur atoms.

The introduction of heavy-heteroatom thiazyl radicals aim to address this problem as the nitrogen atoms suppress dimerisation and the neighbouring sulfur atoms generate pathways for magnetic coupling and/or charge migration^{35,36}. The thiazyl moiety ($-S=N-$) contains three electrons in the π -bond with the third electron residing in an π^* orbital⁹. The unpaired electron

residing in the π^* orbital gives rise to some thiazyl radicals that exhibit bulk magnetic properties and can exist in multiple forms that exhibit different magnetic behaviours¹⁶.

This gave rise to various studies that aimed to introduce a carbon atom that can easily be functionalised³⁷⁻⁴¹. More specifically, the work by Oakley described the synthesis, structural and chemical properties of different isoelectronic members (Figure 1.2) of the five-membered heterocyclic thiazyl radicals³⁶.

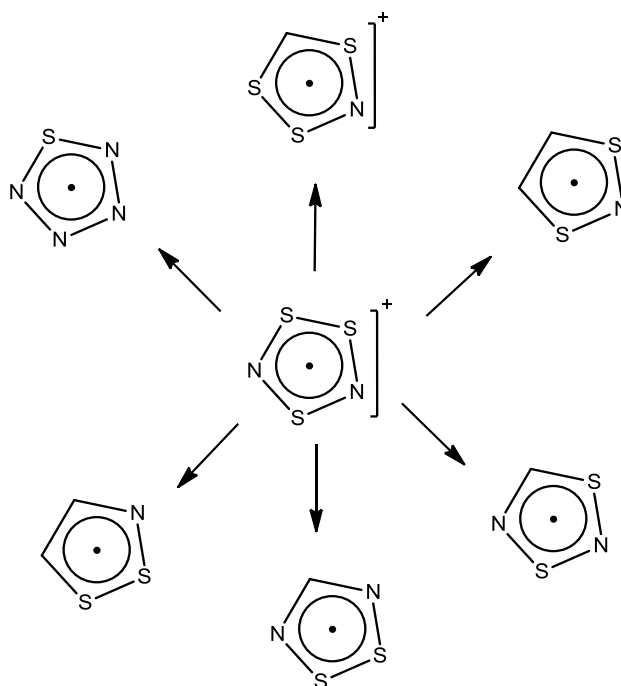
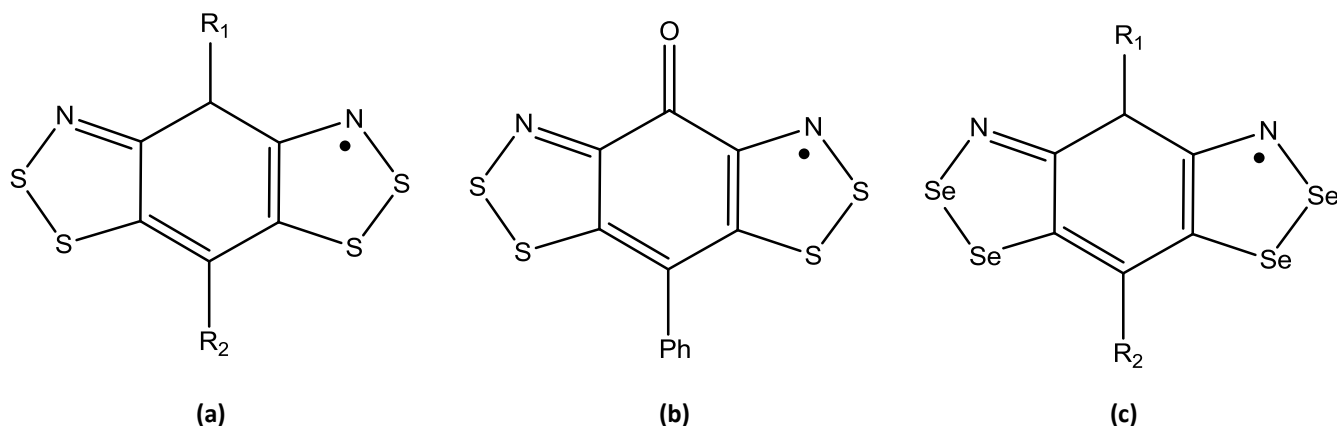


Figure 1.2: Illustration of some of the isoelectronic members of the five-membered heterocyclic thiazyl radicals

Oakley and coworkers studied the network of $S\cdots S$ and $S\cdots N$ interactions in the solid state of thiazyl radicals and the factors that are required to provide pathways for the magnetic exchange and/or charge transport, where these pathways make them attractive candidates when designing materials that display magnetic or conductive properties^{38,42-46}. The bis-1,2,3-dithiazolyl radicals were identified as appealing targets to exhibit intermolecular magnetic and electronic interactions. These thiazyl radicals (Scheme 1.3a) can easily be fine-tuned with the use of large exocyclic ligands (R_1 , R_2) that can both improve magnetic properties and suppress the process of dimerisation⁴⁷. This was found to be particularly successful with a semiquinone-bridged bis-1,2,3-dithiazolyl ($R_1 = O$, $R_2 = Ph$, Scheme 1.3b), which was identified as the first bis-1,2,3-dithiazolyl conductor that exhibits weak ferromagnetism⁴⁸. This study was further extended by replacing the sulfur atoms by their heavier congener, selenium (Scheme 1.3c). This introduces 4p orbitals on the selenium atoms compared to the 3p orbitals on sulfur atoms,

resulting in a larger bandwidth and improved conductivity. Moreover, the heavier selenium atoms result in spin-orbit coupling effects that improve the magnetic effects of these radicals^{49,50}.



Scheme 1.3 The bis-1,2,3-dithiazolyl radicals (a) exhibit some interesting conductive properties, with the semiquinone-bridged bis-1,2,3-dithiazolyl with a keto and phenyl group at position R1 and R2 being one such example (b). The analogous selenium radicals (c) exhibit improved conductive and magnetic properties.

The success by Oakley and coworkers encouraged the design of other stable thiazyl radicals. Two strategies have been commonly utilised to improve the stability of thiazyl radicals^{51,52}. The first strategy involves steric shielding of the atoms on which the unpaired electron resides. This inhibits covalent bond formation that commonly occurs by pairing of the unpaired electrons. The second strategy utilises Coulombic electrostatic repulsions. These forces repel the reactive centres and therefore inhibit the tendency of these systems to form closed-shell configurations. Thermodynamic stability is provided to the radical centre by having a system that consists of several heteroatoms, that delocalises the unpaired electron⁵². The application of these strategies was found to be particularly successful for the family of dithiadiazolyl compounds, some of which exist as purely organic magnets⁵³⁻⁵⁷. This family of thiazyl radicals will be the focus of this study as they exhibit thermal and kinetic stability that allows for some remarkable electric and magnetic properties in the solid state^{9,53}.

1.2. Dithiadiazolyl radicals

The dithiadiazolyl (DTDA) radicals are a particular class of thiazyl radicals where the sulfur atom not involved in the 4-centre-2-electron bond illustrated in Figure 1 is replaced by a carbon

atom, which is then bonded to an additional R-group. This radical can exist in four different isomeric forms, but experimentally only the 1,3,2,4-dithiadiazolyl and the thermodynamically favourable 1,2,3,5-dithiadiazolyl (DTDA) radical have been observed (Figure 1.3)^{58,59}.

The unpaired electron density of DTDA radicals has been shown to reside in a low-lying singly occupied molecular orbital (SOMO)^{60,61}, which gives rise to the potential application of DTDA radicals as organic magnets. The SOMO is illustrated in Figure 1.4 and can be described as an antibonding π^* orbital that is localised on the sulfur and nitrogen atoms.

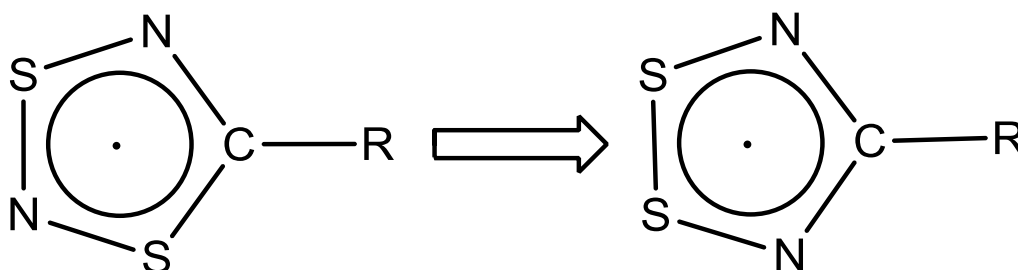


Figure 1.3: Rearrangement of 1,3,2,4-DTDA radical to the 1,2,3,5-DTDA radical.

Furthermore, we observe a node at the carbon atom due to the a_2 symmetry of the SOMO^{62,63}. The nodal carbon plays an important role in the crystal engineering of DTDA radicals, mainly since the nature of the R-group has very little effect on the electronic properties of the DTDA radical⁶⁴. The R-group can be changed to engineer the crystal packing of DTDA radicals without affecting the unpaired electron density⁶⁵.

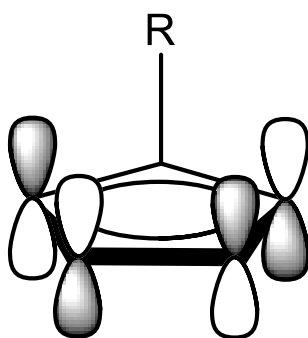


Figure 1.4: SOMO orbital located on the heterocyclic ring of the DTDA radical.

The first crystal structure of a DTDA radical was obtained by Vegas and coworkers⁶⁶. This was achieved by the reduction of $\text{PhCN}_2\text{S}_2^+$ to yield the radical, which was found to crystallise in the space group $P2_12_12_1$. The crystal structure shows pairs of PhCNSSN^{\bullet} (**1**) radicals, resulting from a process commonly referred to as dimerisation (Figure 1.5). Dimerisation

occurs due to a favourable interaction between the SOMOs, resulting in a pairing of the spins and an overall loss of magnetic properties. The geometry of the dimer observed in the crystal of **1** is commonly referred to as a *cisoid* mode of association and exhibits a 4-centre-2-electron bond (Figure 1.6) similar to what was shown in Figure 1.1 for $S_6N_4^{2+}$.

Discovery of **1** resulted in the synthesis of various other DTDA radicals, from which it was observed that there are five different dimerisation modes of association, namely *twisted*, *cisoid*, *transoid*, *trans-cofacial* and *orthogonal* (Figure 1.7)^{51,66-69}.

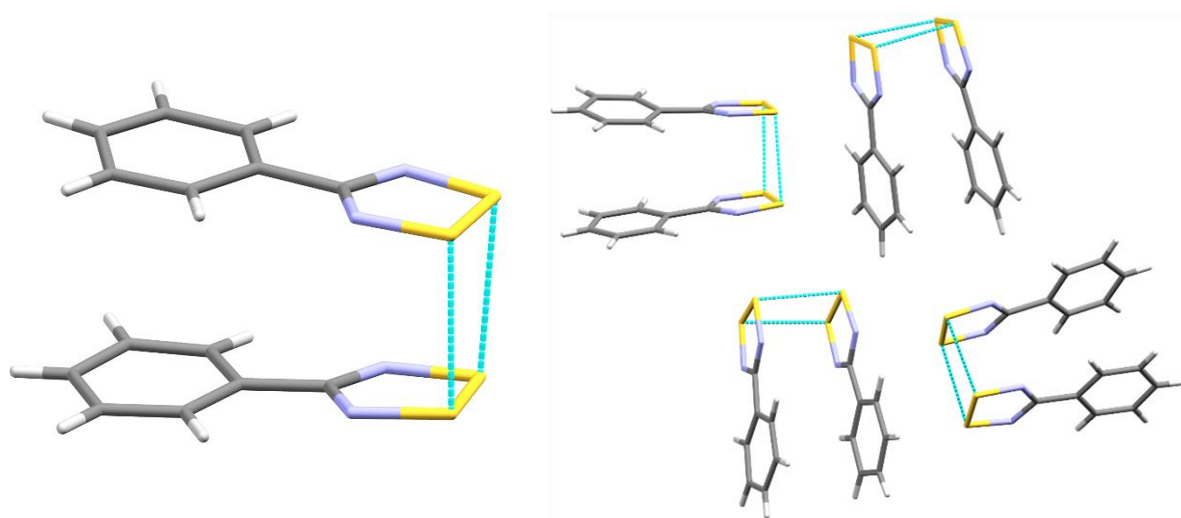


Figure 1.5: The dimeric mode of association observed in the crystal structure of **1** (left). The packing arrangement exhibits several pairs of **1** (right).

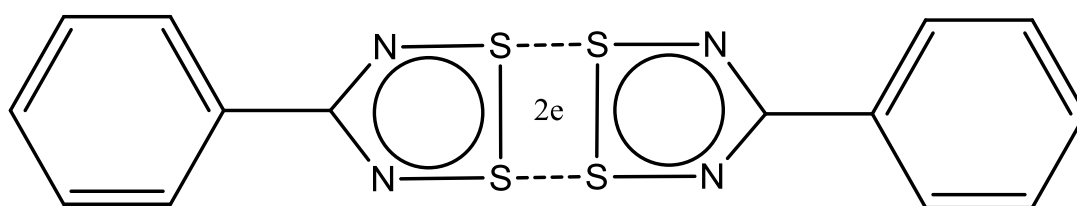


Figure 1.6: The 4-centre-2-electron bond present in **1**.

The solution-state dimerisation enthalpies have been measured for several DTDA radicals to range from -7.4 to -8.8 kcal/mol⁷⁰⁻⁷², while the solid-state dimerisation energies were estimated to be in the region of -1.9 to -2.6 kcal/mol⁷³⁻⁷⁶. The difference between the solution- and solid-state dimerisation enthalpies can be explained by the variation in intermolecular interactions in the two states.

It was only 15 years after the discovery of **1** that the α -phase of $NCC_6F_4CNSSN^{\bullet}$ (**2**) was identified as the first DTDA that does not dimerise in the solid state. Furthermore, it was found

that **1** retains its paramagnetism at room temperature⁵⁷. Radical **2** also crystallises in a second phase, the β -phase, which exhibits weak ferromagnetism at 36 K⁷⁷. It was found that intramolecular N \cdots F repulsion interactions results in large twist angles in fluorinated DTDA radicals, where the twist angle (Φ) can be defined as the torsion angle (N1-C1-C2-C3) between the dithiadiazolyl and perfluoroaryl ring, as illustrated in Figure 1.8.

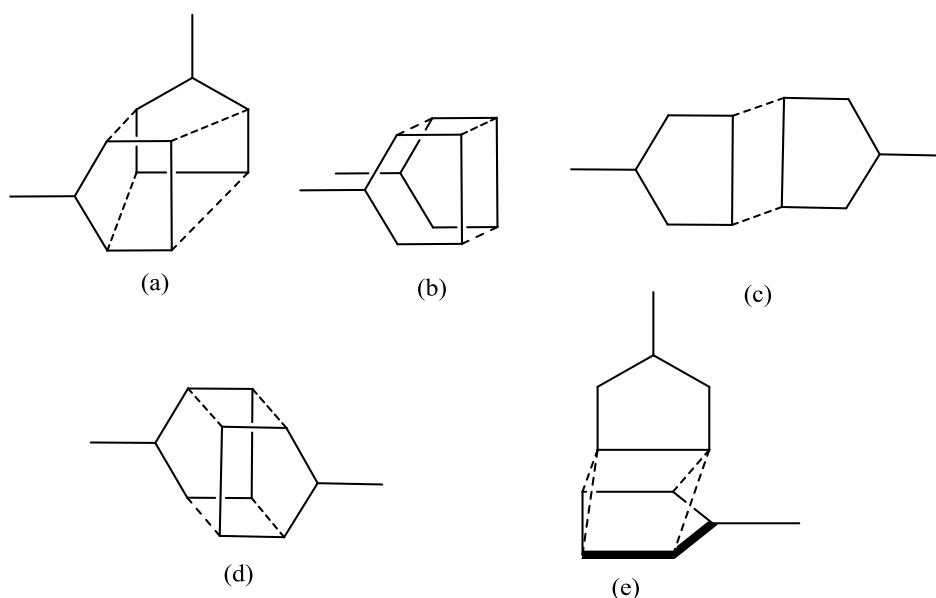


Figure 1.7: Dimer modes of association in DTDA radicals. *Twisted (a), cisoid (b), transoid (c), trans-cofacial (d), orthogonal (e).*

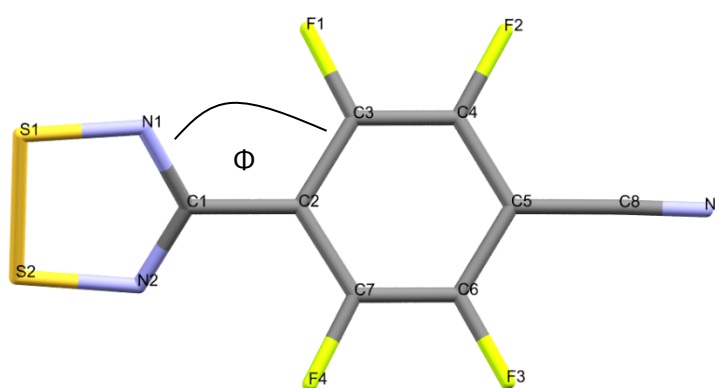


Figure 1.8: Twist angle between atoms N1-C1-C2-C3 of radical 2.

A large twist angle will result in steric repulsion between the perfluoroaryl rings. Sufficient repulsion between the perfluoroaryl rings will not allow for favourable interaction between the SOMOs of each radical, resulting in radicals that remain monomeric and thus retain their unpaired electrons. The absence of fluorinated groups yields smaller twist angles, as there is

no longer a repulsive interaction between the dithiadiazolyl and perfluoroaryl ring (Figure 1.9)^{62,75,78,79}.

Comparison of the crystal structures of **2** with that of other fluorinated radicals reveals that the cyano substituent in the *para* position plays an important role in forming structure-directing CN \cdots S contacts that inhibit dimerisation, whereas the absence of this group results in dimerisation. For example, the C₆F₅CNSSN \cdot does not contain a substituent in the *para* position capable of forming structure-directing contacts and therefore exhibits *cisoid* radical pairs in its crystal structure. The chains of **2** molecules are connected via CN \cdots S contacts and is illustrated in Figure 1.10 for both phases⁸⁰.

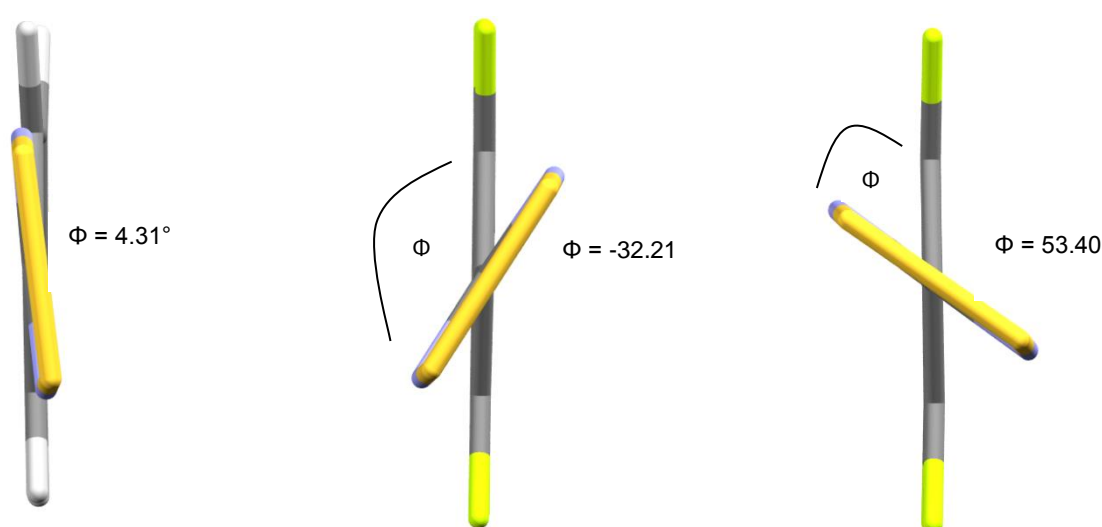


Figure 1.9: Twist angles ($^{\circ}$) of **1** (left), α -**2** (middle), β -**2** (right).

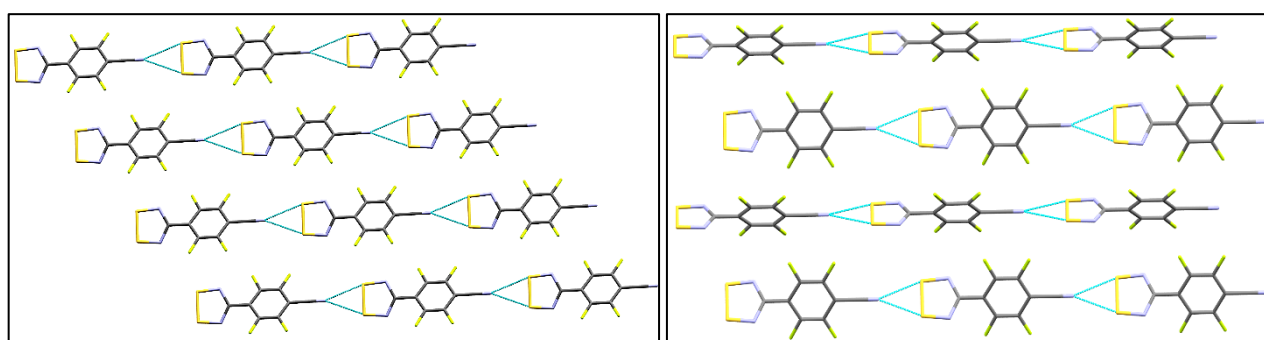


Figure 1.10: Chains of **2** molecules linked via CN \cdots S interactions for the α -phase (left) and the β -phase (right).

This importance of the *para* substituents prompted the preparation of three new perfluoroaryl-dithiadiazolyl radicals with the potential to have large twist angles and form other structure-directing interactions that could inhibit dimerisation and yield a monomeric mode of association that might exhibit magnetic behaviour (Figure 1.11)⁸¹.

The next DTDA radical that did not exhibit dimerised radical pairs in the solid state to be identified, was $\text{BrC}_6\text{F}_4\text{CNSSN}^*$ (**3**)⁸¹. Radical **3** exhibits paramagnetic behaviour, but the solid-state arrangement shows a very different mode of association when compared to the linear mode of association observed for **2**. The mode of association observed in **3** results in a lack of long-range magnetic ordering, which can be described as the communication between radical electrons in the crystalline environment that allows for bulk magnetic ordering. The concept of magnetism in organic radicals will be discussed in detail in the next section.

The radical $\text{O}_2\text{NC}_6\text{F}_4\text{CNSSN}^*$ (**4**) was found to exhibit a linear mode of arrangement very similar to that of **2**; **4** was found to order as a ferromagnet below 1.6K⁸², with its crystal structure showing structure-directing $\text{O}_2\text{N}\cdots\text{S}$ interactions that result in rows of radicals, allowing for long-range ordering through ferromagnetic exchange interactions. The interesting behaviour of this radical prompted an experiment aimed to determine where the spin density resides on the dithiadiazolyl ring. This was achieved by a polarised neutron diffraction (PND) experiment, which is a direct method used to probe the spatial distribution of spin density⁸³. This experiment revealed that the majority of spin density is localised on the sulfur and nitrogen atoms of the radical ring with some negative spin density present on the carbon atom (Figure 1.12).

The negative spin density arises results from the SOMO producing a spin polarisation effect on the electrons that reside in three doubly occupied molecular orbitals. Two of the three doubly occupied orbitals exhibit *b* symmetry, which results in these orbitals not being nodal at the carbon atom. These two orbitals will exhibit β -spin (spin down) that is more localised on the carbon atom than the α -spin (spin up). The total spin density distribution can be described as the difference between the α - and β -spin, and the localisation of β -spin results in the accumulation of negative spin density on the carbon atom as there is no α -spin contribution⁵². The most recently reported perfluoroaryl-dithiadiazolyl radical found to exhibit monomeric radicals in the solid state is $\text{NCC}_6\text{F}_4\text{C}_6\text{F}_4\text{CNSSN}^*$ (**5**)⁵³. This radical shows some similarities to **2** as it behaves like a paramagnet and contains antiparallel rows of radicals linearly arranged by structure-directing $\text{CN}\cdots\text{S}$ interactions.

The ability of bulky substituents to inhibit dimerisation was shown to be successful with the synthesis of $2,4,6\text{-(F}_3\text{C)}_3\text{C}_6\text{H}_2\text{CNSSN}^*$ (**6**). This radical was found to crystallise in two phases (α and β) with different magnetic behaviours, which once again shows how the magnetic response is closely related to the solid-state structure⁶⁵.

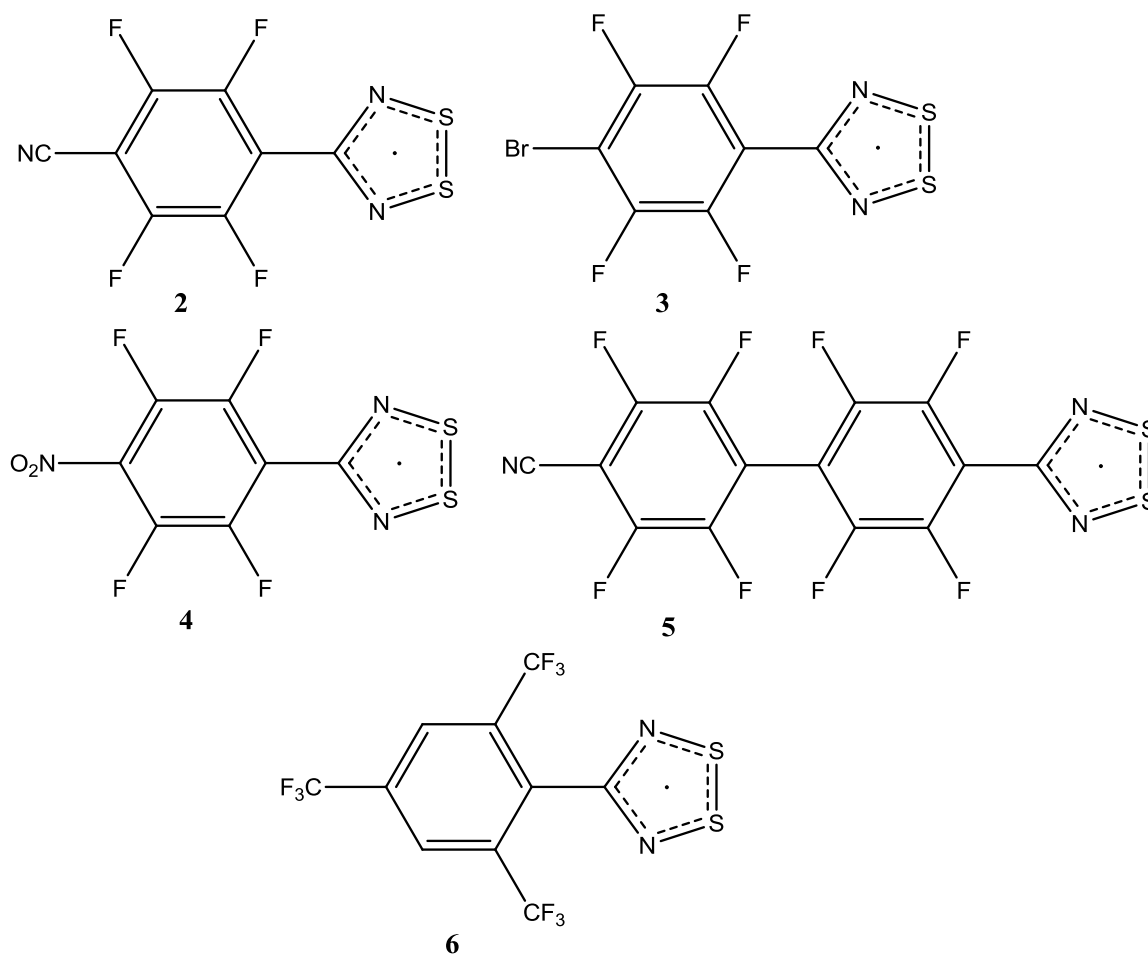


Figure 1.11: DTDA radicals that exhibit monomeric modes of association in the solid state: $\text{NCC}_6\text{F}_4\text{CNSSN}^\bullet$ (2), $\text{BrC}_6\text{F}_4\text{CNSSN}^\bullet$ (3), $\text{O}_2\text{NC}_6\text{F}_4\text{CNSSN}^\bullet$ (4) $\text{NCC}_6\text{F}_4\text{C}_6\text{F}_4\text{CNSSN}^\bullet$ (5) and $(\text{F}_3\text{C})_3\text{C}_6\text{H}_2\text{CNSSN}^\bullet$ (6).

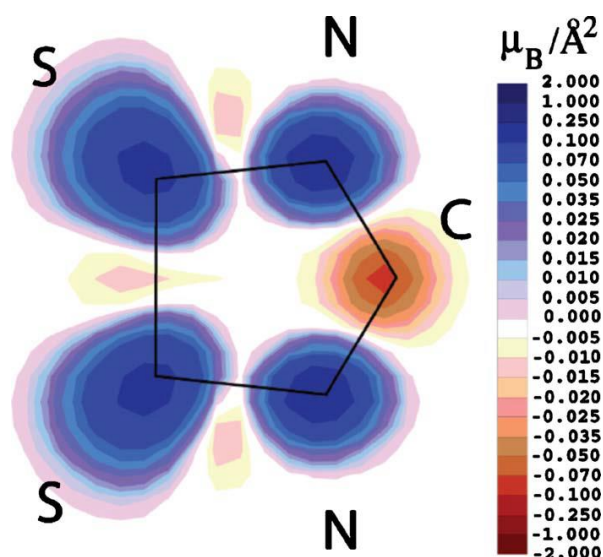


Figure 1.12: The spin density on the dithiadiazolyl ring of 4. Printed with permission from reference 83.

The studies on existing monomeric DTDA radicals suggest that bulky substituents, structure-directing intermolecular interactions and long-range ordering contribute to bulk magnetic

ordering in these organic magnets. Nevertheless, there have been many challenges when attempting to predict the solid-state structure of these radicals^{51,66-69}. This study aims to combine theoretical and experimental techniques in an attempt to predict the mode of association of DTDA radicals in the solid state.

1.3. Magnetism in organic radicals

The discussion on magnetism in the following sections (1.3.1 to 1.3.5) is based on the work by Coey, “Magnetism and Magnetic Materials”⁸⁴, which can be consulted for further details.

The discovery of the intrinsic spin of an electron was described in the work performed by Goudsmit and Uhlenbeck in 1925. Spin can be described as an electron having either an “up” or “down” orientation in a magnetic field. Spin is, furthermore, a source of the electron’s intrinsic magnetic moment, which can be described by the Bohr magneton: $\mu_B = 9.274 \times 10^{-24}$ A m². The properties that are observed in various magnetic materials arise from the magnetic moments present in their atomic electrons. It was shown in 1929 by Heisenberg that the interactions responsible for ferromagnetism are of an electrostatic nature and adhere to the quantum mechanics of the Pauli principle. From these observations Heisenberg derived a Hamiltonian that describes the interaction between two neighbouring atoms with total electronic spins (in units of Planck’s constant $\hbar = 1.055 \times 10^{-34}$ J s) of S_i and S_j , namely

$$H = -2JS_i \cdot S_j, \quad (1.1)$$

where J is the exchange constant. The exchange constant provides some interesting information, as a negative J describes an antiferromagnetic system, whereas a positive J value would describe a ferromagnetic system. In addition to these modes of magnetic ordering there is also paramagnetism, ferrimagnetism and weak ferromagnetism.

A paramagnetic material has the magnetic moments randomly oriented. These magnetic moments will align parallel to the application of an external magnetic field. Once the external field is removed, however, the magnetic moments will no longer be aligned and once again revert to being randomly oriented.

Ferromagnetism describes a material with magnetic moments aligned in a parallel fashion throughout the solid. Exposing this material to an external field will align the magnetic

moments parallel to the field, which results in a material that remains magnetised after the external field is removed. The different magnetic behaviours are illustrated in Figure 1.13.

Antiferromagnetism describes a material in which the magnetic moments are aligned in an antiparallel fashion, which results in no observable net magnetic moment. This behaviour does, however, differ from diamagnetism as the spins are not paired and antiferromagnetic materials can behave as a paramagnet above certain temperatures.

Ferrimagnetism is when antiparallel magnetic moments are different in their magnitude. Simply put, a net magnetic moment will arise from magnetic moments that are aligned in an antiparallel fashion, but differ in their magnitude.

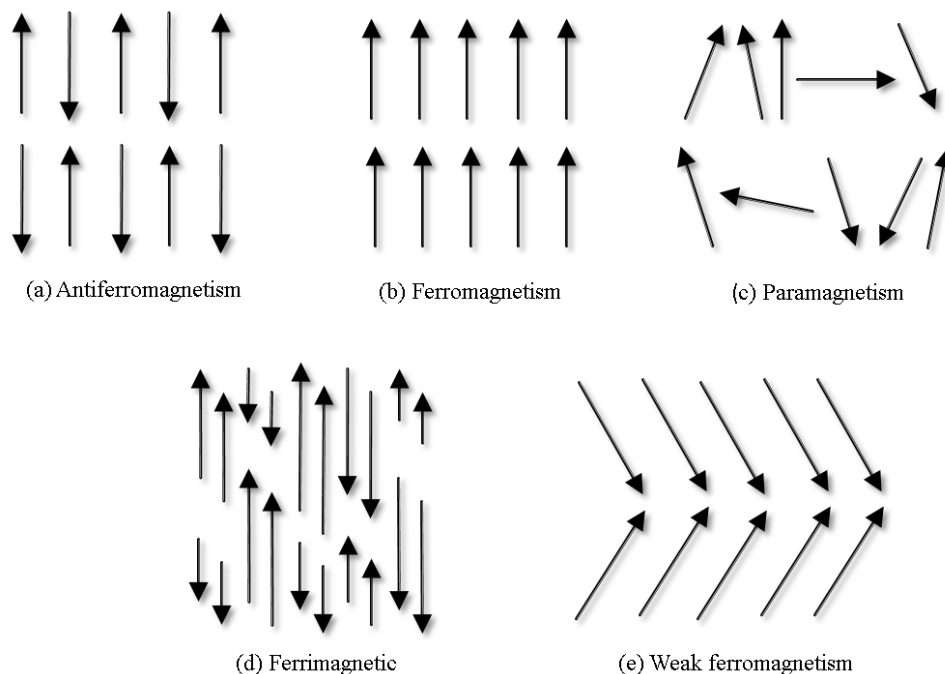


Figure 1.13: Schematic illustration of different magnetic behaviours, namely antiferromagnetism(a), ferromagnetism (b), paramagnetism (c), ferrimagnetism (d), and weak ferromagnetism (e).

Weak ferromagnetic ordering or weak ferromagnetism is observed for canted magnetic moments that are aligned in an antiparallel fashion, which results in a net magnetic moment.

The magnetic field strength is of great importance, as many materials exhibit hysteresis, a phenomenon studied by Ewing in 1881. Hysteresis is closely associated with spontaneous magnetism, which requires an external magnetic field of significant strength in order to reorient magnetic moments over a certain amount of time.

1.3.1. Hysteresis

The most studied magnetic behaviour is the spontaneous magnetisation of ferromagnetic materials and how these materials exhibit an irreversible response of their magnetisation M to an external magnetic field H . This phenomenon is represented by a hysteresis loop as illustrated in Figure 1.14.

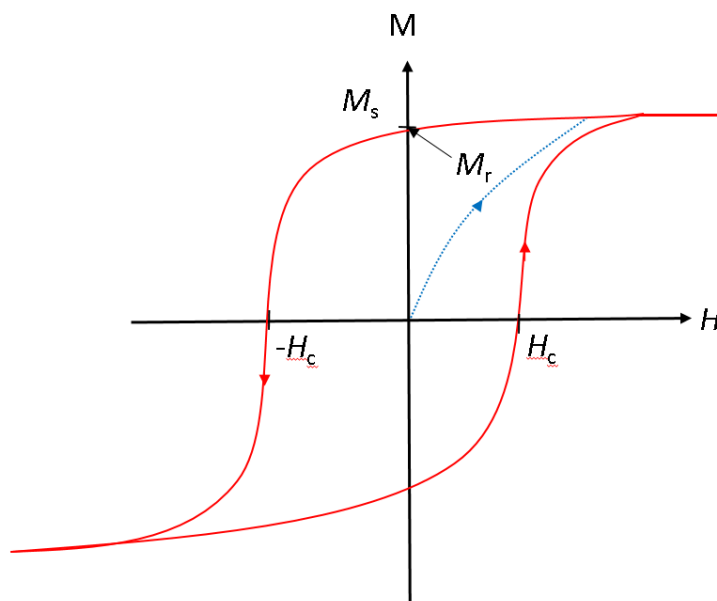


Figure 1.14: Hysteresis plot of a ferromagnetic system with *spontaneous magnetisation* (M_s), *remanence* (M_r) and *coercivity* (H_c). The blue dotted line represents the initial magnetisation.

The plot can also be used to determine properties of ferromagnetic materials, namely, M_s refers to *spontaneous magnetisation*, M_r refers to *remanence* and H_c refers to *coercivity*. *Spontaneous magnetisation* is when we observe magnetisation below the Curie temperature (T_c), which will be discussed later in this section. *Remanence* can be defined as the remnant magnetisation that persists after an external field is removed. *Coercivity* can be described as the resistance of a magnetic material to fluctuations in magnetisation and the field intensity required to fully demagnetise the material.

The shape of the hysteresis loop can also provide useful information. A hard magnetic material exhibits a broad loop and can be described as a permanent magnet that remains magnetised once the field has been removed. Soft magnetic materials exhibit narrow loops, which can be described as temporary magnets that lose their magnetisation once the field has been removed. Each material has external factors that contribute to unique M_r and H_c values, such as differences in sample shape, composition, microscopic properties and surface roughness.

1.3.2. Curie temperature (T_c)

Studies have shown that the spontaneous magnetisation of materials is strongly dependent on temperature. Furthermore, the temperature at which the alignment of the atomic magnetic moments result in magnetisation falling to zero can be defined as the Curie temperature T_c . Above the T_c value $M_s(T)$ is zero, whilst the $M_s(T)$ below T_c is reversible. The typical behaviour of a ferromagnet is illustrated by the plot in Figure 1.15. Once the temperature is elevated above the T_c , it is found that the ferromagnetic order collapses and the material becomes paramagnetic.

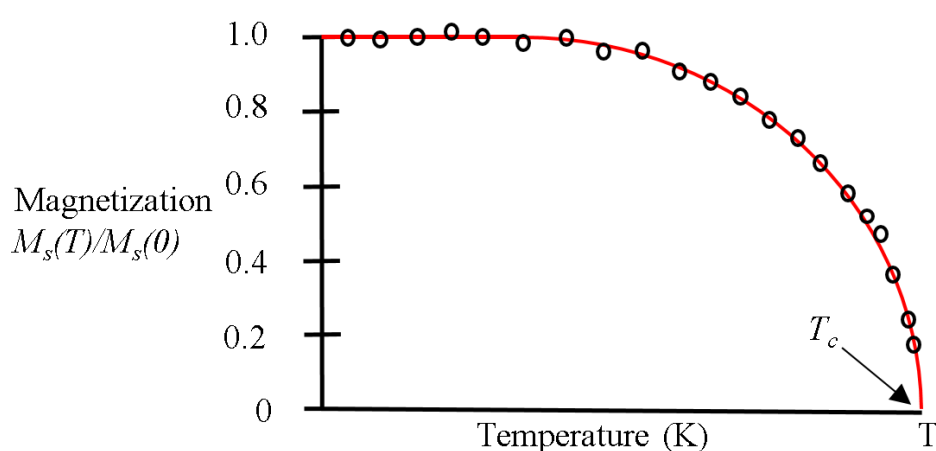


Figure 1.15: Determination of T_c from the temperature-magnetisation relationship.

1.3.3. Magnetic susceptibility

The molar paramagnetic susceptibility is represented by χ and varies with temperature. This is a dimensionless quantity that describes the average magnetisation per mole and can be measured according to equation 1.2

$$\chi = \bar{m}N_A/\vec{H}, \quad (1.2)$$

where \bar{m} is the average magnetisation per mole, N_A is Avogadro's number and \vec{H} is the applied field. We can calculate \bar{m} from equation 1.3

$$\bar{m} = \frac{\mu^2 \vec{H}}{3k_B T} \quad (1.3)$$

where k_B is the Boltzmann constant and μ the magnetic moment vector. A combination of equation 1.2 and 1.3 yields the Curie law

$$\chi = C/T, \quad (1.4)$$

where C is the Curie constant and χ is independent of temperature for some metallic paramagnets and most diamagnets. Interactions between the magnetic moments of individual spins results in a deviation from the ideal Curie Law. In reality, magnetic materials do not exhibit true Curie behaviour, but are rather defined as exhibiting near-Curie behaviour. The variation of magnetic susceptibility with temperature for ferromagnetic, paramagnetic, antiferromagnetic and diamagnetic materials is illustrated in Figure 1.16⁸⁵. The Curie law is sufficient in describing paramagnetism, but an additional parameter is required to describe ferromagnetism and antiferromagnetism. This is achieved by adapting equation 1.4 to yield the Curie-Weiss law

$$\chi = \frac{C}{T - T_c}, \quad (1.5)$$

where T_c is the additional parameter utilised in order to describe the other magnetic ordering behaviours. There is, however, a limit to the Curie-Weiss law as it fails to describe some materials where $T \gg T_c$ we replace T_c with the Weiss constant, θ .

$$\chi = \frac{C}{T - \theta} \quad (1.6)$$

Furthermore, if $\theta = 0$ equation 1.6 becomes equation 1.4 and describes paramagnetic behaviour. If $\theta > 0$ the system exhibits ferromagnetic behaviour and if $\theta < 0$ the system exhibits antiferromagnetic behaviour. In addition, the Néel temperature (T_N) describes the temperature where the antiferromagnetic behaviour becomes paramagnetic, as well as the thermal energy required to disrupt the magnetic ordering of the material.

Equations 1.5 and 1.6 can be utilised in order to measure the magnetic response of organic magnets to an applied field and can identify paramagnetic or diamagnetic materials, where the aforementioned materials do not order magnetically.

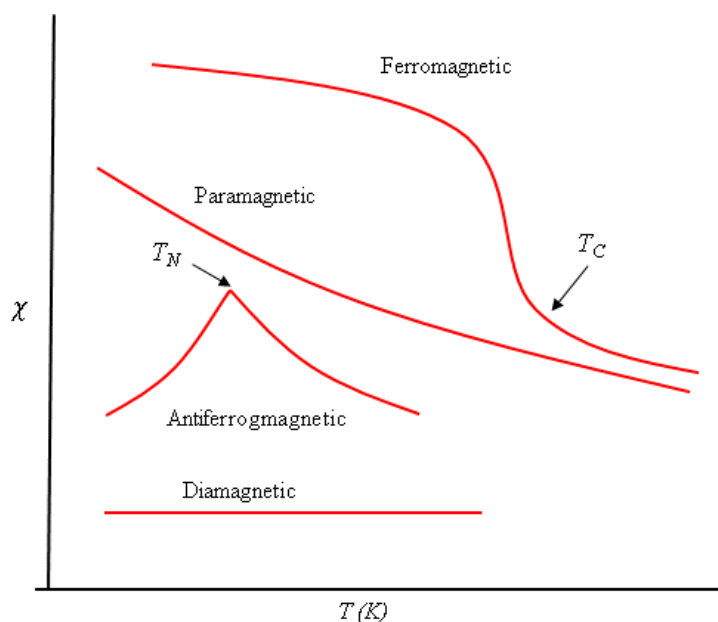


Figure 1.16: Variation of magnetic susceptibility (χ) with temperature (T) for ferromagnetic, paramagnetic, antiferromagnetic and diamagnetic materials. The Néel temperature (T_N) and Curie temperature (T_C) values can also be determined at the indicated areas.

1.3.4. Magnetic exchange

The Pauli principle states that two electrons within the same quantum system cannot have the same quantum state. Two neighbouring electrons can simply be represented by symbols i and j . A consequence of the Pauli principle is that there will be an energy difference between the $\uparrow_i\uparrow_j$ and $\downarrow_i\uparrow_j$ configurations, as the two states will exert repulsion on each other depending on their orientation. In organic magnetic systems we mostly deal with the singlet state (net magnetic moment = 0), doublet state, and the triplet states as illustrated in Figure 1.17. The state can be calculated by $2S + 1$, where the total spin S equals 0, $\frac{1}{2}$ and 1 for the singlet, doublet and triplet states respectively. We will focus on the transformation of a singlet state to triplet state system. In order to calculate the energy of the singlet and triplet states we make use of equation 1.7:

$$\varepsilon = -2 \left(\frac{J}{\hbar^2} \right) \mathbf{s}_1 \cdot \mathbf{s}_2, \quad (1.7)$$

The dot product $\mathbf{s}_1 \cdot \mathbf{s}_2$ can be expanded to $\frac{1}{2} [(\mathbf{s}_1 + \mathbf{s}_2)^2 - \mathbf{s}_1^2 - \mathbf{s}_2^2]$. Depending on whether the angular momentum calculated from the spin quantum numbers $S = s_1 + s_2$ is 0 or 1 (singlet: $\frac{1}{2} - \frac{1}{2} = 0$ or triplet: $\frac{1}{2} + \frac{1}{2} = 1$), the eigenvalues can be calculated as $-\frac{3}{4}\hbar^2$ or $+\frac{1}{4}\hbar^2$. By

calculating the energies of the singlet and triplet states, it is found that the energy splitting between the two states simplifies to $2J$. Heisenberg extended equation 1.7 to apply to systems with many-electron atomic spins \mathbf{S}_1 and \mathbf{S}_2 to yield the famous Hamiltonian, which is the same as equation 1.1

$$\mathcal{H} = -2J\mathbf{S}_1 \cdot \mathbf{S}_2, \quad (1.8)$$

where \mathbf{S}_1 and \mathbf{S}_2 are dimensionless spin operators and \hbar^2 has been incorporated in the exchange constant J . The exchange integral J has dimensions of energy and can be expressed in Kelvin if divided by the Boltzmann constant, $k_B(1.3807 \times 10^{-23} \text{ J.K}^{-1})$.

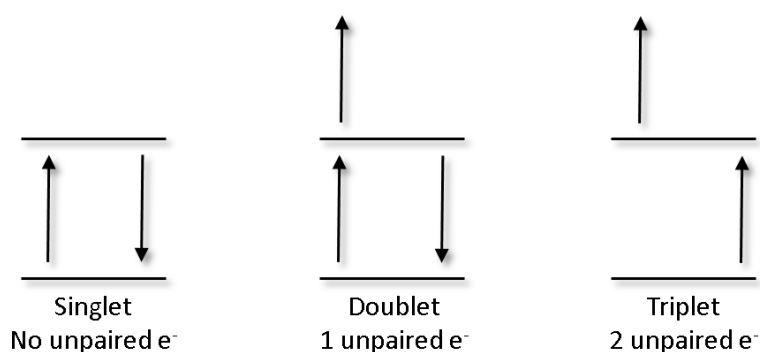


Figure 1.17: Schematic representation of the singlet, doublet and triplet states.

As discussed above, values of $J > 0$ indicate ferromagnetic interactions and $J < 0$ indicates antiferromagnetic interactions. If the system is comprised of different atoms arranged in a lattice, which is the case for the organic radical systems we study, the Hamiltonian is summed over atoms at lattice sites i, j :

$$\mathcal{H} = -2 \sum_{i>j} J_{ij} \mathbf{S}_i \cdot \mathbf{S}_j \quad (1.9)$$

It should also be mentioned that the Heisenberg Hamiltonian can only describe ferromagnetic and antiferromagnetic interatomic exchange coupling values. If we average the local correlations between \mathbf{S}_i and \mathbf{S}_j , we can relate J to T_c

$$T_c = \frac{2ZJS(S+1)}{3k_B} \quad (1.10)$$

where Z is the number of nearest neighbouring atoms. Using gadolinium as an example, we can calculate J/k_B to be 2.3 K utilising the literature value of $T_C = 291 (\pm 3 \text{ K})$, $S = 7/2$ and $Z = 12^{84}$.

Determination of J values is of great importance in DTDA radical chemistry as they provide valuable information regarding the magnetic exchange interactions and how the spins of the unpaired electrons communicate in a three-dimensional pathway.

1.3.5. Superconducting Quantum Interference Device (SQUID)

A range of experimental and theoretical methods can be utilised to calculate J values, but we will only discuss the commonly employed Superconducting Quantum Interference Device (SQUID) method. Magnetisation can be measured by utilising a SQUID magnetometer⁸⁴. This device measures the change in flux of a coil in a magnetic field with a sample positioned at the centre of the coil, as illustrated in Figure 1.18. This method is a very sensitive method capable of achieving values as low as 10^{-10} A m^2 . Measurement of magnetisation is achieved by introducing a solid sample in a gel capsule into the SQUID magnetometer.

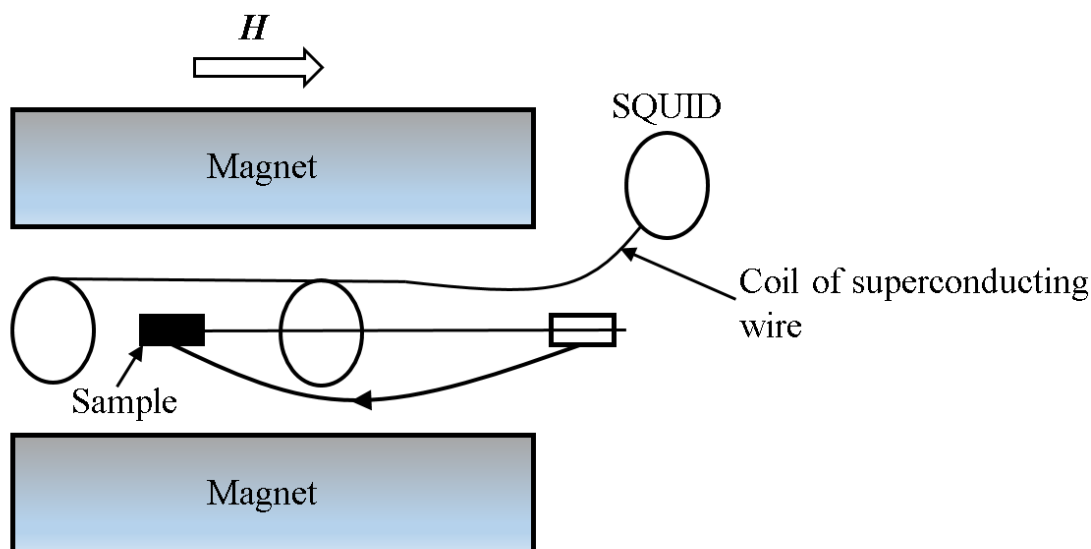


Figure 1.18: SQUID magnetometer diagram, adapted from reference 84.

A field H is then applied to measure the magnetisation M at different field strengths. These values are then plotted to construct what is known as a magnetisation curve. The susceptibility values χ can then be calculated from the slope of this curve, if the volume or density of the

sample is known ($M = \chi H$)⁸⁴. An alternative plot of χT vs temperature (T) can also be determined by keeping the applied field constant, where the plot provides the necessary values to determine J using equation 1.10. The shape of these plots are then analysed (Figure 1.16) to determine whether the sample exhibits ferromagnetic, paramagnetic, antiferromagnetic or diamagnetic behaviour.

1.3.6. Electron Paramagnetic Resonance

The discussion on electron paramagnetic resonance (EPR) in this section is based on the work by Weil and coworkers, “Electron paramagnetic Resonance: Elementary Theory and Practical Applications”⁸⁷, which can be consulted for further details.

Electro Paramagnetic Resonance (EPR) spectroscopy is routinely used to provide qualitative and quantitative analysis of the distribution of spin density in DTDA radicals. The unpaired electrons present in these radicals have spin quantum numbers of $m_s = +\frac{1}{2}$ and

$m_s = -\frac{1}{2}$. EPR spectroscopy focusses on measuring the energy required for a transition between these two spin states. In the absence of a magnetic field we find that these spin states are degenerate, however, this degeneracy is lost once we apply an external magnetic field as illustrated in Figure 1.19.

The lifting of the degeneracy by an externally applied magnetic field can be attributed to the Zeeman effect. This is due to the $m_s = +\frac{1}{2}$ and $m_s = -\frac{1}{2}$ quantum states having unique magnetic dipole moments that react differently to the external magnetic field.

The DTDA radical samples are typically prepared as either a solution or solid in a special quartz EPR tube, but other tubes are utilised in specialised experiments. In a typical EPR experiment, a quartz tube is used for experiments that are performed in the X-band region, which provides the necessary radiation (~ 9.75 G Hz) to detect DTDA radicals. This radiation is then guided towards a sample cavity held between two magnets. In an EPR experiment, the frequency of radiation is kept constant while tuning the magnetic field strength. Spectra can then be obtained by measuring the absorption of radiation, while tuning the magnetic-field strength. The first derivative of the data is usually preferred as this eliminates excess noise and therefore improves the overall signal-to-noise ratio (Figure 1.20).

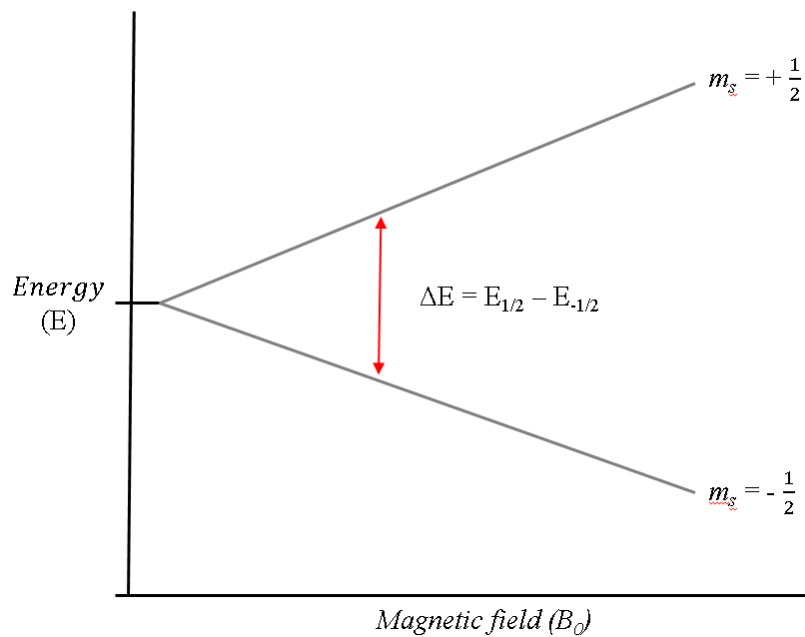


Figure 1.19: Lifting of the degeneracy between the $m_s = +\frac{1}{2}$ and $m_s = -\frac{1}{2}$ spin states once an external magnetic field is applied.

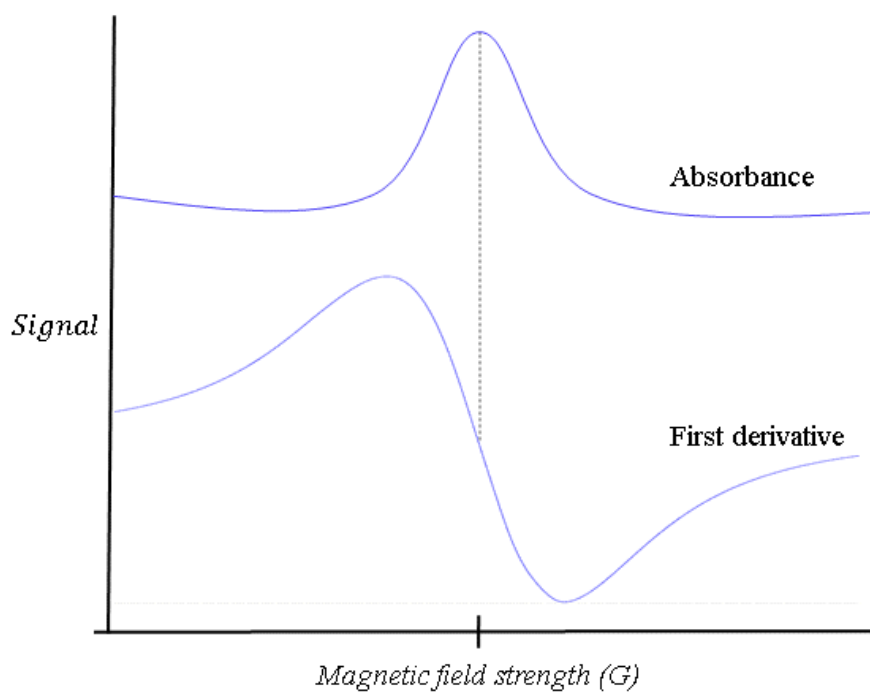


Figure 1.20: Absorbance and first derivative of an EPR spectrum

The spectrum can be used to extract important information, with the fundamental equation of EPR utilised for this purpose

$$E = m_s g_e \mu_b B_0, \quad (1.11)$$

where E is the energy of the electron; m_s is the spin quantum number; g_e is the g-factor of the electron and is a proportionality constant that describes the relationship between the magnetic moment μ and the angular momentum quantum number; μ_b is the Bohr magneton constant and B_0 is the strength of the external magnetic field. If we calculate the difference in energy between the two quantum states shown in Figure 1.19 this equation is simplified to:

$$h\nu = \Delta E = g_e \mu_b B_0 \quad (1.12)$$

The difference in energy is equivalent to a photon of energy ($h\nu$), as absorption of the photon will result in a transition between energy levels. Reorganising equation 1.12, we can calculate the g-factor from:

$$g_e = \frac{h\nu}{\mu_b B_0} \quad (1.13)$$

Literature studies have calculated the g-factor of a free electron to be 2.0023⁸⁸. The g-factors in DTDA radicals do not vary much from the observed value of a free electron, but small changes can be attributed to the presence of atoms with a large atomic mass. The EPR experiments performed in the solid state become much more complex as the g-factor is now influenced by three g-tensors that contribute to the spectrum, exhibiting various peaks of different intensities. The g-factor can thus be rewritten as:

$$g_e = g_{xx} + g_{yy} + g_{zz} \quad (1.14)$$

Another characteristic of EPR spectra is a phenomenon known as hyperfine coupling, which arises from the interactions between the nearby dipoles of neighbouring electron spins or nuclear that generate their own magnetic fields. The EPR signal splits into a number of lines that can be calculated using $2NI + 1$, where N is the number of equivalent nuclei with a spin of I . The spectral pattern will follow Pascal's triangle (Table 1.1). The size of splitting is due to

the hyperfine coupling constant, given as a_E , where the E represents the element to which the electron is coupling. The coupling constant can be measured between peaks or troughs and describes the distribution of unpaired spin density over the molecules⁸⁹.

A typical solution-state EPR spectrum of a DTDA radical is illustrated in Figure 1.21. This spectrum shows coupling of the two ^{14}N nuclei ($I=1$) to give a quintet with signal intensities of 1:2:3:2:1.

Table 1.1: The number of nuclei with their corresponding intensities.

N	Relative intensity
0	1
1	1:1:1
2	1:2:3:2:1
3	1:3:6:7:6:3:1
4	1:4:10:16:19:16:10:4:1
5	1:5:20:45:51:45:20:15:51

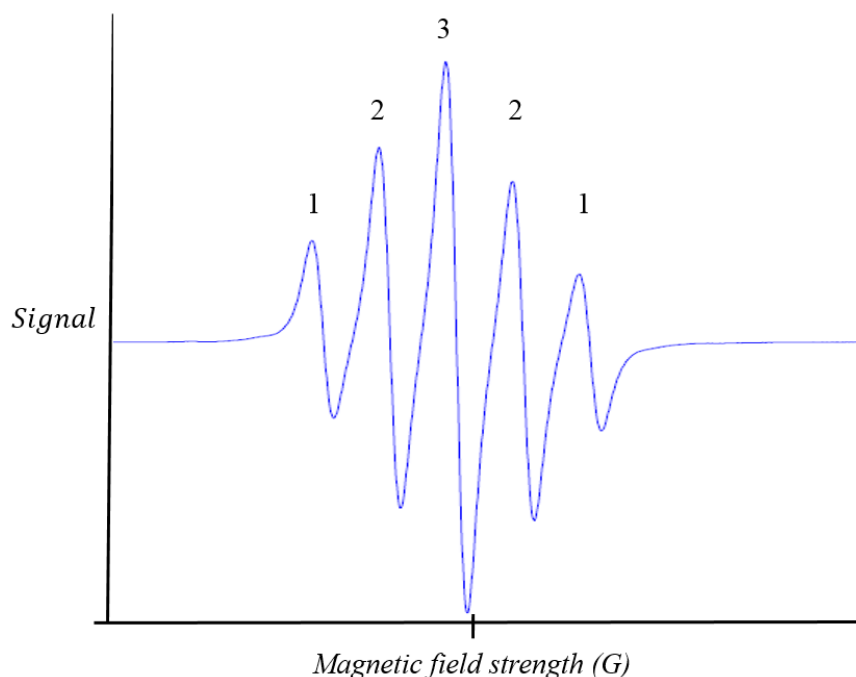


Figure 1.21: Hyperfine coupling of radical 1 exhibiting a 1:2:3:2:1 pattern of intensities due to coupling of two ^{14}N .

1.4. Theoretical calculations

Theoretical studies have been shown to calculate magnetic interactions^{90,91}, EPR⁹², UV-Visible spectroscopy⁹³, spin density⁵², charge-density⁹⁴ and dimerisation enthalpy values⁷⁹ that are in good agreement with experimental data.

These calculations make use of the Density Functional Theory (DFT) method, which can provide an accurate description of open-shell molecules. The DFT method makes use of a set of equations developed by Kohn and Sham⁹⁵ that are analogous to the Hartree-Fock (HF) equations, although they also include correlation effects. The HF method is a very basic method that approximates the wave function and energy of a many-body system. This method assumes that the exact, N-body wave function of the system can be approximated by a single Slater determinant, which is an expression that describes the wave function of a multi-electron system. The variational method is then applied in order to generate N-coupled equations for the N-spin orbitals. The variational method approximates the ground and excited states. A solution to these approximated equations yields Hartree-Fock wave functions from which the energy of the system can be calculated⁹⁶. The Kohn-Sham equations replace the Hartree-Fock equations with an exchange-correlation functional, which includes both exchange and electron correlation effects.

The Kohn-Sham methods can be fitted with the third generation dispersion correction (E_{disp}) as developed by Grimme and coworkers in 2011⁹⁷ to calculation the total energy:

$$E_{DFT-D} = E_{KS-DFT} + E_{disp} \quad (1.15)$$

The E_{disp} in equation 1.15 can be defined as given in the following equation:

$$E_{disp} = -s_6 \sum_{i=1}^{N-1} \sum_{j=1+1}^N \frac{C_6^{ij}}{R_{ij}^6} f_{damp}(R_{ij}). \quad (1.16)$$

The s_6 symbol represents a scaling factor that depends on the specific density functional used, N represents the number of atoms, C_6^{ij} represents the dispersion coefficient for an atom pair ij given by the equation $C_6^{ij} = \sqrt{C_6^i C_6^j}$, and R_{ij} represents the interatomic distance. One of the key ingredients of all DFT-D methods is the damping function f_{damp} , which determines the

short-range behaviour of the dispersion corrections to avoid errors for electrons of atoms in close proximity to one another:

$$f_{damp}(R_{ij}) = \frac{1}{1 + e^{a(R_r - R_{ij})}} \quad (1.17)$$

The R_r symbol represents the sum of the atomic radii, while a is a constant equal to 20.

1.4.1. Geometry optimisation calculations on DTDA radicals

The DFT method can be used to perform geometry optimisation calculations on the crystal structure coordinates of DTDA radicals that exhibit dimerised radical pairs or radicals that adopt a monomeric mode of association. Calculations on open-shell molecules can be performed with three methods that treat the unpaired electrons in the system differently, namely the restricted open-shell, unrestricted and restricted methods. The restricted open-shell method incorporates a spin annihilation step to correct for spin contamination. Spin contamination can be defined as errors occurring when a wave function consists of mixed spin states. This should be avoided as it results in lower total energies and the overall spin density can be affected by errors in geometry and population analysis⁹⁸.

The unrestricted method minimises spin contamination by treating the α - (up) and β (down) spin populations in an independent way. This results in α - and β -molecular orbitals that can be singly occupied or empty.

The restricted method uses molecular orbitals that can be doubly occupied or empty. This will result in different orbital energies as the restricted calculations have less variational freedom than the unrestricted calculations⁹⁹. The differences between these three methods are illustrated using doubly- and singly-filled molecular orbitals in Figure 1.22. All calculations require basis sets, which are used to describe molecular orbitals (Figure 1.22), that are combined to construct an appropriate wave function. Pople-style basis sets provide high quality wave functions that have been fitted with polarisation and diffuse functions to obtain accurate energies¹⁰⁰.

Geometry optimisation calculations that utilise a suitable DFT method and basis set will yield final structures as illustrated in Figures 1.23 and 1.24. The fully optimised geometry of a dimerised pair of **1** is shown in Figure 1.23 and shows the S...S contacts that result from favourable interactions between the SOMOs. The fully optimised geometry of radicals with strong interactions that inhibit dimerisation is shown in Figure 1.24 for the known monomeric

radical 2. The final structures will show the minimum energy configuration, from which various electronic properties can be calculated.

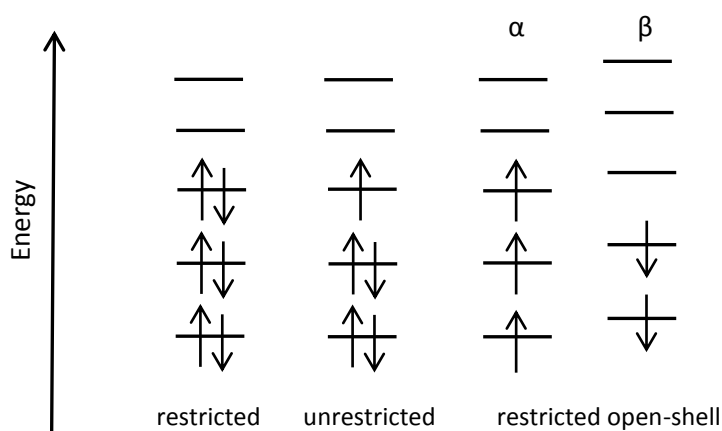


Figure 1.22: The electrons filling molecular orbitals in the restricted, unrestricted and restricted open-shell method.

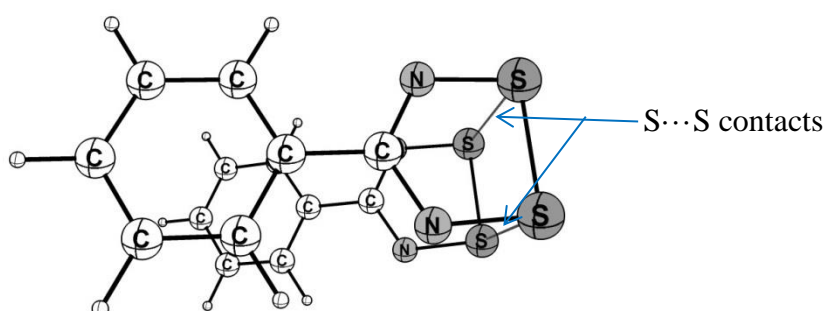


Figure 1.23: The S...S contacts that result in dimerisation of 1.

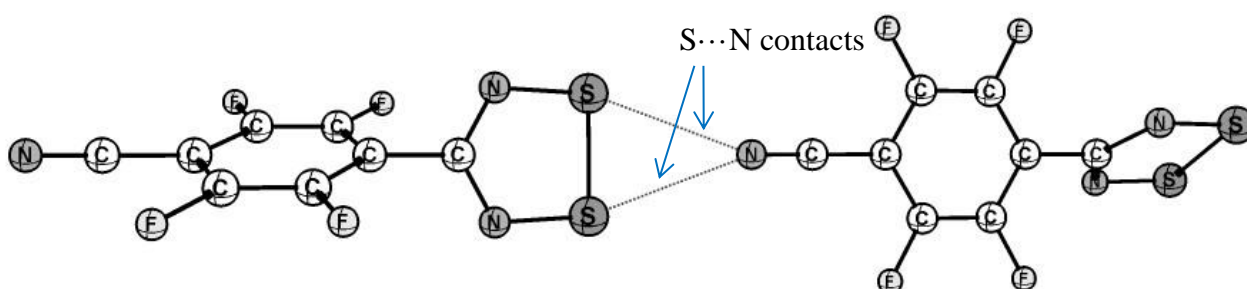


Figure 1.24 The S...NC contacts that result in the monomeric mode of association in 2.

1.4.2. Calculation of intermolecular interaction energies

Optimised geometries of DTDA radicals exhibiting the same mode of association, but with differing R groups, exhibit varying intermolecular interaction energies between DTDA radicals⁷⁵. These energies are obtained by performing counterpoise-corrected calculations that minimise the

basis set superposition error (BSSE)^{101,102}. Most basis sets are susceptible to BSSE, which occurs when the basis-set functions of close fragments overlap. The counterpoise correction was developed by Boys and Bernardi and corrects for the BSSE by calculating the energy of each individual fragment, but utilising all the basis functions of the total system. The uncorrected interaction energy between fragments A and B can be calculated as:

$$\Delta E_{int}(AB) = E_{AB}^{AB}(AB) - E_A^A(A) - E_B^B(B), \quad (1.18)$$

where the superscripts represent the basis-set functions used and the subscripts represent the geometry of the fragment, while the symbol in parentheses represents the chemical system. Thus, $E_{AB}^{AB}(AB)$ represents the energy of the complex of the two fragments A and B and the combination of the basis-sets functions of A and B, calculated at the geometry of the complex. Likewise, the energies of monomers A and B are calculated at their own geometries and basis sets. Equation 1.18 can be corrected for BSSE by calculating the amount by which monomer A is stabilised by the basis set of monomer B (and vice versa). This can be calculated as:

$$\begin{aligned} \Delta E_{BSSE}(A) &= E_A^{AB}(A) - E_A^A(A), \\ \Delta E_{BSSE}(B) &= E_B^{AB}(B) - E_B^B(B), \end{aligned} \quad (1.19)$$

where we subtract the energy of monomer A with its monomer basis set from the energy of monomer A with the basis set of the complex AB (and likewise for monomer B). If we subtract the error in equation 1.19 from the interaction energy in equation 1.18, we can rewrite the equation for interaction energy as:

$$\Delta E_{int}^{CP}(AB) = E_{AB}^{AB}(AB) - E_A^{AB}(A) - E_B^{AB}(B) \quad (1.20)$$

From equation 1.20 we see that the counterpoise correction minimises the BSSE by using the basis set of complex AB for both monomers A and B.

1.4.3. Potential energy surface (PES) scans

Potential energy surface (PES) scans are performed by calculating the energies of a series of structures obtained by varying a specific geometric parameter, e.g. a torsion angle. Scans such

as these are often employed to analyse chemical processes as well as the stability of structures¹⁰³. Three different classes of stationary points can be identified on a PES, namely minimum and maximum to stationary points and saddle points. In this study, the minima correspond to stable structures and the maxima to a transition states (TS). It should be mentioned that the minima and the maxima identified on a 2D plot could be saddle points on a higher dimensional plot.

The energies and corresponding torsion angles can then be used to construct a two-dimensional plot. It was already mentioned in section 1.2 that the twist angle has been shown to strongly influence the mode of association that radicals exhibit in the solid state^{62,78,104}. The twist angle and various other geometrical parameters play an important role in the strength of intermolecular interactions. These intermolecular interactions play also determine why some radicals prefer a monomeric or dimeric mode of association (see Figure 1.7) and can be investigated by performing PES scans on a selected geometrical parameter in one of the DTDA radical systems. One such example is shown in Figure 1.25, where the torsion angle (Φ) is varied between atoms S1-S2-S3-S4 in order to determine how this will affect the S...S contacts that result in dimerisation.

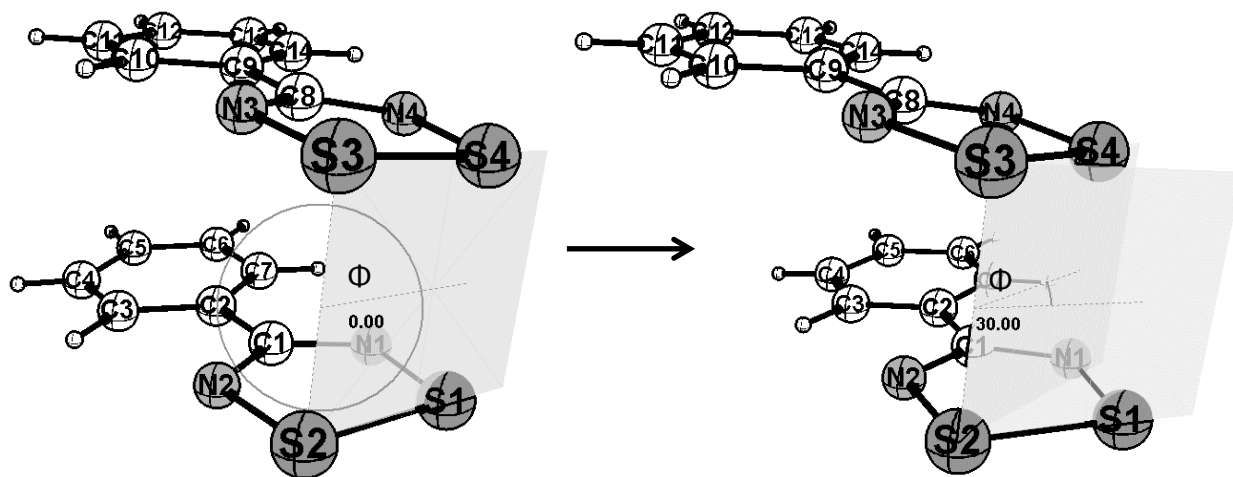


Figure 1.25: PES scan performed by varying the S4-S3-S2-S1 torsion angle (Φ) of the *cisoid* dimer of 1.

1.4.4. Electrostatic Surface Potential

Electrostatic Surface Potential (ESP) maps can be generated using the AIMALL software packages¹⁰⁵. The ESP maps can be used to visualise the size, shape and charge distribution of

DTDA radicals three-dimensionally. The electrostatic potential can be calculated a

$$V = \sum_i \frac{q_i}{\epsilon |r_i - F|}$$

where q_i is the charge at point r_i in a medium of dielectric constant ϵ . The electrostatic potential at each point can then be mapped on an isosurface to produce an ESP map. The ESP map of PhCNSSN[•] calculated at an electron density surface of 0.01 e bohr⁻¹ is shown in Figure 1.26, where the regions of maximum electrostatic potential (blue) values at 100 kcal/mol and minimum electrostatic potential (red) at -45 kcal/mol were chosen to best visualise the ESP map.

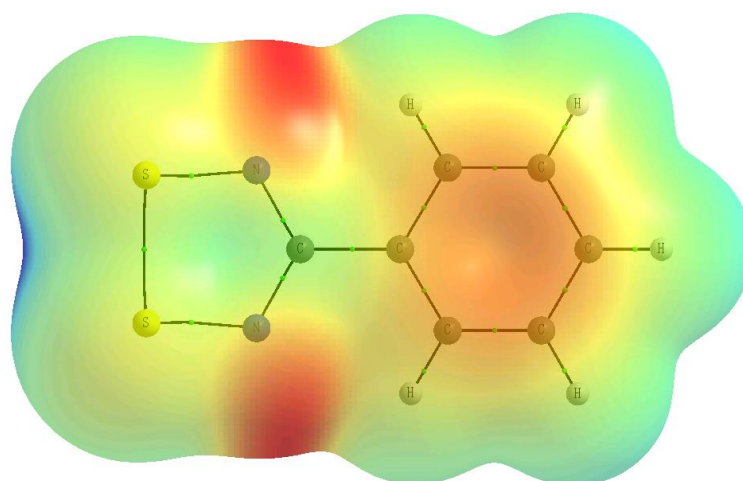


Figure 1.26: ESP map of 1. Maximum electrostatic potential (blue) values at 100 kcal/mol and minimum electrostatic potential (red) at -45 kcal/mol.

1.4.5 Atoms in Molecules

Bader described the theory of Atoms in Molecules (AIM) in 1985¹⁰⁶. The AIM model is based on the ability of a quantum mechanical state function to provide the energy of a molecular structure as well as describe areas where charge density (ρ) is locally depleted and concentrated. The gradient vector of ρ is capable of providing both a qualitative and quantitative understanding of the topology of ρ , where the gradient vector ($\nabla\rho$) is defined as the first derivative of ρ and describes the change in ρ . A three-dimensional atomic partition can be achieved by a zero flux surface and additionally describes a potential-based picture of atoms in molecules¹⁰⁷. The zero flux surface divides the charge distribution of the system into

atoms. At point on the zero flux surface, where $\nabla\rho = 0$, is defined as a critical point (3, -1). The 3 indicates the rank/dimension of the critical point [i.e. 3-dimensional (3D)] and the -1 indicates that the point is at a 2-dimensional (2D) maximum and 1-dimensional (1D) minimum. The -1 can be explained by the minima and maxima in each dimension and has two minima and one maximum, which can be calculated as: $-1 + -1 + 1 = -1$. There are four different kinds of 3D critical points¹⁰⁶, namely:

- | | |
|---------|--|
| (3, -3) | All curvatures of the electron density are negative indicating a local 3D maximum; |
| (3, -1) | Two curvatures are negative, indicating a 2D-maximum, while one is positive and showing a 1D minimum perpendicular to the associated plane defined by the negative curvatures; |
| (3, +1) | Two curvatures are positive, <i>i.e.</i> a 2D-minimum while one curvature is negative at a 1D maximum; |
| (3, +3) | All three curvatures are positive at a local 3D-minimum. |

The second derivative of ρ is defined as the Laplacian ($\nabla^2\rho$). The Laplacian indicates regions where ρ is locally concentrated or depleted, and is given by:

$$L(\mathbf{r}) = \nabla^2\rho(\mathbf{r}).$$

A region where $\nabla^2\rho(\mathbf{r}) < 0$ indicates a concentration of ρ at a point r , while a region where $\nabla^2\rho(\mathbf{r}) > 0$ indicates a depletion of ρ at point r . In this study, the properties of intermolecular interactions will be investigated for radicals in both monomeric and dimeric modes of association.

1.4.6. Pancake bonding

The π bonding in dimerised radicals exhibit features that are analogous to an F-F covalent bond with significant contributions from charge shift effects¹⁰⁸. This mode of bonding has been described as pancake bonding¹⁰⁹ to distinguish it from covalent bonding and π -stacking¹¹⁰, where the latter result from multipole and van der Waals interactions and pancake bonding result from radical electrons delocalised over a dimer. The classification of pancake bonds as

a separate class of intermolecular bonding relies on several elements¹¹⁰⁻¹¹⁶: (a) Stabilising interactions from direct overlap of SOMOs that result in the different dimer configurations (Figure 1.7), (b) Dimers exhibit a singlet configuration, while undimerised radicals exhibit a doublet configuration, (c) The low energy electronic transitions correspond to a HOMO-LUMO transition in the radical complex, (d) This mode of bonding results in bond lengths characteristically shorter than van der Waals radii typically in the range of 2.8 to 3.3 Å and (e) The bonding energies are smaller than those of chemical bonds but larger than those of π -stacking dimers. The interaction between antibonding (π^*) SOMOs results in a two-electron multicentre ($2e/mc$) bonding that stabilises the dimer, which is illustrated in Figure 1.27. Pancake bonds have also been observed in other radical π -dimer systems, for which it has been suggested that the design of stronger pancake bonds may lead to novel organic conductors with magnetic properties¹⁰⁸.

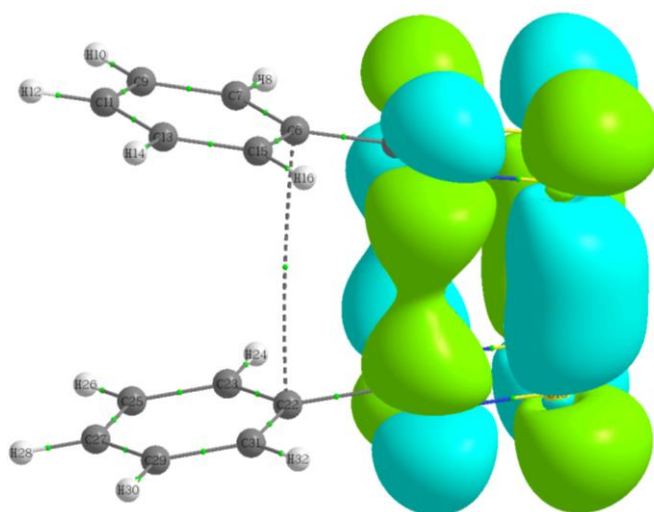


Figure 1.27: The $2e/mc$ pancake bonding of 1.

1.5. General aims

The general aim of this project was to establish a methodology that can be used to predict the preferred configuration of new DTDA.

The first objective was to synthesise a series of DTDA that are known to exhibit some magnetic properties in the solid state. Crystals of suitable quality and size were utilised for high-resolution X-ray diffraction (HXR) and polarised neutron diffraction (PND) experiments, where the two sets of data were jointly refined to visualise the spin density that resides on the DTDA ring. Furthermore, the network of intermolecular interactions that result

in the DTDAs adopting either a monomer or dimer configuration was also investigated. A theoretical study was then used to investigate the role that intermolecular interactions play in why some DTDAs dimerise, while this process is inhibited for other DTDAs. Lastly, the experimental and theoretical results were jointly studied to predict the preferred configuration of DTDAs that have not yet been synthesised.

Thesis overview

Much research has been dedicated to understanding why some DTDA radicals prefer to be monomeric in the solid state, but this phenomenon can still not be explained with certainty owing to the complexity of the factors that influence the solid-state arrangement of these molecules. This thesis will aim to rationalise the formation of monomeric radicals using a combined experimental and theoretical approach. Chapter 2 contains a brief overview of the materials and methods utilised in this thesis.

The synthesis of the 4-(4-cyano-2,3,5,6-tetrafluorophenyl)-1,2,3,5-dithiadiazolyl (**2**), 4-(4'-bromo-2',3',5',6'-tetrafluoro-phenyl)-1,2,3,5-dithiadiazolyl (**3**), 4-(2,3,5,6-tetrafluoro-4-nitrophenyl)-1,2,3,5-dithiadiazolyl (**4**) and 4-(2,6-difluoro-phenyl)-1,2,3,5-dithiadiazolyl (**7**) radicals will be described in Chapter 3. The interesting magnetic behaviour of radicals **2** – **4** make them suitable candidates for a unique experimental technique that jointly refines the data from a high resolution X-ray diffraction (HXRd) and polarised neutron diffractions (PND) experiments, which provides for visualisation of the spin density in these DTDA radicals. Growing large crystals of high quality resulted in identifying some additional interesting properties in radicals **2** – **4** that will also be further investigated. The interesting flexible properties of **2** will also be discussed in this chapter. Radical **7** was additionally synthesised to be used in a co-crystallisation with radical **2**. This experiment did not produce a co-crystal, but was found to encourage the growth of the α -phase of **2**. This experiment will be further explored as well as a possible explanation for why the growth of this phase occurs in the presence of **7**. Also discussed here is a novel co-crystal consisting of 4-(4'-bromo-2',3',5',6'-tetrafluoro-phenyl)-1,2,3,5-dithiadiazolyl radical and 2,3,5,6-tetrafluoro-4-nitrobenzotrile (**3-cox**). Lastly, the joint refinement technique (discussed in section 3.6.2) will also be described to determine the spin-dependent electron density of radical **4**.

In Chapter 4, the results obtained by various computational methods will be discussed in the context of investigating the intermolecular energies present in DTDA radicals. Furthermore,

we will identify why some interactions favour dimerised DTDA radicals, while other interactions yield DTDA radicals that prefer a monomeric mode of association.

In Chapter 5, the results obtained from calculations performed on substituted radicals will be discussed to determine how substitution affects whether radicals prefer monomeric or dimeric modes of association.

Potential Energy Surface (PES) scans (PES) were performed to identify where the strongest intermolecular interactions occur for various monomeric and dimeric modes of association and these are described in Chapter 6. Geometry optimisation calculations of pairs of radicals that have not yet been synthesised, which have arranged in the different modes of association will also be discussed. Finally, energy calculation of fully optimised geometries provide information about which of the radicals prefer to dimerise or remain monomeric in the solid state.

The last chapter reviews the work that has been done on DTDA radicals in this project and how future work could expand on the results that have been reported in this thesis.

References

- (1) Gomberg, M. *Journal of the American Chemical Society* **1900**, 22, 757.
- (2) Gatteschi, D. *Advanced Materials* **1994**, 6, 635.
- (3) Amorati, R.; Lucarini, M.; Mugnaini, V.; Pedulli, G. F.; Minisci, F.; Recupero, F.; Fontana, F.; Astolfi, P.; Greci, L. *The Journal of Organic Chemistry* **2003**, 68, 1747.
- (4) Reddy, T. J.; Iwama, T.; Halpern, H. J.; Rawal, V. H. *The Journal of Organic Chemistry* **2002**, 67, 4635.
- (5) Asandei, A. D.; Chen, Y. *Macromolecules* **2006**, 39, 7549.
- (6) Geiser, U.; Schlueter, J. A. *Chemical Reviews* **2004**, 104, 5203.
- (7) Rostro, L.; Wong, S. H.; Boudouris, B. W. *Macromolecules* **2014**, 47, 3713.
- (8) Miller, J. S. *Materials Today* **2014**, 17, 224.
- (9) Ratera, I.; Veciana, J. *Chemical Society Reviews* **2012**, 41, 303.
- (10) Cirujeda, J.; Ochando, L. E.; Amigó, J. M.; Rovira, C.; Rius, J.; Veciana, J. *Angewandte Chemie International Edition in English* **1995**, 34, 55.
- (11) Lipunova, G. N.; Fedorchenko, T. G.; Chupakhin, O. N. *Russian Chemical Reviews* **2013**, 82, 701.
- (12) Rawson, J. M.; Alberola, A.; Whalley, A. *Journal of Materials Chemistry* **2006**, 16, 2560.
- (13) Neumann, W. P.; Uzick, W.; Zarkadis, A. K. *Journal of the American Chemical Society* **1986**, 108, 3762.
- (14) Mugnaini, V.; Calzolari, A.; Ovsyannikov, R.; Vollmer, A.; Gonidec, M.; Alcon, I.; Veciana, J.; Pedio, M. *The Journal of Physical Chemistry Letters* **2015**, 6, 2101.
- (15) Ballester, M.; Pascual, I. *The Journal of Organic Chemistry* **1991**, 56, 4314.
- (16) Rawson, J. M.; Palacio, F.; Veciana, J.; Arçon, D.; Deumal, M.; Inoue, K.; Kinoshita, M.; Novoa, J. J.; Palacio, F.; Prassides, K.; Rawson, J. M.; Rovira, C., Eds.; *Springer Berlin Heidelberg: Berlin, Heidelberg*, 2001, p 93.
- (17) Koivisto, B. D.; Ichimura, A. S.; McDonald, R.; Lemaire, M. T.; Thompson, L. K.; Hicks, R. G. *Journal of the American Chemical Society* **2006**, 128, 690.
- (18) Takeda, K.; Mito, M.; Kawae, T.; Deguchi, H.; Takagi, S.; Okumura, M.; Kawakami, T.; Yamaguchi, K.; Kinoshita, M. *Chemical Physics Letters* **1999**, 308, 181.
- (19) Ullman, E. F.; Osiecki, J. H.; Boocock, D. G. B.; Darcy, R. *Journal of the American Chemical Society* **1972**, 94, 7049.
- (20) Kinoshita, M. *Philosophical Transactions of the Royal Society of London. Series A: Mathematical, Physical and Engineering Sciences* **1999**, 357, 2855.
- (21) Tamura, M.; Nakazawa, Y.; Shiomi, D.; Nozawa, K.; Hosokoshi, Y.; Ishikawa, M.; Takahashi, M.; Kinoshita, M. *Chemical Physics Letters* **1991**, 186, 401.
- (22) Sugano, T.; Blundell, S. J.; Lancaster, T.; Pratt, F. L.; Mori, H. *Physical Review B* **2010**, 82, 180401.
- (23) Koivisto, B. D.; Hicks, R. G. *Coordination Chemistry Reviews* **2005**, 249, 2612.
- (24) Hicks, R. G.; Hooper, R. *Inorganic Chemistry* **1999**, 38, 284.
- (25) Rakitin, O. A. *ChemInform* **2012**, 43, no.
- (26) Brook, D. J. R.; Lynch, V.; Conklin, B.; Fox, M. A. *Journal of the American Chemical Society* **1997**, 119, 5155.
- (27) Mukai, K.; Yano, T.; Ishizu, K. *Tetrahedron Letters* **1981**, 22, 4661.
- (28) Brook, D. J. R.; Fornell, S.; Stevens, J. E.; Noll, B.; Koch, T. H.; Einfeld, W. *Inorganic Chemistry* **2000**, 39, 562.
- (29) Kamachi, M.; Enomoto, H.; Shibasaka, M.; Mori, W.; Kishita, M. *Polymer Journal* **1986**, 18, 439.
- (30) Mukai, K.; Kawasaki, S.; Jamali, J. B.; Achiwa, N. *Chemical Physics Letters* **1995**, 241, 618.
- (31) Azuma, N.; Ishizu, K.; Mukai, K. *The Journal of Chemical Physics* **1974**, 61, 2294.
- (32) Plater, M. J.; Kemp, S.; Coronado, E.; Gómez-García, C. J.; Harrington, R. W.; Clegg, W. *Polyhedron* **2006**, 25, 2433.

- (33) Banister, A. J.; Clarke, H. G.; Rayment, I.; Shearer, H. M. M. *Inorganic and Nuclear Chemistry Letters* **1974**, 10, 647.
- (34) Meuwesen, A. *Berichte der deutschen chemischen Gesellschaft (A and B Series)* **1931**, 64, 2311.
- (35) Eley, D. D.; Jones, K. W.; Littler, J. G. F.; Willis, M. R. *Transactions of the Faraday Society* **1966**, 62, 3192.
- (36) Yu, X.; Mailman, A.; Lekin, K.; Assoud, A.; Robertson, C. M.; Noll, B. C.; Campana, C. F.; Howard, J. A. K.; Dube, P. A.; Oakley, R. T. *Journal of the American Chemical Society* **2012**, 134, 2264.
- (37) Banister, A. J. *Nature Physical Science* **1972**, 239, 69.
- (38) Oakley, R. T. In *Progress in Inorganic Chemistry*; John Wiley & Sons, Inc.: 1988, p 299.
- (39) Cordes, A. W.; Haddon, R. C.; Oakley, R. T. *Advanced Materials* **1994**, 6, 798.
- (40) Haddon, R. C. *Nature* **1975**, 256, 394.
- (41) Chivers, T. *World Scientific* **2005**.
- (42) Bryan, C. D.; Cordes, A. W.; Goddard, J. D.; Haddon, R. C.; Hicks, R. G.; MacKinnon, C. D.; Mawhinney, R. C.; Oakley, R. T.; Palstra, T. T. M.; Perel, A. S. *Journal of the American Chemical Society* **1996**, 118, 330.
- (43) Cordes, A. W.; Goddard, J. D.; Oakley, R. T.; Westwood, N. P. C. *Journal of the American Chemical Society* **1989**, 111, 6147.
- (44) Leitch, A. A.; Brusso, J. L.; Cvrkalj, K.; Reed, R. W.; Robertson, C. M.; Dube, P. A.; Oakley, R. T. *Chemical Communications* **2007**, 3368.
- (45) Robertson, C. M.; Leitch, A. A.; Cvrkalj, K.; Reed, R. W.; Myles, D. J. T.; Dube, P. A.; Oakley, R. T. *Journal of the American Chemical Society* **2008**, 130, 8414.
- (46) Robertson, C. M.; Myles, D. J. T.; Leitch, A. A.; Reed, R. W.; Dooley, B. M.; Frank, N. L.; Dube, P. A.; Thompson, L. K.; Oakley, R. T. *Journal of the American Chemical Society* **2007**, 129, 12688.
- (47) Beer, L.; Brusso, J. L.; Cordes, A. W.; Haddon, R. C.; Itkis, M. E.; Kirschbaum, K.; MacGregor, D. S.; Oakley, R. T.; Pinkerton, A. A.; Reed, R. W. *Journal of the American Chemical Society* **2002**, 124, 9498.
- (48) Yu, X.; Mailman, A.; Dube, P. A.; Assoud, A.; Oakley, R. T. *Chemical Communications* **2011**, 47, 4655.
- (49) (a) Yu, X.; Mailman, A.; Lekin, K.; Assoud, A.; Robertson, C. M.; Noll, B. C.; Campana, C. F.; Howard, J. A. K.; Dube, P. A.; Oakley, R. T. *Journal of the American Chemical Society* **2012**, 134, 2264.
- (50) Pivtsov, A. V.; Kulik, L. V.; Makarov, A. Y.; Blockhuys, F. *Physical Chemistry Chemical Physics* **2011**, 13, 3873.
- (51) Bryan, C. D.; Cordes, A. W.; Goddard, J. D.; Haddon, R. C.; Hicks, R. G.; MacKinnon, C. D.; Mawhinney, R. C.; Oakley, R. T.; Palstra, T. T. M.; Perel, A. S. *Journal of the American Chemical Society* **1996**, 118, 330.
- (52) Campo, J.; Luzón, J.; Palacio, F.; Rawson, J. *Spin Density Distribution and Interaction Mechanisms in Thiazyl-based Magnets*, 2006.
- (53) Alberola, A.; Less, R.; Palacio, F.; Pask, C.; Rawson, J. *Molecules* **2004**, 9, 771.
- (54) Rawson, J. M.; Luzon, J.; Palacio, F. *Coordination Chemistry Reviews* **2005**, 249, 2631.
- (55) Banister, A. J.; Rawson, J. M. *Studies in Inorganic Chemistry* **1992**, 14, 323.
- (56) Rawson, J. M.; Banister, A. J.; Lavender, I. *Advances in Heterocyclic Chemistry* **1995**, 62, 137.
- (57) Banister, A. J.; Bricklebank, N.; Clegg, W.; Elsegood, M. R. J.; Gregory, C. I.; Lavender, I.; Rawson, J. M.; Tanner, B. K. *Journal of the Chemical Society, Chemical Communications* **1995**, 679.
- (58) Burford, N.; Johnson, J. P.; Passmore, J.; Schriver, M. J.; White, P. S. *Journal of the Chemical Society, Chemical Communications* **1986**, 966.
- (59) Passmore, J.; Sun, X. *Inorganic Chemistry* **1996**, 35, 1313.

- (60) Fairhurst, S. A.; Sutcliffe, L. H.; Preston, K. F.; Banister, A. J.; Partington, A. S.; Rawson, J. M.; Passmore, J.; Schriver, M. J. *Magnetic Resonance in Chemistry* **1993**, 31, 1027.
- (61) Luzón, J.; Campo, J.; Palacio, F.; McIntyre, G. J.; Goeta, A. E.; Ressouche, E.; Pask, C. M.; Rawson, J. M. *Physica B: Condensed Matter* **2003**, 335, 1.
- (62) Haynes, D. A. *CrystEngComm* **2011**, 13, 4793.
- (63) Banister, A. J.; Gorrell, I. B.; Clegg, W.; Jorgensen, K. A. *Journal of the Chemical Society, Dalton Transactions* **1991**, 1105.
- (64) Boéré, R. T.; Roemmele, T. L. *Coordination Chemistry Reviews* **2000**, 210, 369.
- (65) Alberola, A.; Clarke, C. S.; Haynes, D. A.; Pascu, S. I.; Rawson, J. M. *Chemical Communications* **2005**, 4726.
- (66) Vegas, A.; Perez-Salazar, A.; Banister, A. J.; Hey, R. G. *Journal of the Chemical Society, Dalton Transactions* **1980**, 1812.
- (67) Cordes, A. W.; Goddard, J. D.; Oakley, R. T.; Westwood, N. P. C. *Journal of the American Chemical Society* **1989**, 111, 6147.
- (68) Clarke, C. S.; Pascu, S. I.; Rawson, J. M. *CrystEngComm* **2004**, 6, 79.
- (69) Bricklebank, N.; Hargreaves, S.; Spey, S. E. *Polyhedron* **2000**, 19, 1163.
- (70) Fairhurst, S. A.; Johnson, K. M.; Sutcliffe, L. H.; Preston, K. F.; Banister, A. J.; Hauptman, Z. V.; Passmore, J. *Journal of the Chemical Society, Dalton Transactions* **1986**, 1465.
- (71) Brooks, W. V. F.; Burford, N.; Passmore, J.; Schriver, M. J.; Sutcliffe, L. H. *Journal of the Chemical Society, Chemical Communications* **1987**, 69.
- (72) Britten, J.; Hearn, N. G. R.; Preuss, K. E.; Richardson, J. F.; Bin-Salamon, S. *Inorganic Chemistry* **2007**, 46, 3934.
- (73) Decken, A.; Ebdah, M.; Kowalczyk, R. M.; Landee, C. P.; McInnes, E. J. L.; Passmore, J.; Shuvaev, K. V.; Thompson, L. K. *Inorganic Chemistry* **2007**, 46, 7756.
- (74) Shuvaev, K. V.; Decken, A.; Grein, F.; Abedin, T. S. M.; Thompson, L. K.; Passmore, J. *Dalton Transactions* **2008**, 4029.
- (75) Constantinides, C. P.; Eisler, D. J.; Alberola, A.; Carter, E.; Murphy, D. M.; Rawson, J. M. *CrystEngComm* **2014**, 16, 7298.
- (76) Beldjoudi, Y.; Haynes, D. A.; Hayward, J. J.; Manning, W. J.; Pratt, D. R.; Rawson, J. M. *CrystEngComm* **2013**, 15, 1107.
- (77) Banister, A. J.; Bricklebank, N.; Lavender, I.; Rawson, J. M.; Gregory, C. I.; Tanner, B. K.; Clegg, W.; Elsegood, M. R. J.; Palacio, F. *Angewandte Chemie International Edition in English* **1996**, 35, 2533.
- (78) Melen, R. L.; Less, R. J.; Pask, C. M.; Rawson, J. M. *Inorganic Chemistry* **2016**, 55, 11747.
- (79) Domagala, S.; Haynes, D. A. *CrystEngComm* **2016**, 18, 7116.
- (80) Clarke, C. S.; Haynes, D. A.; Smith, J. N. B.; Batsanov, A. S.; Howard, J. A. K.; Pascu, S. I.; Rawson, J. M. *CrystEngComm* **2010**, 12, 172.
- (81) Antorrena, G.; Palacio, F.; E. Davies, J.; Hartley, M.; M. Rawson, J.; B. Smith, J. N.; Steiner, A. *Chemical Communications* **1999**, 1393.
- (82) Alberola, A.; Less, R. J.; Pask, C. M.; Rawson, J. M.; Palacio, F.; Oliete, P.; Paulsen, C.; Yamaguchi, A.; Farley, R. D.; Murphy, D. M. *Angewandte Chemie International Edition* **2003**, 42, 4782.
- (83) Luzon, J.; Campo, J.; Palacio, F.; McIntyre, G. J.; Rawson, J. M.; Less, R. J.; Pask, C. M.; Alberola, A.; Farley, R. D.; Murphy, D. M.; Goeta, A. E. *Physical Review B* **2010**, 81, 144429.
- (84) Fox, A. *Magnetism and Magnetic Materials*, by J.M.D. Coey, 2011; Vol. 52.
- (85) Woolley, J. C.; Brun del Re, R.; Al-Najjar, M.; Lamarche, G. *Journal of Magnetism and Magnetic Materials* **1995**, 145, 23.
- (86) Korolev, A. V.; Kurkin, M. I.; Sokolov, O. B.; Orlova, N. B. *Physics of the Solid State* **2010**, 52, 561.
- (87) A. Weil, J.; Bolton, J.; E. Wertz, J. *Electron paramagnetic Resonance : Elementary Theory and Practical Applications*, 2017.

- (88) Wolos, A.; Szyszko, S.; Drabinska, A.; Kaminska, M.; Strzelecka, S. G.; Hruban, A.; Materna, A.; Piersa, M.; Borysiuk, J.; Sobczak, K.; Konczykowski, M. *Physical Review B* **2016**, *93*, 155114.
- (89) Alonso, P. J.; Antorrena, G.; Martínez, J. I.; Novoa, J. J.; Palacio, F.; Rawson, J. M.; Smith, J. N. B. *Applied Magnetic Resonance* **2001**, *20*, 231.
- (90) Deumal, M.; LeRoux, S.; Rawson, J. M.; Robb, M. A.; Novoa, J. J. *Polyhedron* **2007**, *26*, 1949.
- (91) Luzón, J.; Campo, J.; Palacio, F.; McIntyre, G. J.; Rawson, J. M. *Polyhedron* **2005**, *24*, 2579.
- (92) Rawson, J. M.; Clarke, C. S.; Bruce, D. W. *Magnetic Resonance in Chemistry* **2009**, *47*, 3.
- (93) Beldjoudi, Y.; Osorio-Roman, I.; Nascimento, M. A.; Rawson, J. M. *Journal of Materials Chemistry C* **2017**, *5*, 2794.
- (94) Domagała, S.; Kosci, K.; Robinson, S. W.; Haynes, D. A.; Woźniak, K. *Crystal Growth & Design* **2014**, *14*, 4834.
- (95) Kohn, W.; Sham, L. J. *Physical Review* **1965**, *140*, A1133.
- (96) Frank, N. H. *Physical Review* **1937**, *51*, 577.
- (97) Grimme, S.; Ehrlich, S.; Goerigk, L. *Journal of Computational Chemistry* **2011**, *32*, 1456.
- (98) Davidson, E. R.; Clark, A. E. *International Journal of Quantum Chemistry* **2005**, *103*, 1.
- (99) Glaesemann, K. R.; Schmidt, M. W. *The Journal of Physical Chemistry A* **2010**, *114*, 8772.
- (100) Krishnan, R.; Binkley, J. S.; Seeger, R.; Pople, J. A. *The Journal of Chemical Physics* **1980**, *72*, 650.
- (101) Boys, S. F.; Bernardi, F. *Molecular Physics* **1970**, *19*, 553.
- (102) Simon, S.; Duran, M.; Dannenberg, J. J. *The Journal of Chemical Physics* **1996**, *105*, 11024.
- (103) Rhoad, J. S.; Cagg, B. A.; Carver, P. W. *The Journal of Physical Chemistry A* **2010**, *114*, 5180.
- (104) Beneberu, H. Z.; Tian, Y.-H.; Kertesz, M. *Physical Chemistry Chemical Physics* **2012**, *14*, 10713.
- (105) Keith, T. A. *TK Gristmill Software* **2017**
- (106) Bader, R. F. W. *Accounts of Chemical Research* **1985**, *18*, 9.
- (107) Bader, R. F. W. *Accounts of Chemical Research* **1975**, *8*, 34.
- (108) Cui, Z.-h.; Lischka, H.; Beneberu, H. Z.; Kertesz, M. *Journal of the American Chemical Society* **2014**, *136*, 12958.
- (109) Suzuki, S.; Morita, Y.; Fukui, K.; Sato, K.; Shiomi, D.; Takui, T.; Nakasuji, K. *Journal of the American Chemical Society* **2006**, *128*, 2530.
- (110) Rawson, J. M.; Palacio, F. In *π -Electron Magnetism: From Molecules to Magnetic Materials*; Veciana, J., Arçon, D., Deumal, M., Inoue, K., Kinoshita, M., Novoa, J. J., Palacio, F., Prassides, K., Rawson, J. M., Rovira, C., Eds.; Springer Berlin Heidelberg: Berlin, Heidelberg, 2001, p 93.
- (111) Novoa, J. J.; Lafuente, P.; Del Sesto, R. E.; Miller, J. S. *Angewandte Chemie* **2001**, *113*, 2608.
- (112) Lü, J.-M.; Rosokha, S. V.; Kochi, J. K. *Journal of the American Chemical Society* **2003**, *125*, 12161.
- (113) Jakowski, J.; Simons, J. *Journal of the American Chemical Society* **2003**, *125*, 16089.
- (114) Tian, Y.-H.; Kertesz, M. *Journal of the American Chemical Society* **2010**, *132*, 10648.
- (115) Tian, Y.-H.; Kertesz, M. *The Journal of Physical Chemistry A* **2011**, *115*, 13942.
- (116) Beneberu, H. Z.; Tian, Y.-H.; Kertesz, M. *Physical Chemistry Chemical Physics* **2012**, *14*, 10713.

2 Materials and Methods

Introduction

The potential of DTDA radicals to dimerise depends on a complex interplay of intermolecular interactions within the crystalline environment. A combination of experimental and theoretical methods were utilised to study the intermolecular interactions, so that the results can be used to predict whether DTDA radicals will dimerise or remain monomeric in the solid state. The experimental and computational methods used in this study will be discussed.

2.1. Experimental techniques

2.1.1. Synthesis of 1,2,3,5-dithiadiazolyl radicals

The first reported synthesis of 1,2,3,5-dithiadiazolium chlorides $[\text{RCN}_2\text{S}_2]\text{Cl}$ involved treating trichlorocyclotrithiazene (NSCI) with nitriles RCN ($\text{R}=\text{Ph}$). This was subsequently treated with SCl_2 to yield 4-phenyl-1,2,3,5-dithiadiazolium chloride¹. Several other synthetic procedures have been developed since then in order to yield dithiadiazolium salts^{2,3}.

A more recent method (Figure 2.1) was employed in this work, where the nitrile is reacted with hexamethyldisilazane (HMDS) and n-butyllithium (n-BuLi) in diethyl ether⁴. The intermediate N-lithio salt can be condensed by either SCl_2 or S_2Cl_2 in order to yield dithiadiazolylium cation chloride salt. The primary reducing agent utilised in this procedure was triphenylantimony (Ph_3Sb). If this proved unsuccessful, either silver powder (Ag) or zinc-copper couple (Zn-Cu) were used as a reducing agent, where both required tetrahydrofuran (THF) that had that has been freeze-dry-thawed for 3 cycles. Purification of the dithiadiazolyl radicals was achieved by vacuum sublimation on to a cold finger. This procedure was followed for the synthesis of all dithiadiazolyl radicals. In some cases, the starting nitrile was not available commercially. The synthesis of these nitriles was carried out using established procedure⁵⁻⁷. Details of all synthesis are given in Addendum A on page 218 of this thesis.

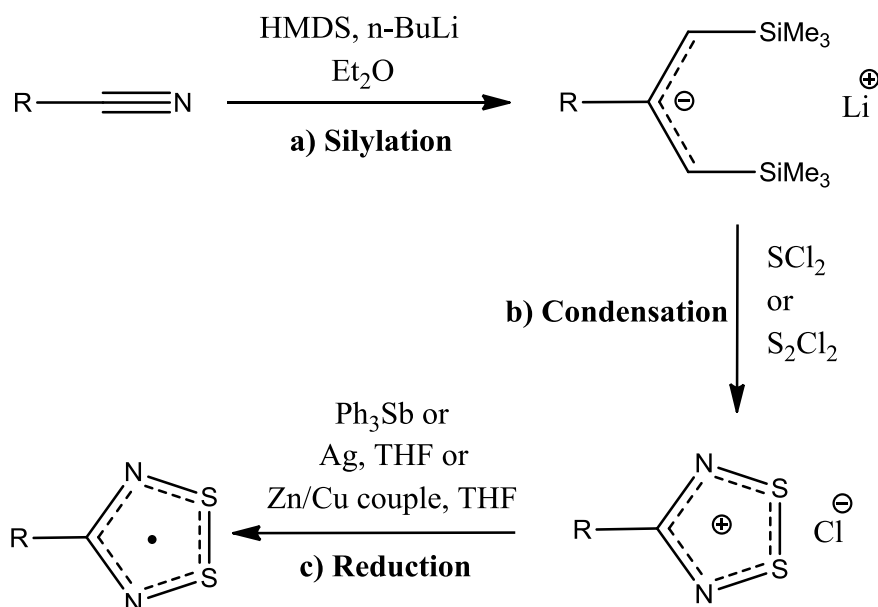


Figure 2.1: The three synthetic steps required to form DTDA radicals, namely silylation (a), condensation (b) and reduction (c).

2.1.2. Single-Crystal X-ray Diffraction Analysis

The crystals obtained in this study were analysed by Single-Crystal X-ray diffraction (SCD). SCD is a popular analytical technique that provides information about the internal lattices of crystalline substances, including unit cell dimensions and molecular structures, yielding information such as bond lengths and bond angles of molecules within the crystals. All crystals that were analysed in this study were inspected under a microscope to select those of an appropriate size and uniform shape. Each crystal chosen for analysis was then mounted on a MiTeGen mount. This was placed onto the goniometer head of the single-crystal diffractometer. All X-ray data were collected on one of the following four instruments:

1. A Bruker 3-circle SMART Apex II X-ray diffractometer equipped with an INCOATEC I μ S HB microfocuss sealed tube (Mo K α radiation $\lambda = 0.71073 \text{ \AA}$) fitted with a multilayer monochromator. Data were captured with a CCD (charge-coupled device) area detector. Data collection was carried out at 100 K using an Oxford Cryosystems cryostat (700 series Cryostream Plus) attached to the diffractometer.
2. A dual source Bruker 3-circle SMART Apex II X-ray diffractometer equipped with an INCOATEC I μ S HB microfocuss sealed tube (Mo K α radiation $\lambda = 0.71073 \text{ \AA}$ or Cu K α radiation $\lambda = 1.54184 \text{ \AA}$) fitted with a multilayer monochromator. Data were captured with a CCD (charge-coupled device) area detector. Data collection was carried out at

100 K using an Oxford Cryosystems cryostat (700 series Cryostream Plus) attached to the diffractometer.

3. A Bruker 4 axis KAPPA D8 Venture X-ray diffractometer equipped with an INCOATEC I μ S 3.0 microfocus sealed tube (Mo K α radiation $\lambda = 0.71073 \text{ \AA}$) fitted with multilayer mirror optics monochromator. Data were captured with a PHOTON II CMOS detector. Data collection was carried out at 100 K using an Oxford Cryosystems cryostat (800 series Cryostream Plus) attached to the diffractometer.
4. A Diffraction Supernova Dual Wavelength Microfocus diffractometer equipped with an ATLAS CCD detector using Mo K α radiation ($\lambda = 0.71073 \text{ \AA}$). The crystal was mounted and cooled to 100 K under a stream of nitrogen using the Oxford Cryosystems gas flow apparatus. This instrument was utilised during a visit to the University of Lorraine.

All data reduction, absorption corrections and unit cell determinations were carried out using the APEXIII diffractometer software developed by Bruker⁸. All structure solution and refinement was carried out using the SHELX⁹ suite of programs under the X-Seed interface¹⁰. The X-seed interface permits the analysis of data that has been obtained from SCD experiments, including visualisation of the crystal structure.

2.1.3. Polarised neutron diffraction

Polarised neutron diffraction (PND) data was obtained from experiments performed at Laboratoire Leon Brillouin in Saclay, France, in order to obtain spin densities for paramagnetic thiazyl radicals¹². The polarised neutron diffractometer has a thermal neutron beam of 1.4 \AA , which is generated by a vertically-focusing graphite monochromator. Polarisation of the beam is achieved by utilising a supermirror bender of 800 mm in length and a working cross-section of 20 x 50 mm installed in the monochromator shielding. The Bidim26 position-sensitive detector used for experiments covers an angular range of $24^\circ \times 24^\circ$ in both vertical and horizontal directions. This allows for the measurement of the flipping ratio of multiple reflections¹³. PND data for the 4-(2,3,5,6-tetrafluoro-4-nitrophenyl)-1,2,3,5-dithiadiazolyl was generously provided by Javier Campo and coworkers¹⁴.

2.1.4. Joint refinement

The joint refinement model was developed by Deutsch and coworkers and incorporated in the MoPro software package¹⁵. This model consists of a pseudo atomic spin-split model that combines the data from high resolution X-ray diffraction (HXRd) and polarised neutron diffraction (PND) experiments¹⁶. This model is capable of refining the charge and spin density states and allowing for the visualisation of the spin-up and spin-down contributions to the electron density distributions. The experimental charge density was modelled by utilising the pseudo atomic multipolar model developed by Hansen and Coppens¹⁷. This experiment was performed to calculate the spin distribution on the heterocyclic radical ring and see how well it compares to theoretical studies. Furthermore, results obtained from the joint refinement model can be used to calculate the properties of the structure-directing intermolecular interactions present in monomeric radicals and help explain why these interactions may overcome the tendency of the radicals to dimerise.

The HXRd data were collected on a Diffraction Supernova Dual Wavelength Microfocus diffractometer equipped with an ATLAS CCD detector using Mo K α radiation ($\lambda = 0.71073$ Å)¹⁸. The crystal was mounted and cooled to 100K under stream of nitrogen using the Oxford Cryosystems gas flow apparatus. An analytical absorption correction was carried out by indexing the faces of the crystal¹⁹. The data sets were merged utilising the SORTAV²⁰ software package giving 5489 unique reflections.

The PND experiment was performed on a D3 lifting-counter diffractometer at the Institut Laue Langevin (ILL)¹⁴. A large crystal with dimensions 1 x 1 x 1 mm³ was placed in a cryomagnet and cooled to 1.5 K. A Heusler crystal was used to monochromate the incoming neutron beam, which was measured to have a wavelength of 0.843 Å and a polarisation of 0.93. A cryoflipper was used to alternate the polarisation between parallel and antiparallel relative to the magnetic field of 9 T was applied to the sample. A total of 296 flipping ratios were obtained to $\sin \theta/\lambda = 0.72$ Å⁻¹. After merging of symmetry-equivalent reflections, a total of 128 independent ratios were available.

The joint refinement analysis of the data was performed in collaboration with Nicolas Claiser from the University of Lorraine, France.

2.1.5. Crystallographic refinement

The independent atom model (IAM) refinement was undertaken using the SHELXL97 software package. The multipolar refinement was carried out with Molymx using the Hansen-Coppens multipolar atom model with an $I/\sigma > 3$ cut-off on reflections throughout the refinement steps. The xyz (positios) and U_{ij} parameters of all atoms were then further refined at high angle ($\sin(\theta)/\lambda > 0.9 \text{ \AA}^{-1}$) to ensure the deconvolution of the thermal motion from the deformation electron density. For each atom, the κ , κ' , P_{val} and P_{lm} values were refined at low angles ($\sin(\theta)/\lambda < 0.9 \text{ \AA}^{-1}$) according to their position and their chemical equivalence. The expansion/contraction parameters of atoms located on the two-fold axis were different from their counterparts on general positions. The C, O and F atoms were modelled to the octapolar level and the S atom to the hexadecapolar level. The refinements were cycled between high (refinement of U_{ij} and xyz) and low (refinement of κ , κ' , P_{val} and P_{lm}) angles. The core and valence scattering factors were obtained from the Clementi & Roetti wavefunctions²¹. Local symmetry and chemical equivalence restraints were applied through all the refinements. Lastly, all the parameters were refined with the whole set of data.

2.1.6. Electron paramagnetic resonance (EPR)

EPR spectroscopy was performed at 298K with a Bruker EMXplus X-band spectrometer (8-inch ER 072 magnet, 2.7 kW power supply, EMX-m40X microwave bridge operating from 9.3 – 9.9 GHz) with a high-sensitivity continuous wave resonator. Experiments were performed in both the solid- and solution-state, where samples were diluted in dichloromethane (DCM). Spectra were then recorded in the area range that describes the coupling to the ^{14}N nuclei in DTDA radicals²².

2.2. Computational methods

2.2.1. Cambridge Structure Database (CSD) searches

The Cambridge Structural Database (CSD)²³ was established in 1965 and is the world's largest repository for crystal structures of small organic and metal-organic compounds. Each crystal structure in the CSD can be identified by a six-letter refcode, a unique identifier assigned to

every new entry in the CSD. In addition to raw three-dimensional structural data, the database also contains bibliographic, chemical and physical property information for close to a million crystal structures analysed using X-ray and neutron diffraction. Each crystal structure undergoes a series of extensive validation and cross-checking tests by expert chemists and crystallographers to ensure the validity of the data. All of the crystal structures that pass these tests can be accessed by various software programs that are associated with the database; these can be subdivided into several interfaces:

Conquest: Searches for crystal structures²⁴

Mercury: Visualisation and analysis of crystal structures²⁵

Prequest: Validation of crystal structure and chemical information for entry to the CSD

Isostar: Intermolecular interaction occurrence studies²⁷

Mogul: Retrieval of molecular geometry data from the CSD¹¹.

All CSD searches in this study were performed on CSD v5.38 with the November 2016 update utilising the ConQuest V1.19 search program. The search for dithiadiazolyl radicals was performed by creating a query that searches for all structures containing the heterocyclic dithiadiazolyl radical $\text{RCN}_2\text{S}_2^{\cdot}$ and for which the 3D coordinates have been determined. The structures were then visualised with Mercury and the coordinates used in further calculations.

2.2.2. Geometry optimisation and calculation of intermolecular interaction energies

Full geometry optimisation was performed with the Gaussian 09 rev. E.01²⁸ software package. Structures were optimised using the B3LYP, UB3LYP and ROB3LYP density functionals and the 6-311++G(d,p)²⁹ basis set with the Stuttgart Effective Core Potential (ECP)³⁰ for structures that contain iodine atoms. The 6-311++G(d,p) basis set was employed, as this split-valence triple zeta Pople type basis set has been fitted with polarisation and diffuse functions that allow for optimal molecular geometries³¹. The Stuttgart ECP was downloaded from the EMSL basis set exchange. Grimme's D3 dispersion correction was applied to all optimisations³². Frequency calculations were performed in order to determine if the minimum energy conformation had been obtained. The log files of fully optimised structures are included in the Appendix.

Counterpoise-corrected single point calculations³³ were performed on fully optimised structures using the B3LYP, UB3LYP and ROB3LYP density functionals and the 6-311++G(d,p) basis set, with the addition of the D3 dispersion correction.

2.2.3. Visualisation of structures

All structure coordinates were obtained from the CSD, converted to Cartesian coordinates and saved in xyz Cartesian coordinates format using the Mercury v3.9 suite²⁵. Short contacts were identified as contacts where the interatomic distances are shorter than the sum of the van der Waals radii listed in the Mercury suite. All output files from Gaussian were visualised and rendered with the Chemcraft visualisation suite³⁴. Chemcraft was also utilised to visualise vibrational frequencies to confirm that optimised structures were at minimum energy conformation.

2.2.4. Atoms in Molecules (AIM) analysis

The quantum theory of Atoms In Molecules (AIM) was developed by Bader and coworkers³⁵. This theory makes use of quantum observables such as the electron density $\rho(\mathbf{r})$ and other energy densities to make sense of interesting molecular properties. Various mathematical operations can be performed on $\rho(\mathbf{r})$, to reveal additional features of a molecule. These features can be extracted from wave function (*.wfx files) and cube (*.cube & *cube files) files, generated by a Gaussian 09 rev. E.01 single-point calculation. AIM analysis was performed on various radical structures that were obtained from the CSD to identify what molecular properties contribute to the dimerisation process. All radicals in this study have an aromatic group at the R-group position. Various electron-withdrawing and -donating substituents were added to the ring to investigate the effect on $\rho(\mathbf{r})$. The AIM analysis was performed utilising the AIMALL v.17.01.25 software package³⁶, generating figures that show the $\rho(\mathbf{r})$ values at each bond critical point (BCP). The effect of these substituents was investigated by comparing the electron density values at the BCPs in substituted compounds. All wave function integrations were performed using the default software settings.

2.2.5. Electrostatic potential

The AIMALL software package³⁶ was used to generate electrostatic surface potential (ESP) maps. All ESP maps were generated from the same *.wfx files used for AIM analysis. The default ESP map is calculated at 0.001 e bohr⁻¹ (electron density), but for the purpose of this study, this was changed to 0.01 e bohr⁻¹ to better visualise the radical molecules. The default settings were used when mapping the ESP on to an isosurface in order to produce an ESP map. All ESPs were generated on a colour scale showing maximum (blue) values at 100 kcal/mol and a minimum (red) at -45 kcal/mol (see for example Chapter 1, Figure 1.26).

2.2.6 Energy decomposition analysis

Energy decomposition analysis (EDA) was performed on all fully optimised radical structures utilising an adaptation of the Morokuma and Ziegler³⁷⁻³⁹ bond energy decomposition scheme that has been incorporated into the Amsterdam Density Functional (ADF) software package^{40,41}. The B3LYP method in combination with the TZP⁴² all-electron basis set was utilised for all EDA calculations. It should be mentioned that the ADF software package employs Slater-type orbitals (STOs), whereas the Pople basis sets utilised in Gaussian 09 rev. E.01 are based on Gaussian-type orbitals. Relativistic effects were accounted for with the zeroth order regular approximation (ZORA)⁴³⁻⁴⁷. The BJ-damping scheme was used instead of zero-damping, as this has been shown to provide slightly better results for noncovalent interactions³¹. The parameters for this correction are not included in ADF and were specified manually according to the Grimme group⁴⁸. Diffuse fit functions were also included to avoid numerical problems, which are common when using large basis sets. In order to perform EDA calculations on radicals that have an uneven number of spin-up (α) and spin-down (β) electrons, we performed unrestricted calculations. EDA analysis of unrestricted fragments is not possible in the ADF package, but this problem was resolved by the manual input of α - and β -spin electrons occupations on each fragment. This allows for unrestricted bonding analysis using restricted fragments.

2.2.7 Multifunctional Wavefunction Analyzer (Multiwfn)

The Multiwfn software package⁴⁹ was used to generate Non-Covalent Interaction (NCI) plots. These plots allow for visualisation and identification of non-covalent interactions, which are identified as peaks that appear in the reduced density gradient⁵⁰.

References

- (1) Alange, G. G.; Banister, A. J.; Bell, B.; Millen, P. W. *Journal of the Chemical Society, Perkin Transactions 1* **1979**, 1192.
- (2) Alberola, A.; Collis, R. J.; Less, R. J.; Rawson, J. M. *Journal of Organometallic Chemistry* **2007**, 692, 2743.
- (3) Rawson, J. M.; Alberola, A.; Whalley, A. *Journal of Materials Chemistry* **2006**, 16, 2560.
- (4) Robinson, S. W.; Haynes, D. A.; Rawson, J. M. *CrystEngComm* **2013**, 15, 10205.
- (5) Luzon, J.; Campo, J.; Palacio, F.; McIntyre, G. J.; Rawson, J. M.; Less, R. J.; Pask, C. M.; Alberola, A.; Farley, R. D.; Murphy, D. M.; Goeta, A. E. *Physical Review B* **2010**, 81, 144429.
- (6) Alberola, A.; Less, R. J.; Pask, C. M.; Rawson, J. M.; Palacio, F.; Oliete, P.; Paulsen, C.; Yamaguchi, A.; Farley, R. D.; Murphy, D. M. *Angewandte Chemie International Edition* **2003**, 42, 4782.
- (7) Birchall, J. M.; Haszeldine, R. N.; Jones, M. E. *Journal of the Chemical Society C: Organic* **1971**, 1343.
- (8) APEX3, S., and SADABS; Bruker AXS Inc.: Madison, WI,; **2016**.
- (9) Sheldrick, G. *Acta Crystallographica Section A* **2008**, 64, 112.
- (10) Barbour, L. J. *J. Supramol. Chem.* **2001**, 1, 189.
- (11) Bruno, I. J.; Cole, J. C.; Kessler, M.; Luo, J.; Motherwell, W. D. S.; Purkis, L. H.; Smith, B. R.; Taylor, R.; Cooper, R. I.; Harris, S. E.; Orpen, A. G. *Journal of Chemical Information and Computer Sciences* **2004**, 44, 2133.
- (12) Gillon, B.; Goujon, A.; Willemin, S.; Larionova, J.; Desplanches, C.; Ruiz, E.; André, G.; Stride, J. A.; Guérin, C. *Inorganic Chemistry* **2007**, 46, 1090.
- (13) Gukasov, A.; Goujon, A.; Meuriot, J.-L.; Person, C.; Exil, G.; Koskas, G. *Physica B: Condensed Matter* **2007**, 397, 131.
- (14) Luzón, J.; Campo, J.; Palacio, F.; McIntyre, G. J.; Goeta, A. E.; Ressouche, E.; Pask, C. M.; Rawson, J. M. *Physica B: Condensed Matter* **2003**, 335, 1.
- (15) Deutsch, M.; Claiser, N.; Souhassou, M.; Gillon, B. *Physics Procedia* **2013**, 42, 10.
- (16) Deutsch, M.; Claiser, N.; Pillet, S.; Chumakov, Y.; Becker, P.; Gillet, J.-M.; Gillon, B.; Lecomte, C.; Souhassou, M. *Acta Crystallographica Section A* **2012**, 68, 675.
- (17) Hansen, N. K.; Coppens, P. *Acta Crystallographica Section A* **1978**, 34, 909.
- (18) Gal, Z.; White, F.; Griffin, A.; Presly, O.; Thompson, A.; Frampton, C. *Acta Crystallographica Section A* **2011**, 67, C754.
- (19) Clark, R. C.; Reid, J. S. *Acta Crystallographica Section A* **1995**, 51, 887.
- (20) Blessing, R. *Journal of Applied Crystallography* **1997**, 30, 421.
- (21) Clementi, E.; Roetti, C. *Atomic Data and Nuclear Data Tables* **1974**, 14, 177.
- (22) Haneman, D. *Japanese Journal of Applied Physics* **1974**, 13, 371.
- (23) Allen, F. *Acta Crystallogr, Sect. B* **2002**, 58, 380.
- (24) Bruno, I. J.; Edgington, P. R.; Kessler, M.; Macrae, C. F.; McCabe, P.; Pearson, J.; Taylor, R.; Cole, J. C. *Acta Cryst.* **2002**, 58.
- (25) Macrae, C. F.; Edgington, P. R.; McCabe, P.; Pidcock, E.; Shields, G. P.; Taylor, R.; Towler, M.; van de Streek, J. *Journal of Applied Crystallography* **2006**, 39, 453.
- (26) Zhu, H.; Grant, D. J. W. *International Journal of Pharmaceutics* **1996**, 139, 33.
- (27) Bruno, I. J.; Cole, J. C.; Lommerse, J. P. M.; Rowland, R. S.; Taylor, R.; Verdonk, M. L. *J Comput Aided Mol Des* **1997**, 11, 525.
- (28) Frisch, M. J., et al. *Wallingford CT* **2009**.
- (29) Krishnan, R.; Binkley, J. S.; Seeger, R.; Pople, J. A. *The Journal of Chemical Physics* **1980**, 72, 650.
- (30) Igel-Mann, G.; Stoll, H.; Preuss, H. *Molecular Physics* **1988**, 65, 1321.
- (31) Ditchfield, R.; Hehre, W. J.; Pople, J. A. *The Journal of Chemical Physics* **1971**, 54, 724.

- (32) Grimme, S.; Ehrlich, S.; Goerigk, L. *Journal of Computational Chemistry* **2011**, *32*, 1456.
- (33) Simon, S.; Duran, M.; Dannenberg, J. *The Journal of Chemical Physics* **1996**, *105*, 11024.
- (34) Chemcraft, <http://chemcraftprog.com>
- (35) Bader, R. F. W.: Atoms in molecules. *Accounts of Chemical Research* **1985**, *18*, 9-15.
- (36) Keith, T. A. *TK Gristmill Software* **2017**
- (37) Morokuma, K. *J. Chem. Phys.* **1971**, *55*, 1236.
- (38) Kitaura, K.; Morokuma, K. *International Journal of Quantum Chemistry* **1976**, *10*, 325.
- (39) Ziegler, T.; Rauk, A. *Inorganic Chemistry* **1979**, *18*, 1558.
- (40) Bickelhaupt, F. M.; Baerends, E. J. In *Reviews in Computational Chemistry*; John Wiley & Sons, Inc.: **2007**, p 1.
- (41) te Velde, G.; Bickelhaupt, F. M.; Baerends, E. J.; Fonseca Guerra, C.; van Gisbergen, S. J. A.; Snijders, J. G.; Ziegler, T. *Journal of Computational Chemistry* **2001**, *22*, 931.
- (42) Van Lenthe, E.; Baerends, E. J. *Journal of Computational Chemistry* **2003**, *24*, 1142.
- (43) van Lenthe, E.; van Leeuwen, R.; Baerends, E. J.; Snijders, J. G. *International Journal of Quantum Chemistry* **1996**, *57*, 281.
- (44) Lenthe, E. v.; Snijders, J. G.; Baerends, E. J. *The Journal of Chemical Physics* **1996**, *105*, 6505.
- (45) Lenthe, E. v.; Ehlers, A.; Baerends, E.-J. *The Journal of Chemical Physics* **1999**, *110*, 8943.
- (46) Lenthe, E. v.; Baerends, E. J.; Snijders, J. G. *The Journal of Chemical Physics* **1993**, *99*, 4597.
- (47) Lenthe, E. v.; Baerends, E. J.; Snijders, J. G. *The Journal of Chemical Physics* **1994**, *101*, 9783.
- (48) <http://www.thch.uni-bonn.de/tc/downloads/DFT-D3/functionals.html> Accessed 10 July **2017**
- (49) Lu, T.; Chen, F. *Journal of Computational Chemistry* **2012**, *33*, 580.
- (50) Contreras-García, J.; Johnson, E. R.; Keinan, S.; Chaudret, R.; Piquemal, J.-P.; Beratan, D. N.; Yang, W. *Journal of Chemical Theory and Computation* **2011**, *7*, 625.

3 Synthesis and properties of some 1,2,3,5-dithiadiazolyl radicals

Introduction

The discovery of the first organic ferromagnet, *p*-nitrophenyl nitroxide (*p*-NPNN), has resulted in a considerable amount of research dedicated to the design of purely organic magnetic materials^{1,2}. Organic-based magnets have been proposed as cheap alternatives to metal-based materials that often require energy- and cost-intensive metallurgical procedures using rare elements³. The family of 1,2,3,5-dithiadiazolyl (DTDA) radicals has received a lot of attention in the field of organic magnets owing to the stability of these radicals, and the ease with which they can be chemically modified.

This chapter will focus on investigation of the properties of 4-(4-cyano-2,3,5,6-tetrafluorophenyl)-1,2,3,5-dithiadiazolyl (**2**), 4-(4'-bromo-2',3',5',6'-tetrafluorophenyl)-1,2,3,5-dithiadiazolyl (**3**) and 4-(2,3,5,6-tetrafluoro-4-nitrophenyl)-1,2,3,5-dithiadiazolyl (**4**). These radicals were selected as they form part of a small group of DTDA's that do not exhibit a dimerised pair in the solid state. The inhibition of dimerisation results from a network of intermolecular interactions that also allows for communication between spin density that reside on the radical molecules, which in turn results in interesting magnetic properties. Furthermore, the network of intermolecular interactions in these radical systems also results in some additional properties that will further be investigated. This chapter aims to investigate what role the network of intermolecular interactions plays in inhibiting the process of dimerisation and also how these interactions can result in other interesting properties.

The original objective of the study was to obtain large crystals of radicals **2**, **3** and **4** that could be used for high-resolution x-ray diffraction (HXRDX) and polarised neutron diffraction (PND) experiments that can be jointly refined to visualise the spin-up and spin-down contributions to the spin density. This experiment could provide some insight into why the network of intermolecular interactions in these radicals result in sufficient communication between radical molecules to allow for their interesting magnetic properties. However, in the process it was found that radicals **2**, **3** and **4** have interesting properties that had not yet been investigated. This chapter focusses primarily on these properties.

Handling of the crystals of **2** revealed that the needle-shaped crystals exhibit flexible properties. These properties were investigated using specialised experimental imaging techniques. These images and the crystal structure will then be used to propose a potential mechanism that explains the origin of the flexible properties.

The 4-(2,6-difluorophenyl)-1,2,3,5-dithiadiazolyl (**7**) radical was identified as an ideal candidate to be used in a co-crystallisation experiment as it exhibits a mixture of monomeric

and dimeric radical molecules in the solid state. Crystals of **2** and **7** were co-crystallised since they both have fluorinated groups at the *ortho* position. It was mentioned in Chapter 1 that *ortho* fluorine groups result in $N\cdots F$ repulsive interactions that yield large twist angles, which can in turn inhibit dimerisation. Interestingly, the co-crystallisation of **2** and **7** did not yield a co-crystal, but instead a polymorph of **2** that has been reported to only grow at temperatures below 0°C . A possible mechanism will be proposed to explain how different polymorphs can be obtained in the presence of another DTDA radical.

The synthesis of **3** proved to be interesting as it yielded a co-crystal of **3** with its starting material, 2,3,5,6-tetrafluoro-4-nitrobenzonitrile. The unexpected mode of association of the co-crystal suggested that co-crystallisation could be used as a method to obtain other co-crystals.

The joint refinement of the HXRD and PND data of **4** was undertaken to determine the spin-up and spin-down contributions, and other properties of the bonds to explain why **4** prefers the linear mode of association via strong structure directing $\text{NO}_2\cdots\text{S}$ contacts.

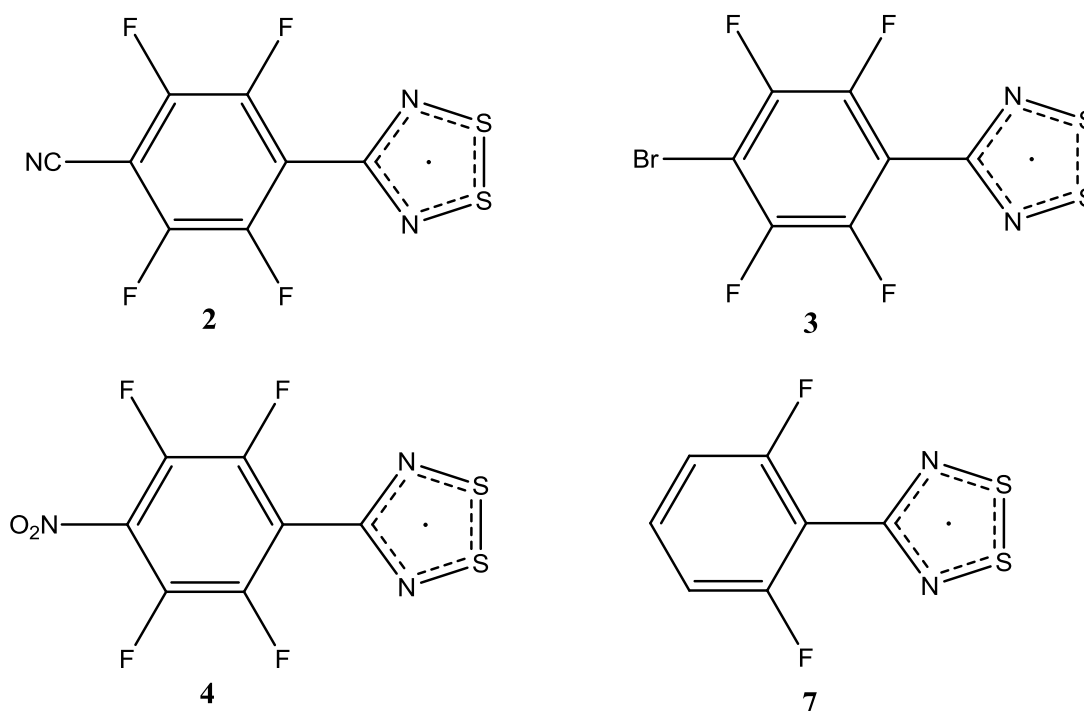
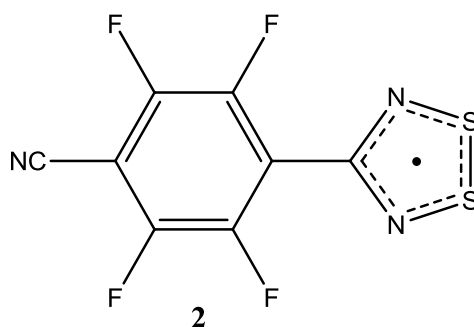


Figure 3.1: The DTDA radicals discussed in this chapter.

The synthetic procedure used to obtain **2** – **4** and **7** was fully described in Chapter 2 and Addendum A. The synthesis of 2,3,5,6-tetrafluoro-4-nitrobenzonitrile and 4-bromo-2,3,5,6-tetrafluorobenzonitrile are fully reported in Addendum A. The radicals were purified at

different sublimation temperatures or using different sublimation conditions (i.e. temperature, vacuum) to yield crystals with the interesting properties discussed below.

3.1. Properties of the α -and- β -phase 4-(4-cyano-2,3,5,6-tetrafluoro-phenyl)-1,2,3,5-dithiadiazolyl radical (**2**)



DTDA radical **2** has two known monomeric polymorphs that can be obtained under different sublimation conditions. Small, black block-shaped crystals of the α -phase are prepared by heating the crude radical to 110 °C, while keeping the substrate (cold finger) at -10 °C⁴, while black needle-shaped crystals of the β -phase⁵ are obtained by heating the crude radical to 110 °C and circulating water through a cold finger (20 °C)⁴. Efforts to cut the large needle-shaped β -phase crystals of **2** to a suitable size for other experiments proved problematic, as it has been well established that dithiadiazolyl radicals are sensitive to air and moisture⁶. On the other hand, if the crystals were bent, they were seen to exhibit some flexible behaviour. It should be mentioned that these crystal could be repeatedly bent (forward and reverse motion) and only exhibit some structural damage to the crystal once an excessive force was applied along a face of the crystal that is not flexible. These flexible properties were further investigated as described below.

3.2. Flexible properties of the β -phase of **2**

Literature studies on flexible organic crystals attribute the flexible properties to a multitude of weak and dispersive interactions present in the crystal. Furthermore, these intermolecular interactions act as structural buffers that inhibit deformation or rupture of the crystal^{7,8}. It was observed that bending a needle of the β -phase of **2** yielded bent crystals as illustrated in Figure

3.2. An excessive amount of force exercised along the face of the crystal that is not flexible will result in shattering of the crystal as illustrated in Figure 3.3.

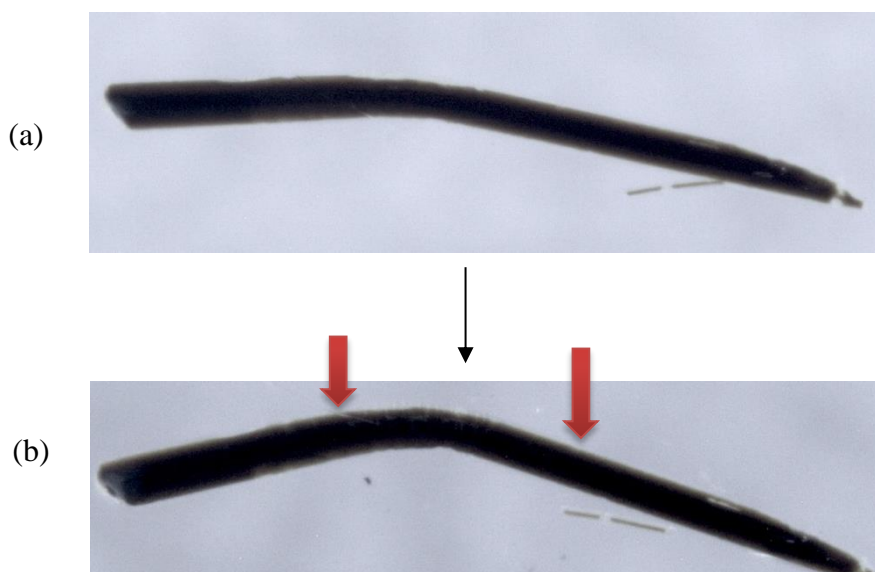


Figure 3.2: The crystal of the β -phase of **2** (a) is bent by applying force at the areas marked by red arrows (b).

Handling of the crystals proved a delicate process, as the crystals generally shatter when working in the glovebox. Therefore, crystals were handled under a stream of constant nitrogen supplied by a funnel connected to a Schlenk line.

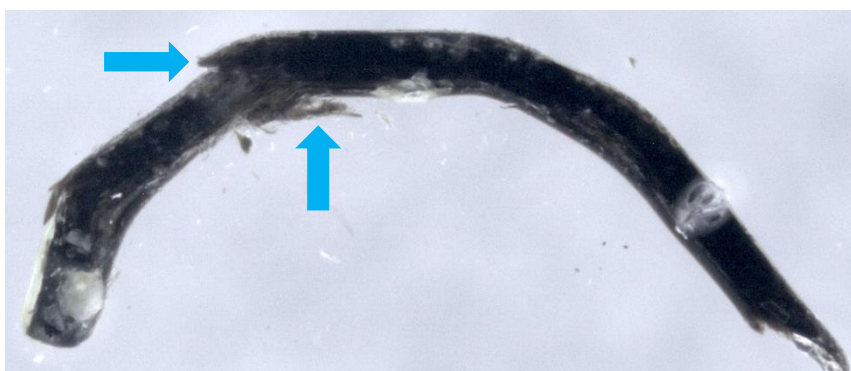


Figure 3.3: The crystal of the β -phase of **2** shatters (blue arrows) if excessive mechanical force is applied along a face of the crystal that is not flexible.

Scanning electron microscopy (SEM) was used to explain what is observed in Figure 3.2 and 3.3, as it allows for visualisation of the crystals at the micrometer (μm) scale. SEM images were obtained by the Naumov group at the New York University, Abu Dhabi. Crystals of **2** were removed from a Schlenk and SEM images were obtained within one hour of their removal (Figure 3.4); the needle-shaped crystals exhibit very smooth surfaces.

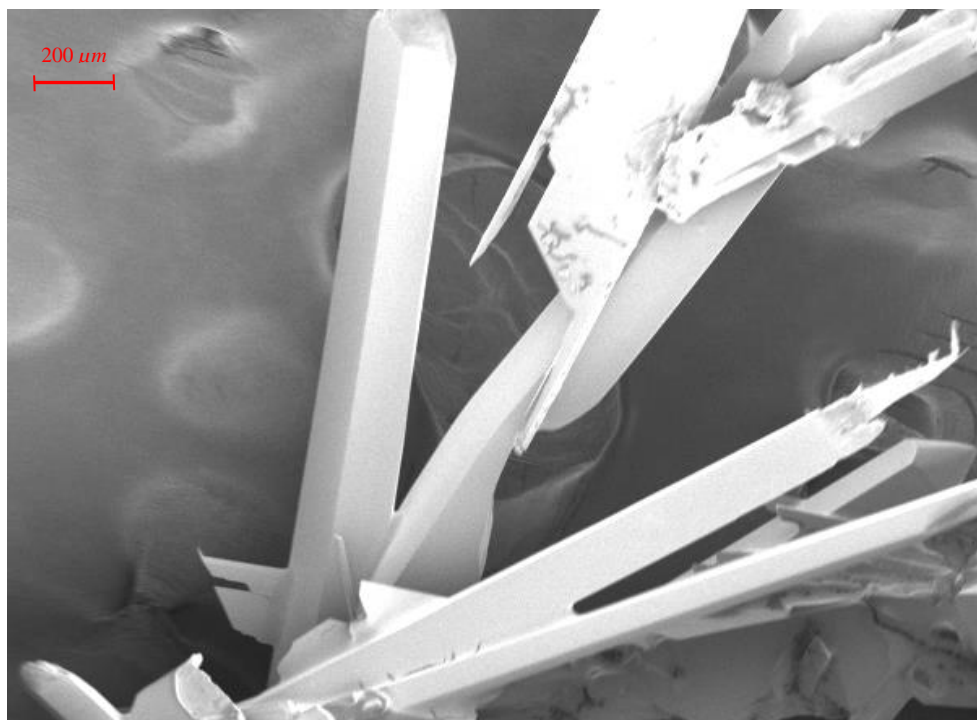


Figure 3.4: Needle-shaped crystal of 2 with smooth surfaces showing no defects.

However, on handling crystals for longer than 2 hours (Figure 3.5), or storing crystals in a Schlenk tube for more than two weeks, some defects appear on the surface of the crystals, indicative of decomposition (indicated by red circles). This decomposition is marked by both a brittleness of the crystal in combination with a clear colour change as evidenced by the darker smudge.

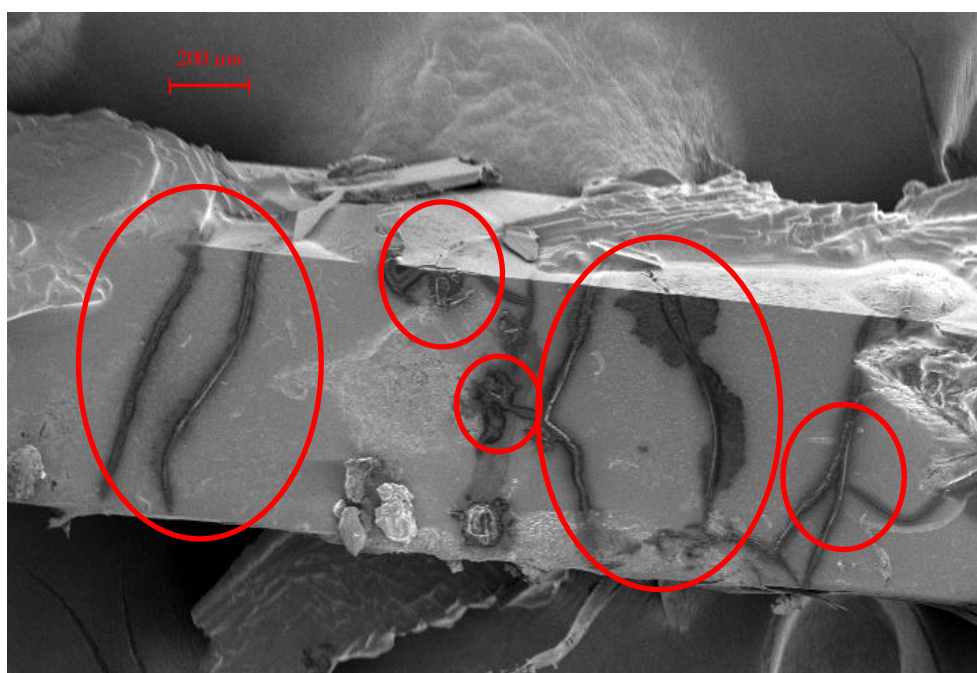


Figure 3.5: Needle-shaped crystal of 2 with decomposed areas marked by red spheres.

SEM images were also used to visualise the change to the surface of the crystal upon bending. This was achieved by using a sharp-pointed blade and forceps. The forceps were used to stabilise the edges of the crystal while a force was applied at the centre as illustrated in Figure 3.5.

The SEM image of a crystal that was bent by 15° (Figure 3.7) indicates no damage to the crystalline surface. Small defects on the crystal surface indicated by blue circles are merely impurities consisting mostly of sulfur powder and excess Ph_3Sb , which was confirmed by surface elemental analysis.

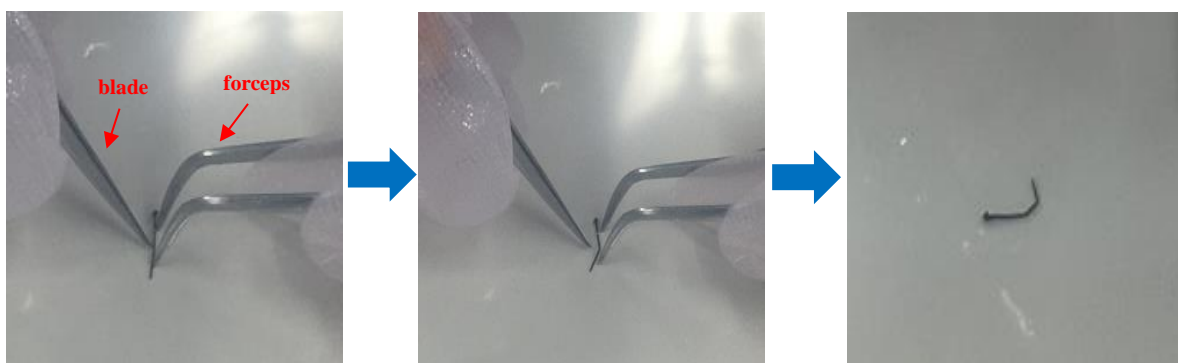


Figure 3.6: Forceps and blade used to bend β -phase crystal of 2 (left) to a bent crystal (right). Image used with permission from Naumov group at the New York University, Abu Dhabi.

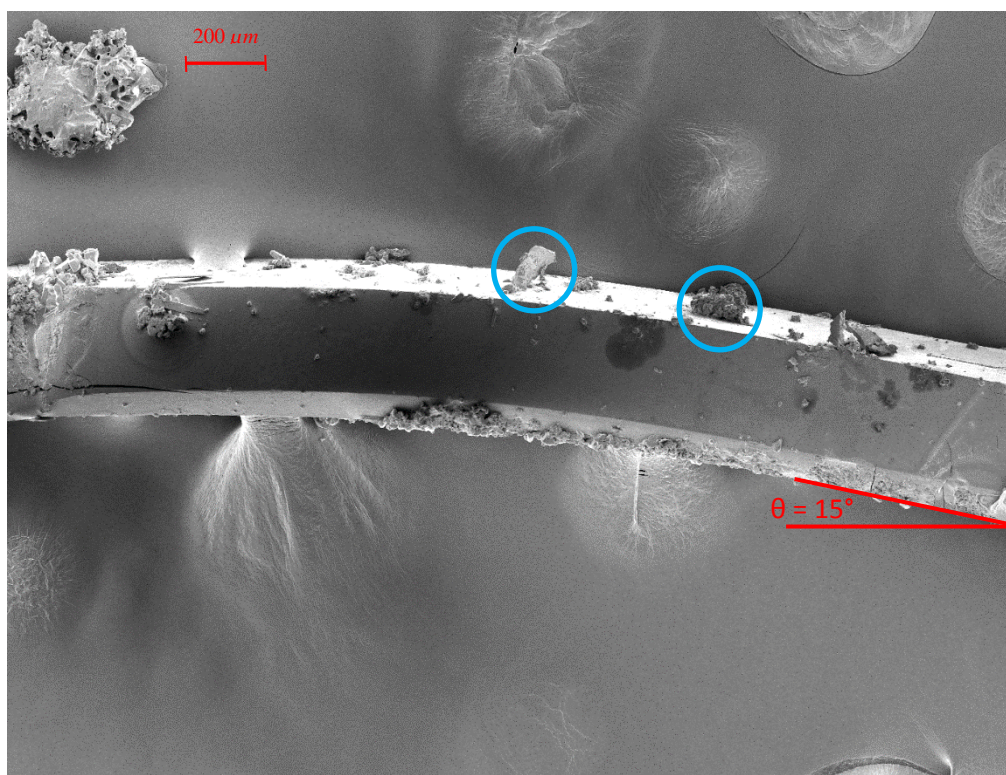


Figure 3.7: Needle-shaped crystal of 2, with a maximum measured angle of approximately 15° . Blue circles indicate the surface defects.

Another crystal was then bent and the angles of bending were measured from the SEM images to be 20° and 40° (Figure 3.8). The SEM image (Figure 3.8) of this crystal shows no damage to the crystal surface at the smaller measured angle of 20° , while there is some damage to crystal surface at 40° (Figure 3.8, middle). The overall needle-shape of the crystal is maintained, but some small cracks appear on the crystal surface. This illustrates that even though these crystals do exhibit some flexibility, this is limited to angles below 40° .

It was mentioned that it has been previously noted that flexible organic crystals often result from a network of weak interactions^{7,8}. The crystal structure of **2** was redetermined by SCD and revealed a network of intermolecular interactions that could provide **2** with elastic properties. The role of the intermolecular interactions in **2** was probed by investigating the short-range (within the sum of the van der Waals radii) and long-range contacts (defined as the sum of the van der Waals radii + 0.3 \AA) present in the crystalline packing of this radical. The linear arrangement of **2** resulting from directional $\text{CN}\cdots\text{S}$ contacts is illustrated in Figure 3.9 viewed along the b axis. Additional $\text{F}\cdots\text{C}$ contacts occur between linear chains of radicals. The two repeating short-range contacts are marked by red spheres; the other contacts indicated are long-range contacts.

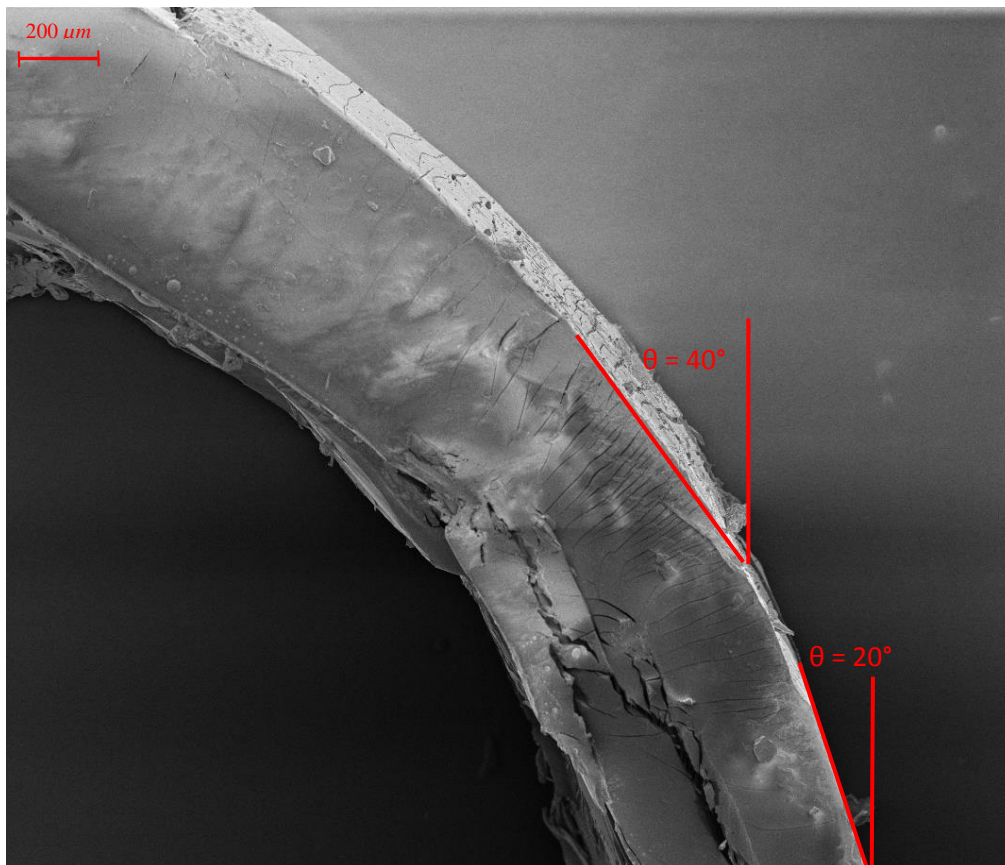


Figure 3.8: Needle-shaped crystal of **2**. Smaller angle at bottom of approximately 20° and larger angle of 40° .

Literature studies have also suggested a second factor that could contribute to the flexibility of crystals is the presence of uneven packing arrangements that interlock, which prevents the long-range gliding motion of molecular planes⁹. This is shown by the uneven arrangement of rows of **2**, which is illustrated in Figure 3.9. This packing arrangement starts at row A with the next rows above and below shifting to the right. Stacks of radicals pack along the *c* axis (Figure 3.9) with short and long-range contacts between the radicals aligned linearly as well as between rows (i.e. radicals from row A interacting with radicals from row B).

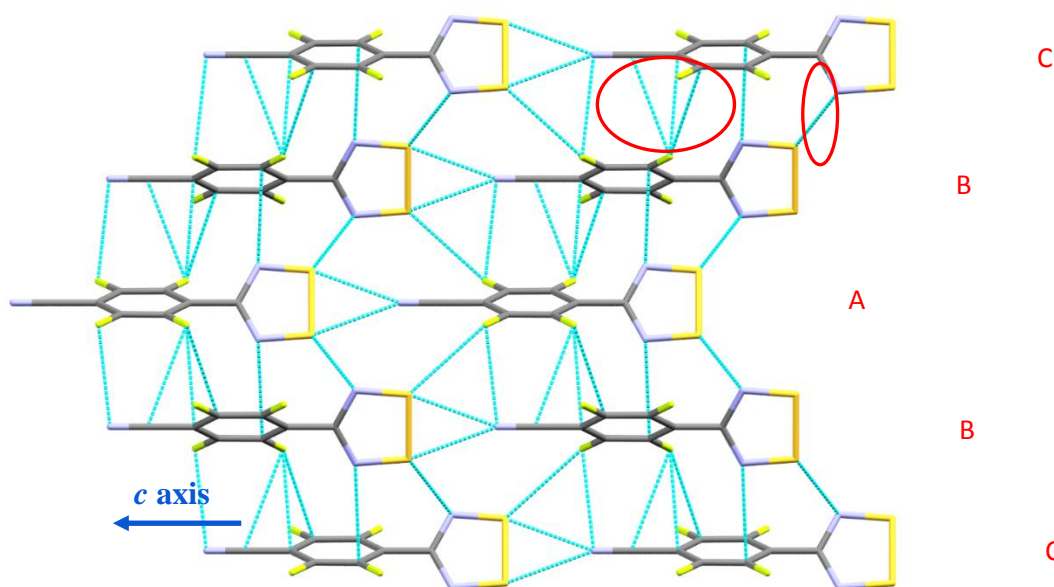


Figure 3.9: Intermolecular contacts present in the crystalline packing of **2** viewed down the *b* axis. The pattern originates at A and is followed by each row being shifted to the right as seen for rows B and C. The short-range contacts are marked with red spheres. All other contacts are long-range contacts.

Long-range π - π interactions between aromatic molecules have been shown to be favourable, and can be utilised to predict geometries that consist of stacked aromatic molecules¹⁰. The presence of other long-range interactions within **2** result in rows of linear chains as illustrated in Figure 3.10. These long-range interactions could possibly contribute to the flexible properties of organic crystals¹¹.

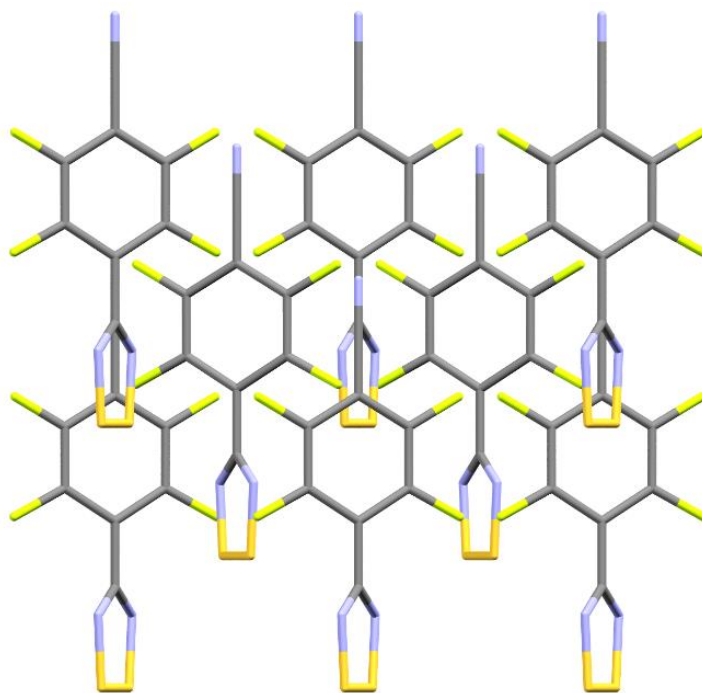


Figure 3.10: The linear chains of **2 viewed directly along the a axis resulting from long-range intermolecular interaction.**

A specialised Electron Paramagnetic Resonance (EPR) experiment was performed on a crystal of **2** before and after it was bent. A series of EPR images are taken for every region of a crystal, which are then integrated to give a final image that allows for visualisation of the whole crystal. This experiment was performed in collaboration with the Naumov group at the New York University, Abu Dhabi. The EPR experiment was performed on the complete crystal and reveals areas of radical concentration. Green, red and yellow areas represent concentrated areas of radical molecules, whereas blue and purple areas represent the absence of radical molecules. Before bending the crystal we observe that the complete crystal exhibits concentrated areas of radicals (Figure 3.11). However, once the crystal is bent, there is a decrease in radical concentration observed at the bent areas (Figure 3.12). This indicates a pairing of radicals.

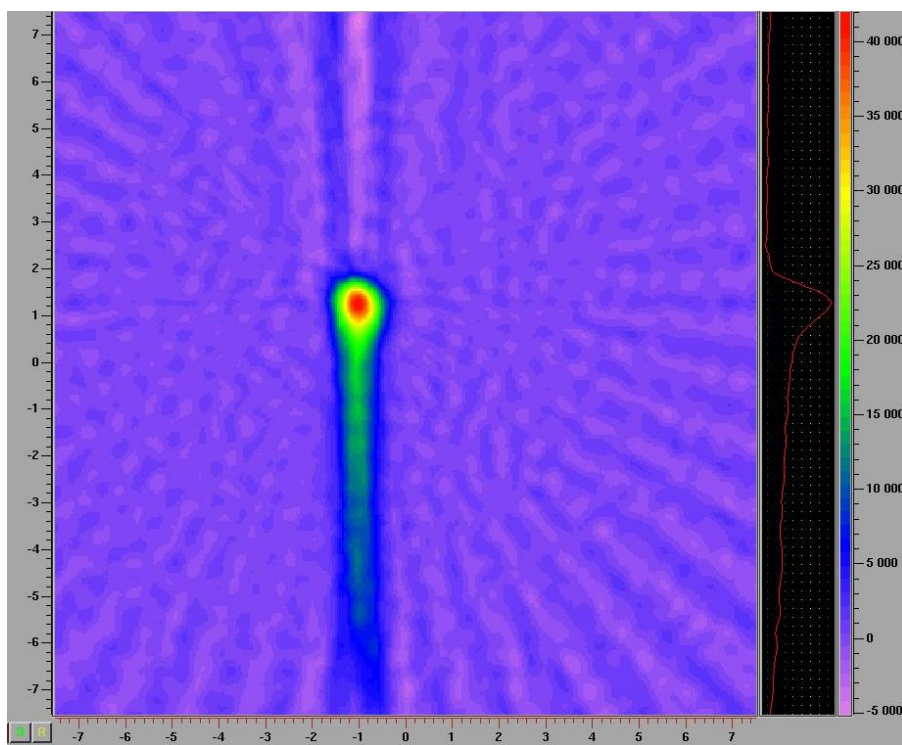


Figure 3.11: EPR experiment performed on the crystal before bending is performed.

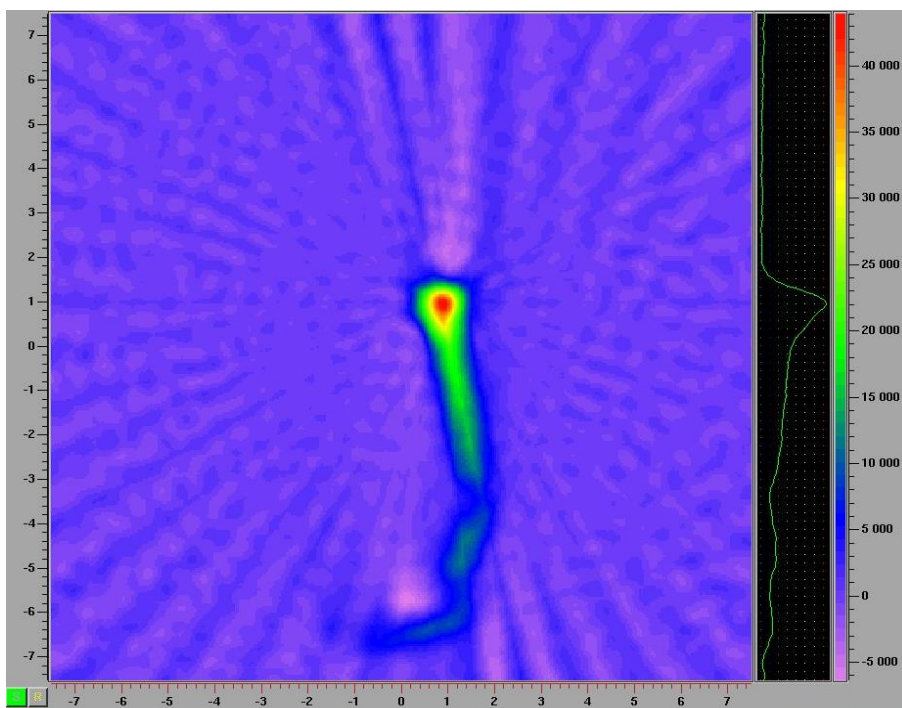


Figure 3.12: EPR experiment performed on the crystal after bending has been performed.

Analysis of the crystal structure shows that movement along the a and c axes would be required in order to form a dimerised pair of **2** (Figure 3.13). This corresponds to the bent crystal illustrated in Figure 3.14, which has been indexed and shows the bending along the a and c axes.

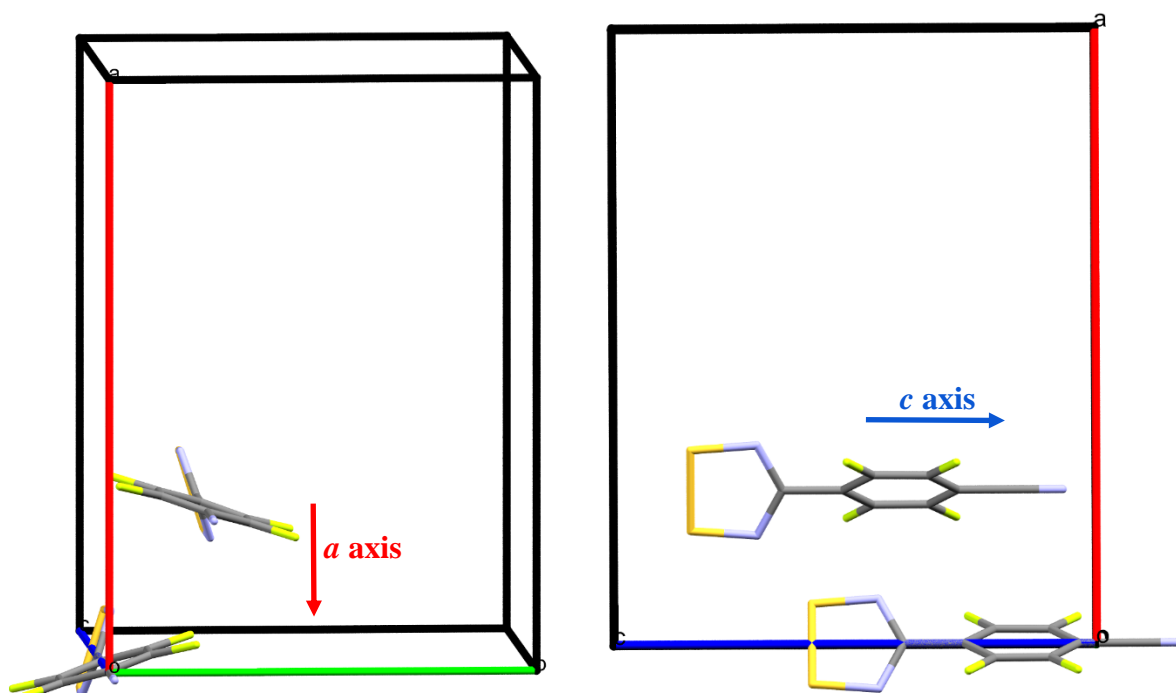


Figure 3.13: Movement along the *a* and *c* axes is required in order to yield dimerised pairs of **2**.

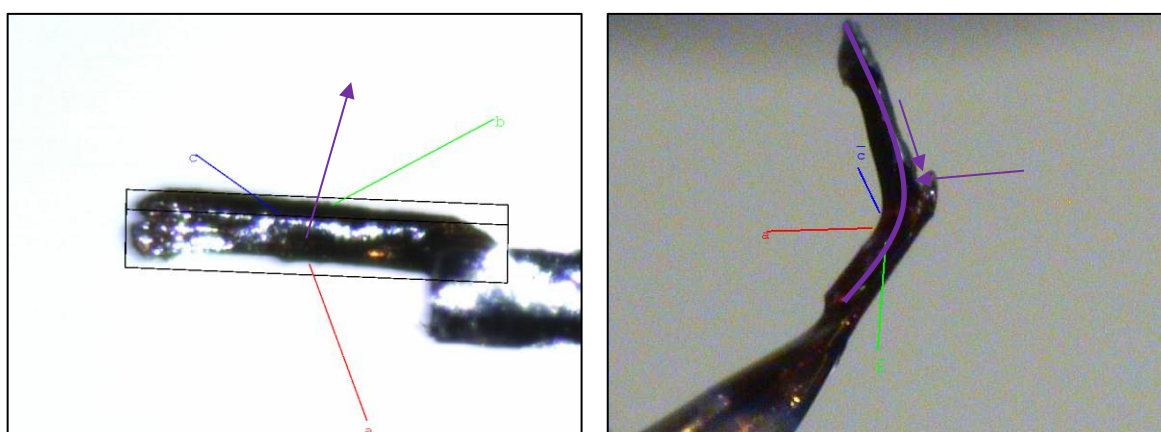


Figure 3.14: The crystal faces of a straight (left) and bent crystal (right). The crystal can bend along the *a* and *c* axes. This movement is shown by the purple arrow on the left figure. For the bent crystal, the purple line represents the bending of the crystal, while the purple arrows illustrate the movements along the *a* and *c* axes. The *b* axis is oriented out-of-plane and towards the reader.

A possible mechanism that could allow for the flexibility of **2** is shown in Figure 3.15, where molecule **a** moves along both the *a* and *c* axes to yield a dimerised pair with a second molecule **b**. Furthermore, we propose that movement along the *b* axis would disrupt the structure-directing CN \cdots S contacts that occur along the *c* axis, resulting in crystal damage. The flexibility is therefore strongly dependent on the CN \cdots S contacts and the limit of their movement along the *a* and *c* axes.

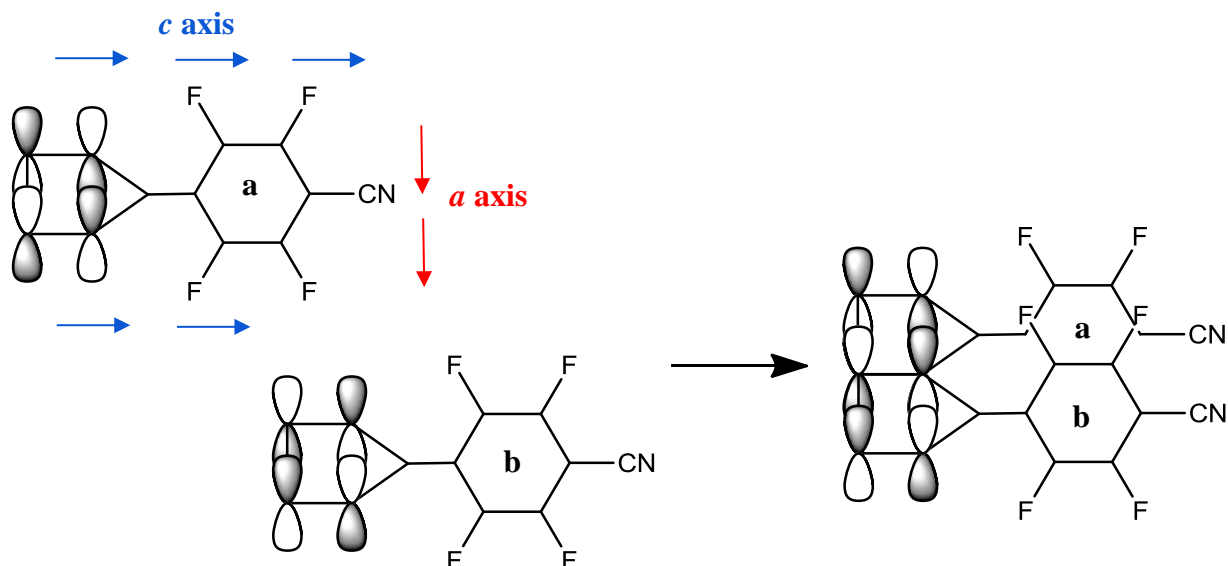


Figure 3.15: Movement of molecule a along the *a* and *c* axes to form a dimerised pair with molecule b.

The possible movement of chains of radicals to exhibit bulk flexible properties is shown in Figure 3.16. The crystal structure contains rows of radicals in a C-B-A-B-C arrangement, as shown in Figure 3.9. As the molecules move along the *a* and *c* axes, rows of radicals form dimerised pairs and symmetry between rows is no longer observed, as the movement along the *a* and *c* axes is not equivalent for all regions of the crystal.

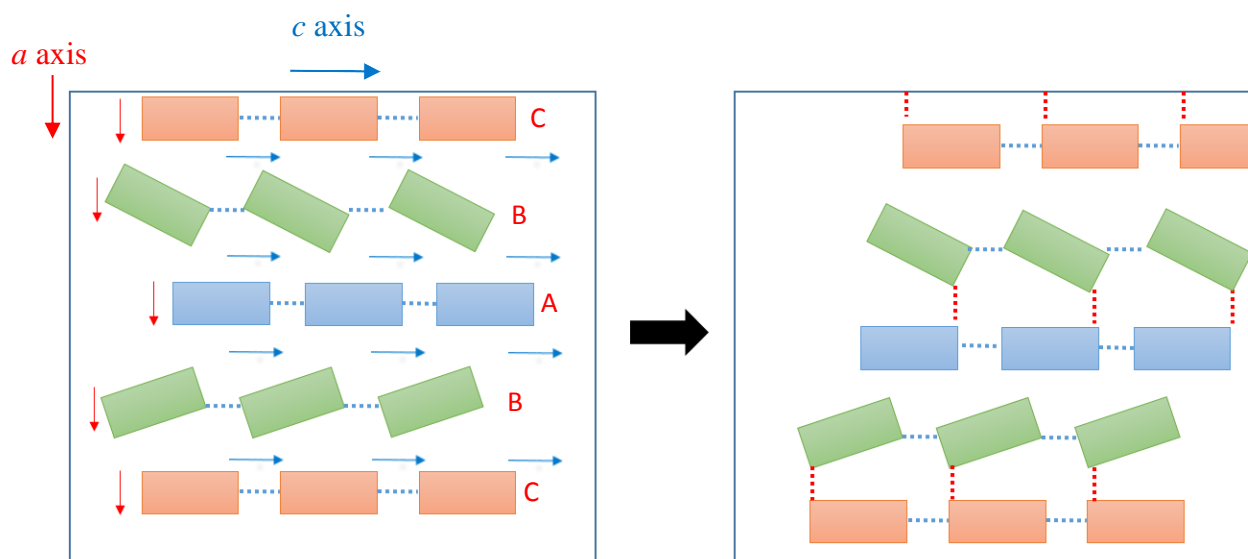


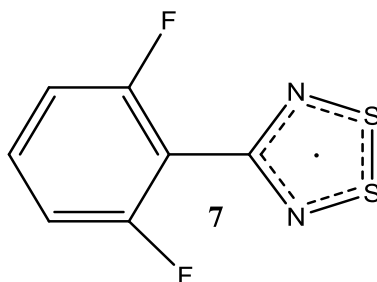
Figure 3.16: Rows of radicals move along the *a* and *c* axes, which results in dimerisation between rows of radical that are no longer symmetrical.

An X-ray diffraction experiment on a bent crystal revealed a different space group to that of **2**, but the data were always of poor quality and hence the crystal structure could not be determined

and will require further investigation. To our knowledge, this the first example of a DTDA-radical that exhibits any flexible properties.

3.3. Properties of the 4-(2,6-difluorophenyl)-1,2,3,5-dithiadiazolyl radical

(7)



This fluorinated radical is particularly interesting, as it is known to exist in three different polymorphic forms. The crystal packing of the γ -polymorph contains two crystallographically unique molecules that organise in such a way that 50% are dimerised and the other 50% are monomeric¹¹⁻¹³. The unique molecules are illustrated in Figure 3.17 and show a transoid mode of association for the dimerised pair and S \cdots S and S \cdots N contacts in the monomeric association¹⁴. The radicals in the dimeric and monomeric modes of association exhibit large twist angles, indicating that large twist angles are not sufficient to inhibit dimerisation and additional structure-directing contacts are required to yield radicals in a monomeric mode of association.

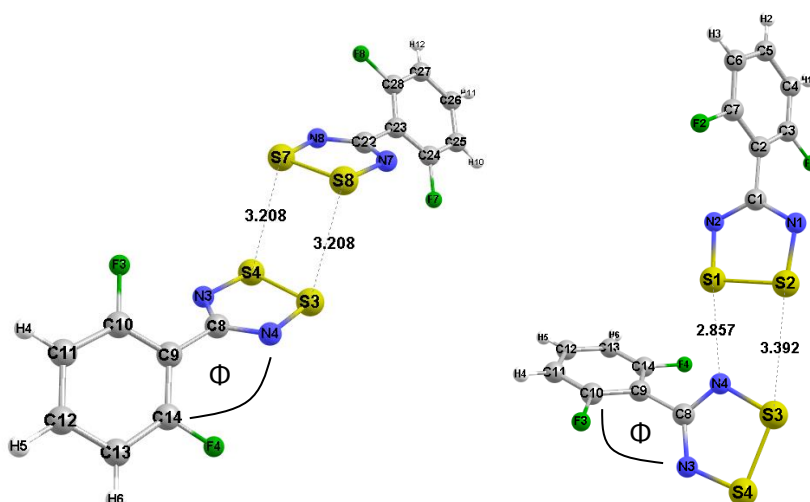


Figure 3.17: Contacts (Å) within the sum of the van der Waals radii for a dimeric pair (left) and a monomeric mode of association (right) of 7. Twist angle Φ (N4-C8-C9-C14) = 53.52° (left) and Φ (N2-C11-C15-C14) = 68.95° (right).

The ability of **7** to form structure-directing contacts that result in a monomeric association suggests that these contacts can be utilised to form co-crystals that exhibit a monomeric mode of association.

3.4. Attempted co-crystallisation of radicals **2** and **7**

Studies have aimed to deliberately form DTDA-DTDA co-crystals, but have yielded limited success: only two structures that exhibit a heterodimer pair of DTDA's have been reported in the literature^{15,16} (Figure 3.18). The first co-crystal consists of the 4-perfluoropyridyl-1,2,3,5-dithiadiazolyl and 4-phenyl-1,2,3,5-dithiadiazolyl radicals (Figure 3.18a)¹⁵, while the second co-crystal consists of 4-perfluorophenyl-1,2,3,5-dithiadiazolyl and 4-phenyl-1,2,3,5-dithiadiazolyl radicals (Figure 3.18b)¹⁶.

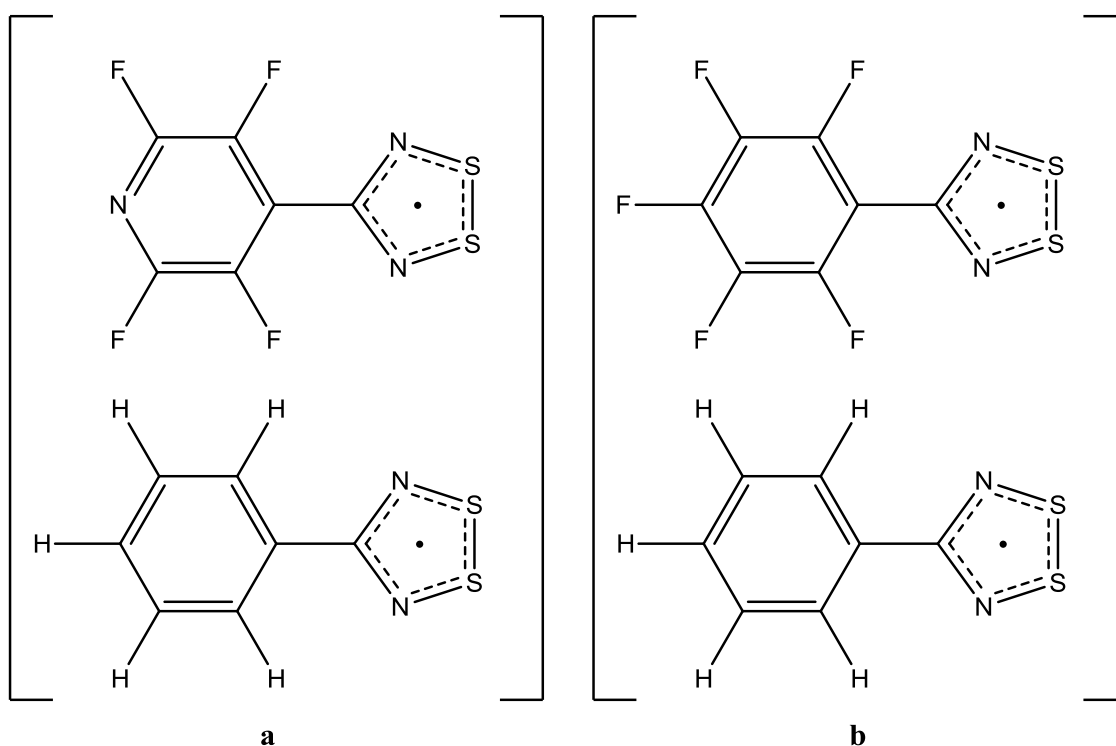


Figure 3.18: The two co-crystals (4-perfluoropyridyl-1,2,3,5-dithiadiazolyl)(4-phenyl-1,2,3,5-dithiadiazolyl) (a) and (4-perfluorophenyl-1,2,3,5-dithiadiazolyl)(4-phenyl-1,2,3,5-dithiadiazolyl) (b).

A survey of the CSD reveals that several other co-crystals containing one DTDA co-crystallised with other neutral molecules exist. The other DTDA-containing co-crystals exhibit DTDA homodimers, which form stabilising intermolecular interactions with the other co-

crystal component. The lack of co-crystals containing different DTDA's would suggest that homodimer DTDA's are favoured.

As part of another project with an MSc student (T. Carstens), the co-crystallisation of **2** and **7** was attempted as both of the DTDA-radicals have known monomeric forms and it was hoped that this would encourage the formation of a co-crystal containing two different monomers. Various thermodynamic and kinetic factors play an important role in the crystallisation process, which may result in difficulties when trying to obtain a desired polymorph. Furthermore, the presence of intermolecular interactions can play a crucial role in determining which polymorph will be obtained, although studies have shown that the use of specific solvent systems can control polymorph formation¹². Solvent effects influence the chemical reactivity of different molecules in a system, and have been shown to affect whether the thermodynamic or kinetic product is obtained¹⁷. Zhunuspayev and coworkers showed how different polymer products could be obtained by simply using different solvent systems¹⁸, owing to complexation being a multistage process; the ability of the solvent to form hydrogen bonds can also accelerate the formation of nanoparticles. This in turn results in larger particles that are prone to precipitation. Solvent-solute interactions are generally of a weak nature, as stronger interactions will result in the solvent molecules being incorporated into the system, thereby yielding solvates. The use of solvents with different hydrogen-bonding potentials was shown to affect the crystallisation of carbamazepine (CBZ)¹². The two polymorphs identified were the primitive monoclinic (form I) and the trigonal (form III) polymorphs. A system containing solvents that are capable of accepting hydrogen bonds promotes the formation of form III, while a solvent with the ability to act as both a hydrogen-bond acceptor and donor promotes the formation of both polymorphs.

Similarly, additives in sublimation can also affect the polymorphs obtained¹⁹. The addition of acetamide to CBZ reduced the sublimation temperature by 20 °C and yielded pure form I of CBZ. It was further found that if no acetamide were present, the sublimation would yield forms I and III. Kamali and coworkers proposed that an enhancement mechanism results in a volatile CBZ-acetamide hydrogen-bonded aggregate, which can transport CBZ to crystal nucleation sites at lower temperatures. It was concluded that the presence of van der Waals contacts between CBZ and the acetamide additive enhances the growth of a particular polymorph at a lower temperature²⁰.

A similar phenomenon was observed on attempting to co-crystallise equal mole ratios of radicals **2** and **7** in a sealed tube, where the tube was placed in an oil bath and heated to 95 °C. The sublimation temperature was chosen simply because it is an intermediate value

between the two sublimation temperatures, 100 °C and 80 °C, used to obtain **2** and **7**. Upon inspection of the sealed tube after approximately 24 h it was observed that a mixture of black blocks and needles had grown in different regions of the tube owing to a temperature gradient. XRD analysis of the crystals confirmed that the blocks and needles represent the α - and β -polymorphs of radical **2**, respectively. The crystallographic data for both polymorphs are included in Table 3.1.

It is clear that the presence of radical **7** affects the energy of the system as it has previously been reported that the α -polymorph is obtained at -10° , whereas α -phase crystals were obtained at 95° in our experiment. The differences between the two phases is in their linear modes of association (Figures 3.19 and 3.20), where slightly shorter CN \cdots S contacts and smaller twist angles are present in the α -phase. These differences result in very different packing arrangements for each of the phases. The main difference between the two packing arrangements is that the α -phase packs as antiparallel chains of **2**, whereas the β -phase packs as parallel chains of **2** (Figure 3.21).

This is the first example of a mixture of α - and β -phase crystals being obtained at high temperatures by the inclusion of an equimolar amount of another radical. However, we believe that this technique could be used to find new phases of radicals that have not previously been shown to be polymorphic.

Table 3.1: Crystallographic data and refinement parameters for the α and β polymorphs of **2.**

Polymorph	α -phase of 2	β -phase of 2
Empirical formula	C ₈ N ₃ F ₄ S ₂	C ₈ N ₃ F ₄ S ₂
Temperature	100 K	100 K
Wavelength	0.71073 Å	0.71073 Å
Crystal system	Triclinic	Orthorhombic
Space group	$P\bar{1}$	$Fdd2$
a (Å)	7.544	15.0071(1)
b (Å)	8.075	10.7511(8)
c (Å)	9.470	11.9107(9)
α (°)	65.72	90.00
β (°)	69.55	90.00
γ (°)	67.46	90.00
V (Å ³)	473.6	1921.7(2)
Z	2	8
Goodness-of-fit on F^2	1.127	1.063
R indices (all data)	$RI = 0.0301,$ $wR2 = 0.0632$	0.0190 0.0498

We suspect that similar interactions to those observed for the enhancement mechanism described by Kamali and coworkers play a role in the crystallisation of **2**¹⁸. Molecules of **7** likely form temporary intermolecular interactions that promote the formation of the α -polymorph of **2**.

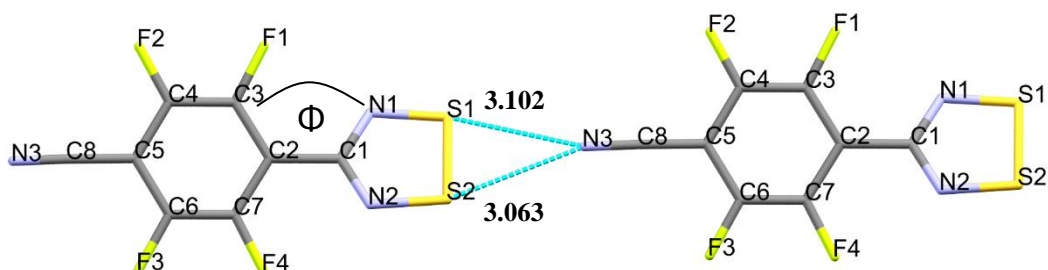


Figure 3.19: The CN...S contacts (Å) present in the α -phase of **2**. The twist angle Φ (N1-C1-C2-C3) = -32.21° .

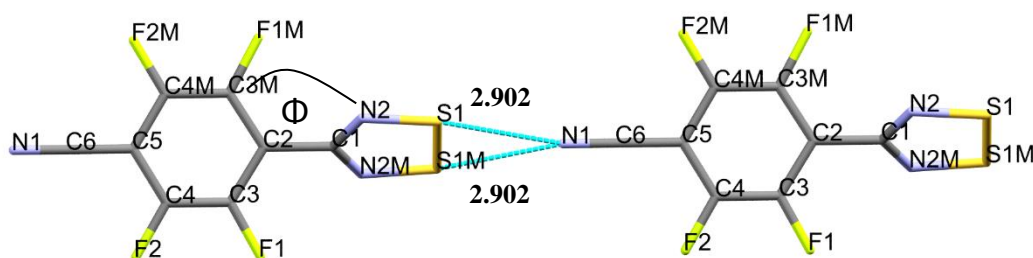


Figure 3.20: The CN...S contacts (Å) present in the β -phase of **2**. The twist angle Φ (N2-C1-C2-C3M) = 53.40° .

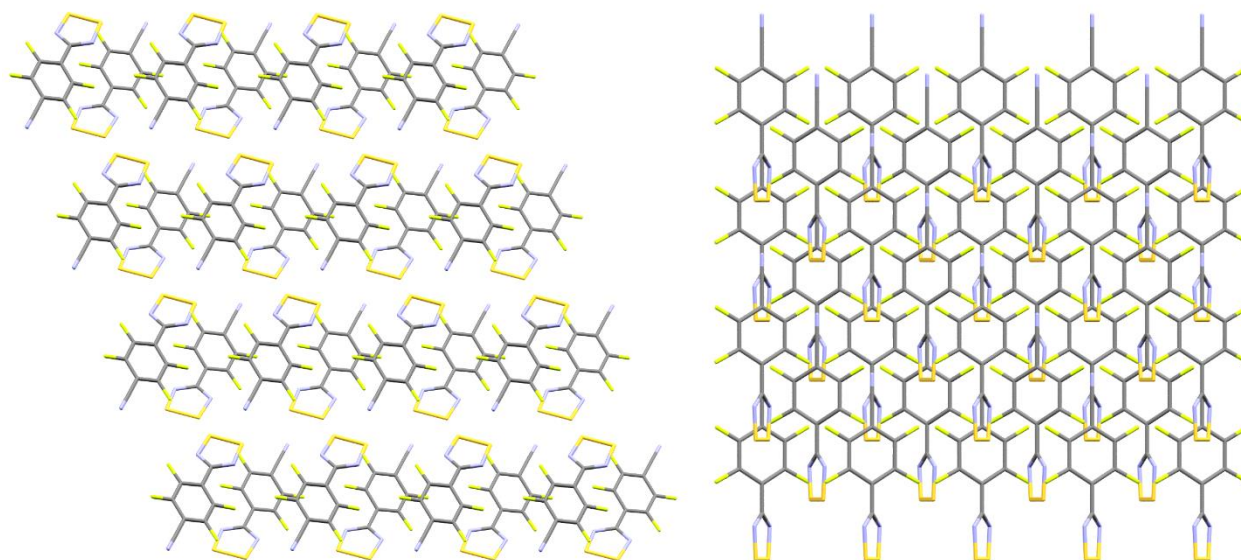


Figure 3.21: The packing arrangement of the α -phase (left) and the β -phase (right) as viewed down the a axis.

The presence of volatile material in a system is known to increase the vapour pressure²¹ and can be utilised to promote the formation of a desired polymorph. The addition of molecules of **7** in the sealed tube therefore results in a change in vapour pressure, which promotes the growth of α -phase crystals of **2**. Furthermore, an increase in vapour pressure will result in the system being subjected to an external stress that could promote crystal formation²². Diffusion occurs from high to low pressure, which explains why the α - and β -phase crystals grow in different regions of the sealed tube.

Studies on polymorphism have shown that the potential energies of different polymorphs are dominated by competing intermolecular interactions that promote the molecular packing of specific polymorphs²³. On this basis, we can propose that there are competing interactions between **2** and **7**, which result in changes in the overall energy of system to the extent that formation of the α -phase is favoured. This is similar to cases where different phases can be grown from different solvent systems.

A recent study by Rawson⁴ showed that the α -phase can be obtained by slow vacuum sublimation at 110 °C, keeping the cold finger at -10 °C with the aid of a temperature-controlled bath. The needle-shaped β -phase was obtained selectively by slow vacuum sublimation at 110 °C, keeping the cold finger at 20 °C. Thermal studies showed that the α -phase converts to the β -phase on heating of the crystals above 110 °C, with an endothermic transition that identifies the β -phase as the thermodynamically-favoured polymorph. The formation of the α phase of **2** in the presence of **7** suggests that the enhancement mechanism provides stabilisation to the system via the formation of intermolecular interactions between molecules of **2** and **7**. Potential interactions that could lead to the stabilisation are shown in Figure 3.22.

In order to determine what stabilisation should be provided by the additive, we can calculate the relative difference in energy between the α - and β -phases of **2**. Figures 3.19 and 3.20 show that the most pronounced difference between the α - and β -phase lies with the change in the twist angle.

A potential energy surface (PES) scan was performed by rotating the twist angle from -32.21° to 53.40° in increments of 10° in order to determine the difference in energy between the two phases (Figure 3.23). Single point calculations were performed at each incremental point at the UB3LYP-D3/6-311++G(d,p) level theory in the doublet state (one unpaired electron). All of the data points were then assembled to construct the PES scan illustrated in Figure 3.24. The relative energies were plotted by subtracting the energy of the conformation found in the β -phases from each incremental point. The PES plot shows that the β -phase is 1.53 kcal/mol (6.4 kJ/mol) more stable than the α -phase. A large energy barrier is observed between the α

and β phase, but the change between the two phases is most likely to occur along the pathway indicated in red as it is much more energetically viable. The small energy barrier along the red pathway indicates that **2** could interconvert between the α - and β -phase at room temperature.

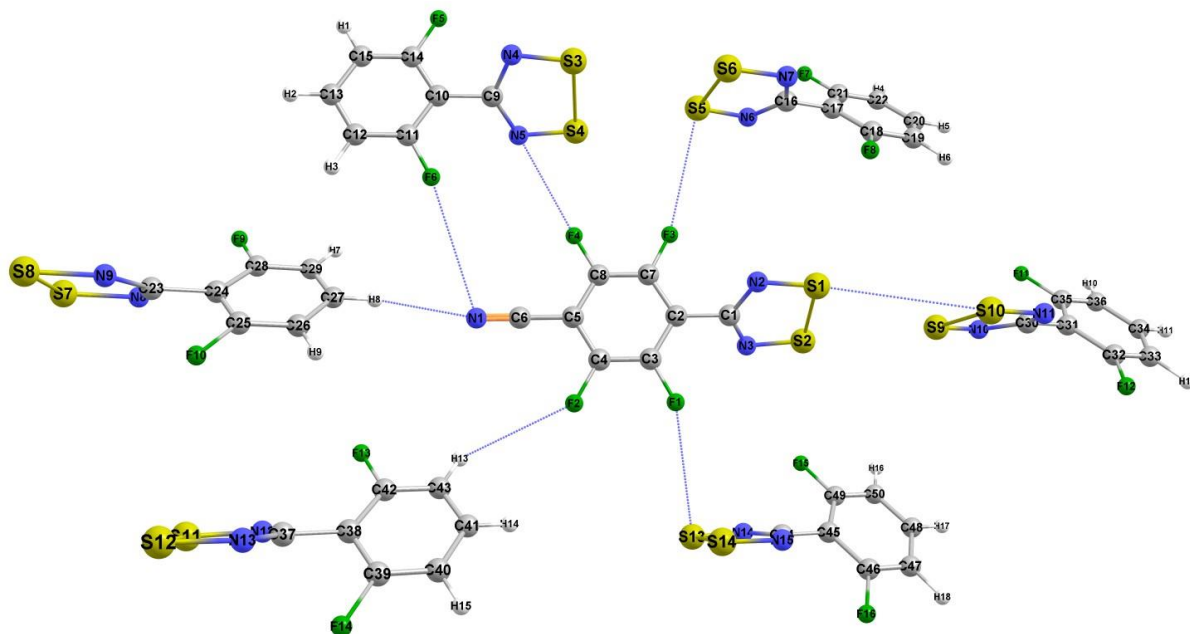


Figure 3.22: The potential interactions that can form between **2** and **7**, to provide the necessary stabilisation to promote growth of the α -phase.

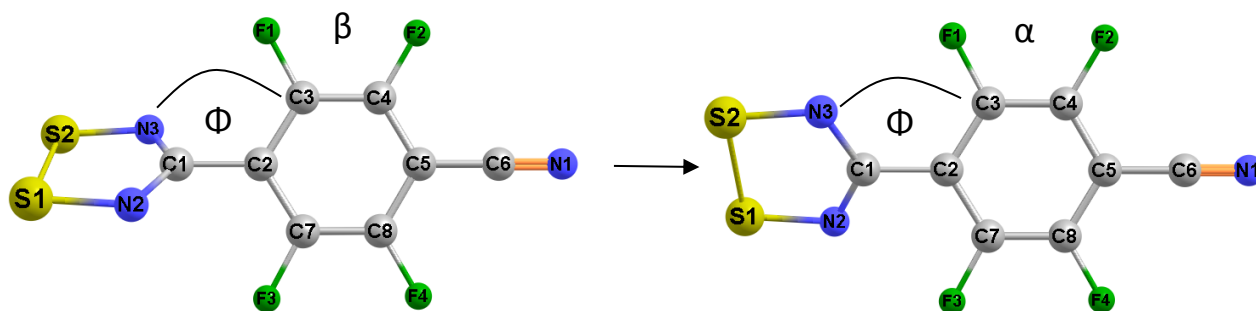


Figure 3.23: The torsion angle Φ is required to rotate from 53.40° (left) to -32.21° (right) in order to yield the α -phase.

A series of calculations were performed to determine what intermolecular interactions could provide the necessary stability to promote the growth of α -phase crystals. Pairs of **2-2** and **2-7** radicals were arranged in both dimeric and monomeric modes of association (Figure 3.25).

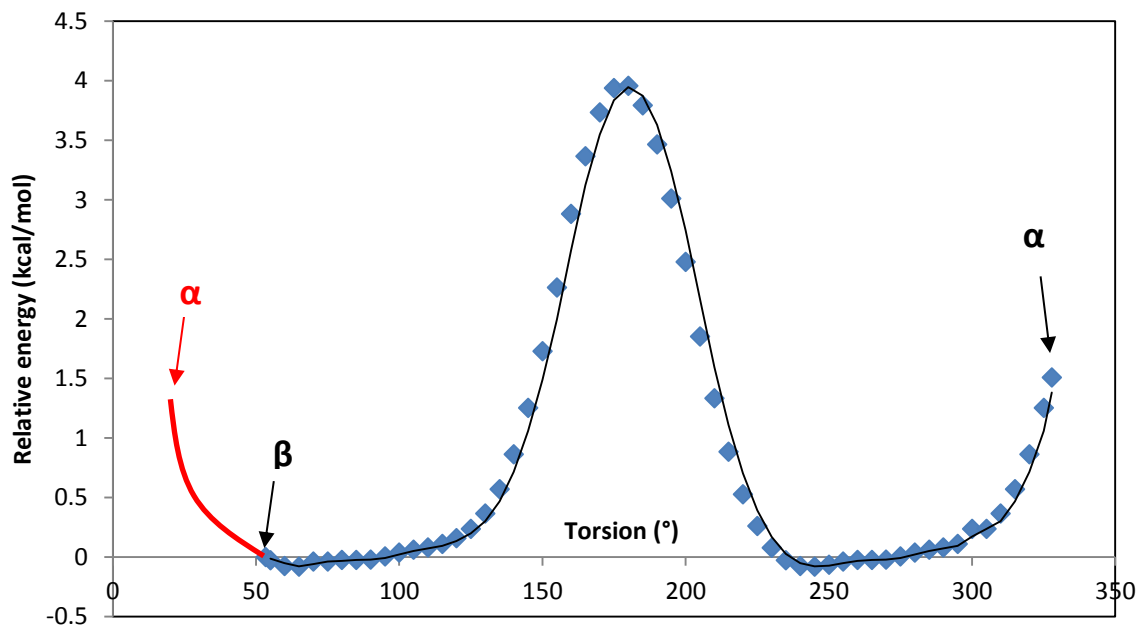


Figure 3.24: PES torsion angle showing the energy with twist angles for 2. Torsion angle corresponding to the conformation found in β - and α -phase are also indicated.

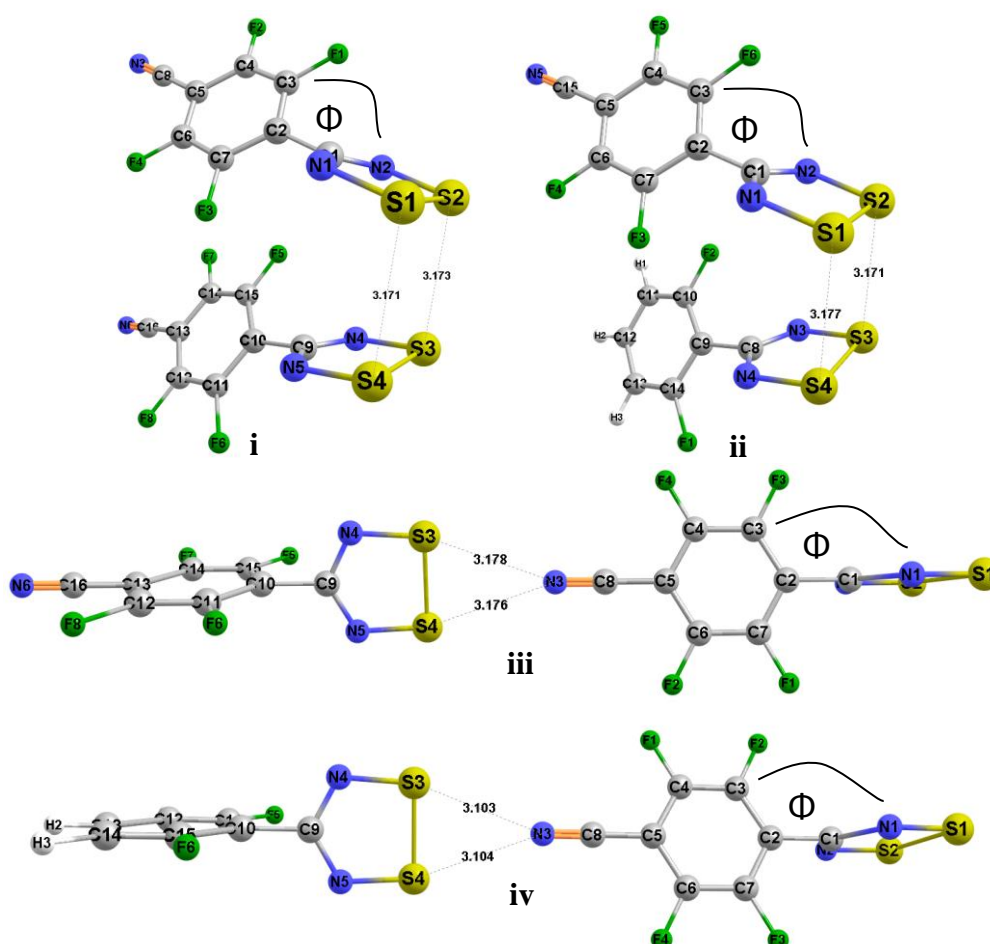


Figure 3.25: The optimised geometries of 2-2 (i) and 2-7 (ii) in the *cisoid* mode of association and 2-2 (iii) and 2-7 (iv) in the monomeric linear mode of association.

Geometry optimisation, with frequency calculations to ensure that minimum energy conformations had been identified, were subsequently performed in both the singlet and triplet states at the UB3LYP-D3/6-311++G(d,p) level of theory. The *cisoid* and linear modes were selected to represent the dimeric and monomeric modes of association, respectively. Counterpoise-corrected single point calculations were then performed on the fully optimised geometries at the UB3LYP-D3/6-311++G(d,p) level of theory, with the results summarised in Table 3.2.

The values in Table 3.2 show attractive energies for singlet state calculations performed on dimeric radicals **2-7** and **2-2**, while attractive energies are also shown for triplet state calculations performed on the **2-7** and **2-2** pairs in a monomeric linear mode of association. Importantly, both the dimeric and linear energies of the radicals **2-7** pairs result in a large twist angles similar to that observed for the α -phase of **2**. The linear pair of **2-2** exhibit the strongest attractive energy in Table 3.2, which indicates that this is the most energetically favourable association. The more stable **2-2** association also shows why crystals of **2** grow in the solid state, and not a co-crystal consisting of **2** and **7**. From the crystal structures and calculations performed on **2** and **7** we propose a mechanism that explains why the α -phase of **2** will grow in the presence of **7** (Figure 3.26).

Table 3.2: Interaction energies (kcal/mol) and twist angles (°) obtained for different pairs of 2-2 and 2-7. Twist angles shown for different radical pairs in Figure 3.25. Calculations were calculated in both the singlet and triplet states.

Association	Mode	Singlet	Triplet	Twist angle
2-2	dimeric	-1.39	6.19	-53.35
2-7	dimeric	-1.83	5.68	-50.97
2-2	linear	17.61	-5.15	-90.18
2-7	linear	17.31	-3.94	-90.19

Radical **7** forms an adduct with radical **2** via the formation of stabilising interactions, which results in a rotation of the twist angle in radical **2** from 53.40° to -32.21° (Figure 3.26-a). Rows of radical **2** then associate via more favourable **2-2** interactions in a linear mode of association (Table 3.2), which results in a disassociation between radicals **2** and **7**, and the formation of α -phase crystals (Figure 3.26-b).

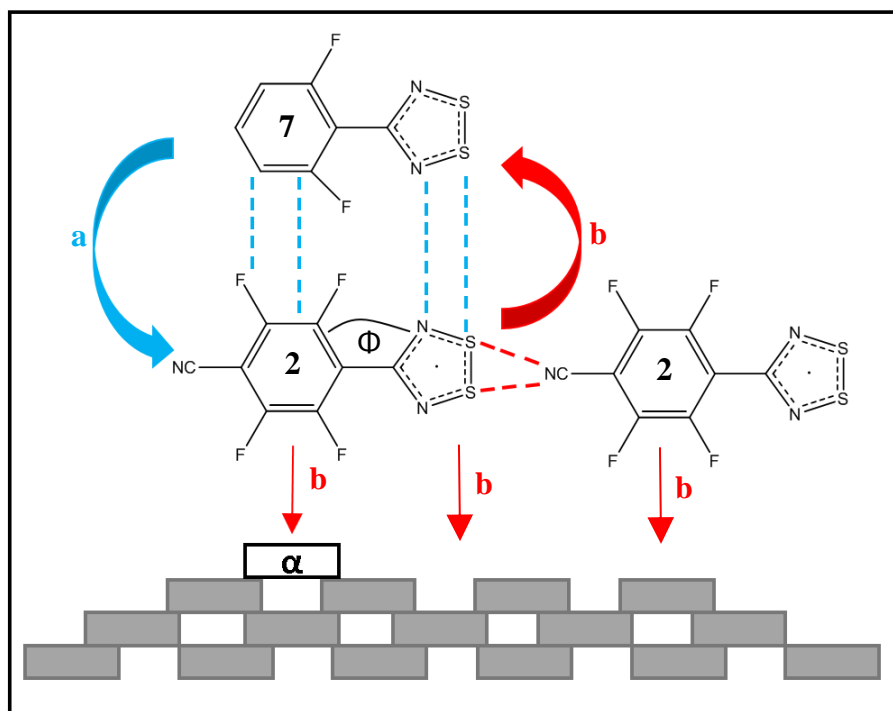
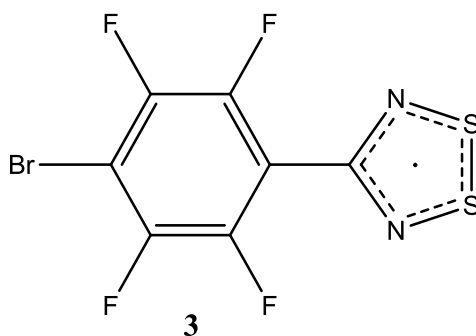


Figure 3.26: Scheme for the enhancement mechanism, which results in the formation α -phase crystals of 2 by the presence of additive 7. Adduct formation (a) between 2 and 7 provides stabilisation and rotation of twist angle (Φ). Disassociation of adduct to afford more favourable interactions between linear chains of 2, which result in the formation of α -phase crystals.

3.5. Properties of the 4-(4'-bromo-2',3',5',6'-tetrafluorophenyl)-1,2,3,5-dithiadiazolyl radical (3)



The sublimation of the 4-(4'-bromo-2',3',5',6'-tetra-fluorophenyl)-1,2,3,5-dithiadiazolyl at 80 °C yielded red crystalline blocks. The crystal structure of the red block was solved in $P\bar{1}$ and was shown to be a co-crystal (**3-cox**) consisting of dimers of 4-(4'-bromo-2',3',5',6'-tetra-fluorophenyl)-1,2,3,5-dithiadiazolyl radicals that adopt a *cisoid* mode of association, with the second component consisting of 4-bromo-2,3,5,6-tetrafluorobenzonitrile. The crystallographic

data of **3-cox** are given in Table 3.3. This is the first example of a DTDA containing radical molecules that could be co-crystallised with its nitrile starting material.

The differences between the contacts present in the crystal structure of **3** and **3-cox** are shown in Figure 3.27. The monomeric mode of association of **3** does not allow for interaction between the SOMOs, while **3-cox** exhibits S...S contacts that result in dimerised pairs. The contacts between the dimerised pair and the 4-bromo-2,3,5,6-tetrafluorobenzonitrile result in smaller twist angles, which allow for interaction between the SOMOs (Figure 3.27).

Table 3.3: Crystallographic data of 3-cox.

3-cox	
Empirical formula	C ₁₆ N ₄ F ₈ S ₄ Br ₂ :C ₇ NF ₄ Br
Temperature	100 K
Wavelength	0.71073 Å
Crystal system	Triclinic
Space group	$P\bar{1}$
<i>a</i> (Å)	7.4548(7)
<i>b</i> (Å)	10.6442(9)
<i>c</i> (Å)	17.0787(15)
α (°)	96.350(3)
β (°)	91.607(3)
γ (°)	95.127(3)
<i>V</i> (Å ³)	1340.50
<i>Z</i>	2
Goodness-of-fit on F^2	1.084
R indices (all data)	$R1 = 0.0202$ $wR2 = 0.0498$

The crystal packing²⁴ of **3** shows a network of S...N and S...F contacts between neighbouring heterocyclic rings, whereas the crystal structure of the co-crystal exhibits S...S, S...N and F...F contacts between dimer radicals pairs and the nitrile molecule (Figure 3.28). Atom labels are omitted from Figure 3.28 to show short-range contacts, with a similar atom colours scheme as shown in Figure 3.27. The difference between the types of contacts in these two crystal structures suggests that structure-directing interactions play a much more important role in the formation of monomeric radicals than previously thought. The presence of fluorine groups on the aryl ring allows for the formation of various other contacts as shown in Figure 3.28, but these contacts in combination with S...N contacts need to be more favourable than the S...S and N...N contacts that result in the dimerised pairs in **3-cox**. The fluorine atoms of **3-cox** form contacts with the nitrile molecule that could possibly be more favourable than the contacts observed in **3**, which then results in small twist angles and dimerised radical pairs.

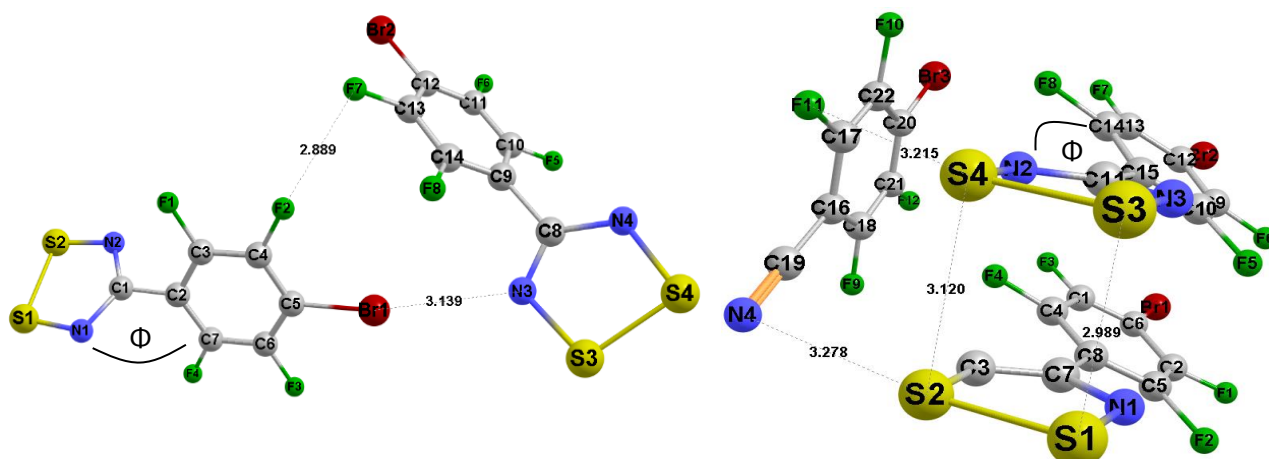


Figure 3.27: The contacts (Å) within the sum of the van der Waals radii for **3** (from reference 24, left) and **3-cox** (right). Twist angle Φ (N1-C1-C2-C7) = 54.00° (left) and Φ (N2-C11-C15-C14) = 26.65(2)° (right). Distances with e.s.d.s values for crystal structure (right): 3.278(2) Å, 3.215(2) Å, 3.120(7) Å and 2.989(8) Å.

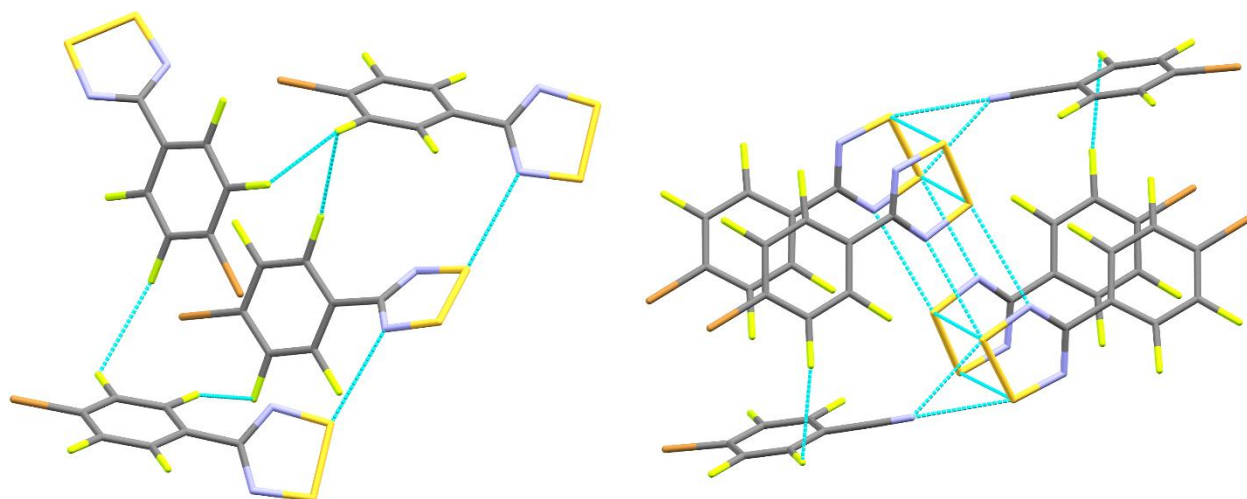


Figure 3.28: Partial packing of **3** (left) and **3-cox** (right). Dotted lines indicate close contacts within the sum of the van der Waals radii.

A CSD survey was performed to search for other homodimer DTDA that have been co-crystallised with another component to yield a neutral molecule. The search only yield one other example of a homodimer DTDA, which consists of 4-(4-trifluoromethylphenyl)-1,2,3,5-dithiadiazolyl that has been co-crystallised with triphenylstibine (**cox-stb**)²⁵. **Cox-stb** contains short S...N contacts that result in dimerised pairs of 4-(4-trifluoromethylphenyl)-1,2,3,5-dithiadiazolyl molecules in *cisoid* mode of association, with additional S...C contacts between the dimerised pair and the triphenylstibine. The crystal structure of **cox-stb** (Figure 3.29, right) reveals dimerised pairs interacting with the triphenylstibine to result in a very similar pattern and arrangement of molecules when compared to that of **3-cox** (Figure 3.28, right). The packing arrangement in both **3-cox** and **cox-stb** suggest that the intermolecular interactions

between the dimerised pairs and the other neutral molecule could play a role in these radicals preferring a *cisoid* mode of association.

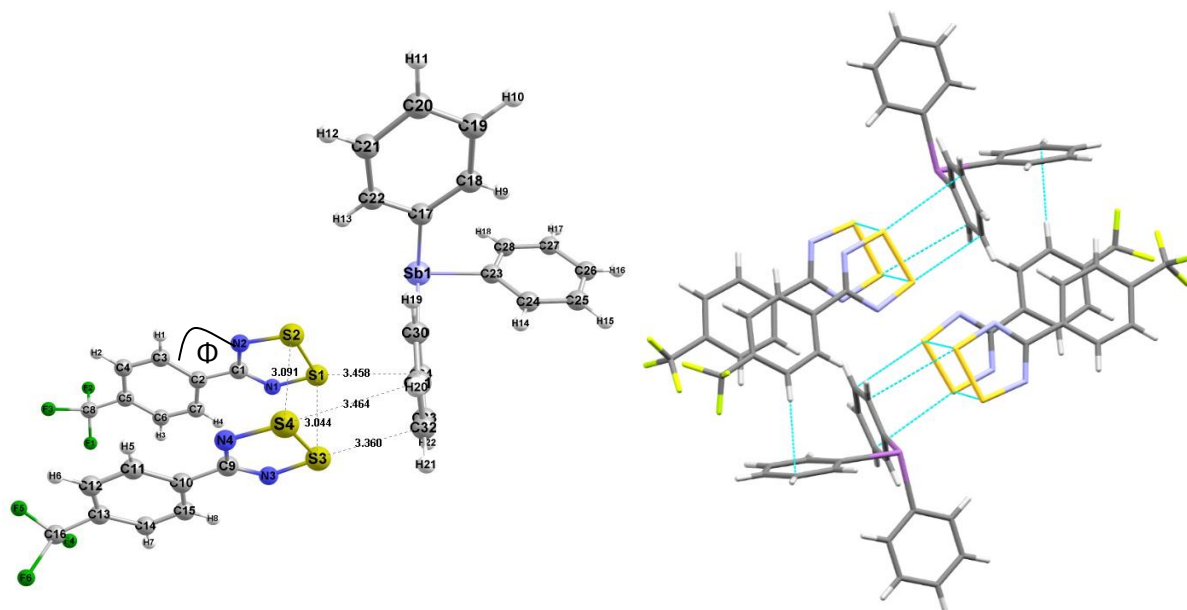
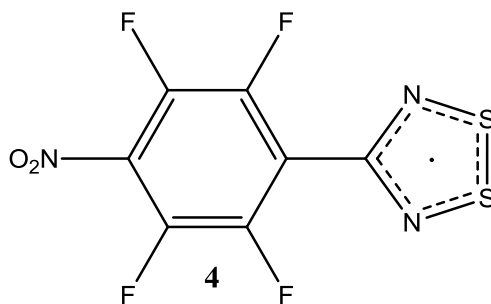


Figure 3.29: The short-range contacts between a *cisoid* dimerised pair of 4-(4-trifluoromethylphenyl)-1,2,3,5-dithiadiazolyl and triphenylstibine in cox-stb (left) from reference 25. Twist angle Φ (N2-C1-C2-C3) = 11.90°. The crystal structure of cox-stb (right) taken from reference 25.

3.6. Properties of the 4-(2,3,5,6-tetrafluoro-4-nitrophenyl)-1,2,3,5-dithiadiazolyl radical (4)



Radical **4** was synthesised and crystallised in order to collect high resolution X-ray data, and PND data so that joint refinement of these two data sets could be carried out using a new methodology that was developed by Deutsch and coworkers, and has been incorporated into the MoPro software package²⁶⁻²⁸. The joint refinement technique has proved to be successful when describing the spin density of metal-containing systems^{26,28,29}, but this experiment would be the first attempt to visualise the spin density of an organic radical system. Sublimation of crude radical at 100 °C yields black crystal blocks. The crystals of this radical have been reported to exhibit a monomeric mode of association and orders as a ferromagnet below 1.6 K³⁰.

3.7. Joint refinement of experimental charge and spin densities of **4**

HXRD data were obtained for **4** at the University of Lorraine, in collaboration with Nicolas Claiser. The PND data was generously supplied by Javier Luzon and coworkers³¹. The joint refinement of the HXRD and PND data was performed to establish spin contributions and determine topological properties of the intramolecular and intermolecular interactions in **4**. Crystallographic refinement of both data sets (Table 3.4) was performed utilising the IAM refinement using the SHELXL97³² software package. Multipolar refinement was carried out with Mollynx using the Hansen-Coppens multipolar atom model. Crystallographic refinement was followed by determination of the electron density [$\rho(r)$] and Laplacian [$\nabla^2\rho$] topological properties. These two values provide some information about the concentration or depletion of electron density at different regions of the radical. Furthermore, we can generate static deformation density, residual density and spin density maps (from joint refinement maps) with the *MoPro* software package^{26,28}. The asymmetric unit and molecular structure of **4** are illustrated in Figure 3.30.

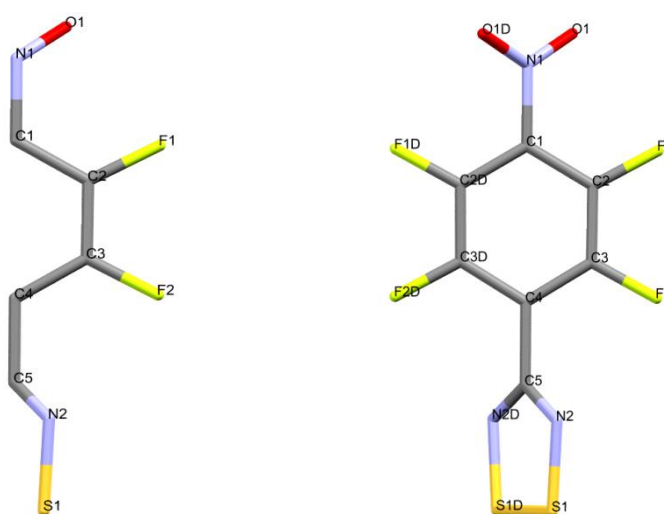


Figure 3.30 Asymmetric unit (left) and molecular shape of **4** (right), generated by a two-fold symmetry operator.

The topological properties of the bonds in **4** are summarised in Table 3.5. The first and second columns shows the distance (d_{X-Y}) between the two bonded atoms, X and Y. The $\rho(r)$ and $\nabla^2\rho$ columns provide the information about the bond critical points (BCPs) along the bonds. A minimum density of $0.71 \text{ e } \text{\AA}^{-3}$ is observed between the sulfur atoms (S1—S1D). A positive $\nabla^2\rho$ value indicates an area of charge depletion (presence of a positive charge), whereas a

negative $\nabla^2\rho$ value indicates local charge concentration (presence of a negative charge). The charge depletion between the sulfur atoms explains why a linear arrangement is observed for this radical. The electronegative oxygen atom of the nitro group is attracted to the area of charge depletion and forms a structure-directing intermolecular interaction. This interaction and the linear mode of association are illustrated in Figure 3.31, where the X1 symbol represents the area of charge depletion between the two sulfur atoms.

Table 3.4: Experimental conditions of HXRD and PND data collection of 4.

Chemical formula:	<i>p</i> -O ₂ NC ₆ F ₄ CNSSN	
<i>a</i> , <i>c</i> (Å) / <i>V</i> (Å ³)	8.1075 (1) , 14.8393(1) / 975.4103(9)	
$\alpha = \beta = \gamma$	90°	
Space group	<i>P4</i> ₁ <i>2</i> ₁ <i>2</i>	
Experiments	HXRD (CRM2)	PND
Temperature (K)	100	1.5
Magnetic field (T)	-	9
Wavelength (Å)	0.71073	0.843
($\sin(\theta)/\lambda$) _{max} (Å ⁻¹)	1.35	0.71
Refinement		
R(%)	2.01	1.39
wR2(%)	2.28	1.07
1-R (%)	-	11.71
GoF	1.399	1.687
Number of reflections	5489, I>3 σ	296, I>0.0 σ

A residual density map shows the difference between the total electron density $\rho(\mathbf{r})$ and a reference density $\rho_{\text{ref}}(\mathbf{r})$, which helps to describe how effective the reference density is in representing the system. This map therefore illustrates the difference between the observed and calculated structure factors. The amount of residual density accounts for the noise in experimental data and any modelling inadequacies. A sufficient refinement of the data will produce an ideal residual density map that exhibits a small number of residual electrons³³.

The residual density map of **4** (Figure 3.32) is mostly flat and featureless, with a small amount of residual density on the fluorine, sulfur and nitrogen (nitro group) atoms. The largest amount of unmodelled residual density is found between the sulfur atoms, which has been reported to be a potential symptom of anharmonicity³⁴.

Table 3.5: The topological properties of the BCPs of the bonds in 4.

Bonds	d_{x-y} (Å)	$\rho(r)$ ($e \text{ \AA}^{-3}$)	$\nabla^2 \rho$ ($e \text{ \AA}^{-5}$)
S1—S1D	2.088	0.71	1.01
S1—N2	1.637	1.57	-5.64
C5—N2	1.331	2.26	-16.64
C5—C4	1.486	1.65	-8.76
C3—C4	1.391	2.10	-17.44
C3—C2	1.388	1.98	-16.58
C3—F2	1.330	1.96	-10.43
C2—F1	1.326	1.96	-9.32
C1—C2	1.392	2.08	-16.15
C1—N1	1.455	1.70	-9.35
O1—N1	1.222	3.41	-12.87

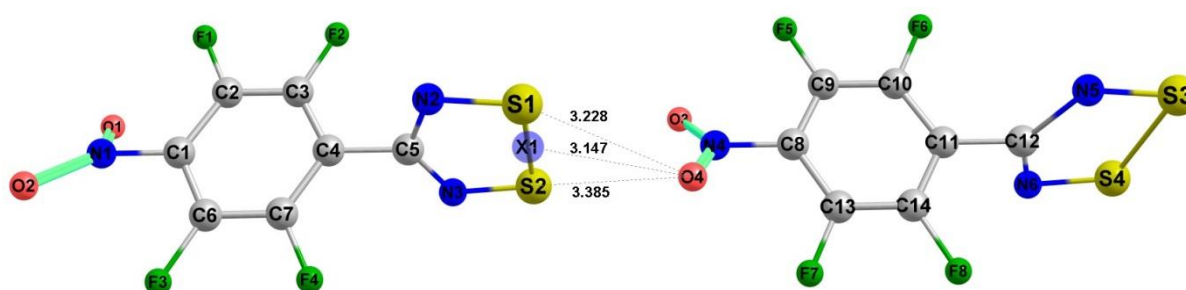


Figure 3.31: The intermolecular interactions between two radicals of 4 in a linear mode of association. The dummy atom, X1, represents an area of positive charge between the sulfur atoms.

Deformation density can be defined as the difference between the actual electron density and the density that has been calculated for the reference molecule, fitted with unbiased positional and thermal parameters. The deformation density reveals how the valence electron density has been redistributed by the effect of chemical bonding and intermolecular interactions³⁵. Thermal motion can be eliminated in order to yield a static deformation density map. This map allows for the visualisation of regions of electron density depletion (red areas) and concentration (blue areas) on the radical. The static deformation map of radical 4 is shown in Figure 3.33, where a depletion of electron density is shown between the sulfur atoms, and a concentration of electron density on the sulfur atoms.

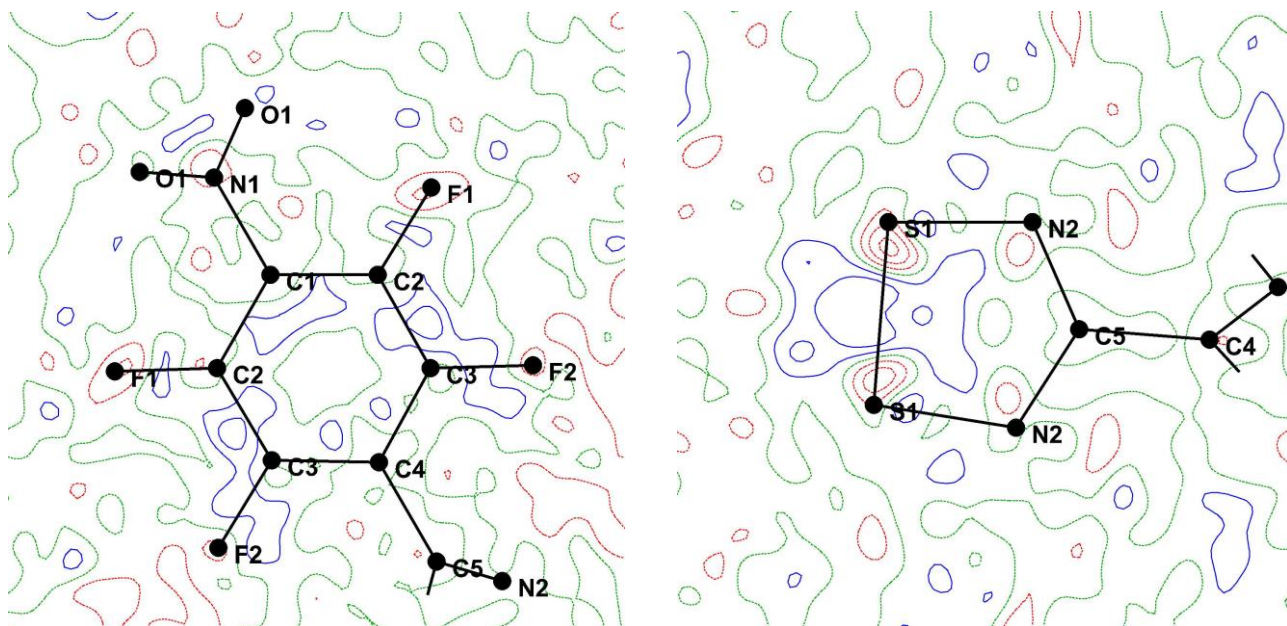


Figure 3.32: Residual density ($\sin \theta/l < 0.9 \text{ \AA}^{-1}$) in the perfluorophenyl ring (left) and S-N ring (right) of 4. Contours at 0.05 e \AA^{-3} . Blue indicates positive regions and red indicates negative regions.

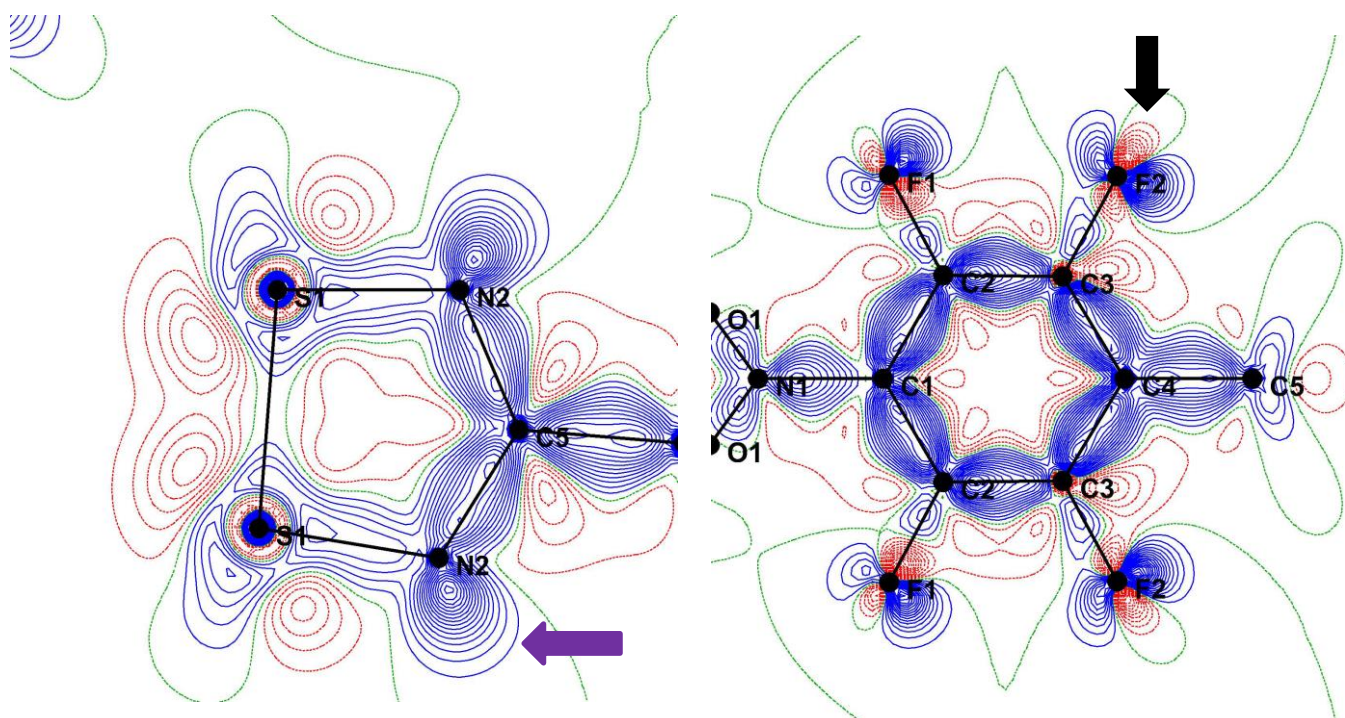


Figure 3.33: Static deformation density map of the S-N ring (left) and perfluorophenyl ring (right) of 4. Contours at 0.05 e \AA^{-3} . The sigma hole on a fluorine atom is indicated by a black arrow, while the lone pair on the nitrogen atom is indicated by a purple arrow.

The deformation density map also illustrates an accumulation of electron density on the covalent bonds and a depletion of electron density on the fluorine atoms, which is indicative of a sigma hole (black arrow). A sigma hole is rarely observed for fluorine atoms, as a combination of its high electronegativity and *sp*-hybridisation results in an influx of electronic charge, which neutralises the sigma hole³⁶. Nevertheless, the fluorine atoms in DTDA radicals play an important role as their sigma holes allows for the formation of various contacts that influence the solid-state architecture³⁷.

The presence of lone pairs on the heterocyclic ring nitrogen atoms (purple arrow) explains the formation of S \cdots N contacts between neighbouring radical molecules.

Rawson and coworkers have proposed that dimerisation is inhibited in perfluoroaryl DTDA radicals due to intramolecular N \cdots F repulsion leading to large twist angles between the heterocyclic and aryl rings and strong structure-directing interactions that result in a monomeric mode of association to reduce interaction between the SOMOs^{38,39}. The novel co-crystal (section 3.3.5, Figures 3.28 and 3.29) containing radical **1** suggests that strong structure-directing interactions play a more important role than previously thought, as the co-crystal exhibits a dimerised mode of association with small twist angles of 26.56°.

The deformation map shows NO₂ \cdots S contacts that provide the necessary stabilisation to inhibit dimerisation in radical **4**; several other contacts can be observed in the crystal packing of radical **4** (Figure 3.34).

The topological properties of these contacts were determined and are summarised in Table 3.6, where X and Y represent the interacting atoms shown in Figure 3.34.

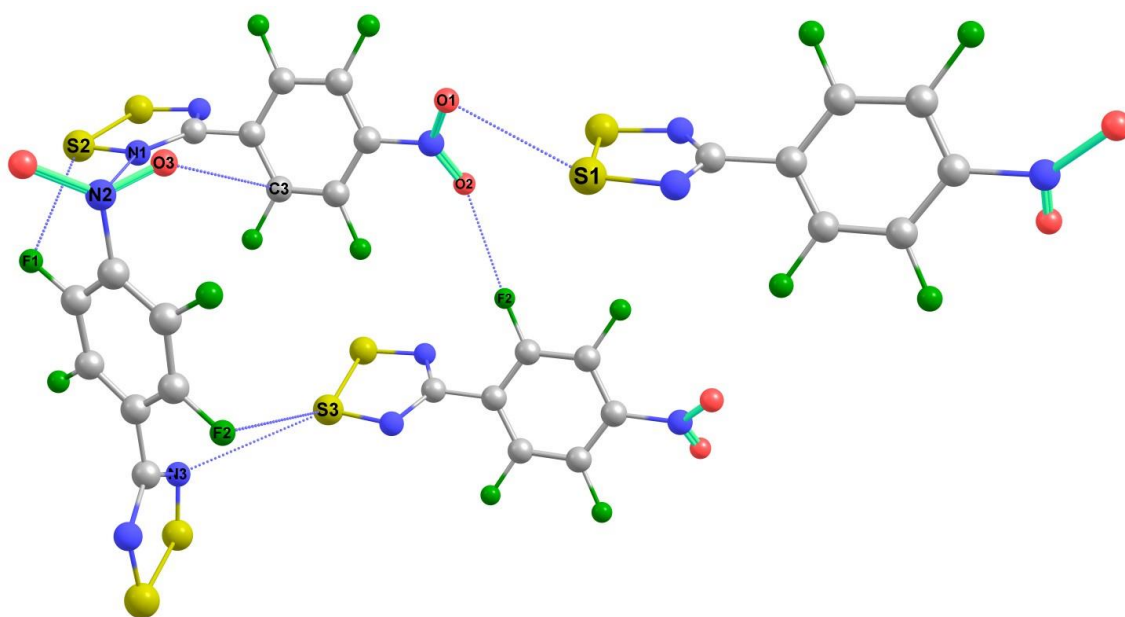


Figure 3.34: The intermolecular interactions present in the crystal packing of radical **4**.

Table 3.6: The topological properties of the BCPs of the intermolecular interactions in **4, involving atoms X and Y.**

Interactions	d_{X-Y} (Å)	$\rho(r)$ ($e \text{ \AA}^{-3}$)	$\nabla^2\rho$ ($e \text{ \AA}^{-5}$)
S1...O1	3.192	0.04	0.52
F2...O2	2.711	0.06	1.18
C3... O3	3.054	0.05	0.73
N1... N2	3.036	0.05	0.77
S2...F1	3.159	0.04	0.62
S3...N3	3.657	0.02	0.31
F2... S3	3.400	0.03	0.33

The $\nabla^2\rho$ values in Table 3.6 indicate a concentration of electron density between the atoms for the different intermolecular interactions. The F2...O2 contact exhibits an interatomic distance that is 0.28 Å less than the sum of the van der Waals radii, and a large depletion of electron density along the bond path, indicated by a $\nabla^2\rho$ value of 1.18 $e \text{ \AA}^{-5}$. This interaction forms part of the network of interactions between rows of linearly-arranged molecules of **4**, allowing for communication between the rows and result in the bulk magnetic ordering observed in the solid state⁴⁰. This strong fluorine-containing contact could also contribute to the large twist angle that inhibits dimerisation. It should be mentioned that a single contact is unlikely to sufficiently stabilise the monomeric mode of association or magnetic ordering, but all of the contacts in Table 3.6 contribute to the properties that radical **4** and other magnetic DTDA radicals exhibit.

The spin density and atomic spin populations obtained by joint refinement were compared to values obtained by Luzon and coworkers using PND data³¹. The Luzon group followed two different approaches in order to model the spin density distribution of the PND experiment; a magnetic wave-function (WF) approach⁴¹ and a multipolar (MP) expansion approach⁴². Table 3.7 summarises the spin-density values as calculated utilising the joint refinement, WF and MP expansion approach. Spin values were calculated for all atoms utilising the joint refinement of HXRD and PND data, but only for the atoms in the heterocyclic radical ring using the WF and MP approach. For the sake of this study we shall only discuss the spin densities present on atoms in the heterocyclic radical ring. The largest positive spin densities obtained in the joint refinement resides on the nitrogen atoms with slightly smaller value on the sulfur atom. These spin density values correspond to EPR studies that have shown that the unpaired spin density exists largely on the nitrogen and sulfur atoms of the heterocyclic radical ring⁴³. Some negative density is found to reside on the carbon atom. The total spin density can be described as the difference between the total α - and β -spins and often results in some negative spin density

being observed in areas where the SOMO α -spin has no contribution⁴⁴. The negative spin density observed at the carbon atom is due to a polarisation effect produced from the SOMO orbital interacting with certain doubly occupied orbitals.

The unrestricted Hartree-Fock formalism splits all orbitals into α (spin up) and β (spin down) orbitals in order to better describe unpaired spin density. An electronic exchange interaction originates from the interactions between the alpha orbitals and the SOMO. This allows for α orbitals to have greater overlap with the SOMO than the β orbitals. The difference in overlap for α and β orbitals will result further differences in spatial distribution and produces a polarised negative spin density at the carbon atom⁴³. The spin density map obtained from the joint refinement is illustrated in Figure 3.35, where spin-up contours are in red and spin-down contours in blue. The spin density is almost entirely localised in the p_z orbitals of the nitrogen and sulfur atoms, with the larger density on the nitrogen atoms, as indicated by the values of 0.25 and 0.22 for the nitrogen and sulfur atoms given in Table 3.7. The spin-down contours present at the carbon atom illustrates the negative spin density observed in Table 3.7.

Table 3.7: Spin populations obtained for the atoms in 4, using different models. Grey shading indicates the atoms in the heterocyclic radical ring.

Atoms	Net charges (Bader)	Spin (joint ref.)	Spin (WF PND only)	Spin (MP PND only)
S1	0.588	0.22(2)	0.301(1)	0.282(1)
N2	-0.687	0.25(1)	0.222(1)	0.245(1)
C5	0.683	-0.12(3)	-0.046(1)	-0.057(1)
F1	-0.668	0.02(2)	-	-
F2	-0.700	-0.01(2)	-	-
O1	-0.278	0.07(2)	-	-
N1	0.207	-0.03(2)	-	-
C1	0.295	-0.06(3)	-	-
C2	0.369	0.01(2)	-	-
C3	0.725	0.05(2)	-	-
C4	-0.080	0.02(3)	-	-

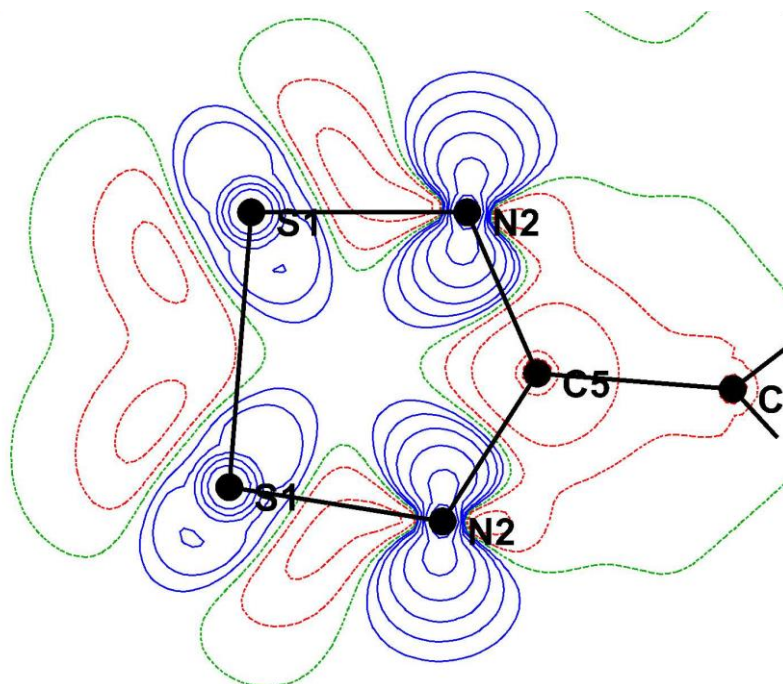


Figure 3.35: Spin density from joint refinement in plane S1-N2-C5. Contours at $0.01 \cdot 2^n$, $n=0, \dots, 12$. Blue indicates positive spin density, while red indicates negative spin density.

The results obtained with the WF and MP approaches agree, by showing that the largest positive spin values reside on the sulfur atoms, with smaller positive spin-density values residing on the nitrogen atoms and some negative spin-density residing on the carbon atom. Smaller negative density values were calculated for the carbon atom with the WF and MP methods when compared to values obtained by joint refinement.

The WF approach has been shown to suffer some difficulty in describing experimental spin density owing to the constraints of this method⁴¹. It has also been shown that groups in the *ortho* position will result in a torsion angle twist, which in turn will polarise the electron density away from the nitrogen atom onto the electronegative fluorine atom. This provides an explanation for the smaller spin values that were obtained for nitrogen atoms when using the WF approach. The relative spin densities of the sulfur, nitrogen and carbon atoms are illustrated in Figure 3.36, where we observe a large blue area of spherical spin density at the sulfur and nitrogen atoms, while a small area of negative spin density is found at the carbon atom.

The MP approach has the advantage of allowing for the displacement of spin density from the sulfur and neighbouring nitrogen atoms. The results from both the WF and MP approaches show that the spin density is almost entirely localised on the nitrogen and sulfur atoms of the heterocyclic ring, with a small amount of negative spin density located on the carbon atom induced by spin polarisation. This is indicative of the presence of a SOMO that consists of an

antibonding π orbital that extends over the nitrogen and sulfur atoms (see section 1.2, Chapter 1)⁴¹. The relative spin densities obtained by the MP method are illustrated in Figure 3.37.

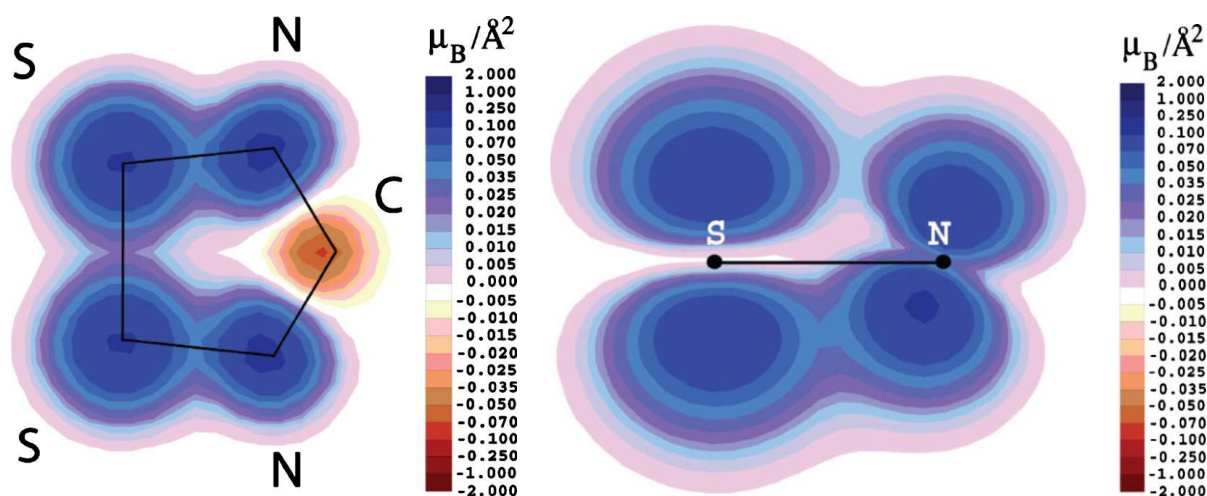


Figure 3.36: Spin density of the heterocyclic radical ring in 4 from reference 27. Contours at $0.01 \cdot 2^n$, $n = 0, \dots, 12$. Spin density from WF modeling in S1-N2-C5 plane (left) and in the perpendicular plane containing S1-N2 bonds (right).

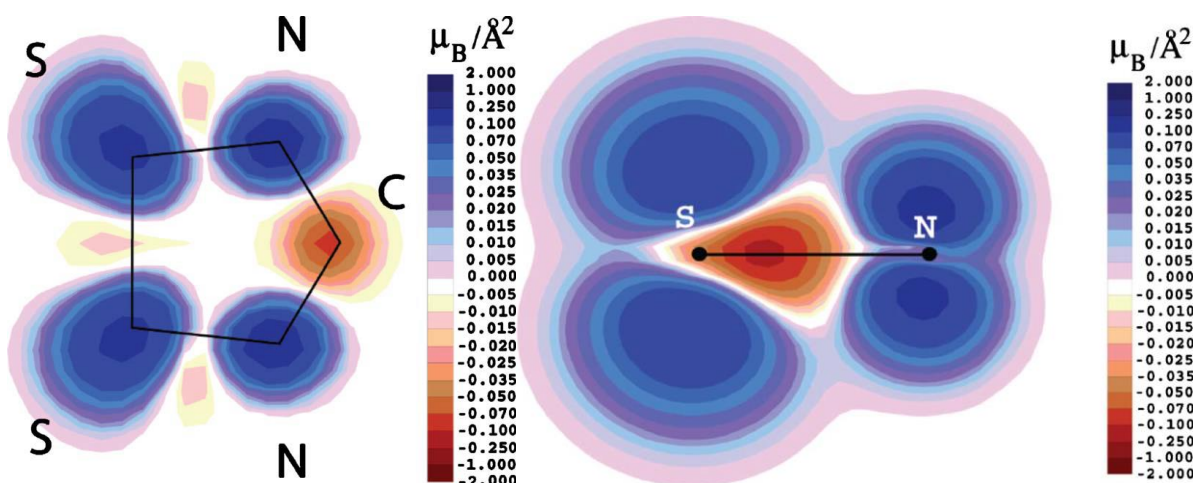


Figure 3.37: Spin density of the heterocyclic radical ring in 4 from reference 27. Contours at $0.01 \cdot 2^n$, $n = 0, \dots, 12$. Spin density from MP expansion modeling in S1-N2-C5 plane (left) and in the perpendicular plane containing S1-N2 bonds (right).

The spin densities obtained by the WF approach are less spherical than those obtained with the MP approach. The MP method results are more similar to the spin densities obtained with joint refinement, suggesting that the MP approach describes spin density more accurately than the WF method as it has fewer constraints.

To summarise, the joint refinement experiment was successfully utilised to describe the spin density on a DTDA and compares well to literature results. This method can therefore be utilised to describe the spin density of other radical systems or similar systems that do not

contain metal atoms. Furthermore, the joint refinement experiment confirmed the existence of structure-directing intermolecular interactions between the nitro group and the area of depletion between the sulfur atoms. Various intermolecular interactions were identified that form part of a network of interactions utilised in order to reduce the tendency of **4** to dimerise. Comparison of joint refinement spin density values to those obtained by the WF and MP approach revealed that the unpaired electron is indeed delocalised on the heterocyclic ring, which is in agreement with previous work done on dithiadiazolyl radicals³¹. However, spin densities determined by joint refinement suggest that more spin density is located on the nitrogen atoms and not on the sulfur atoms as the WF and MP method suggest. The presence of more spin density on the nitrogen atoms suggests that these atoms play a more important role than previously thought in facilitating the interaction between SOMOs, which results in a dimerised radical pair.

These results therefore suggest that when designing DTDA radicals with the potential to exhibit magnetic properties in the solid state, the R-group should be functionalised in such a way to shield the nitrogen atoms or make them less reactive, thereby reducing the likelihood of interactions forming between the SOMOs. In addition, the R-group should contain functional groups that can form intermolecular interactions with the nitrogen and sulfur atoms, thus both inhibiting dimerisation and allowing for communication between the unpaired electrons. The formation of strong interactions between the R-group and the nitrogen atoms of two neighbouring radicals will then result in a large twist angle, which also inhibits interactions between the SOMOs.

3.8. Calculation of spin densities on radical *p*-NCC₆F₄CN₂SSN (2**), *p*-BrC₆F₄CN₂SSN (**3**) and *p*-O₂NC₆F₄CN₂SSN (**4**)**

A theoretical study aimed to compare the spin densities obtained with various computational method to experimentally spin density values. Theoretical spin densities were calculated for **2,3** and **4** utilising four different methods, namely the “Atoms In Molecules” AIM⁴⁵, fuzzy atoms⁴⁶, Mulliken⁴⁷ and Hirshfeld methods⁴⁸. It should be mentioned that **7** was excluded as it does not order magnetically. The AIM and fuzzy atom methods utilise .wfx files generated at the UB3LYP-D3/6-311G(d,p) level of theory. The spin densities calculated using the AIM method are shown in Figures 3.38 - 3.40. The majority of the spin density is located on the

sulfur and nitrogen atoms of the heterocyclic radical rings with some negative spin density on the carbon atom.

The fuzzy atoms method uses atoms as regions in three-dimensional physical space with boundaries that are not sharp, but rather forming a continuous transition from one to another. Spin density values were calculated using the Multiwfn 3.3.8 software package⁴⁹ and again indicate that the majority of the spin density is located on the sulfur atoms in all three radicals. The Mulliken and Hirshfeld spin density values were obtained by performing population analysis calculations in Gaussian 09 Rev E01⁵⁰.

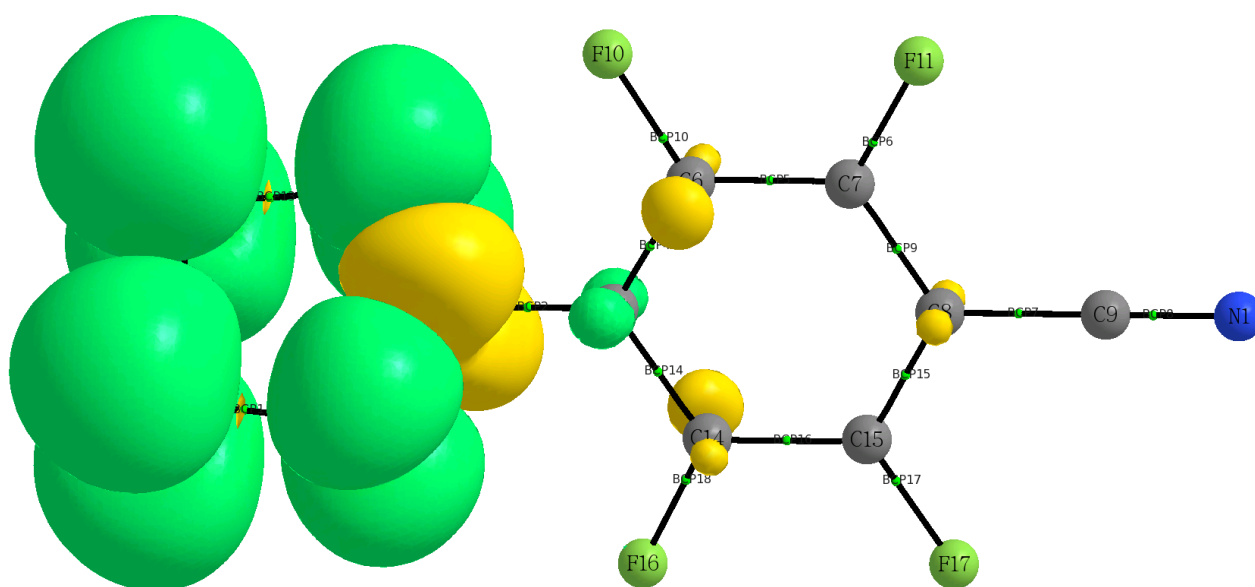


Figure 3.38: Spin density of radical 2, p -NCC₆F₄CNSSN[•].

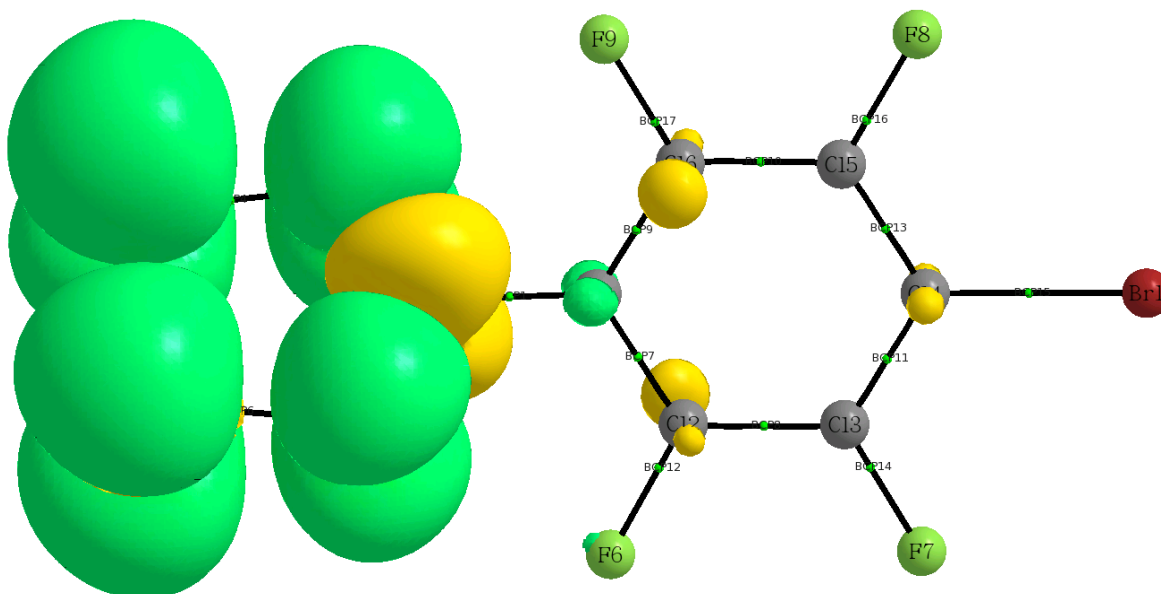


Figure 3.39: Spin density of radical 3, p -BrC₆F₄CNSSN[•].

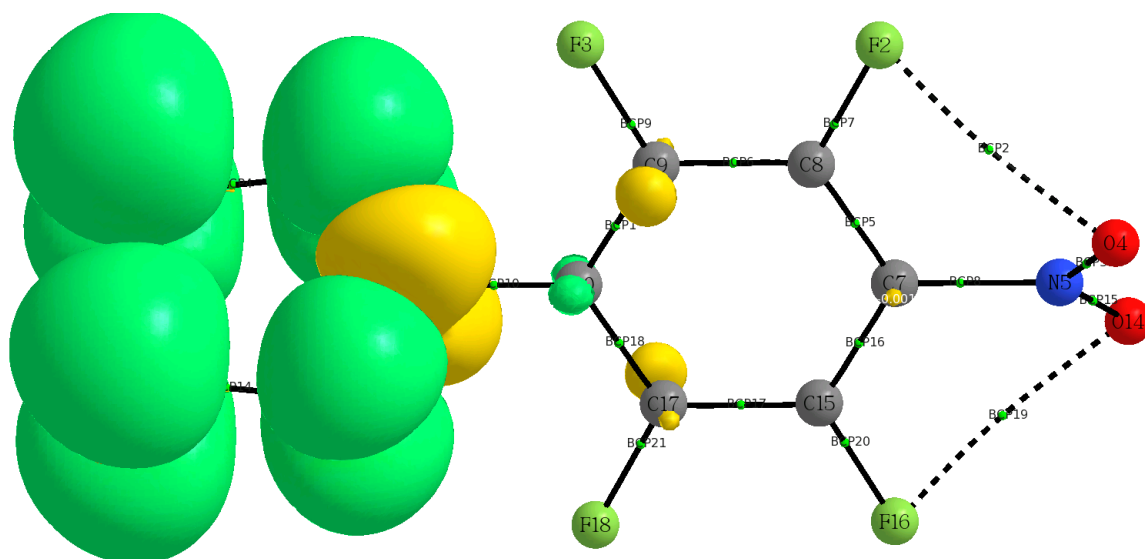


Figure 3.40: Spin density of radical **4**, $p\text{-O}_2\text{NC}_6\text{F}_4\text{CNSSN}^*$.

All spin density values are given in Tables 3.8 – 3.10. The relative percentage differences (% Δ) from the joint refinement are also included in Table 3.10 in order to compare the experimental and theoretical spin density values. All of the theoretical methods placed the largest component of the spin density on the sulfur atoms. The spin density values in Table 3.9 do not exhibit similar spin density values as observed in Tables 3.8 and 3.10. This is mainly due to the unique mode of association in **1**, which does not exhibit a linear mode of association as observed in **2** and **4**. The Mulliken values exhibit relatively small differences between the spin density values on the sulfur and nitrogen atoms. The negative spin density value on the carbon atom is similar to the one observed for **4**. The spin density values in Table 3.8 and 3.10 show similar values on the sulfur and nitrogen atom pairs.

Table 3.8: Spin density values calculated with the AIM, Fuzzy atoms, Mulliken and Hirshfeld method for **2**.

Atom	Method used to obtain spin density			
	AIM	Fuzzy atoms	Mulliken	Hirshfeld
S1	0.29	0.29	0.30	0.29
S2	0.29	0.29	0.30	0.29
N1	0.26	0.25	0.28	0.23
N2	0.26	0.25	0.28	0.23
C5	-0.08	-0.06	-0.15	-0.03

Table 3.9: Spin density values calculated with the AIM, Fuzzy atoms, Mulliken and Hirshfeld method for 3.

Method used to obtain spin density				
Atom	AIM	Fuzzy atoms	Mulliken	Hirshfeld
S1	0.28	0.28	0.29	0.28
S2	0.29	0.30	0.31	0.30
N1	0.25	0.24	0.27	0.22
N2	0.26	0.25	0.28	0.24
C5	-0.08	-0.06	-0.13	-0.03

Table 3.10: Spin density values calculated with the AIM, Fuzzy atoms, Mulliken and Hirshfeld method for 4.

Method used to obtain spin density									
Atom	Joint Refinement	AIM	%Δ	Fuzzy atoms	%Δ	Mulliken	%Δ	Hirshfeld	%Δ
S1	0.22	0.29	23.6	0.29	23.6	0.30	26.2	0.29	24.4
S2	0.22	0.29	23.6	0.29	23.6	0.30	26.2	0.29	24.4
N1	0.25	0.25	1.6	0.25	1.6	0.28	9.4	0.23	-8.2
N2	0.25	0.25	1.6	0.25	1.6	0.28	9.4	0.23	-8.2
C5	-0.12	-0.08	-53.9	-0.08	-53.9	-0.13	7.7	-0.03	-252.9

Comparison of the theoretical values and those obtained with the joint refinement method (Table 3.10) show that the theoretical methods describe spin density values and are in good agreement with the values obtained with the joint refinement technique.

The Mulliken method was found to best describe the spin density values for two reasons. Firstly, it was able to provide spin density values with small differences between the sulfur and nitrogen atoms, which is similar to what was observed using the joint refinement method. Secondly, it is the only method shown to describe the negative spin density value on the carbon atom in good agreement with values obtained with the joint refinement method.

Both the experimental and theoretical methods show that the majority of spin density resides on the sulfur and nitrogen atoms of the heterocyclic ring, but additional joint refinement experiments must be performed on other magnetic DTDA radicals in order to confirm that this method describes spin density more accurately than the WF and MP methods.

Conclusion

This chapter described the properties of three perfluoroaryl and one *ortho* fluorinated DTDA radicals, namely 4-(4-cyano-2,3,5,6-tetra-fluorophenyl)-1,2,3,5-dithiadiazolyl (**2**), 4-(4'-bromo-2',3',5',6'-tetrafluorophenyl)-1,2,3,5-dithiadiazolyl (**3**), 4-(2,3,5,6-tetrafluoro-4-nitrophenyl)-1,2,3,5-dithiadiazolyl (**4**) and 4-(2,6-difluorophenyl)-1,2,3,5-dithiadiazolyl (**7**). Attempted co-crystallisation of **2** and **7** was not successful, but instead a mixture of block- and needle-shaped crystals was obtained. XRD was utilised in order to identify these crystals as the α - and β -phase of **2**. This proved an interesting result as it was previously reported that the α -phase of **2** could only be obtained at low temperatures of $-10\text{ }^{\circ}\text{C}$ on a cold finger during sublimation. The enhancement mechanism was proposed as a possible explanation for observation, where α -phase of **2** will be obtained by the presence of additive **7**.

The needle-shaped β -phase crystals were further found to exhibit flexible properties. The crystal structure and the EPR results obtained for both straight and bent crystals suggest that rows of **2** move along the *a*- and *c* axes to yield dimeric pairs of **2**.

Synthesis and sublimation of **3** yielded crystals of the desired product and a novel co-crystal, **3-cox**. The crystal structure of **3-cox** was found to consist of dimeric pairs of **3** co-crystallised with the starting material, 4-bromo-2,3,5,6-tetrafluorobenzonitrile. The radicals in **3-cox** exhibit dimers in a *cisoid* mode of association, with S \cdots S contacts within the sum of the van der Waals radii and small twist angles, when compared to other perfluoroaryl radicals. The interactions between the radical pair and the starting material would suggest that structure-directing contacts could play a more important role in inhibiting dimerisation than previously thought. Radicals will dimerise if there are no structure-directing contacts, or if there are other favourable interactions that allow for dimerisation, as can be observed in the crystal structure of **3-cox**. The presence of structure-directing contacts or bulky groups will therefore result in large twist angles, which inhibit interaction between the SOMOs.

The joint refinement of HXRD and PND data was performed on **4** in order to static deformation density maps, topological properties of intermolecular interactions, spin-density values and spin density maps. The static deformation maps showed the presence of a sigma hole on the fluorine atoms and lone pair electrons on the heterocyclic-ring nitrogen atoms that form various intermolecular interactions. Furthermore, the linear mode of arrangement could be rationalised by structure-directing interactions between the areas of charge concentration on the oxygen atoms and the areas of charge depletion between the sulfur atoms. The spin density values were found to be in good agreement with literature results, but indicated larger spin density on

the nitrogen atoms, where previous literature results showed larger spin density residing on the sulfur atoms.

Theoretical methods were utilised to calculate spin density values for all three perfluoroaryl DTDA radicals (**2** – **4**). The Mulliken method was found to provide the most accurate results when compared to experimental spin density values. It was, however, observed that all methods describe more spin density residing on the sulfur atoms, whereas the joint refinement method showed that more spin density resides on the nitrogen atoms. The ability of the experimental and theoretical methods to describe spin density can only be confirmed once additional experiments have been performed.

The results in this chapter have shown that a network of intermolecular interactions in DTDA radicals play an important role to determine whether radicals will prefer to dimerise or exhibit a monomeric mode of association. These intermolecular interactions allow for communication between the spin densities of radical molecules, but influence the solid-state architecture and results in some interesting properties that have not yet been reported. The network of intermolecular interactions in DTDA radicals therefore play a very important role and sufficient understanding of these interactions could even result in the crystal engineering of DTDA radicals with tailored properties. The nature and strength of intermolecular interactions in known DTDA radicals will be investigated in the next chapter. The results from this study could provide the necessary information to design novel DTDA radicals that exhibit magnetic or other interesting properties.

References

- (1) Tamura, M.; Nakazawa, Y.; Shiomi, D.; Nozawa, K.; Hosokoshi, Y.; Ishikawa, M.; Takahashi, M.; Kinoshita, M. *Chemical Physics Letters* **1991**, *186*, 401.
- (2) Akutsu, H.; Yamada, J.-i.; Nakatsuji, S. i. *Synthetic Metals* **2001**, *120*, 871.
- (3) Miller, J. S. *Materials Today* **2014**, *17*, 224.
- (4) Beldjoudi, Y.; Arauzo, A.; Palacio, F.; Pilkington, M.; Rawson, J. M. *Journal of the American Chemical Society* **2016**, *138*, 16779.
- (5) Banister, A. J.; Bricklebank, N.; Clegg, W.; Elsegood, M. R. J.; Gregory, C. I.; Lavender, I.; Rawson, J. M.; Tanner, B. K. *Journal of the Chemical Society, Chemical Communications* **1995**, 679.
- (6) Bryan, C. D.; Cordes, A. W.; Goddard, J. D.; Haddon, R. C.; Hicks, R. G.; MacKinnon, C. D.; Mawhinney, R. C.; Oakley, R. T.; Palstra, T. T. M.; Perel, A. S. *Journal of the American Chemical Society* **1996**, *118*, 330.
- (7) Ghosh, S.; Mishra, M. K.; Kadambi, S. B.; Ramamurty, U.; Desiraju, G. R. *Angewandte Chemie International Edition* **2015**, *54*, 2674.
- (8) Owczarek, M.; Hujsak, K. A.; Ferris, D. P.; Prokofjevs, A.; Majerz, I.; Szklarz, P.; Zhang, H.; Sarjeant, A. A.; Stern, C. L.; Jakubas, R.; Hong, S.; Dravid, V. P.; Stoddart, J. F. **2016**, *7*, 13108.
- (9) Bahatyrova, S.; Frese, R. N.; van der Werf, K. O.; Otto, C.; Hunter, C. N.; Olsen, J. D. *Journal of Biological Chemistry* **2004**, *279*, 21327.
- (10) Hunter, C. A.; Sanders, J. K. M. *Journal of the American Chemical Society* **1990**, *112*, 5525.
- (11) Fatila, E. M.; Jennings, M. C.; Goodreid, J.; Preuss, K. E. *Acta Crystallographica Section C* **2010**, *66*, o260.
- (12) Kelly, R. C.; Rodríguez-Hornedo, N. *Organic Process Research & Development* **2009**, *13*, 1291.
- (13) Khoshkhoo, S.; Anwar, J. *Journal of Physics D: Applied Physics* **1993**, *26*, B90.
- (14) Clarke, C. S.; Haynes, D. A.; Smith, J. N. B.; Batsanov, A. S.; Howard, J. A. K.; Pascu, S. I.; Rawson, J. M. *CrystEngComm* **2010**, *12*, 172.
- (15) Allen, C.; Haynes, D. A.; Pask, C. M.; Rawson, J. M. *CrystEngComm* **2009**, *11*, 2048.
- (16) Robinson, S. W.; Haynes, D. A.; Rawson, J. M. *CrystEngComm* **2013**, *15*, 10205.
- (17) Reichardt, C. *Organic Process Research & Development* **2007**, *11*, 105.
- (18) Zhunuspayev, D. E.; Mun, G. A.; Hole, P.; Khutoryanskiy, V. V. *Langmuir* **2008**, *24*, 13742.
- (19) Kamali, N.; Erxleben, A.; McArdle, P. *Crystal Growth & Design* **2016**, *16*, 2492.
- (20) Walshe, N.; Crushell, M.; Karpinska, J.; Erxleben, A.; McArdle, P. *Crystal Growth & Design* **2015**, *15*, 3235.
- (21) Boyd, F. R.; England, J. L.; Davis, B. T. C. *Journal of Geophysical Research* **1964**, *69*, 2101.
- (22) Miyahara, M.; El Goresy, A.; Ohtani, E.; Nagase, T.; Nishijima, M.; Vashaei, Z.; Ferroir, T.; Gillet, P.; Dubrovinsky, L.; Simionovici, A. *Proceedings of the National Academy of Sciences* **2008**, *105*, 8542.
- (23) Ectors, P.; Zahn, D. *Physical Chemistry Chemical Physics* **2013**, *15*, 9219.
- (24) Antorrena, G.; Palacio, F.; E. Davies, J.; Hartley, M.; M. Rawson, J.; B. Smith, J. N.; Steiner, A. *Chemical Communications* **1999**, 1393.
- (25) Boere, R. T. *CrystEngComm* **2016**, *18*, 2748.
- (26) Deutsch, M.; Claiser, N.; Pillet, S.; Chumakov, Y.; Becker, P.; Gillet, J.-M.; Gillon, B.; Lecomte, C.; Souhassou, M. *Acta Crystallographica Section A* **2012**, *68*, 675.
- (27) Deutsch, M.; Claiser, N.; Souhassou, M.; Gillon, B. *Physics Procedia* **2013**, *42*, 10.
- (28) Deutsch, M.; Gillon, B.; Claiser, N.; Gillet, J.-M.; Lecomte, C.; Souhassou, M. *IUCrJ* **2014**, *1*, 194.
- (29) Kibalin, I. A.; Yan, Z.; Voufack, A. B.; Gueddida, S.; Gillon, B.; Gukasov, A.; Porcher, F.; Bataille, A. M.; Morini, F.; Claiser, N.; Souhassou, M.; Lecomte, C.; Gillet, J. M.; Ito, M.; Suzuki, K.; Sakurai, H.; Sakurai, Y.; Hoffmann, C. M.; Wang, X. P. *Physical Review B* **2017**, *96*, 054426.

- (30) Alberola, A.; Less, R. J.; Pask, C. M.; Rawson, J. M.; Palacio, F.; Oliete, P.; Paulsen, C.; Yamaguchi, A.; Farley, R. D.; Murphy, D. M. *Angewandte Chemie International Edition* **2003**, *42*, 4782.
- (31) Luzón, J.; Campo, J.; Palacio, F.; McIntyre, G. J.; Goeta, A. E.; Ressouche, E.; Pask, C. M.; Rawson, J. M. *Physica B: Condensed Matter* **2003**, *335*, 1.
- (32) Sheldrick, G. M. *Acta Crystallogr, Sect. A* **2008**, *64*, 112.
- (33) Meindl, K.; Henn, J. *Foundations of residual-density analysis*, 2008; Vol. 64.
- (34) Domagała, S.; Kosciuszko, K.; Robinson, S. W.; Haynes, D. A.; Woźniak, K. *Crystal Growth & Design* **2014**, *14*, 4834.
- (35) Jelsch, C.; Teeter, M. M.; Lamzin, V.; Pichon-Pesme, V.; Blessing, R. H.; Lecomte, C. *Proceedings of the National Academy of Sciences* **2000**, *97*, 3171.
- (36) Clark, T.; Hennemann, M.; Murray, J. S.; Politzer, P. *Journal of Molecular Modeling* **2007**, *13*, 291.
- (37) Bauzá, A.; Mooibroek, T. J.; Frontera, A. *ChemPhysChem* **2015**, *16*, 2496.
- (38) Rawson, J. M.; Less, R. J.; Smith, J. N. B.; Palacio, F.; Antorrena, G. *Molecular Crystals and Liquid Crystals Science and Technology. Section A. Molecular Crystals and Liquid Crystals* **1999**, *334*, 275.
- (39) Rawson, J. M.; Banister, A. J.; Lavender, I. In *Advances in Heterocyclic Chemistry*; Katritzky, A. R., Ed.; Academic Press: 1995; Vol. 62, p 137.
- (40) Rawson, J. M.; Luzon, J.; Palacio, F. *Coordination Chemistry Reviews* **2005**, *249*, 2631.
- (41) Ressouche, E.; Boucherle, J. X.; Gillon, B.; Rey, P.; Schweizer, J. *Journal of the American Chemical Society* **1993**, *115*, 3610.
- (42) Brown, P. J.; Capiomont, A.; Gillon, B.; Schweizer, J. *Journal of Magnetism and Magnetic Materials* **1979**, *14*, 289.
- (43) Alonso, P. J.; Antorrena, G.; Martínez, J. I.; Novoa, J. J.; Palacio, F.; Rawson, J. M.; Smith, J. N. B. *Applied Magnetic Resonance* **2001**, *20*, 231.
- (44) Davis, M. S.; Morokuma, K.; Kreilick, R. W. *Journal of the American Chemical Society* **1972**, *94*, 5588.
- (45) Bader, R. F. W. *Accounts of Chemical Research* **1985**, *18*, 9.
- (46) Mayer, I.; Salvador, P. *Chemical Physics Letters* **2004**, *383*, 368.
- (47) Mulliken, R. S. *The Journal of Chemical Physics* **1955**, *23*, 1833.
- (48) Hirshfeld, F. L. *Theoret. Chim. Acta* **1977**, *44*, 129.
- (49) Lu, T.; Chen, F. *Journal of Computational Chemistry* **2012**, *33*, 580.
- (50) Frisch, M. J.; Trucks, G. W.; Schlegel, H. B.; Scuseria, G. E.; Robb, M. A.; Cheeseman, J. R.; Scalmani, G.; Barone, V.; Mennucci, G.; Petersson, A.; Nakatsuji, H.; Caricato, M.; Li, X.; Hratchian, H. P.; Izmaylov, A. F.; Bloino, J.; Zheng, G.; Sonnenberg, J. L.; Hada, M.; Ehara, M.; Toyota, K.; Fukuda, R.; Hasegawa, J.; Ishida, M.; Nakajima, T.; Honda, Y.; Kitao, O.; Nakai, H.; Vreven, T.; Jr., J. A. M.; Peralta, J. E.; Ogliaro, F.; Bearpark, M.; Heyd, J. J.; Brothers, E.; Kudin, K. N.; Staroverov, V. N.; Keith, T.; Kobayashi, R.; Normand, J.; Raghavachari, K.; Rendell, A.; Burant, J. C.; Iyengar, S. S.; Tomasi, J.; Cossi, M.; Rega, N.; Millam, J. M.; Klene, M.; Knox, J. E.; Cross, J. B.; Bakken, V.; Adamo, C.; Jaramillo, J.; Gomperts, R.; Stratmann, R. E.; Yazyev, O.; Austin, A. J.; Cammi, R.; Pomelli, C.; Ochterski, J. W.; Martin, R. L.; Morokuma, K.; Zakrzewski, V. G.; Voth, G. A.; Salvador, P.; Dannenberg, J. J.; Dapprich, S.; Daniels, A. D.; Farkas, O.; Foresman, J. B.; Ortiz, J. V.; Cioslowski, J.; Fox, D. J. Gaussian, Inc.: Wallingford CT **2013**.

4 A computational study of the modes of association in 1,2,3,5-dithiadiazolyl radicals

Introduction

It was discussed in previous chapters that DTDA radicals are attractive candidates in the crystal engineering of molecular magnets¹, but that a multi-centre two-electron $\pi^* - \pi^*$ interaction between the singly occupied molecular orbitals (SOMOs) will result in an overall loss in magnetic properties². It was shown that a combination of large twist angles and structure-directing contacts result in a reduced tendency of radicals to dimerise³⁻⁵. These studies have shown that structure-directing contacts play an important role in whether DTDA radicals will prefer a monomeric or dimeric mode of association.

In this chapter, an investigation of the properties of structure-directing contacts of radicals in a monomeric or dimeric modes of association will be reported. Various computational software packages were utilised to study the crystal structures. All calculations were performed in the gas phase, which does not take into account any of the lattice or solid-state effects that play an important role in the three dimensional architecture of DTDA radicals. The aim was to determine whether simple gas phase calculations could be used to establish whether a particular DTDA would crystallise as a monomer or as a dimer. These calculations were therefore initially carried out on a series of radicals for which at least one crystal structure is known.

For the remainder of this thesis monomeric radicals will refer to two DTDA radicals that exhibit a monomeric mode of association, whereas dimeric radicals will refer to a pair of dimerised radicals. Firstly, geometry optimisation and intermolecular interaction energy calculations were performed on Cartesian coordinates of dimeric and monomeric radicals, for which the crystal structures are available in the Cambridge Structural Database (CSD). A potential energy surface (PES) scan was performed to determine how variation of torsion angles will affect the interaction strength in monomeric and dimeric radicals. An Energy Decomposition Analysis (EDA) aimed to determine what contributions result in strong or weak binding energies in monomeric and dimeric radicals. A topological analysis was used to determine the Bond Critical Point (BCP) properties of contacts in monomeric and dimeric radicals. Lastly, an Electrostatic Surface Potential (ESP) map was calculated for each monomeric and dimeric radical to visualise the size, shape and the charge distribution of these molecules and their intermolecular interactions in three dimensions.

4.1. 1,2,3,5-Dithiadiazolyl radicals in the CSD

A Cambridge Structural Database⁶ (CSD, Version 5.38 Nov 2016) survey was performed in order to obtain a subset of DTDA radicals using the search parameters illustrated in Figure 4.1. The figure shows two different queries (a and b) that search for DTDA radicals, but yield different results, which is why the search was set up to contain both queries. The search fragment contains an aryl R group as we wished to investigate aryl-functionalised DTDA radicals.

The search yielded 125 hits, which included monomeric and dimeric radicals, of which five monomeric and six dimeric radicals were selected for further calculations. These radicals were selected as high quality XRD data are available and they exhibit well-studied modes of association between the radicals, of which the most common ones are illustrated in Figure 4.2. The five monomeric radicals have already been discussed in Chapter 1, while the six dimeric radicals were selected as they have varying numbers of fluorinated substituents at different positions on the aryl ring, as it has been shown that the presence of fluorinated groups can result in the formation of various intermolecular interactions⁷. The nature of the intermolecular interactions in monomeric and dimeric radicals should provide some information about why these radicals exhibit different modes of association.

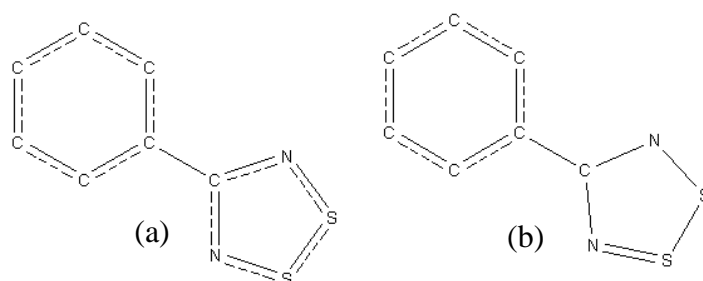


Figure 4.1: Query (a) and (b) used to search the CSD for all available DTDA radicals.

The Cartesian coordinates of the selected radical crystal structures were exported from the CSD in xyz format. The list of radicals studied is given in Table 4.1, where the table contains the CSD refcodes and the corresponding chemical name for each radical. Additionally, each radical was given a compound number used to be used in later tables, where codes **1 – 6** represent the radicals discussed and Chapter 1 and codes **8 – 12** are additional radicals to be used in the calculations in this chapter. The list has been further divided into dimeric and monomeric radicals.

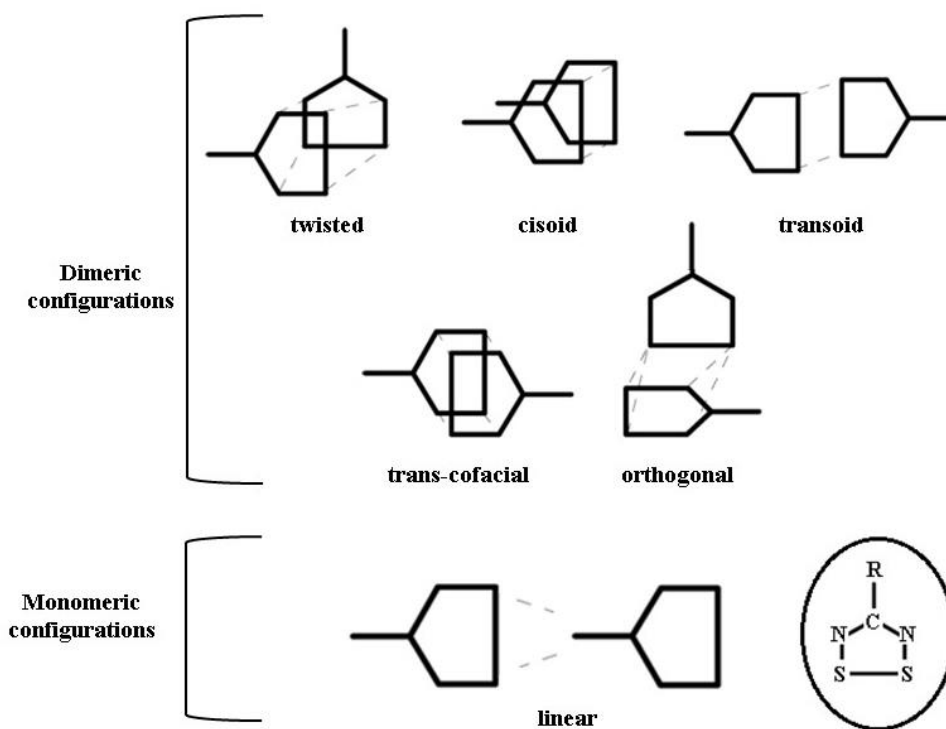


Figure 4.2: Different modes of associations for both dimeric and monomeric radicals.

Table 4.1: CSD refcodes, chemical names and compound number for each of the dimeric (a) and monomeric (b) radicals. The properties of the radicals 2,3 and 4 were reported in Chapter 3.

	CSD refcode	Chemical Name	Compound number
(a)	PHTHAZO1	4-phenyl-1,2,3,5-dithiadiazolyl	1
	QEFGIT	4'-fluorophenyl-1,2,3,5-dithiadiazolyl	8
	QEFGOZ	2'-fluorophenyl-1,2,3,5-dithiadiazolyl	9
	QUNQOG	4-perfluorophenyl-1,2,3,5-dithiadiazolyl	10
	QUNQUM	(4-phenyl-1,2,3,5-dithiadiazolyl)(4-perfluorophenyl)-1,2,3,5-dithiadiazolyl	11
	VUQHEV	4-(3',4',5'-trifluorophenyl)-1,2,3,5-dithiadiazolyl	12
(b)	YOMXUT03	4-(4'-cyano-2',3',5',6'-tetrafluorophenyl)-1,2,3,5-dithiadiazolyl	2
	GOTQEL	4-(4'-bromo-2',3',5',6'-tetrafluorophenyl)-1,2,3,5-dithiadiazolyl	3
	ILUKIJ	4-(2',3',5',6'-tetrafluoro-4-nitrophenyl)-1,2,3,5-dithiadiazolyl	4
	HAKYOI	4-(4"-cyanoperfluoro-1',1"-biphenyl-4'-yl)-1,2,3,5-dithiadiazolyl	5
	HAWRAZ	4-(2',4',6'-tris(trifluoromethyl)phenyl)-1,2,3,5-dithiadiazolyl	6

The crystal structures of the dimeric radicals in Table 4.1 exhibit $\pi^* - \pi^*$ stacking contacts that have been described as pancake bonds (Figure 4.3)^{8,9}, which involve $S \cdots S$, $S \cdots N$ and $N \cdots N$ contacts between the heterocyclic radical rings.

The crystal structures of the monomeric radicals in Table 4.1 exhibit a linear mode of association, resulting from strong structure-directing contacts. It was, however, observed that the crystal structures of radicals 2 and 6 do not exhibit a typical linear mode of association (Figure 4.4), but rather a combination of $S \cdots N$ contacts between the heterocyclic rings, as well as various additional close contacts to fluorine.

The calculations in the following sections aim to explain why small differences between the R groups of monomeric and dimeric have a large effect on the mode of association of these radicals.

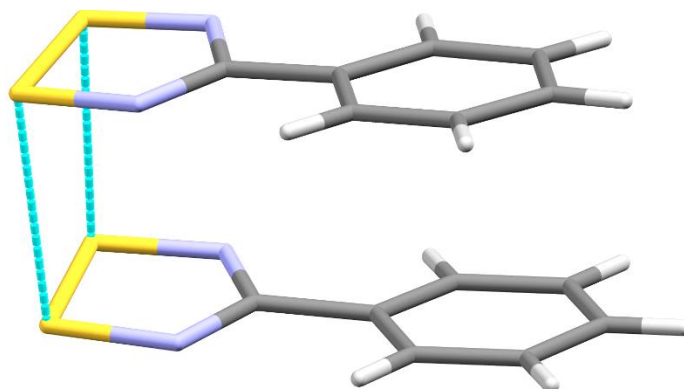


Figure 4.3: The π^* - π^* stacking contacts that result in pancake bonding in the 1.

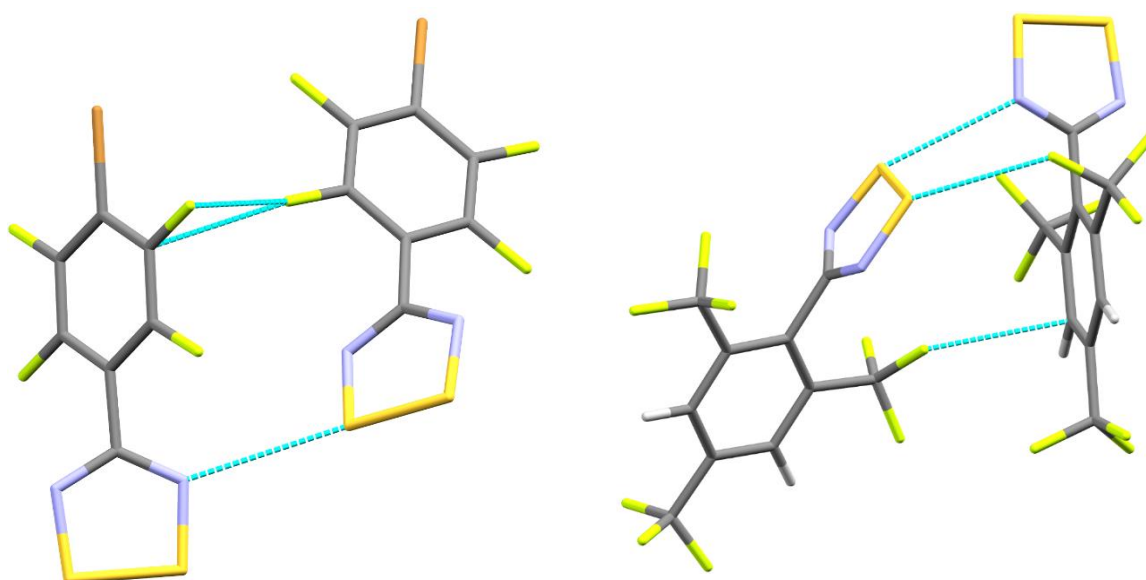


Figure 4.4: The modes of association observed for 3 (left) and 6 (right).

4.2. Geometry optimisation of monomeric and dimeric radicals

Beneberu and co-workers⁸ performed several calculations to determine which DFT methods can accurately describe the intradimer interactions in DTDA. Their results showed that the M06 functional with the 6-31G(d) basis set is preferred level of theory to accurately describe the structural properties of DTDA dimers. These calculations, however, focussed on the simple HCNSSN' radical. The calculations performed in this work focus on DTDA that exhibit both monomeric and dimeric modes of association. As a major part of this study focusses on radicals that exhibit a monomeric configuration, a series of calculations had to be performed to identify an efficient level of theory that provides accurate results for both monomers and dimers, and

does not require excessive computational time. In addition, our study required calculations performed in the triplet state, while the calculations performed by Beneberu and coworkers focussed on singlet state systems as they found that calculating radicals in a triplet state can yield large spin contamination values⁸.

The ability of different methods to describe the structural properties of radicals were evaluated by performing geometry optimisation and intermolecular interaction calculations on the monomeric (**2 - 6**) and dimeric (**1 , 8 – 12**) radicals in Table 4.1 by utilising different functionals. The UPBEPBE, UM06, UB97 and UB3LYP functionals were utilised in combination with the 6-311++G(d,p) basis set, where this particular polarised triplet zeta basis set was used as it has been shown to provide accurate interaction energy results when compared to calculations performed at high level WFT⁸. Additional frequency calculations were performed to confirm that the minimum energy conformation has been obtained for each calculation. The third generation dispersion correction (D3) was also applied to all functionals to better describe the dispersion in these systems, since this was identified by Beneberu and coworkers as being critical for accurate description of the dimerisation behaviour⁸. The optimised geometries of dimeric radicals (**1, 8 -12**) utilising different functionals were all found to yield final structures that exhibit dimerised pairs. For triplet state calculations performed on monomeric radicals (**2-6**), the functionals were compared with respect to their interactions energies and spin contamination values. These values are summarised in Table 4.2 for radical **2**. $\langle S^2 \rangle$ should be $\frac{1}{2}(\frac{1}{2}+1) = 0.75$ for an unpaired electron, hence these values suggest that spin contamination is only a problem for the UM06-D3 method. This is different to the work of Beneberu and coworkers who found that only the M06 method yielded acceptable results⁸. The interaction energy calculations performed at each level of theory were found yield favourable interactions. The small difference between the energies obtained at the different levels of theory would suggest that all of these functionals are capable of describing the binding in DTDA's.

Table 4.2: E_{int}^{CP} values obtained from calculations performed on radical **2** with the UPBEPBE-D3, UM06-D3, UB97-D3 and UB3LYP-D3 methods in combination with the 6-311++G(d,p) basis set. The spin contamination ($\langle S^2 \rangle$) of **2** after annihilations is reported for each method.

Radical 2	UPBEPBE-D3	UM06-D3	UB97-D3	UB3LYP-D3
E_{int}^{CP} (kcal/mol)	-4.88	-5.56	-4.45	-5.14
$\langle S^2 \rangle$	0.7500	0.7617	0.7500	0.7500

The results obtained by Beneberu and co-workers⁸ suggest that the UB3LYP method is not capable of describing the binding of dimers. It was, however, found here that the use of the polarised triplet zeta basis set with diffuse functions, 6-311++G(d,p) in combination with the D3 can sufficiently describe the binding of DTDA's either monomeric and dimeric modes of association. Additionally, the UB3LYP method was found to yield final structures with no imaginary frequencies for calculations performed on monomeric and dimeric radicals, while the other methods often yield imaginary frequencies and require additional calculations before the final minimum energy conformation can be obtained. The UB3LYP method in combination with the 6-311++G(d,p) basis set and the D3 correction was therefore selected as the level of theory used for further calculations as it is capable of describing the binding in both monomeric and dimeric radicals.

Geometry optimisations were performed for dimeric and monomeric radicals utilising the restricted open-shell (ROB3LYP), unrestricted (UB3LYP) and B3LYP methods in combination with the 6-311++G(d,p) basis set with the D3 correction. The ROB3LYP-D3 method uses doubly-occupied orbitals as far as possible and then treats the singly-occupied orbitals separately¹⁰. The UB3LYP-D3 method creates two complete sets of orbitals, one for the alpha (α) electrons and one for the beta (β) electrons¹¹. B3LYP-D3 has been included for comparison, as it has not been fitted to deal with unpaired electrons. Additional calculations were performed with the UB3LYP and the B3LYP that have not been fitted with the D3 corrections to investigate what effect this would have on the resulting energies. Vibrational analysis was performed on all stationary points in order to confirm that the energy minimum confirmation had been obtained.

The monomeric and dimeric radicals were optimised in both the singlet and triplet multiplicity states in order to determine what effect paired and unpaired electrons will have on the final geometries.

Various studies have shown that long-range periodicity in crystals is a product of directional specific short-range contacts^{12,13}. To simplify, the crystalline environment will affect the strength of the intermolecular interactions between two radicals. The effect of these short-range contacts was taken into account as far as possible by performing calculations on two radicals as they are arranged in the crystal structure, with a geometry optimisation performed on the hydrogen atoms. These calculations were included to investigate how the crystalline environment will influence the strength of intermolecular interactions. It should be mentioned that these calculations will not provide an accurate representation of a crystalline environment and can therefore only be used for comparison purposes. The results from these calculations will henceforth be denoted by the "crystal" keyword. The strength of the intermolecular

interactions will be calculated for final structures obtained by geometry optimisation calculations.

4.3. Calculating the strength of intermolecular interactions

After geometry optimisation calculations, single-point calculations were performed at the UB3LYP-D3/6-311++G(d,p) level of theory to determine the counterpoise-corrected interaction energies^{14,15} (E_{int}^{CP}) in the singlet and triplet states are given in Tables 4.3 - 4.6. The UB3LYP-D3 method was used for all single-point calculations, as it has been shown to provide accurate results for systems containing noncovalent interactions¹⁶.

The geometry optimisation and single-point calculations were performed in both the singlet and triplet states to observe how paired or unpaired electrons will influence the final structures and energies. It was expected that dimeric radicals would show more favourable energies in the singlet state as it describes paired electrons, while monomeric radicals would give more favourable energies in the triplet state as it described unpaired electrons. Furthermore, the different states will result in very different E_{int}^{CP} values, as calculations performed in different spin states will favour different intermolecular interactions.

Tables 4.3 and 4.4 contain data relating to dimeric radicals, while Tables 4.5 and 4.6 contain data relating to monomeric radicals. The title of each table contains information regarding the multiplicity and level of theory at which the single-point calculations were performed. The first column contains the multiplicity and method used for each geometry optimisation calculation. The remaining columns contain the interaction energies values (E_{int}^{CP}) obtained for each radical. Attractive energies ($E_{int}^{CP} < 0$) indicate that the intermolecular interactions are stabilising and the final structure exhibits a favourable mode of association, while repulsive energies ($E_{int}^{CP} > 0$ kcal/mol) indicate that the intermolecular interaction are destabilising and the final structure exhibits an unfavourable mode of association. Attractive energies obtained by performing calculations in the singlet state for radicals that have been optimised in the singlet state indicate that the radical pair favours interactions between the SOMOs, i.e. that these radicals are stable as dimers. Similarly, if attractive energies are obtained by performing calculations in the triplet state for radicals that have been optimised in the triplet state, this indicates that the final structure no longer favours interaction between the SOMOs as it prefers unpaired electrons. This is clearly illustrated in Figure 4.5, which shows dimeric radicals that have optimised in the singlet state (Figure 4.5, left) and triplet state (Figure 4.5, right). Optimisation of a dimeric radical in the triplet state results in the radical molecules drifting apart, with a final geometry

that does not exhibit S···N or S···S contacts within the sum of the van der Waals radii. The arrangement of radicals on the right has a less favourable interaction energy than the arrangement on the left, confirming that this radical pair is more stable as a dimer.

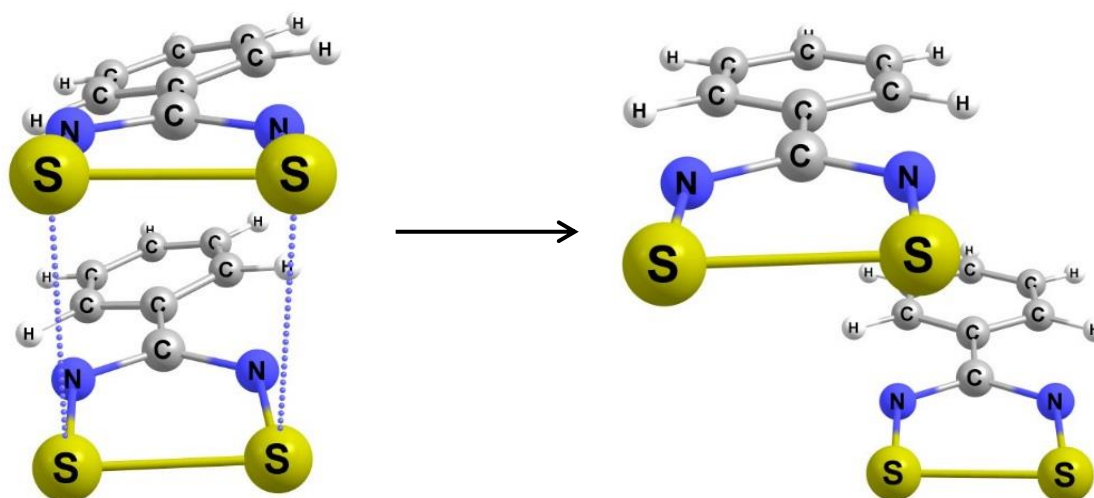


Figure 4.5: Optimised geometries of the 1 in the singlet (left) and the triplet (right) state.

Table 4.3: E_{int}^{CP} values (kcal/mol) calculated at the UB3LYP-D3/6-311++G(dp) level of theory in the triplet state for radicals known to crystallise as dimers. The first column gives the method used for geometry optimisation; 'crystal' indicates that the crystal structure geometry was used with optimisation of only the hydrogen atoms.

Compound number	1	8	9	10	11	12
Crystal	9.76	9.96	9.20	8.24	7.27	6.18
Singlet B3LYP	6.68	6.85	5.92	5.94	4.50	6.02
Singlet B3LYP-D3	6.59	5.84	5.43	4.51	4.42	5.43
Triplet B3LYP	-3.53	-4.17	-5.70	-4.51	-6.80	-4.47
Triplet UB3LYP	-3.53	-4.17	-5.70	-4.51	-6.80	-4.47
Triplet UB3LYP-D3	-7.76	-9.21	-8.11	-10.68	-9.37	-9.56
Triplet ROB3LYP-D3	-8.47	-9.15	-5.64	-5.85	-4.39	-5.52

Table 4.3 shows repulsive energies ($E_{int}^{CP} > 0$ kcal/mol) for radicals in the crystal geometry as well as radicals that were optimised in the singlet state utilising the B3LYP method. Including the D3 correction results in slightly less repulsive energies, which corresponds to studies that have shown that the S···S contacts present in these pairs contain a large dispersion component^{17,18}.

Attractive energies ($E_{int}^{CP} < 0$ kcal/mol) were obtained for all radicals that were optimised in the triplet state with the B3LYP, UB3LYP, UB3LYP-D3 and ROB3LYP-D3 methods. The final geometries of the structures in Table 4.3 show that that performing optimisations on dimeric radicals in the triplet state will yield final structures that no longer favour interactions between the SOMOs and favour unpaired electrons.

No difference is observed between energies for radicals optimised with the B3LYP and UB3LYP method in the triplet state. If a calculation specifies that the structure contains paired electrons (singlet state), Gaussian will automatically perform restricted B3LYP calculations, irrespective of the UB3LYP keyword being specified. Alternatively, if the calculation specifies that the structure contain unpaired electrons (triplet state), Gaussian will automatically perform an unrestricted B3LYP calculation. The restricted open-shell method has an advantage over the unrestricted method by reducing any spin contamination and thus describing the spin of the system accurately¹⁹. It should be mentioned that the use of the ROB3LYP-D3 method resulted in various convergence and geometry optimisation difficulties for the DTDA radical systems that were studied. It is for this reason that the UB3LYP-D3 method was preferred when calculating the properties of radicals in this study.

Table 4.4: E_{int}^{CP} values (kcal/mol) calculated at the UB3LYP-D3/6-311++G(dp) level of theory in the singlet state for radicals known to crystallise as dimers. The first column gives the method used for geometry optimisation; 'crystal' indicates that the crystal structure geometry was used with optimisation of only the hydrogen atoms.

Compound number	1	8	9	10	11	12
Crystal	-5.62	-6.04	-5.42	-5.37	-7.99	-6.73
Singlet B3LYP	-2.45	-2.55	-3.80	-1.58	-4.71	-3.89
Singlet B3LYP-D3	-5.48	-6.07	-5.78	-4.67	-7.52	-6.56
Triplet B3LYP	14.21	14.49	12.64	14.59	12.78	13.49
Triplet UB3LYP	14.21	14.49	12.64	14.59	12.78	13.49
Triplet UB3LYP-D3	10.31	8.33	10.06	9.32	7.57	5.90
Triplet ROB3LYP-D3	10.58	7.28	11.82	5.49	7.54	6.58

Table 4.4 shows the opposite trend to what was observed in Table 4.3, with attractive energies obtained for radicals in the geometry found in the crystal structure and the radicals that were optimised with the B3LYP and B3LYP-D3 methods in the singlet state. This is due to interactions between the SOMOs being favourable for dimeric radicals that have been optimised in the singlet state. Applying the D3 correction shows a significant increase in the strength of intermolecular interactions, which confirms that applying this correction provides a more accurate description of the contacts between dimerised pairs that contain a large dispersion component.

The radicals in crystal geometries also yield strong attractive energies, owing to the crystalline environment orienting radicals in such a way to allow for stronger interaction between the SOMOs. This effect is illustrated in Figure 4.6, which shows short S··S contacts present in the crystal geometry when being compared to the optimised geometry of radical **1** optimised with the B3LYP-D3 method.

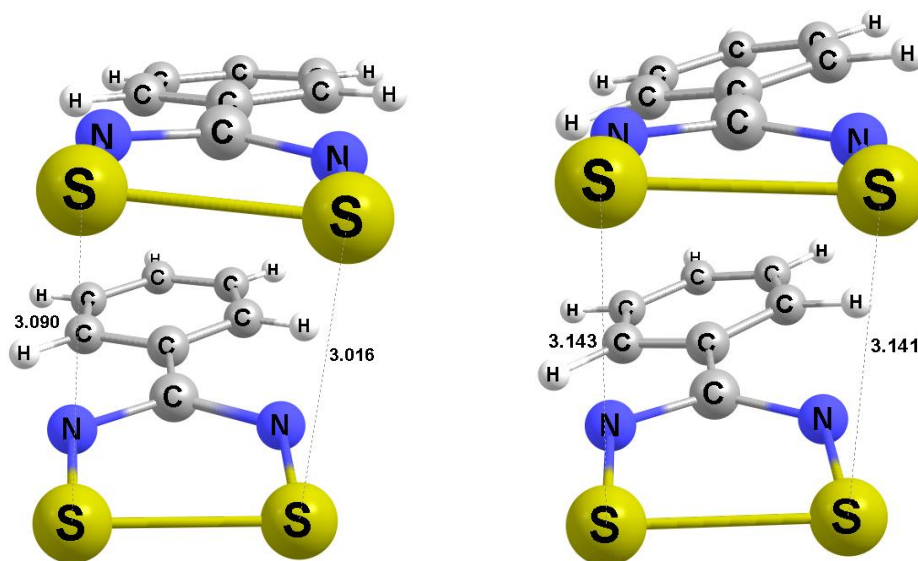


Figure 4.6: S...S contacts (Å) of radical 1 in the crystal geometry (left) and when optimised with the B3LYP-D3 method in the singlet state (right).

Table 4.5: E_{int}^{CP} values (kcal/mol) calculated at the UB3LYP-D3/6-311++G(dp) level of theory in the triplet state for radicals known to crystallise as monomers. The first column gives the method used for geometry optimisation; 'crystal' indicates that the crystal structure geometry was used with optimisation of only the hydrogen atoms.

Compound number	2	3	4	5	6
Crystal	-4.50	-4.28	-4.04	-4.91	-8.16
Singlet B3LYP	-5.16	6.43	-4.08	-4.84	-0.88
Singlet B3LYP-D3	-5.08	4.20	-4.03	-4.83	-1.64
Triplet B3LYP	-5.16	-2.72	-4.05	-4.86	-7.72
Triplet UB3LYP	-5.16	-2.72	-4.05	-4.86	-7.72
Triplet UB3LYP-D3	-5.14	-8.81	-4.17	-4.85	-9.05
Triplet ROB3LYP-D3	-2.19	-2.72	-4.07	-4.86	-2.13

Table 4.5 shows attractive energies for all monomeric radicals, with radical **3** being the one exception as it exhibits a repulsive energy for the geometry that has been optimised in the singlet state. The repulsive energies indicate that monomeric radicals do not favour paired electrons even if optimised in the singlet state. The crystal geometries and optimised geometries of radicals **2**, **3** and **6** are illustrated in Figure 4.7. The optimised structure of radical **2** reveals that irrespective of whether the calculation is performed in the singlet or triplet state, the radical will remain in the linear mode of association.

A similar trend was observed for the remaining monomeric radicals that prefer the linear mode of association, namely, **4** and **5**. The linear mode of association is observed even when calculations are performed in the singlet state would suggest that this mode of association is significantly more stable than the dimeric mode of association. The radical **3** exhibits a different

trend, as it favours a monomeric mode of association in the crystal structure and a *trans-cofacial* dimeric mode of association if optimised in the singlet state, resulting in the repulsive energy shown in Table 4.6. The crystals structures and the optimised geometries of **2** and **6** do not exhibit a change in their mode of association (Figure 4.7).

Table 4.6: E_{int}^{CP} values (kcal/mol) calculated at the UB3LYP-D3/6-311++G(dp) level of theory in the singlet state for radicals known to crystallise as monomers. The first column gives the method used for geometry optimisation; 'crystal' indicates that the crystal structure geometry was used with optimisation of only the hydrogen atoms.

Compound number	2	3	4	5	6
Crystal	19.11	19.52	18.99	19.23	6.56
Singlet B3LYP	18.74	-4.88	19.16	19.24	3.64
Singlet B3LYP-D3	17.71	-4.90	18.68	19.06	2.85
Triplet B3LYP	17.97	18.51	19.10	19.23	9.90
Triplet UB3LYP	17.97	18.51	19.10	19.23	9.90
Triplet UB3LYP-D3	17.98	6.96	19.00	19.24	7.83
Triplet ROB3LYP D3	20.72	6.37	19.60	19.23	2.64

The values given in Table 4.6 show repulsive energies for all monomeric radicals, with radical **3** once again being an exception as it exhibits an attractive energy. The repulsive energies obtained for all of the other monomeric radicals show that pairing of the electrons is unfavourable for all optimised geometries, while the dimeric mode of association observed for radical **3** in Figure 4.7 would suggest that it favours interaction between the SOMOs, resulting in the attractive energy given in Table 4.6. This would suggest that **3** could exist as another polymorph or a co-crystal that exhibits a dimerised radical pair. This explains why this attractive interaction was observed in the crystal structure of the co-crystal (**3-cox**) described in Chapter 3, which was found to exhibit a dimerised pair of **3**.

The crystal packing of **3-cox** shows an approximately perpendicular arrangement of the dimer pair and the 4-bromo-2,3,5,6-tetrafluorobenzonitrile. The twist angles in the radicals in **3-cox** are 26.56°, whereas the twist angles in **3** are 54.00° (Figure 4.9). The dimeric mode of association observed in **3-cox** would suggest that the intermolecular interactions between the radical pair of **3** and 4-bromo-2,3,5,6-tetrafluorobenzonitrile play an important role in why dimerisation is observed in the crystal structure of **3-cox** (Figure 4.8).

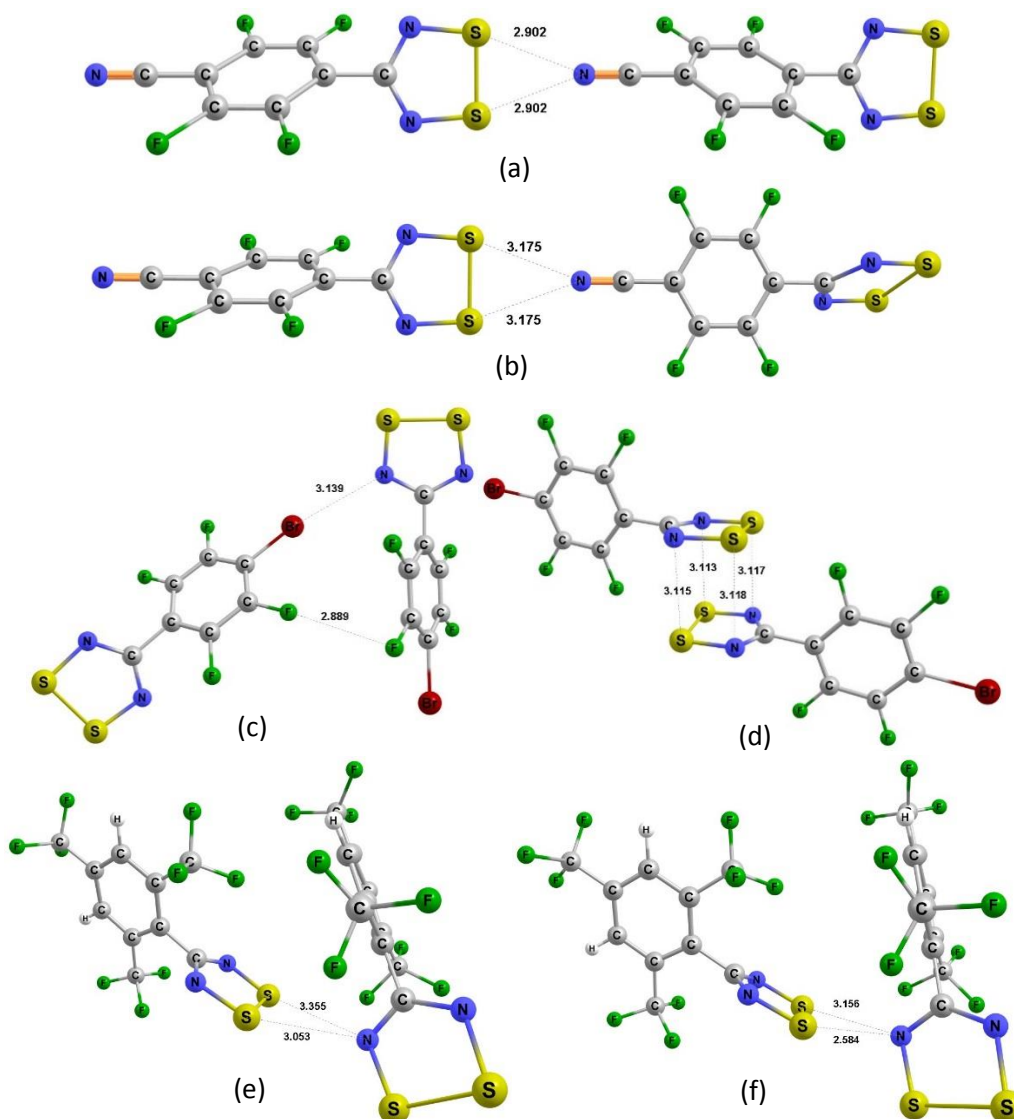


Figure 4.7: Crystal geometries of 2 (a), 3 (c) and 6 (e). Optimised geometries of the 2 (b), 3 (d) and 6 (f) performed in the singlet state at the B3LYP-D3/6-311++G(dp) level of theory.

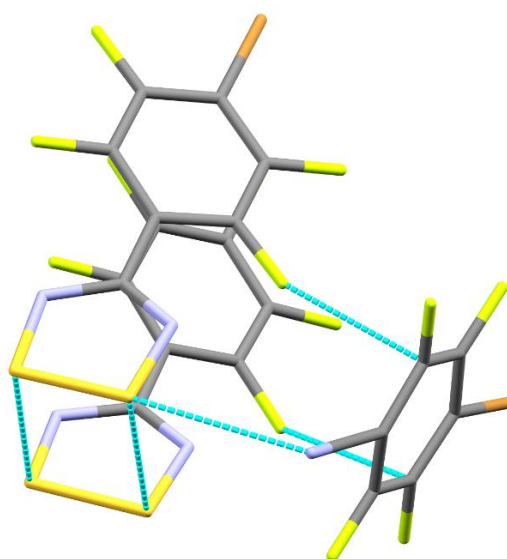


Figure 4.8: The contacts in the crystal structure of 3-cox, which consists of a dimerised pair of 3 and 4-bromo-2,3,5,6-tetrafluorobenzonitrile.

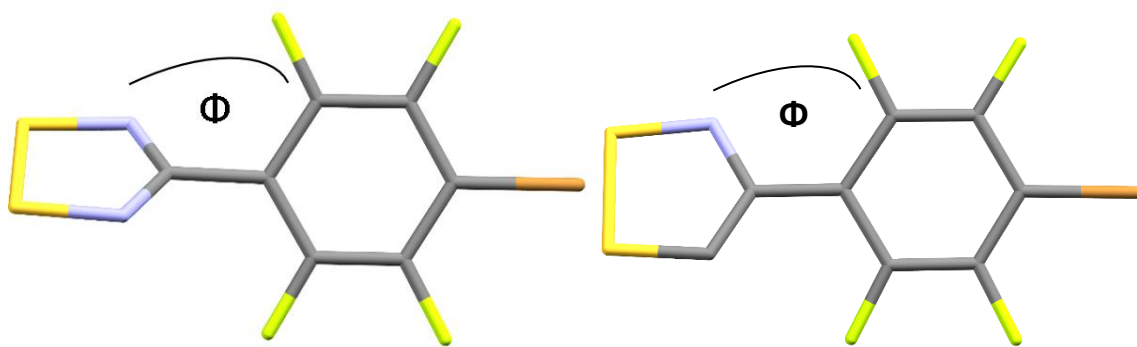


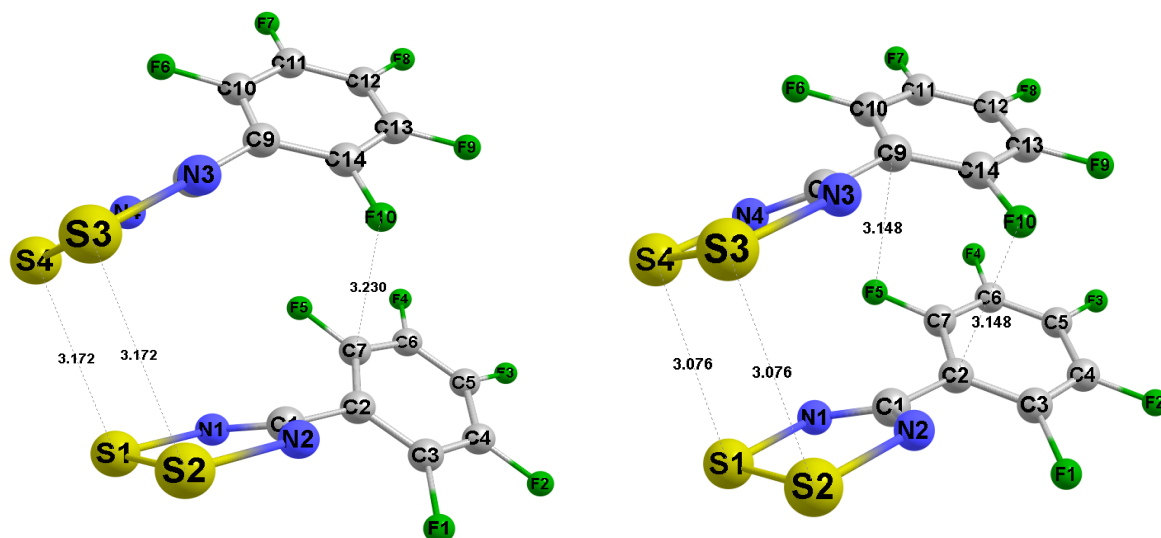
Figure 4.9: Twist angle of radical molecule in **3** (left, $\Phi = 54.00$) and **3-cox** [right, $\Phi = 26.56(2)$].

The structures optimised in the singlet state also show a weakly repulsive energy for **6** compared to those of **2**, **4** and **5**. The crystal structure and optimised geometry of **6** (Figure 4.7) exhibits some similarities to the orthogonal mode of association shown in Figure 4.2. The interaction energy of -0.88 kcal/mol in Table 4.5 is weak when compared to the radicals that exhibit a linear mode of association, while the interaction energy of 3.64 kcal/mol in Table 4.6 is also weakly repulsive when compared to the radicals that exhibit a linear mode of association. The weakly attractive and repulsive energies in Tables 4.5 and 4.6 would suggest that this radical could exist as another polymorph containing dimers. In fact, a study by Alberola and coworkers describes a polymorph of this radical, where the asymmetric unit contains one monomeric radical and four molecules that form dimeric radical pairs²⁰.

The predominant difference between the molecular structures of the radicals in Tables 4.3 – 4.6 is that the monomeric radicals contain fluorinated substituents at the *ortho* position. It was discussed in previous chapters that studies on monomeric radicals have shown that a combination of large twist angles resulting from *ortho*-fluoro groups and structure-directing contacts reduces the tendency of DTDA radicals to dimerise^{2,21-23}. The calculated twist angles were measured for the dimeric and monomeric radicals that have been optimised in the singlet and triplet states and are summarised in Table 4.7. The table shows large twist angles for the monomeric radicals, whereas there is no particular trend for the dimeric radicals. In particular, the fluorinated aryl ring in **11** results in a large twist angles similar to those observed for the monomeric radicals. In Figure 4.10, the crystal structure of **11** is compared to the structure optimised in the singlet state. The dimerisation of **11** shows that large twist angles will not necessarily inhibit dimerisation and an additional substituent at the *para* position is required that is capable of forming structure-directing contacts.

Table 4.7: Measured twist angles (°) of dimeric and monomeric radicals that have been optimised in the singlet and triplet states at the B3LYP-D3/6-311++G(dp) and UB3LYP-D3/6-311++G(dp) levels of theory.

Dimeric	Singlet	Triplet	Monomeric	Singlet	Triplet
1	-1.56	4.12	2	63.53	58.86
8	-0.25	12.84	3	88.29	-61.14
9	-18.45	-19.86	4	63.69	-58.94
10	52.91	45.31	5	-62.12	-62.33
11	6.23	22.34	6	71.94	-109.61
12	0.70	-10.23			

**Figure 4.10: The optimised geometry (left) and a dimer from the crystal structure (right) of radical 11.**

To summarise, the energies reported in Tables 4.3 – 4.6 show that radicals that dimerise in the solid state will exhibit attractive energies if they are allowed to optimise in the singlet state and interaction energies are calculated in the singlet state. Additionally, radicals that dimerise in the solid state will exhibit attractive energies if they are allowed to optimise in the triplet state and interaction energies are calculated in the triplet state, however the resulting geometries in these cases are not dimers. The monomeric radicals show a different trend as they only exhibit attractive energies if interaction energy calculations are performed in the triplet state, irrespective of the state used to perform geometry optimisation calculations. The monomeric radicals that exhibit a linear mode of association exhibit similar final structures for geometry optimisation calculations performed in the singlet and triplet states, which indicates that the linear mode of association is very stable. A series of geometry optimisations and single point calculations can therefore be performed on radicals to determine if a monomeric or dimeric mode of association will be preferred. The results from these calculations performed on radicals that have not yet been synthesised will be reported in Chapter 6.

Care should be taken for monomeric and dimeric radicals that exhibit weakly attractive or repulsive energies if optimised in the singlet and triplet states (such as found for **3**), as these properties are indicative of a radical that could exist as multiple polymorphs or exhibit different modes of association in co-crystals. Comparison of the monomeric and dimeric structures show that a large twist angle and structure-directing contacts will inhibit dimerisation. The next section aims to explain how a change in the twist angle and a torsion angle will influence the intermolecular interactions in monomeric and dimeric radicals.

4.4. The potential energy surface (PES)

The effect of the twist angle and torsion angle on the intermolecular interaction energies in monomeric and dimeric radicals could provide some information about why these radicals prefer different modes of association.

This section will focus on two torsion angles. The first torsion angle is between the four sulfur atoms that interact in a dimerised radical pair. The second torsion angle is the familiar twist angle in the radical monomer. A scan of the potential energy surface (PES) was carried out, where one torsion angle was varied stepwise and the energies calculated at each point. These energies were then used to construct a 2D plot. The 2D plot was used to identify which geometries correspond to the minima and maxima at different torsion angles.

Torsion angles were varied in increments of 10° in the range $0^\circ - 360^\circ$, where the interaction energies were calculated at each increment. A fixed scan was performed by keeping all other distances, angles and torsion angles constant while varying just one selected torsion angle. Interaction energies were calculated in both the singlet and the triplet state for the dimeric radical to determine how paired and unpaired electrons are affected by a change in torsion angle. The interaction energies were only calculated in the triplet state for the monomeric radical as its mode of association does not allow any interaction between the SOMOs.

The first system to be analysed was the dimeric radical pair of **1** with the torsion angle between atoms S3-S4-S1-S2 being varied (Figure 4.11). Radical **1** was selected because it exhibits a *cisoid* type mode of association in its crystal structure exhibits strong interactions between the SOMOs. The singlet state and triplet state PES scans were performed, with the 2D plots shown in Figures 4.12 and 4.13, respectively.

The results of the singlet-state calculation for **1** shown in Figure 4.12 reveals that the strongest interaction energy occurs at a torsion angle of 0° (Figure 4.12-a), corresponding to a *cisoid* mode of association. This small torsion angle allows for strong interaction between the SOMOs, which is confirmed by short contacts of 3.174 \AA (S1...S4) and 3.158 \AA (S2...S3)

between the heterocyclic rings. Further, maxima can be identified at torsion angles of 60° and 300° , which are symmetry related, and 180° corresponding to *twisted*-like (Figure 4.12-b) and *trans-antarafacial* (Figure 4.12-c) modes of association, respectively. It should be mentioned that these modes of association correspond to maxima as this is a fixed scan.

The strong interaction in the *cisoid* mode of association exhibits an attractive energy of -1.6 kcal/mol, whereas repulsive energies of 8.55 kcal/mol and 12.36 kcal/mol are observed at the maxima. Investigation of the CSD reveals that the majority of the DTDA radicals adopt the more stable and lower energy *cisoid* mode of association. This is expected from the Boltzmann distribution, where the distribution of the states means that those with a lower energy will be more occupied than states with higher energies²⁴.

The strongest interaction between pairs of **1** in the triplet state are observed at torsion angles of 60° and 300° (Figure 4.13), which correspond to the maxima in Figure 4.12. Calculations in the triplet state will favour geometries that do not allow for attractive interactions between the SOMOs (Figure 4.13), which is why geometries with attractive energies can be identified at 60° and 300° , whereas the attractive energies for singlet state calculations favour geometries that allow for interaction between the SOMOs (Figure 4.12).

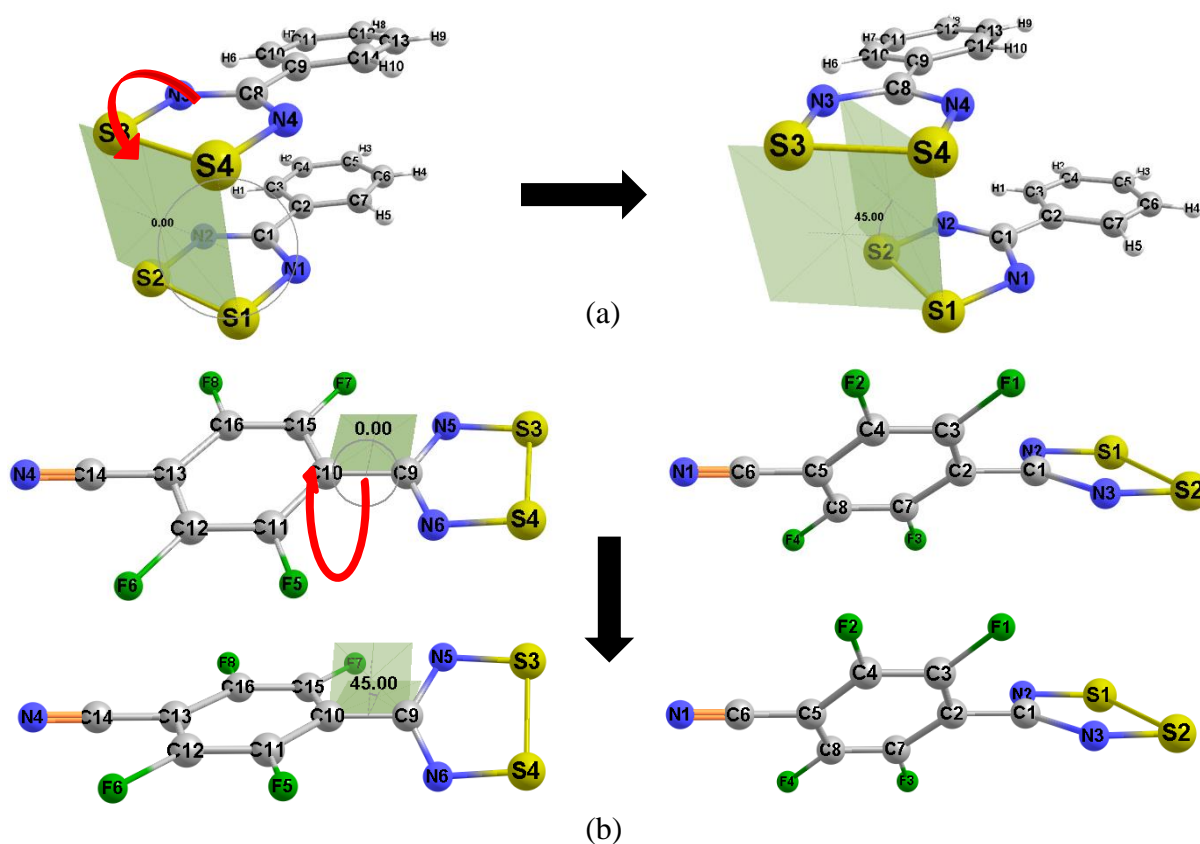


Figure 4.11: Variation in torsion angle (a) between S3-S4-S1-S2 in **1** and between C15-C10-C9-N5 (b) in **2**.

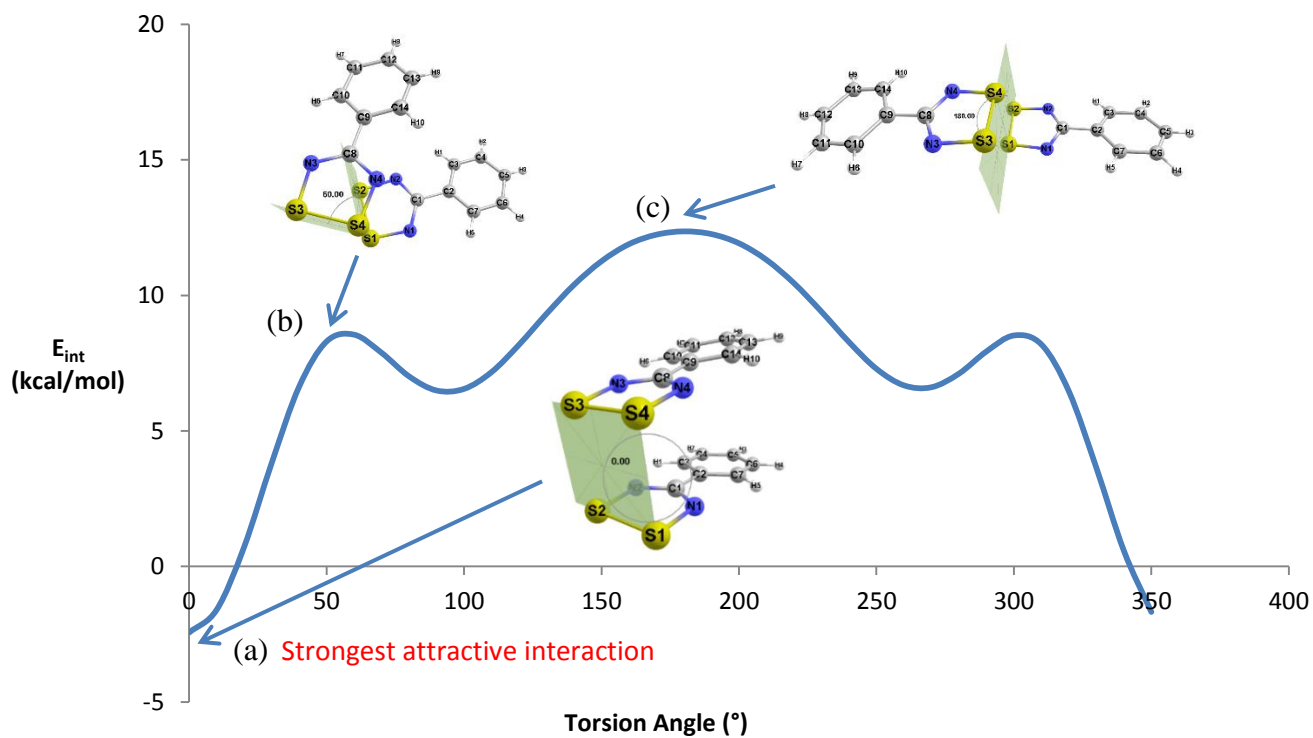


Figure 4.12: PES scan of torsion angle ($^{\circ}$) S3-S4-S1-S2 for radical pair of 1 calculated at the UB3LYP-D3/6-311++G(dp) level of theory in the singlet state. Inserts show geometries of selected minima and maxima at positions a, b and c.

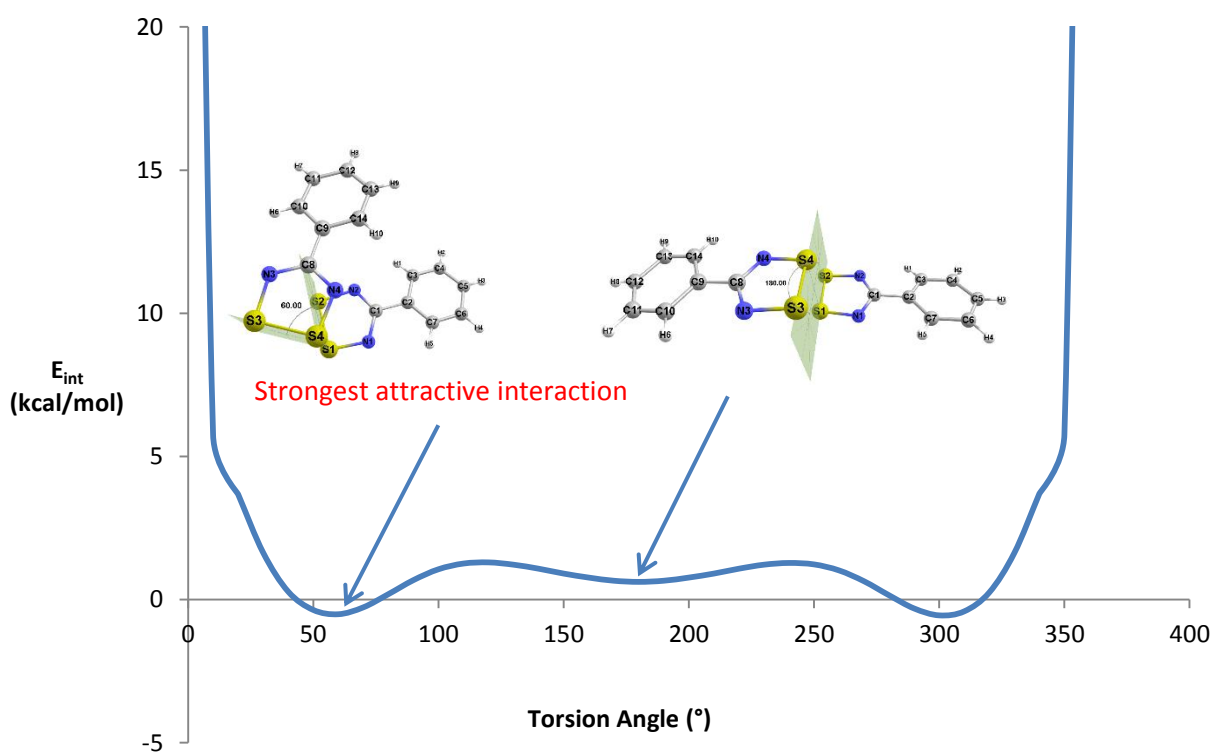


Figure 4.13: PES scan of torsion angle ($^{\circ}$) S3-S4-S1-S2 for radical pair of 1 calculated at the UB3LYP-D3/6-311++G(dp) level of theory in the triplet state. Inserts show geometries of selected minima and maxima.

The second radical system to be analysed, was two molecules of **2** in the linear mode of association, where the twist angle between atoms C15-C10-C9-N5 was varied (Figure 4.14). Radical **2** was selected for the monomeric radical scan as its crystal structure exhibits a linear mode of association with CN \cdots S contacts that can easily be studied by a change in the twist angle.

The 2D plot of the PES scan for **2** shows that the geometries corresponding the two strongest attractive interactions occurs at torsion angle ranges of 70° – 110° and 250° – 290° (Figure 4.14). These torsion angles minimise the steric repulsion that results from interactions between *ortho* fluorine and heterocyclic ring nitrogen atoms and therefore yield the strongest attractive interaction of -5.15 kcal/mol. In contrast, in the 180° geometry, the *ortho* fluorine and heterocyclic ring nitrogen atoms undergo strong steric repulsion, which weakens the interaction energy and results in a weaker attractive interaction of -4.95 kcal/mol. The strong attractive interactions at large twist angles agree with studies that have shown that the presence of fluorine atoms at the *ortho* position results in large twist angles, reducing the tendency of DTDA radicals to dimerise^{2,21-23}.

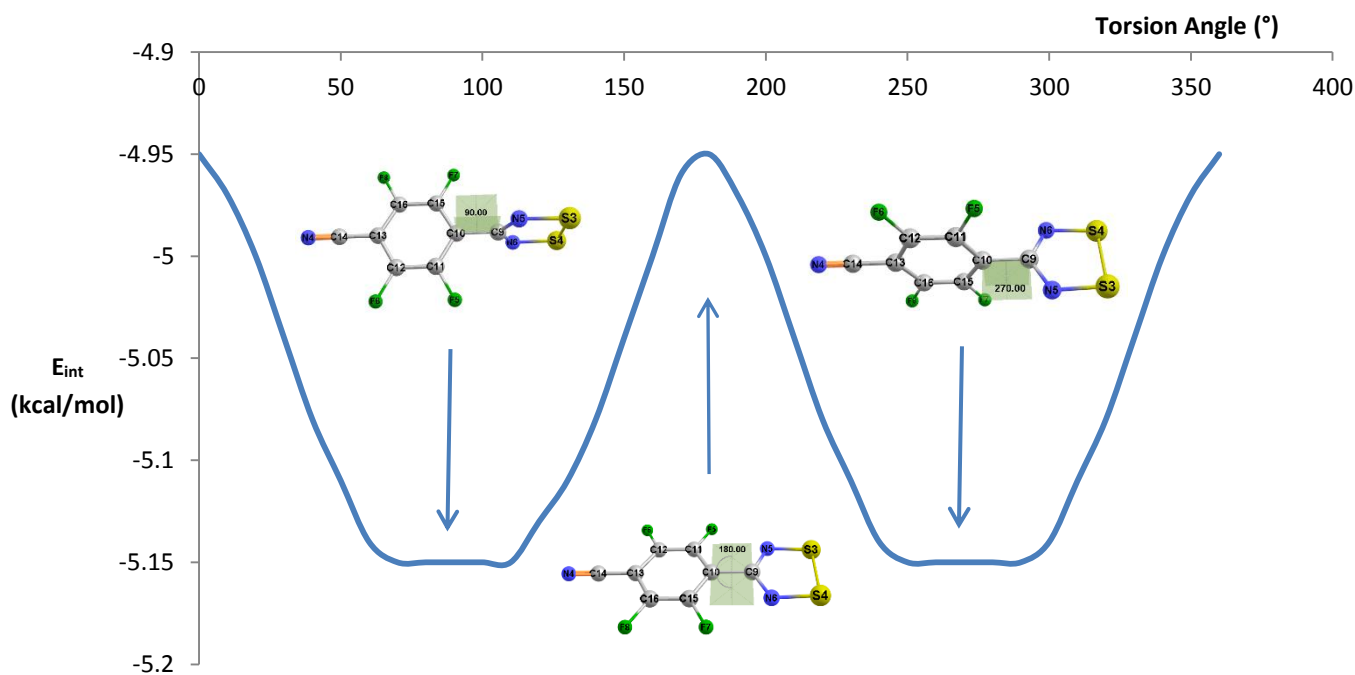


Figure 4.14: PES scan of torsion angle (°) C15-C10-C9-C5 for radical 2 calculated at the UB3LYP-D3/6-311++G(dp) level of theory in the triplet state. Inserts show geometries of selected minima and maxima.

To summarise, in this section it has been shown that the *cisoid* dimeric mode of association exhibits the strongest attractive energies when compared to the *twisted*-like and *trans-antarafacial* dimeric modes of association. Furthermore, the strongest attractive energies are

observed at large twist angles for monomeric radicals as this minimised the steric repulsion between the fluorine and nitrogen atoms. The next section will focus on the nature of intermolecular contacts in DTDA radicals and why they result in monomeric and dimeric modes of association.

4.5. Energy decomposition analysis of triplet and singlet radicals

An energy decomposition analysis (EDA) can be performed on gas-phase interactions²⁵. An EDA analysis can, however, not be performed on unrestricted fragments, but the fragments can be treated like unrestricted fragments by specifying the occupations of each radical molecule, where the occupations are the number of filled or half-filled orbitals. These fragments are then brought together in order to yield the complete molecular arrangement. The final structure of dimeric and monomeric radicals were obtained from geometry optimisation performed in section 4.2, where dimeric radicals have been optimised in the singlet state and the monomeric radicals have been optimised in the triplet state at the B3LYP-D3/UB3LYP-D3/6-311++G(d,p) level of theory.

All EDA calculations in this study were performed using the unrestricted B3LYP method in combination with the TZP basis set on both monomeric and dimeric radicals in the singlet and triplet states. The basis set used for calculating interaction energies could unfortunately not be used for EDA calculations, but a similar-sized basis was used, as the focus of this study was simply to investigate the difference in binding energies between monomeric and dimeric radicals. The calculations were further fitted with the Grimme D3 correction as well as BJ damping, which provide more accurate results for noncovalent interactions.

An EDA analysis is capable of calculating the different contributions to the total bonding energy:

$$\Delta E_{\text{Tot}} = \Delta E_{\text{disp}} + \Delta E_{\text{el}} + \Delta E_{\text{orb}} + \Delta E_{\text{Pauli}},$$

where the components consist of dispersion (ΔE_{disp}), electrostatic (ΔE_{el}), orbital (ΔE_{orb}) and Pauli (ΔE_{Pauli}). It should be mentioned that one drawback of the EDA analysis is its inability to separate the charge transfer and polarisation components²⁶. The nature of these contributions to the bonding energy in monomeric and dimeric radicals could provide some information about why radicals prefer different modes of association in the solid state. We expect the ΔE_{orb} contribution to be large for dimeric radicals as the strong interaction between the SOMOs

results in stable radical pairs, while the other contributions will play a more important role in the interactions found in monomeric radicals.

The contributions to the bonding energy of dimeric and monomeric radicals are given in Table 4.8, which show a noticeable difference to the intermolecular interaction energies in Tables 4.3 - 4.6. The bonding energy can be defined as the difference between the energy of the complex and the energies of the two isolated fragments in their minimum energy conformations. The interaction energy is the difference between the energies of the complex minus the energies of the isolated fragments in the geometry they adopt in the complex. The difference between the bonding and interaction energy can be described as the distortion energy required to bring the monomers into the geometry required for the complex configuration. The total binding energy can be described as follows:

$$\Delta E_{Tot} = \Delta E_{prep} + \Delta E_{int},$$

where the preparation energy ΔE_{prep} is the energy required to distort the fragments to the geometry which they have in the complex. ΔE_{int} is the instantaneous interaction energy between two fragments that was shown in Tables 4.3 – 4.6²⁷, while the ΔE_{Tot} or bonding energies are shown in Table 4.8.

Table 4.8: EDA results for dimeric (a) and monomeric (b) radicals. Total energy = dispersion + electrostatic + orbital + Pauli. All values reported are in kcal/mol.

		ΔE_{Tot}	ΔE_{disp}	ΔE_{el}	ΔE_{orb}	ΔE_{Pauli}
Compound number		Total	Dispersion	Electrostatic	Orbital	Pauli
(a)	1	-21.29	-7.17	-11.78	-26.98	24.64
	8	-10.55	-12.01	-12.10	-14.26	27.81
	9	-12.58	-14.04	-12.28	-15.77	29.51
	10	-8.61	-10.65	-11.74	-13.29	27.07
	11	-12.11	-13.33	-13.29	-14.64	29.15
	12	-11.43	-12.74	-11.96	-14.88	28.15
(b)	2	-8.25	-2.08	-5.97	-4.92	4.73
	3	-13.54	-13.55	-8.36	-6.34	14.70
	4	-7.17	-2.38	-4.44	-4.34	3.98
	5	-7.82	-2.02	-5.32	-4.67	4.19
	6	-13.19	-11.70	-9.48	-6.66	14.65

Table 4.8 shows that ΔE_{orb} is the largest contribution to the binding energy for all dimeric radicals, while large ΔE_{el} and ΔE_{disp} contributions are also observed. It has been shown in

studies reported in the literature that these contributions play an important role in the dimerisation of radicals²⁸. A study performed by Beneberu and coworkers found that the binding energy in a dimerised pairs of DTDAs is not dominated by dispersion or any other component, but a combination of components is required to result in a bonding interaction between the SOMOs of neighbouring radical molecules⁸. This corresponds well to the results in Table 4.8 for dimeric radicals, which contains similar ΔE_{disp} , ΔE_{el} and ΔE_{orb} components to the binding energies of dimeric radicals.

The ΔE_{orb} contribution is two to three times larger in dimeric radicals when compared to monomeric radicals. This arises from the overlap of π^* orbitals and other contacts between the dimerised radicals, which result in increased charge transfer, polarisation and electron pair bonding effects to result in a large ΔE_{orb} contribution. Figure 4.15 (top) illustrates the significant π^* orbital overlap present in the highest occupied molecular orbital (HOMO) of the dimeric radical pair of **1**, which corresponds to overlap of the SOMOs resulting in pancake bonds. In contrast, the SOMOs of the monomeric radicals in Figure 4.15 (bottom) exhibit no overlap, resulting in a smaller ΔE_{orb} contribution to the overall bonding energy.

The ΔE_{el} and ΔE_{disp} values for dimeric radicals are significantly larger than those for the monomeric radicals that exhibit a linear mode of association, namely **2**, **4** and **5**. The larger ΔE_{el} contribution results from the various electrostatic interactions between dimerised radicals, whereas fewer electrostatic interactions occur in the monomeric modes of association (Figure 4.15). S...S contacts are known to exhibit larger ΔE_{disp} contributions due to a major dispersion component²⁸.

The ΔE_{el} and ΔE_{disp} values of **3** and **6** are large when compared to the other monomeric radicals. Their modes of association appear to be intermediate to the pancake bonding observed for dimeric radicals and the linear mode of association observed in some monomeric radicals, which results in some interaction between the SOMOs. Furthermore, the mode of association also exhibits S...N, F...F and Br...N contacts, which contribute to the larger ΔE_{el} and ΔE_{disp} values.

The ΔE_{Pauli} contribution to the total binding energy was found to be close to 30 kcal/mol for all dimeric radicals, but less than 15 kcal/mol for the monomeric radicals. Inspection of the HOMOs in Figure 4.15 shows that the SOMOs of the dimeric radicals come into significantly closer contact than what is observed for the monomeric radicals. The close contact of occupied orbitals results in Pauli repulsion, which in turn results in steric repulsion and the large repulsive ΔE_{Pauli} contribution observed for radicals that exhibit a dimeric mode of association. The linear mode of arrangement found for some monomeric radicals minimises contact between the SOMOs, resulting in significantly smaller ΔE_{Pauli} contributions.

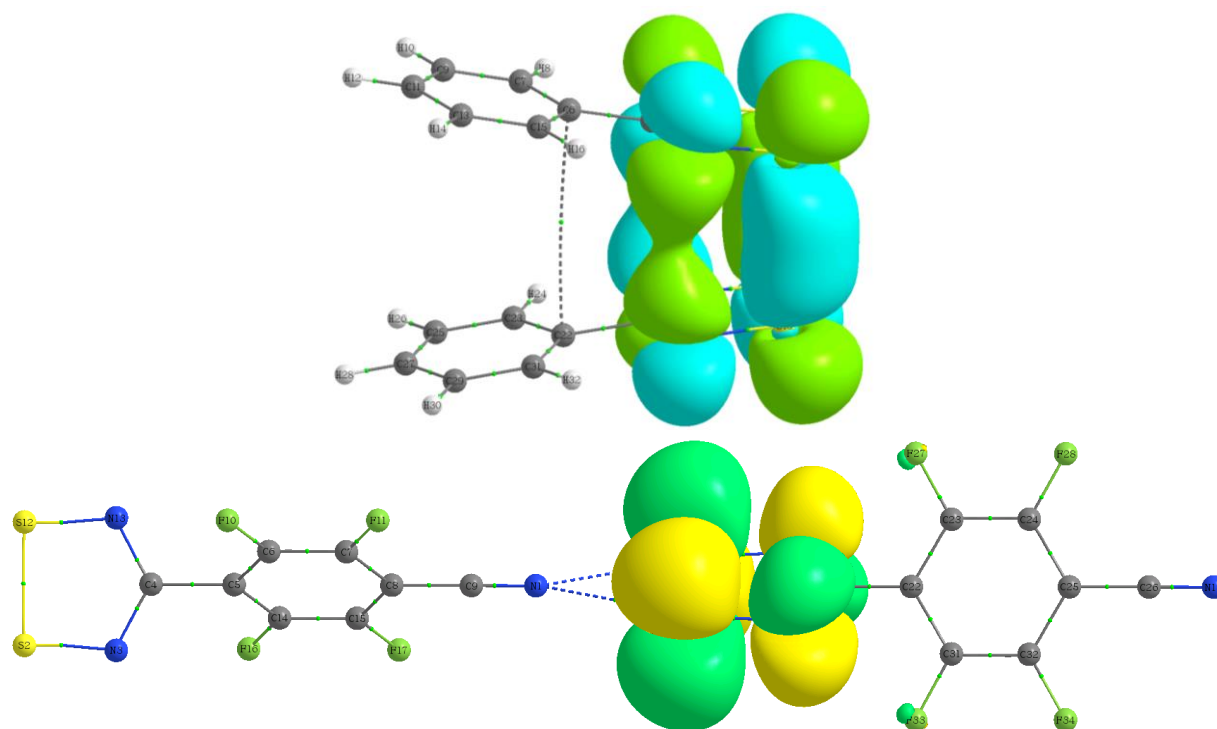


Figure 4.15: HOMOs of **1** (top) showing overlap of the SOMOs and the **2** (bottom).

Comparison of all values for the dimeric radicals show much larger ΔE_{Pauli} values compared to the ΔE_{orb} values, with radical **1** being the one exception. Radical **1** exhibits the largest ΔE_{orb} value in Table 4.8, where the absence of fluorinated groups on the aryl ring contributes to the small twist angles that allow for strong orbital interactions between the SOMOs.

The ΔE_{Pauli} contribution being larger than the ΔE_{orb} contribution in most dimeric radicals shows that the attractive interaction between the SOMOs does not result in the strong binding energies, but it is rather a combination of the ΔE_{orb} , ΔE_{el} and ΔE_{disp} contributions. These results show that a combination of interactions between the SOMOs and other contacts between the radicals are required for dimerisation to occur.

The strength of the binding energies are surprisingly similar for the monomeric and dimeric radicals, with **1** being the one exception. This would suggest that the structure-directing contacts in monomeric radicals could possibly exhibit stronger binding energies than those that could form if these radicals were to dimerise.

The properties of the intermolecular contacts in monomeric and dimeric radicals will be reported in the next section.

4.6. Topological analysis of the electron density in DTDA radicals.

Topological properties of the dimeric and monomeric radicals were investigated by use of Atoms In Molecules (AIM) analysis²⁹. AIM extended wave function files (.wfx files) were generated from fully optimised structures, allow for the writing of wave function data of unlimited size, range and precision.

The AIM plots of all dimeric and monomeric radicals are illustrated in Figure 4.16, with the dimeric radicals shown in Figures 4.16a – 4.16f and monomeric radicals shown in Figures 4.16g – 4.16k. The bond critical points (BCPs) are marked by red spheres, with the properties of each BCP summarised in a small table (Tables a – k) next to each figure. According to Nakanishi and coworkers, the properties at the BCPs, namely the electron density [$\rho(r)$], the Laplacian of the electron density [$\nabla^2\rho$] and the total energy density [H], can be used to classify intermolecular interactions as van der Waals interaction, H-bond, covalent bonds, molecular complex (CT-MC), hypervalent trigonal bipyramidal adducts (CT-TBP) or weak covalent bonds³⁰. The properties for each of these interactions are summarised in Table 4.9.

Table 4.9: Classification of different intermolecular contacts with AIM parameters according to Nakanishi and coworkers³⁰. Values given in atomic units.

Interaction	$\rho(r)$	$\nabla^2\rho$	H
Van der Waals	$0.00 < \rho(r) < 0.01$	$0.00 < \nabla^2\rho < 0.04$	$0.000 < H < 0.002$
H-bond	$0.01 < \rho(r) < 0.04$	$0.04 < \nabla^2\rho < 0.12$	$-0.004 < H < 0.002$
CT-MC	$0.01 < \rho(r) < 0.03$	$0.02 < \nabla^2\rho < 0.06$	$-0.001 < H < 0.002$
CT-TBP	$0.03 < \rho(r) < 0.12$	$-0.01 < \nabla^2\rho < 0.10$	$-0.060 < H < -0.003$
Weak covalent bonds	$0.05 < \rho(r) < 0.17$	$-0.10 < \nabla^2\rho < 0.07$	$-0.130 < H < -0.030$

Analysis of the AIM results for the dimeric radicals reveals that all structures contain two S...S contacts, with BCP properties that are similar to those of H-bond or CT-MC contacts.

Radicals **1**, **8** and **9** (Figures 4.16a - 4.16c) exhibit N...N and C...C contacts where the BCPs have properties characteristic of van der Waals contacts. The large twist angle in radical **10** (Figure 4.16d) results in the formation of C...F and one F...F contacts between the perfluoroaryl rings. The F...F contact has can be classified as a halogen bond, which can be described as an interaction facilitated by a σ -hole, and has emerged as a new paradigm in noncovalent interactions that can be utilised in solid-state engineering of novel materials^{31,32}. The formation of these contacts could also play a role in the dimerisation of this radical, despite the large twist angle. This once again shows that fluorine atoms are capable of forming various structure-directing contacts.

Measurement of the S...S and N...N contact distances in **1** (Figure 4.16a) and **10** is illustrated in Figure 4.17, which shows shorter contact distances in **1** that does not contain a fluorinated aryl ring. This shows that a large twist angle results in an increase in distance between the heterocyclic rings and therefore decreased interaction between the SOMOs, which is reflected in the weaker binding energy for **10** (Table 4.8).

Radical **11** (Figure 4.16e) contains radical molecules from **1** (Figure 4.16a) and **10** (Figure 4.16d). The measured S...S and N...N contact distances are illustrated in Figure 4.18, showing that the large twist angle results in the fluorine atoms resulting in a steric hindrance that increases the contact distances (blue circles).

Domagała and coworkers²³, compared the BCP properties of the S...S intermolecular contacts between **1** (Figure 4.16a), **10** (Figure 4.16d) and **11** (Figure 4.16e) radicals. The $\rho(r)$ and $\nabla^2\rho$ values of the S...S contacts given in Figure 4.16a, Figure 4.16d and Figure 4.16e for these three radicals are in good agreement with the values obtained in reference 23.

Radical **12** in Figure 4.16f has fluorine atoms at the *meta* and *para* positions, but not the *ortho* position. The radical exhibits small twist angles and a BCP pattern similar to that observed for the **1**, **8** and **9** (Figures 4.16a - 4.16c) radicals, which shows that only fluorine atoms at the *ortho* position will result in large twist angles.

The unusual nature of the modes of association in monomeric radicals **3** and **6** (Figures 4.16h and 4.16k) is confirmed by the combination of S...N, F...F contacts and other contacts with BCPs properties characteristic of van der Waals contacts. The presence of more BCPs between the radicals in these two monomeric radicals show why they exhibit stronger binding energies when compared those of the other monomeric radicals in Table 4.8.

Radicals **2**, **4** and **5** (Figures 4.16g, 4.16i and 4.16j) exhibit a linear mode of association due to structure-directing contacts between the group at the *para* position and the sulfur atoms of the heterocyclic radical ring of neighbouring radical, where these contacts exhibit BCPs with properties characteristic of van der Waals contacts. These radicals favour interaction between areas of partial negative and positive charge, which is evident by the $-\text{NO}_2^{\delta-} \cdots \text{S}^{\delta+}$ and $-\text{CN}^{\delta-} \cdots \text{S}^{\delta+}$ intermolecular interactions between these radicals.

This section has reported the properties of the various contacts that results from radicals adopting monomeric and dimeric modes of association. The next section will aim to visualise these contacts and what effect the formation of these contacts will have on the rest of the radical system.

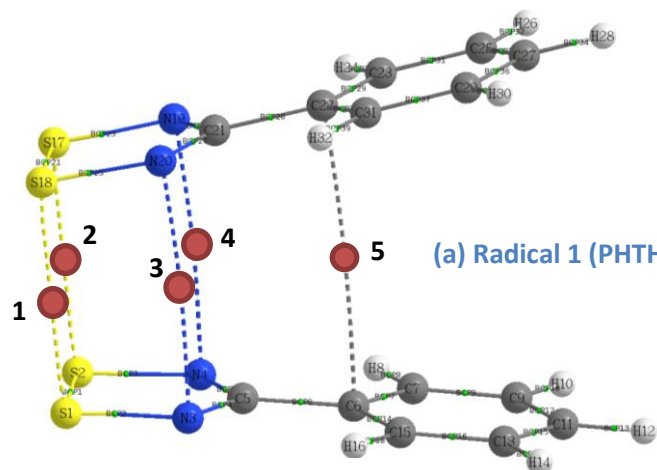


Table a with properties of BCPs (a.u.)

BCP #	Atoms	$\rho(r)$	$\nabla^2\rho$	H
1	S1 - S18	0.0210	0.040	0.0001
2	S2 - S17	0.0210	0.041	-0.0001
3	N3 - N20	0.0040	0.011	0.0003
4	N4 - N19	0.0044	0.012	0.0003
5	C6 - C22	0.0016	0.004	0.0002

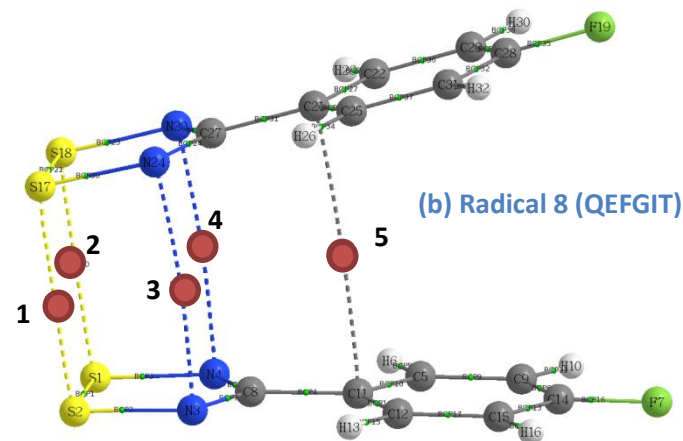


Table b with properties of BCPs (a.u.)

BCP #	Atoms	$\rho(r)$	$\nabla^2\rho$	H
1	S2 - S17	0.0209	0.0405	-0.0001
2	S1 - S18	0.0209	0.0406	-0.0001
3	N3 - N24	0.0047	0.0120	0.0003
4	N4 - N20	0.0047	0.0120	0.0003
5	C11 - C21	0.0019	0.0053	0.0003

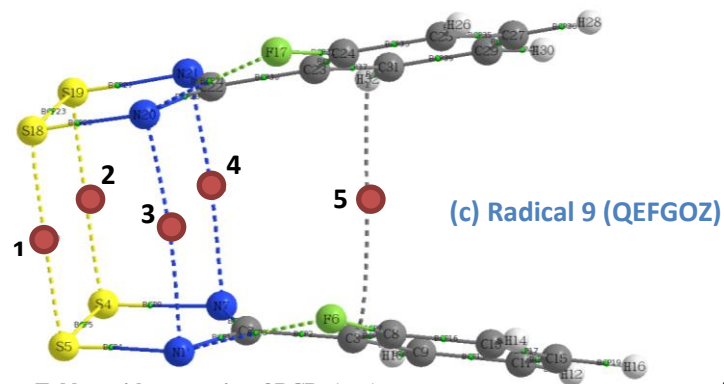


Table c with properties of BCPs (a.u.)

BCP #	Atoms	$\rho(r)$	$\nabla^2\rho$	H
1	S5 - S18	0.0201	0.0394	0.0001
2	S4 - S19	0.0223	0.0424	-0.0003
3	N1 - N20	0.0044	0.0117	0.0003
4	N7 - N21	0.0053	0.0130	0.0003
5	C3 - C31	0.0027	0.0068	0.0003

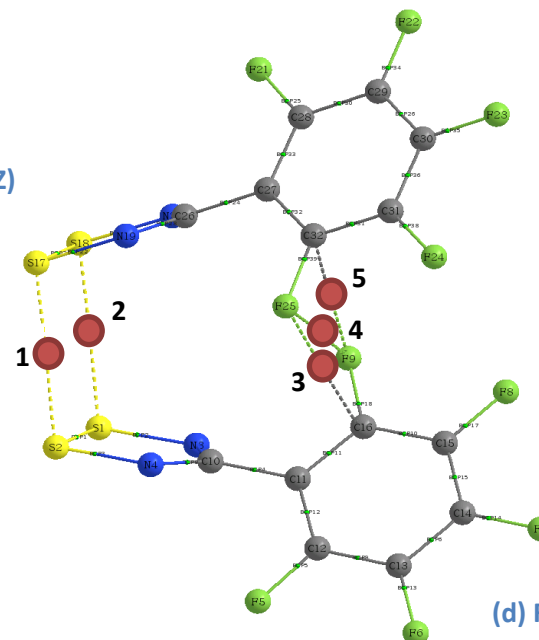


Table d with properties of BCPs (a.u.)

BCP #	Atoms	$\rho(r)$	$\nabla^2\rho$	H
1	S2 - S17	0.0208	0.0404	0.0001
2	S1 - S18	0.0208	0.0404	0.0001
3	C16 - F25	0.0043	0.0202	0.0011
4	F9 - F25	0.0045	0.0241	0.0010
5	F9 - C32	0.0043	0.0202	0.0011

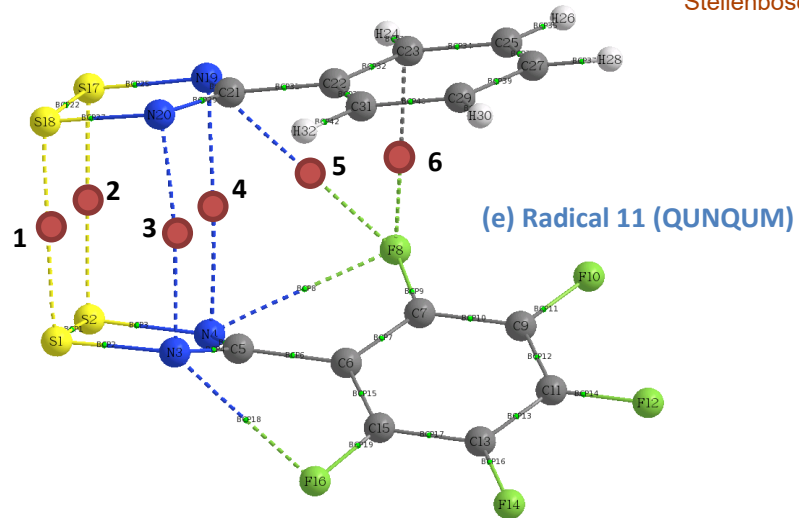


Table e with properties of BCPs (a.u.)

BCP #	Atoms	$\rho(r)$	$\nabla^2\rho$	H
1	S1 - S18	0.0238	0.0447	-0.0005
2	S2 - S17	0.0181	0.0359	0.0002
3	N3 - N20	0.0059	0.0143	0.0003
4	N4 - N19	0.0036	0.0100	0.0003
5	F8 - N19	0.0022	0.0104	0.0006
6	F8 - C23	0.0044	0.0171	0.0008

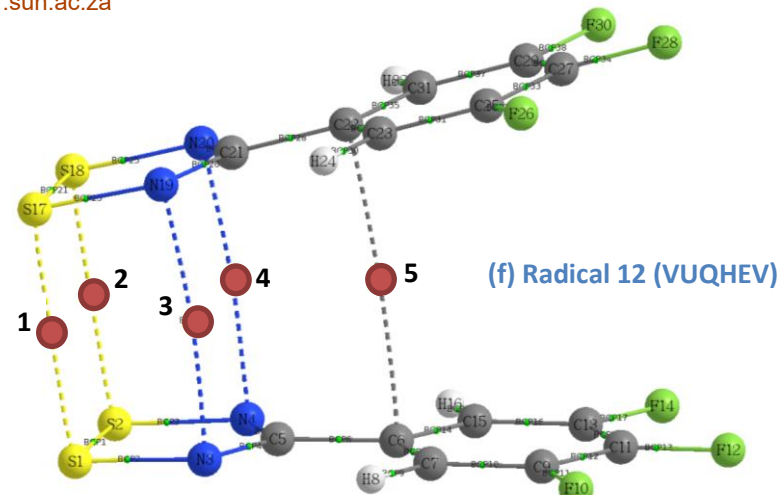


Table f with properties of BCPs (a.u.)

BCP #	Atoms	$\rho(r)$	$\nabla^2\rho$	H
1	S1 - S17	0.0213	0.0411	-0.0001
2	S2 - S18	0.0208	0.0403	-0.0001
3	N3 - N19	0.0052	0.0129	0.0003
4	N4 - N20	0.0050	0.0126	0.0003
5	C6 - C22	0.0022	0.0062	0.0003

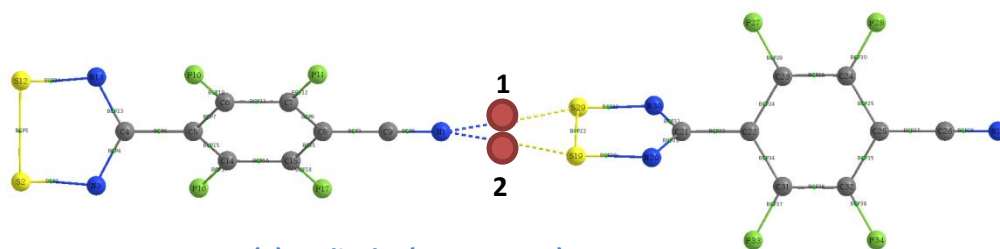


Table g with properties of BCPs (a.u.)

BCP #	Atoms	$\rho(r)$	$\nabla^2\rho$	H
1	N1 - S29	0.0089	0.0321	0.0410
2	N1 - S19	0.0089	0.0321	0.0410

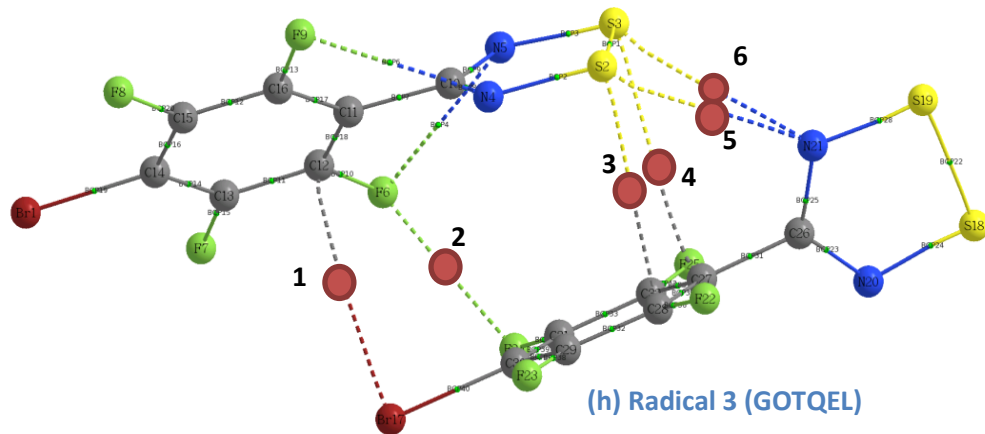


Table h with properties of BCPs (a.u.)

BCP #	Atoms	$\rho(r)$	$\nabla^2\rho$	H
1	C12 - Br17	0.0055	0.0173	0.0009
2	F6 - F24	0.0077	0.0363	0.0009
3	S2 - C28	0.0084	0.0256	0.0011
4	S3 - C27	0.0061	0.0175	0.0008
5	S2 - N21	0.0079	0.0254	0.0010
6	S3 - N21	0.0079	0.0250	0.0009

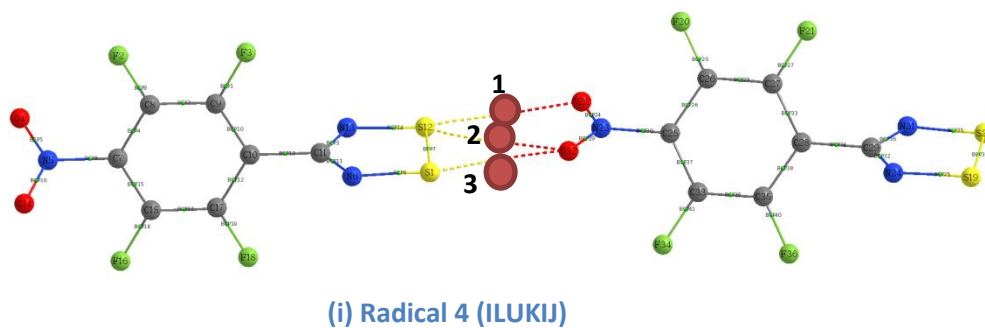


Table j with properties of BCPs (a.u.)

BCP #	Atoms	$\rho(r)$	$\nabla^2\rho$	H
1	S12 - O22	0.0050	0.0188	0.0239
2	S12 - O32	0.0072	0.0276	0.0347
3	S1 - O32	0.0083	0.0318	0.0401

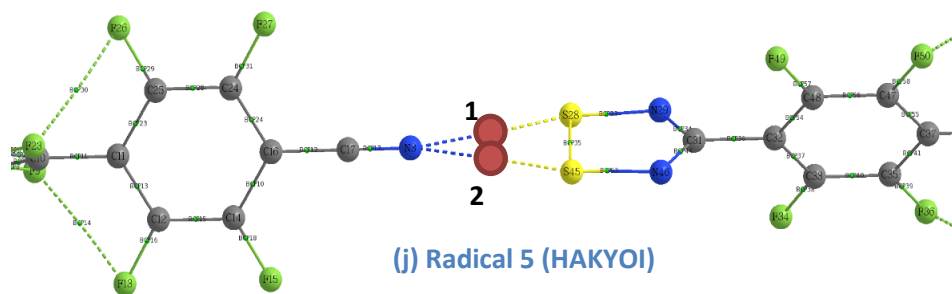


Table j with properties of BCPs (a.u.)

BCP #	Atoms	$\rho(r)$	$\nabla^2\rho$	H
1	N3 - S28	0.0087	0.0315	0.0403
2	N3 - S45	0.0087	0.0315	0.0403

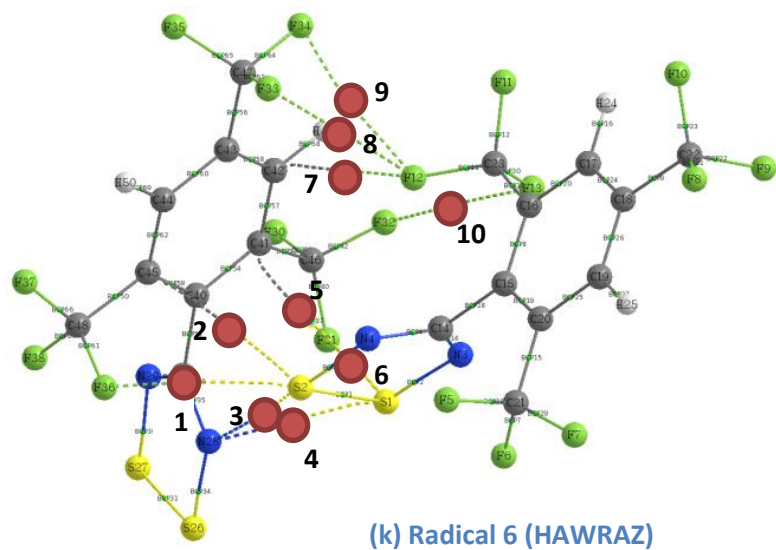


Table k with properties of BCPs (a.u.)

BCP #	Atoms	$\rho(r)$	$\nabla^2\rho$	H
1	S2 - F36	0.0066	0.0272	0.0338
2	S2 - C45	0.0064	0.0185	0.0249
3	S2 - N28	0.0075	0.0269	0.0344
4	S1 - N28	0.0094	0.0298	0.0392
5	S1 - C41	0.0053	0.0152	0.0205
6	S1 - F31	0.0068	0.0262	0.0330
7	F12 - C42	0.0074	0.0317	0.0392
8	F12 - F33	0.0045	0.0235	0.0281
9	F12 - F34	0.0037	0.0204	0.0241
10	F13 - F32	0.0008	0.0053	0.0061

Figure 4.16: AIM plots of dimeric and monomeric radicals: 1 (a), 8 (b), 9 (c), 10 (d), 11 (e), 12 (f), 2 (g), 3 (h), 4 (i), 5 (j) and 6 (k).

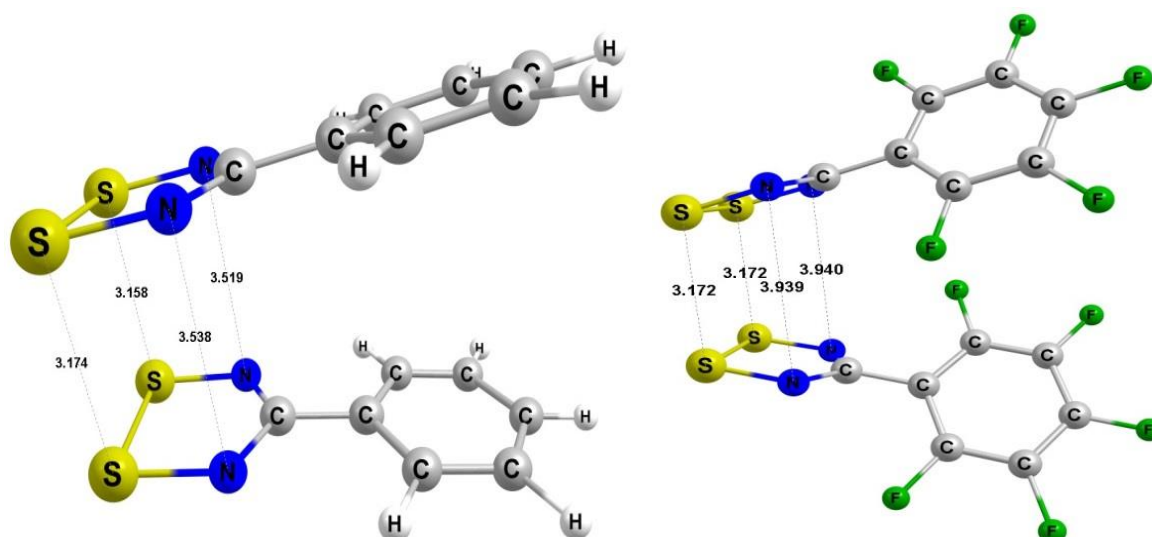


Figure 4.17: S...S and N...N contacts in radicals 1 (left) and 10 (right).

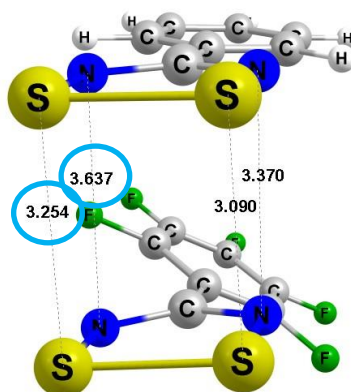


Figure 4.18: The S...S and N...N contacts in radical 11. The elongation of the S...S by the twisting of the fluorinated ring is marked by blue spheres.

4.7 Electrostatic surface potential

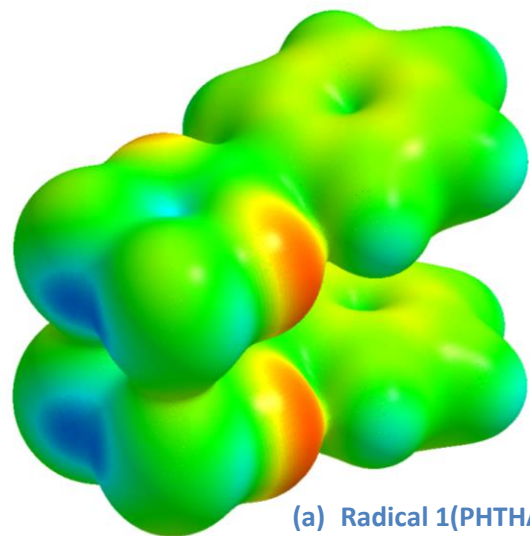
The AIMAll software package was used to calculate Electrostatic Surface Potential (ESP) maps for monomeric and dimeric radicals in order to visualise the charge distribution of these molecules in three dimensions. The ESP plots are shown in Figure 4.19a – 4.19l. These maps show the areas that result in the formation of structure-directing electrostatic interactions that facilitate or inhibit dimerisation. Furthermore, these maps can also show why large twist angles are observed in some radicals. All ESP plots were calculated at an electron density surface of $0.01 e \text{ bohr}^{-1}$. This was changed from the default $0.001 e \text{ bohr}^{-1}$ in order to better visualise the different regions. All ESPs are depicted using a colour scale showing maximum (blue) values at 100 kcal/mol and a minimum (red) at -45 kcal/mol .

The ESPs of the dimeric radicals (Figures 4.19a - 4.19f) exhibit red areas of negative potential on the heterocyclic ring corresponding to the nitrogen atoms, as well as blue areas of positive

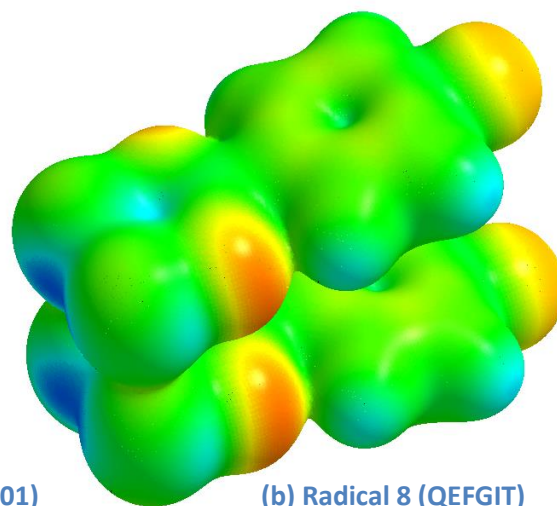
potential between the sulfur atoms, where the areas of negative and positive potential are generally areas of charge accumulation and charge depletion, respectively. The yellow and cyan colours show areas of lower positive or negative potential. The majority of the molecular surfaces appear green, which is indicative of areas that are relatively neutral.

Furthermore, the dimeric radical ESPs show areas of larger negative potential on the nitrogen atoms of radicals with *ortho*-fluorine groups. This is illustrated by the negative potential on the nitrogen atoms of radicals **10** and **11** (Figures 4.19d and 4.19e), where **10** contains two fluorinated phenyl rings, while the co-crystal **11** consists of one fluorinated and one non-fluorinated radical molecule. Positions **1** and **2** (Figure 4.19d) show a clear difference between the values of negative potential on the nitrogen atoms, which are -28.97 and -34.80 kcal/mol, respectively. The larger negative potentials on the nitrogen atoms of fluorinated radicals allow for the formation of S \cdots N and various other structure-directing contacts that can reduce the tendency of radicals to dimerise.

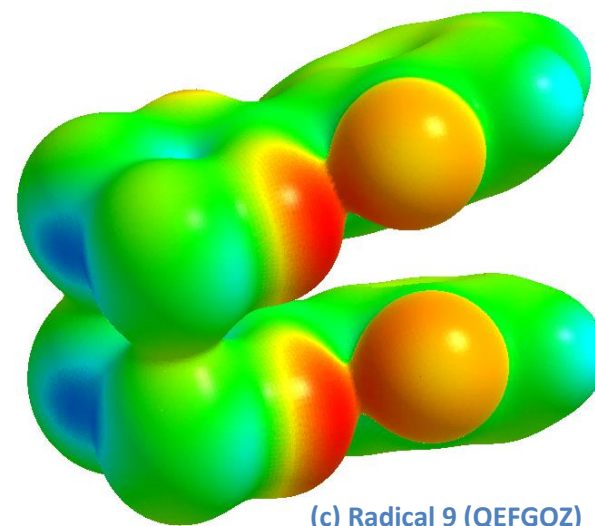
The fluorinated aryl rings of radicals **10** and **12** (Figures 4.19d - 4.19f) exhibit cyan coloured areas of positive potentials at the carbon atoms. The electronegative fluorine atoms draw electron density from the carbon atoms, which results in the areas of negative potential on the fluorine atoms and an increase in positive potential on the carbon atoms, which results in the formation of C \cdots F contacts in radical **10** (Figure 4.19d). The large twist angles in fluorinated aryl rings result in a weakening of the interaction between the aryl rings. This can be visualised by constructing Non-Covalent Interaction (NCI) plots of radicals **1** and **10**, as shown in Figure 4.20. These plots highlight the intermolecular interactions between radicals, where the colours provide additional information regarding the type of interaction present. Radical **1** (Figure 4.20, left) exhibits a smooth surface of intermolecular interactions occurring between the aryl rings, while **10** (Figure 4.20, right) exhibits a much more distorted surface of intermolecular interactions between its fluorinated aryl rings, which suggests weaker $\pi - \pi$ stacking interactions between fluorinated phenyl rings. This is also confirmed by the stronger binding energy observed for **1** in Table 4.8.



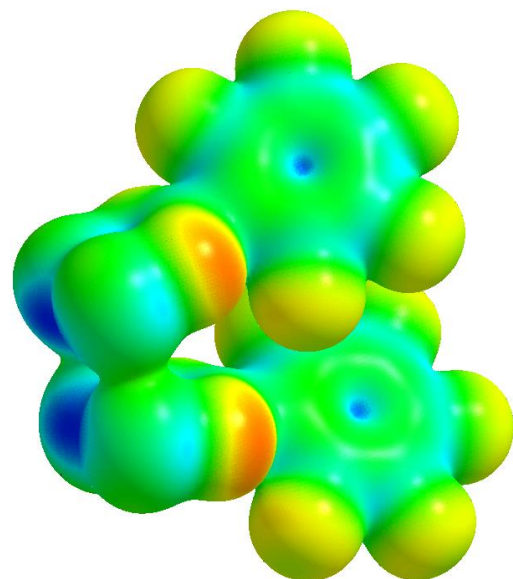
(a) Radical 1(PHTHAZ01)



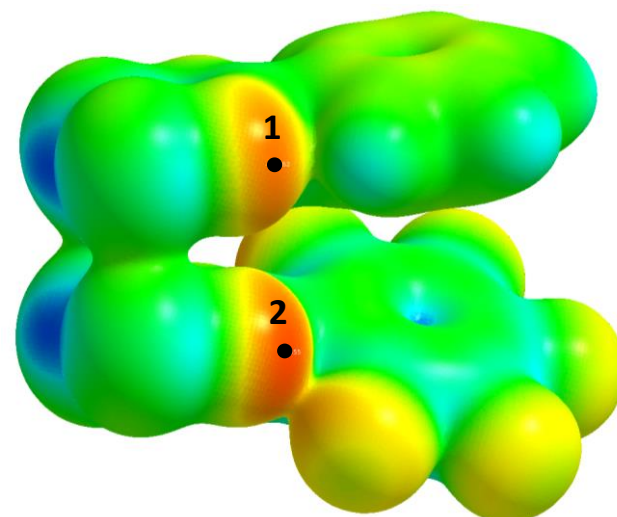
(b) Radical 8 (QEFGIT)



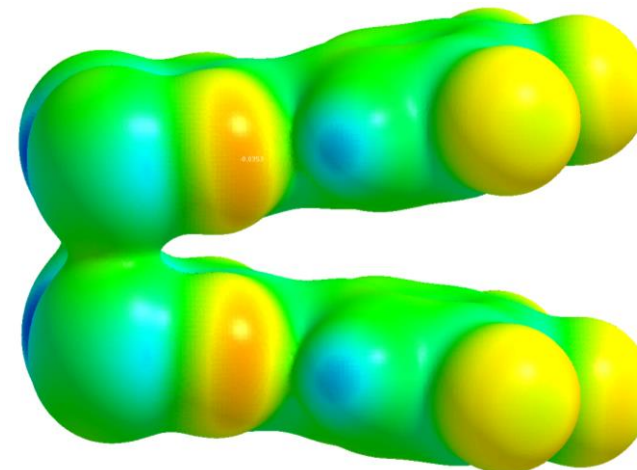
(c) Radical 9 (QEFGOZ)



(d) Radical 10 (QUNQOG)



(e) Radical 11 (QUNQUM)



(f) Radical 12 (VUQHEV)

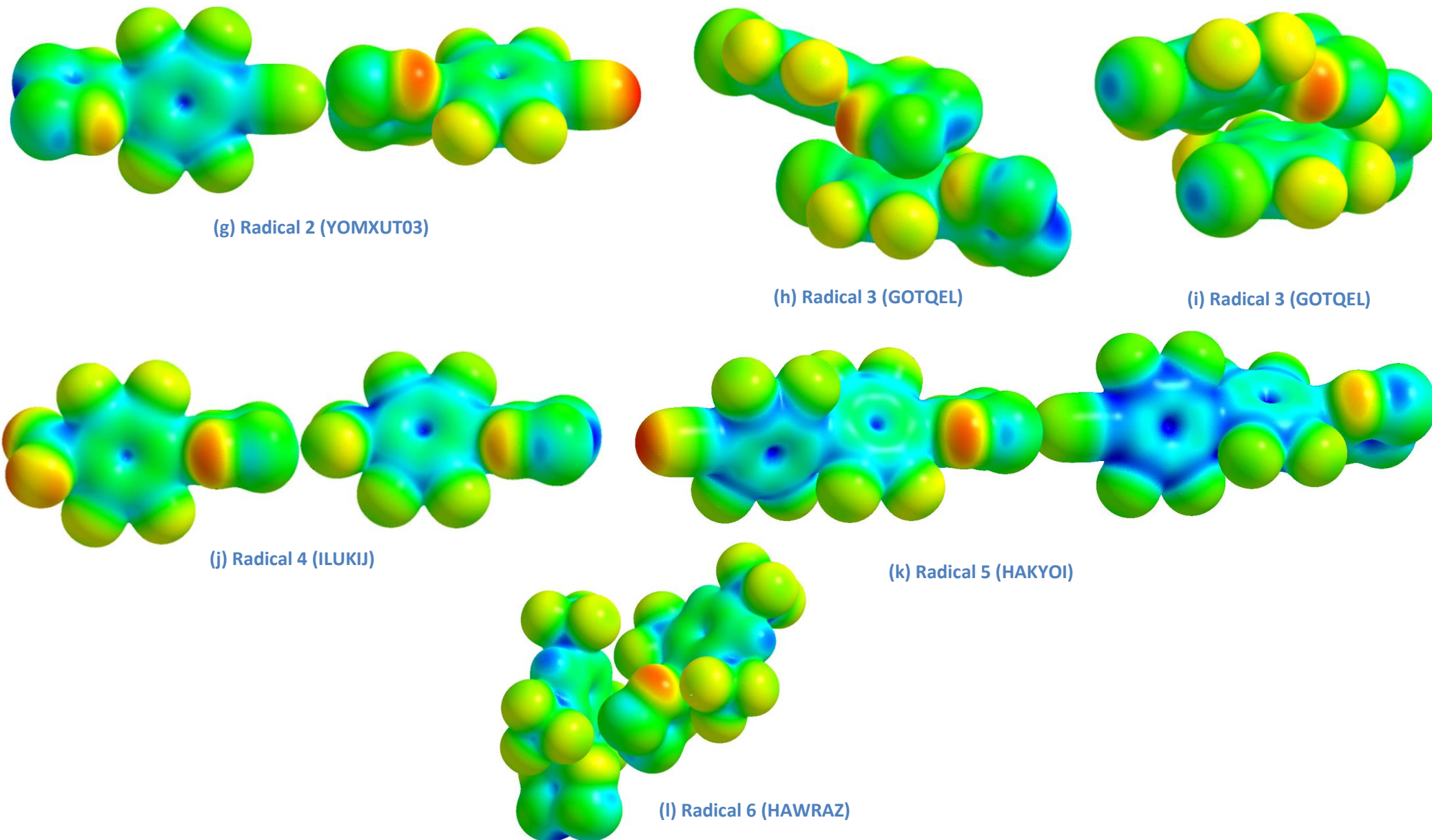


Figure 4.19: ESP plots of dimeric and monomeric radicals: 1 (a), 8 (b), 9 (c), 10 (d), 11 (e), 12 (f), 2 (g), 3 (h), 3 viewed from different angle (i), 4 (j), 5 (k) and 6 (l).

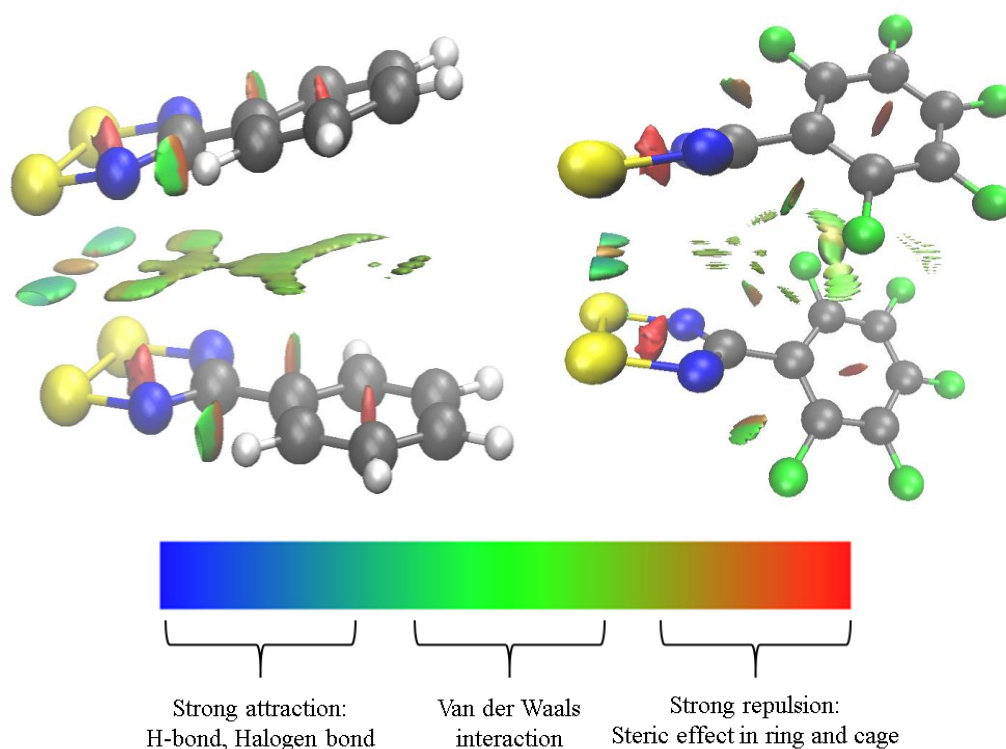


Figure 4.20: NCI plots of 1 (left) and 10 (right). The colour scheme used to describe the nature of intermolecular interaction is given below.

Clarke and coworkers³³ calculated molecular ESPs to rationalise the structures of DTDA radicals. The total ESPs were calculated for a series of fluorinated DTDA radicals, which revealed regions of positive potential near the sulfur and hydrogen atoms, whereas regions of negative potential were identified near the heterocyclic nitrogen and aromatic fluorine atoms. The regions of positive and negative potential on the heterocyclic and fluorinated aryl rings are in good agreement with the ESPs calculated in this study and show that these regions are capable of forming various electrostatic interactions.

Radical **3** shown in Figures 4.19h and 4.19i exhibits a positive potential on the bromine atom, which is indicative of a σ -hole that results in the formation of various contacts. Part of the solid-state packing arrangement of radical **3** is illustrated in Figure 4.21, which shows the σ -hole on the bromine atom forming a contact with the area of negative potential on the nitrogen atom. The Br \cdots N contact in Figure 4.21 shows that a positive potential on a *para* substituent can form structure-directing contacts that favour a monomeric mode of association.

Radical **6** in Figure 4.19i also exhibits structure-directing contacts via the *para* substituent. The area of positive charge on the sulfur atom forms an interaction with the one of fluorine atoms that forms part of the trifluoromethyl group at the *para* position, which is illustrated by part of the solid-state packing arrangement of **6** in Figure 4.22.

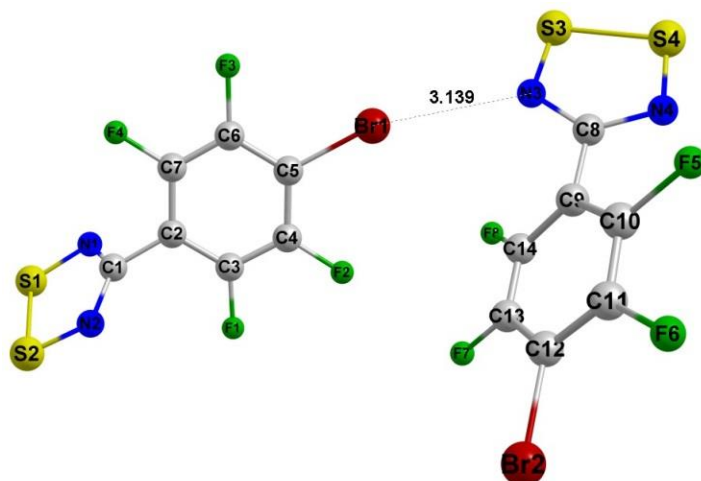


Figure 4.21: Formation of the Br...N contact in radical 3.

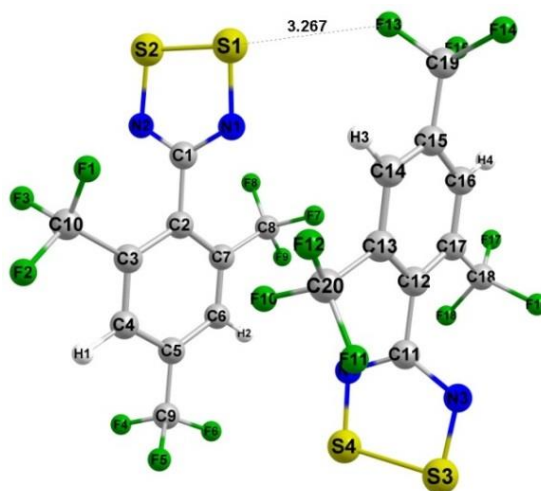


Figure 4.22: The S...F contact in radical 6.

The linear mode of association of radical **4** is illustrated in Figure 4.19j, which exhibits the structure-directing contact between the areas of negative potential on the oxygen atoms of the nitro group with the area of positive potential between the sulfur atoms. The areas marked as **1** and **2** on Figure 4.19j exhibit energies of -31.16 and -20.25 kcal/mol, respectively.

A further effect of the structure-directing contacts is a larger positive potential on the carbon atoms of the aryl ring, which results in the formation of O...C contacts in the solid-state arrangement, as shown in Figure 4.23.

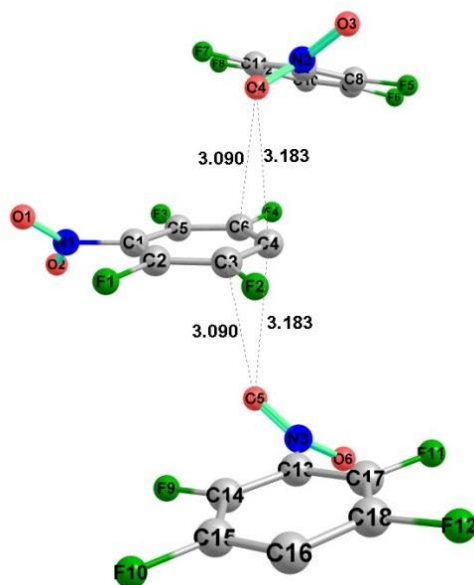


Figure 4.23: The formation of O...C contacts between the aryl rings and the nitro group of neighbouring radicals of **4**. The heterocyclic radical rings were omitted in order to show the contacts.

Radical **2** (Figure 4.19g) exhibits a linear mode of association, which is due to the formation of a structure-directing contact between the negative potential on the nitrogen atom of the cyano group with the area of positive potential between the sulfur atoms. The contact results in a larger negative potential on the nitrogen atoms when compared to radical **4**, resulting in the formation of the C...N contacts between the antiparallel rows of radical in the solid-state arrangement (Figure 4.24). This would also suggest that these contacts are the driving force behind the antiparallel arrangement of radicals of **2** discussed in Chapter 3.

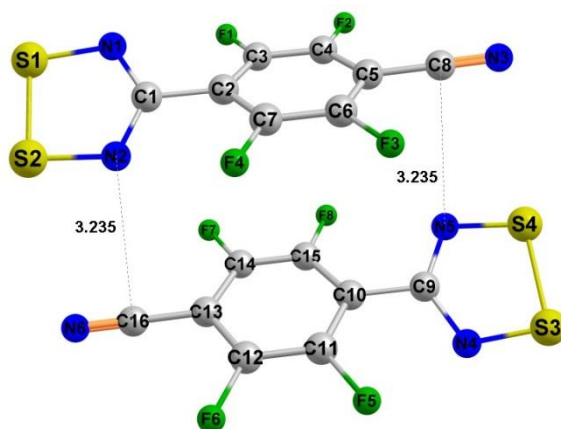


Figure 4.24: The N...C contacts between radical fragments of **2**.

Radical **5** shown in Figure 4.19k exhibits a very similar structure to radical **2** (Figure 4.19g). The same structure-directing contact can be observed between the negative potential on the nitrogen atoms of the cyano group and the positive potential between the sulfur atoms. Radical

6 does, however, have another fluorinated phenyl ring, which results in the formation of additional F...F and N...F contacts in the solid-state arrangement (Figure 4.25).

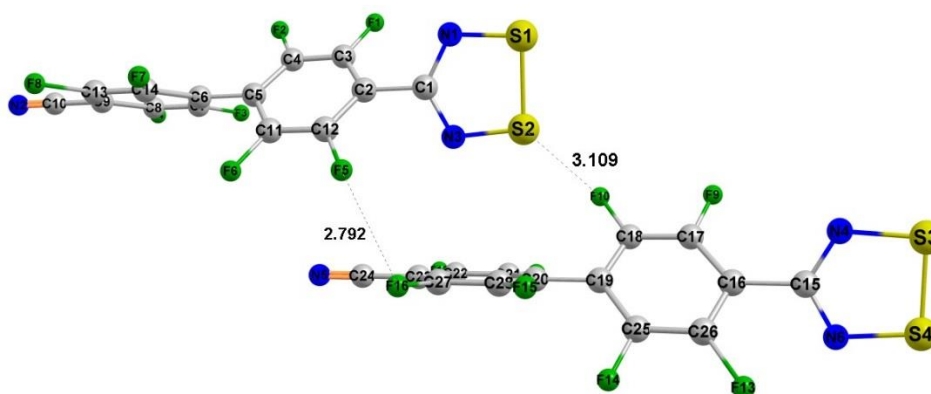


Figure 4.25: The F...F and S...F contact in **6**.

To summarise, investigation of the three dimensional ESP maps showed that fluorinated groups at the *ortho* position will result in a larger negative potential on the nitrogen atoms, which can then interact with an area of positive potential on *para* substituents to form structure-directing contacts that reduce the tendency of radicals to dimerise. This was observed by the Br...N and F...N contacts that result in the monomeric mode of association in radicals **3** and **6**. Furthermore, the linear mode of association in monomeric radicals is facilitated by the formation of structure-directing contacts between a negative potential on the *para* substituent with the positive potential between the sulfur atoms. These results agree with the results obtained by Clarke and coworkers⁷.

It is therefore important to be aware of the complexity of the different steric and electronic effects that should be considered when designing radical-based magnets. This is resonated by Stephen Blundell, who remarked that “few (radicals) are stable enough to be assembled into crystalline structures and, even when that is possible, aligning these spins ferromagnetically is usually impossible”³⁴.

Conclusions

In this chapter, the results produced using various calculations were used to rationalise why DTDA dimerise or prefer to remain monomeric in the solid state. Dimeric radicals optimised in the singlet state were found to yield attractive energies if calculations were performed in the singlet state, whereas repulsive energies were obtained if these calculations were performed in the triplet state. Contrastingly, dimeric radicals optimised in the triplet state were found to yield

attractive energies if calculations were performed in the triplet state, whereas repulsive energies were obtained if calculations were performed in the singlet state. Investigation of the optimised geometries revealed that dimeric radicals will yield final structures that favour interaction between the SOMOs if optimised in the singlet state, while final structures that do not favour interaction between the SOMOs will be obtained if optimised in the triplet state.

The monomeric radicals exhibit a very different trend. These radicals yield attractive intermolecular interaction energies for all single point calculations that were performed in the triplet state, irrespective of the state used during geometry optimisation. The final geometries were found to exhibit very little change when optimised in the singlet or triplet state, which shows that the linear mode of association is energetically very stable.

Radical **3** was found to be the one exception as it yields a final structure in the *trans-cofacial* mode of association if optimised in the singlet state. Energy calculations showed that attractive energies were obtained for calculations performed in the singlet and triplet states, which suggests that radical **3** could exist as another polymorph or co-crystal that allows for interaction between the SOMOs, which yields dimerised pairs. The crystal structure of a novel co-crystal (**3-cox**) was found to exhibit dimerised pairs of **3**, which confirms what the calculation of the energies predicted. If another monomeric radical were shown to exhibit a dimeric mode of association with attractive energies for calculations performed in the singlet state, this could indicate that the radical could exist in another dimeric polymorph or co-crystal that exhibits dimerised pairs.

PES scans were performed on one dimeric and one monomeric radical, namely **1** and **2**, by varying two different torsion angles. The 2D plot of the dimeric radical PES scan showed that the *cisoid* mode at 0° of configuration exhibits the strongest attractive energy. The 2D plot of the monomeric radical PES scan showed that the strongest attractive energies occur found at large twist angles that minimise the steric repulsion between the nitrogen and fluorine atoms, whereas strongly repulsive energies are found at a twist angle of 180° that maximises the steric repulsion between these atoms.

EDA analysis of dimeric radicals showed that a combination of dispersion, electrostatic and orbital contributions balance the large repulsive Pauli effect and yield strong binding energies. EDA analysis of monomeric radicals showed that radicals **3** and **6** show stronger binding energies when being compared to the other monomeric radicals. This is due to the F...F and S...N contacts that are present in these radicals, but not in the radicals that exhibit a linear mode of association. All of the monomeric radicals also exhibit lower repulsive Pauli repulsion effects, as there is very little interaction between the SOMOs.

The binding energies of dimeric and monomeric radicals were shown to be comparable in strength, which would suggest that the intermolecular interactions that result in the monomeric modes of association could be more favourable than the interactions that would occur if these radicals were to dimerise.

The topological analysis of dimeric radicals revealed that the S...S contacts have BCPs with properties similar to those of H-bonds and CT-MC contacts. It was further found that most dimeric radicals exhibit C...C contacts with BCPs properties similar to those of van der Waals contacts. These contacts will not be present in radicals with a fluorinated aryl ring, as the large twist angle results in the formation of other contacts between the aryl rings.

The topological analysis of radicals **3** and **6** showed that their monomeric modes of association exhibit more contacts when compared to the monomeric radicals in a linear mode of association, which explains why radicals **3** and **6** exhibit stronger binding energies. The other monomeric radicals that associate in a linear mode exhibit BCPs at CN...S and NO₂...S contacts with properties similar to those of van der Waals contacts.

The ESP maps of dimeric radicals confirmed that fluorinated aryl rings result in a large twist angle, which in turn results in larger negative potential on the nitrogen atoms and a positive potential on the carbon atoms of the aryl ring. The change in potential on these atoms allow for the formation of various contacts that will influence the solid-state architecture.

The ESP maps of monomeric radicals showed that the larger negative potential on the nitrogen atom results in the formation of Br...N and F...N contacts in radicals **3** and **6**, respectively. Furthermore, the linear mode of association in radicals **2**, **4** and **5** result from areas of negative potential on the *para* substituent interacting with an area of positive potential between the sulfur atoms.

The results in this chapter have shown that different substituents on the aryl ring strongly influence the preferred mode of association and strength of interactions in DTDA radicals. The next chapter will contain a theoretical study, that aims to determine if placing selected substituents on the aryl ring can be utilised to favour dimeric or monomeric modes of association.

References

- (1) Rawson, J. M.; Luzon, J.; Palacio, F. *Coordination Chemistry Reviews* **2005**, *249*, 2631.
- (2) Haynes, D. A. *CrystEngComm* **2011**, *13*, 4793.
- (3) Banister, A. J.; Bricklebank, N.; Clegg, W.; Elsegood, M. R. J.; Gregory, C. I.; Lavender, I.; Rawson, J. M.; Tanner, B. K. *Journal of the Chemical Society, Chemical Communications* **1995**, 679.
- (4) Alberola, A.; Less, R. J.; Pask, C. M.; Rawson, J. M.; Palacio, F.; Oliete, P.; Paulsen, C.; Yamaguchi, A.; Farley, R. D.; Murphy, D. M. *Angewandte Chemie International Edition* **2003**, *42*, 4782.
- (5) Antorrena, G.; Palacio, F.; E. Davies, J.; Hartley, M.; M. Rawson, J.; B. Smith, J. N.; Steiner, A. *Chemical Communications* **1999**, 1393.
- (6) Allen, F. *Acta Crystallogr, Sect. B* **2002**, *58*, 380.
- (7) Clarke, C. S.; Haynes, D. A.; Smith, J. N. B.; Batsanov, A. S.; Howard, J. A. K.; Pascu, S. I.; Rawson, J. M. *CrystEngComm* **2010**, *12*, 172.
- (8) Beneberu, H. Z.; Tian, Y.-H.; Kertesz, M. *Physical Chemistry Chemical Physics* **2012**, *14*, 10713.
- (9) Cui, Z.-h.; Lischka, H.; Beneberu, H. Z.; Kertesz, M. *Journal of the American Chemical Society* **2014**, *136*, 12958.
- (10) Glaesemann, K. R.; Schmidt, M. W. *The Journal of Physical Chemistry A* **2010**, *114*, 8772.
- (11) Mitani, M.; Mori, H.; Takano, Y.; Yamaki, D.; Yoshioka, Y.; Yamaguchi, K. *The Journal of Chemical Physics* **2000**, *113*, 4035.
- (12) Resnati, G.; Boldyreva, E.; Bombicz, P.; Kawano, M. *IUCrJ* **2015**, *2*, 675.
- (13) Price, S. L. *CrystEngComm* **2004**, *6*, 344.
- (14) Simon, S.; Duran, M.; Dannenberg, J. *The Journal of Chemical Physics* **1996**, *105*, 11024.
- (15) Boys, S. F.; Bernardi, F. *Molecular Physics* **1970**, *19*, 553.
- (16) Takatani, T.; Hohenstein, E. G.; Malagoli, M.; Marshall, M. S.; Sherrill, C. D. *The Journal of Chemical Physics* **2010**, *132*, 144104.
- (17) Tsuzuki, S.; Orita, H.; Sato, N. *The Journal of Chemical Physics* **2016**, *145*, 174503.
- (18) Li, A.; Muddana, H. S.; Gilson, M. K. *Journal of Chemical Theory and Computation* **2014**, *10*, 1563.
- (19) Goodpaster, J. D.; Barnes, T. A.; Manby, F. R.; III, T. F. M. *The Journal of Chemical Physics* **2012**, *137*, 224113.
- (20) Alberola, A.; Clarke, C. S.; Haynes, D. A.; Pascu, S. I.; Rawson, J. M. *Chemical Communications* **2005**, 4726.
- (21) Constantinides, C. P.; Eisler, D. J.; Alberola, A.; Carter, E.; Murphy, D. M.; Rawson, J. M. *CrystEngComm* **2014**, *16*, 7298.
- (22) Melen, R. L.; Less, R. J.; Pask, C. M.; Rawson, J. M. *Inorganic Chemistry* **2016**, *55*, 11747.
- (23) Domagala, S.; Haynes, D. A. *CrystEngComm* **2016**, *18*, 7116.
- (24) Z. Chen, C.; Shu, D. Tan *In International Journal of Heat and Mass Transfer* **2017**, *105*, 741.
- (25) Ziegler, T.; Rauk, A. *Theoret. Chim. Acta* **1977**, *46*, 1.
- (26) Phipps, M. J. S.; Fox, T.; Tautermann, C. S.; Skylaris, C.-K. *Chemical Society Reviews* **2015**, *44*, 3177.
- (27) Li, P.; Shen, Z.; Wang, W.; Ma, Z.; Bi, S.; Sun, H.; Bu, Y. *Physical Chemistry Chemical Physics* **2010**, *12*, 5256.
- (28) Gao, W.; Feng, H.; Xuan, X.; Chen, L. *Journal of Molecular Modeling* **2012**, *18*, 4577.
- (29) Bader, R. F. W. *Accounts of Chemical Research* **1985**, *18*, 9.
- (30) Nakanishi, W.; Hayashi, S.; Narahara, K. *The Journal of Physical Chemistry A* **2008**, *112*, 13593.
- (31) Kolář, M. H.; Hobza, P. *Chemical Reviews* **2016**, *116*, 5155.

- (32) Wang, H.; Wang, W.; Jin, W. J. *Chemical Reviews* **2016**, *116*, 5072.
- (33) Clarke, C. S.; Haynes, D. A.; Smith, J. N. B.; Batsanov, A. S.; Howard, J. A. K.; Pascu, S. I.; Rawson, J. M. *CrystEngComm* **2010**, *12*, 172.
- (34) Blundell, S. J. *Contemporary Physics* **2007**, *48*, 275.

5 The effect of aryl ring substituents on the intermolecular interactions in DTDA radicals

Introduction

The results presented in Chapter 4 showed that the substituents on the aryl ring play an important role in the mode of association that is observed for DTDA radicals in the solid state. The results reported in this chapter aimed to investigate how placing different substituents at the *ortho*, *meta* and *para* of the aryl ring affect the intermolecular interactions in DTDA radicals that favour different modes of association.

It should be mentioned that this study aimed to investigate theoretical DTDA radicals that are not necessarily synthetically viable. The aim of this study was simply to investigate what effect placing different substituents at different positions on the aryl ring would have on the strength of the intermolecular interactions in these radicals, and their preferred configuration. This was achieved by performing a series of geometry optimisations and interaction energy calculations on substituted radicals to determine which substituents will yield intermolecular interactions that favour monomeric or dimeric modes of association.

An additional study was performed to investigate whether replacing the fluorine atoms on known monomeric radicals with heavier halogen atoms would affect the mode of association in these radicals. Geometry optimisation and interaction energy calculations were performed on the radicals containing heavier halogen atoms to determine how they affect the mode of association and interaction energies of these radicals.

5.1. Geometry optimisation calculations on DTDA radicals with different substituents at the *ortho*, *meta* and *para* positions

It has been mentioned in previous chapters that subtle changes to the R group will have little effect on the electronic properties of DTDA radicals, but it will greatly influence the solid-state architecture of the radical system^{1,2}. In this study, the effect of changes to the R group on dimerisation and intermolecular interactions was investigated by placing different functional groups as substituents at the *ortho*, *meta* and *para* positions of the aryl ring (Figure 5.1). Six substituents were selected that range from weakly electron donating to strongly withdrawing based on their induction and resonance strengths: namely methyl (-CH₃), hydroxyl (-OH), acyloxy (-OOCCH₃), fluoro (-F), carboxylic acid (-COOH) and nitro groups (-NOO). The electron-donating groups (EDGs) are also known as activating groups as they donate electron density to the conjugated π system of the aromatic group via resonance and inductive effects³. Additionally, EDGs (-CH₃, -OH, -OOCCH₃) are known to increase the electron density at *ortho*

and *para* positions. The electron-withdrawing groups (EWGs) (-F, -COOH, -NOO) are known as deactivating groups as they remove electron density from the conjugated π system result in decreased electron density at the *meta* position. The optimised geometry of radical **1** was used as the backbone structure to which the substituents were added, after which further calculations were performed. Only one substituent was added to a single radical molecule to observe how this would affect the complete radical system.

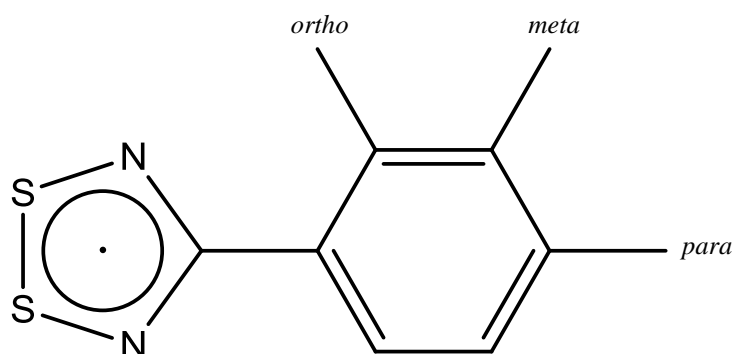


Figure 5.1: Illustration of a DTDA radical with an aryl group, where substituents can be placed at the *ortho*, *meta* and *para* positions.

The chemical name of each substituted radical is given in Table 5.1, in addition to the code used throughout this chapter (see p 18 for sketches of molecules).

Table 5.1: The chemical name and code of each substituted radical investigated in this chapter.

Chemical Name	Compound number
4-(3'-fluorophenyl)-1,2,3,5-dithiadiazolyl	13
4-(3'-carboxyphenyl)-1,2,3,5-dithiadiazolyl	14
4-(3'-nitrophenyl)-1,2,3,5-dithiadiazolyl	15
4-(2'-methylphenyl)-1,2,3,5-dithiadiazolyl	16
4-(2'-hydroxyphenyl)-1,2,3,5-dithiadiazolyl	17
4-(2'-acyloxyphenyl)-1,2,3,5-dithiadiazolyl	18
4-(4'-methylphenyl)-1,2,3,5-dithiadiazolyl	19
4-(4'-hydroxyphenyl)-1,2,3,5-dithiadiazolyl	20
4-(4'-acyloxyphenyl)-1,2,3,5-dithiadiazolyl	21

The radicals in Table 5.1 were fully optimised at the UB3LYP-D3/6-311++G(d,p) level of theory in the singlet and triplet states. The triplet state was included as the substituents investigated in this study could result in large twist angles or undergo strong intermolecular interactions that overcome the dimerisation energy. Vibrational analysis was performed to confirm that the obtained structure was at a minimum energy conformation in each case.

Intermolecular interaction energies were calculated for final structures of optimised substituted radicals by performing counterpoise-corrected calculations at the UB3LYP-D3/6-311++G(d,p)

level of theory in the singlet ($\Delta E_{\text{Singlet}}$, Table 5.2) and triplet state ($\Delta E_{\text{Triplet}}$, Table 5.2). The energies of the substituted radicals were also compared to the unsubstituted phenyl radical (ΔE_{diff} , Table 5.2). The twist angles (Twist, Table 5.2) between the substituted phenyl ring and the heterocyclic radical ring were measured for all singlet and triplet states optimised geometries of radicals and are summarised in Table 5.2. The interatomic distance of all S...S contacts were additionally included in Table 5.2 to see if there is a correlation between the strength of intermolecular interactions and the contact distances.

5.2. Intermolecular interaction energies for substituted radicals

The results of calculations performed in the singlet state show small twist angles, short S...S contacts and attractive energies for radicals that exhibit a *cisoid* dimeric mode of association. The strongest attractive energy is observed for radical pair **14**, which exhibits a *cisoid* mode of association as illustrated in Figure 5.2. Radical pairs **16**, **18**, **19**, **20** and **21** exhibit weaker interactions when compared to radical **1**, which is due to these radicals having substituents that result in final structures that exhibit fewer S...S and N...N contacts, as illustrated for radical pair **18** in Figure 5.2. Radical pairs **16** and **19** exhibit repulsive energies, which is due to the preferred mode of association in the final structure that results in less favourable interaction between the SOMOs, as illustrated in Figure 5.3 for radical pair **19**.

Table 5.2: The interaction energies (kcal/mol), S...S contact distances and twist angles of substituted radical pairs calculated in the singlet and triplet states. ΔE_{diff} is the difference between the interaction energy of each radical and that of **1.**

Compound number	$\Delta E_{\text{Singlet}}$	ΔE_{diff}	S1-S3	S2-S4	Twist	$\Delta E_{\text{Triplet}}$	ΔE_{diff}	S1-S3	S2-S4	Twist
1	-5.53	-	3.17 Å	3.16 Å	-1.56°	-7.74	-	4.23 Å	3.88 Å	4.12°
13	-6.09	-0.56	3.15 Å	3.14 Å	-13.39°	-9.05	-1.31	4.77 Å	5.36 Å	-2.78°
14	-7.24	-1.71	3.13 Å	3.16 Å	-12.83°	-10.22	-2.48	4.76 Å	5.50 Å	12.14°
15	-6.91	-1.38	3.14 Å	3.15 Å	7.01°	-10.31	-2.58	3.87 Å	4.12 Å	-1.70°
16	1.06	6.59	4.27 Å	5.62 Å	32.09°	-5.80	1.94	4.87 Å	3.99 Å	34.50°
17	-6.27	-0.74	3.20 Å	3.08 Å	-24.02°	-9.41	-1.67	4.54 Å	5.75 Å	27.79°
18	-3.26	2.27	3.96 Å	4.15 Å	9.52°	-10.21	-2.47	5.63 Å	4.71 Å	-23.98°
19	0.13	5.66	3.09 Å	4.58 Å	-1.59°	-5.77	1.97	4.00 Å	4.83 Å	-0.91°
20	-0.78	4.75	4.48 Å	4.49 Å	-17.63°	-6.09	1.65	4.98 Å	3.97 Å	-10.86°
21	-3.00	2.53	3.66 Å	3.83 Å	-3.40°	-9.25	-1.51	4.53 Å	4.68 Å	-0.80°

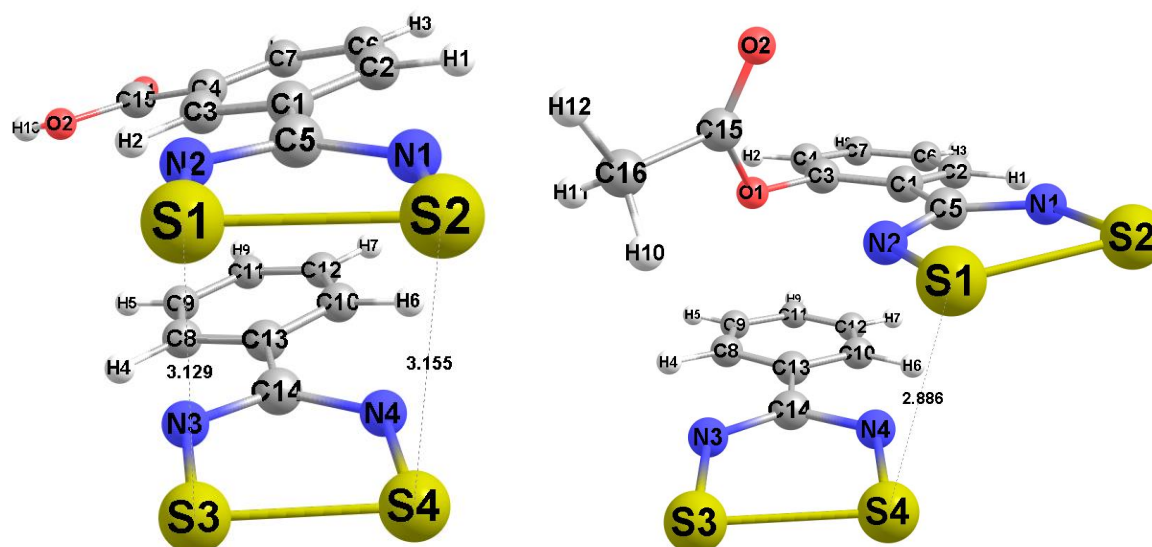


Figure 5.2: Optimised geometries of radical pairs 14 (left) and 18 (right) from calculations performed in the singlet state.

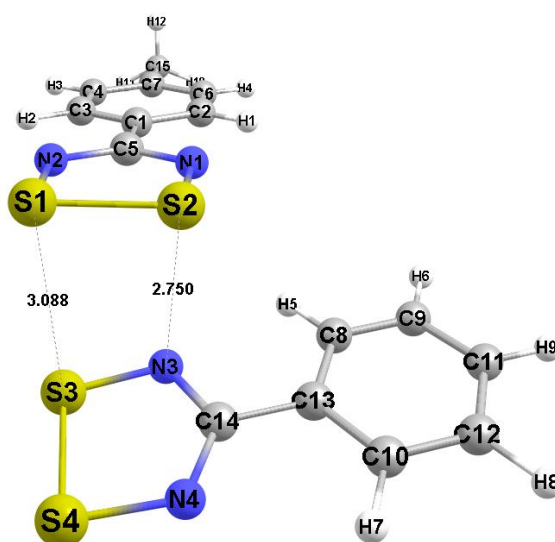


Figure 5.3: The optimised geometry of radical pair 19 from calculations performed in the singlet state.

The values in Table 5.2 show attractive energies for all radical pairs when calculations are performed in the triplet state. The radicals that exhibit stronger interactions when compared to radical **1** exhibit final structures with S...S and N...N contacts that are not within the sum of the van der Waals radii, but rather C...C contacts between the aryl rings as illustrated in Figure 5.4. Radical pairs **16**, **19** and **20** exhibit weaker interactions than radical pair **1** and exhibit final structures with S...N contacts similar to those observed for radicals **3** and **6** described in Chapter 4 (Figure 5.5).

The interaction energies obtained from the singlet and triplet states calculations shed light on how substituents at the *ortho*, *meta* and *para* positions of the aryl ring can affect the preferred

geometries of DTDA radicals. Firstly, placing an EDG placed at the *ortho* position will provide the necessary steric repulsion to yield large twist angles, which results in less interaction between the SOMOs, which compliments previous work that focussed on what affects the potential of DTDA radicals to dimerise^{2,4-6}. Secondly, an EDG placed at the *para* position minimises interactions between SOMOs, and promotes the formation of other strong intermolecular interactions, as illustrated by the *para* substituted structures in Figures 5.3 and 5.5.

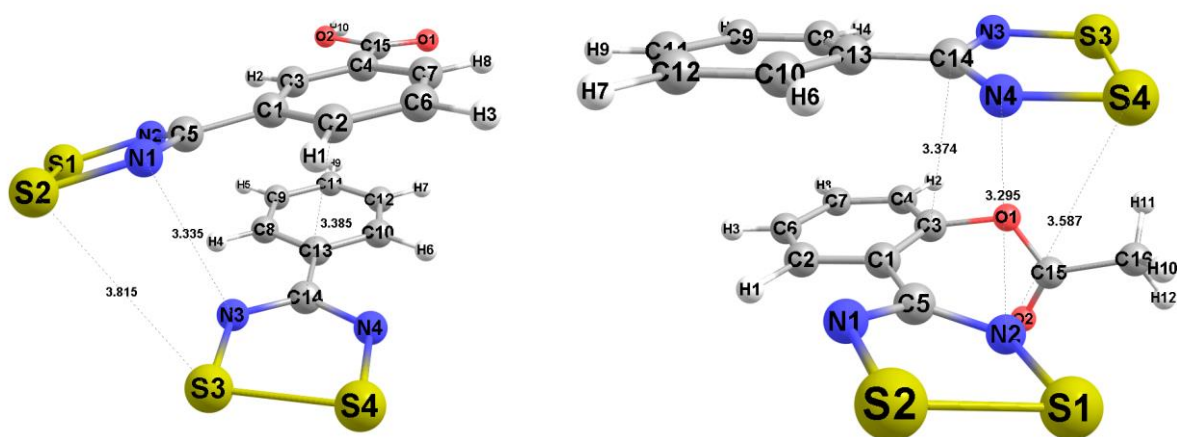


Figure 5.4: Optimised geometry of radical pairs 14 (left) and 17 (right) from calculations performed in the triplet state.

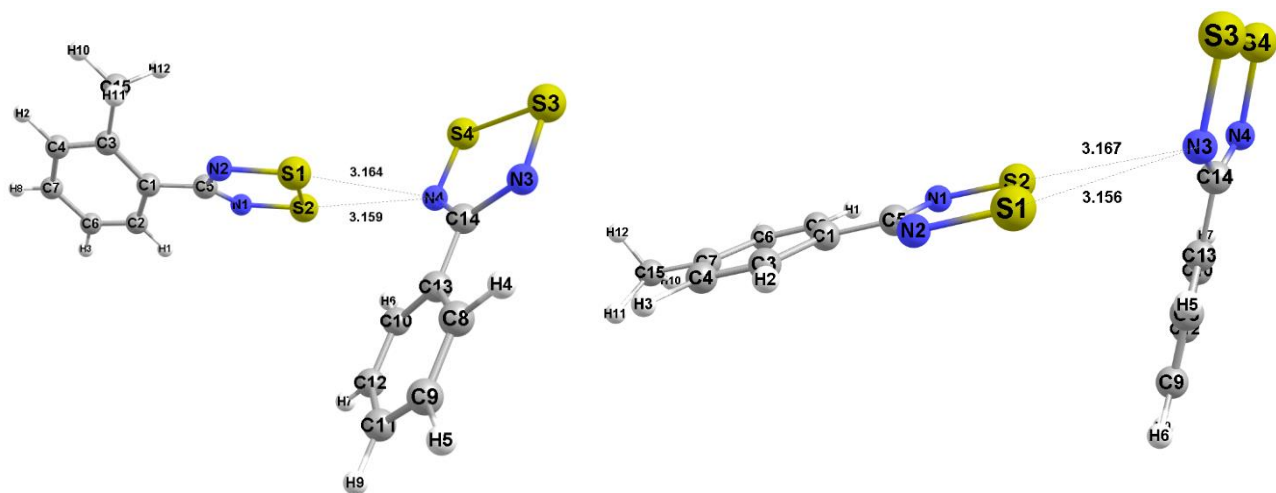


Figure 5.5: Optimised geometry of radical pairs 16 (left) and 19 (right) from calculations performed in the triplet state.

5.3. Topological analysis of in substituted radicals

The topological properties of the substituted radicals were investigated by use of the Atoms In Molecules (AIM) analysis⁷. This analysis aims to explain why certain substituents result in stronger or weaker interactions as reflected in the ΔE values given in Table 5.2. AIM plots with the electron density [$\rho(r)$], Laplacian of the electron density [$\nabla^2\rho$] and the total energy density [H] at the BCPs involved in intermolecular interactions are presented in Figure 5.6 over the next three pages.

Substituted radicals optimised in the singlet state

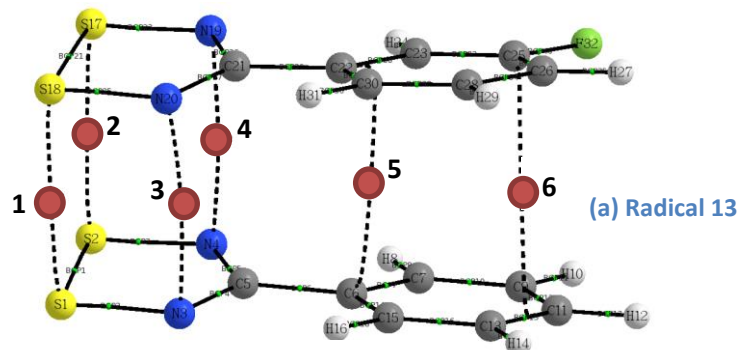


Table a with properties of BCPs (a.u.)

BCP #	Atoms	$\rho(r)$	$\nabla^2\rho$	H
1	S1 - S18	0.0214	0.0418	-0.0003
2	S2 - S17	0.0215	0.0420	-0.0003
3	N3-N20	0.0082	0.0196	0.0004
4	N4 - N19	0.0084	0.0200	0.0004
6	C11 - C25	0.0049	0.0127	0.0006
9	C6 - C22	0.0064	0.0180	0.0008

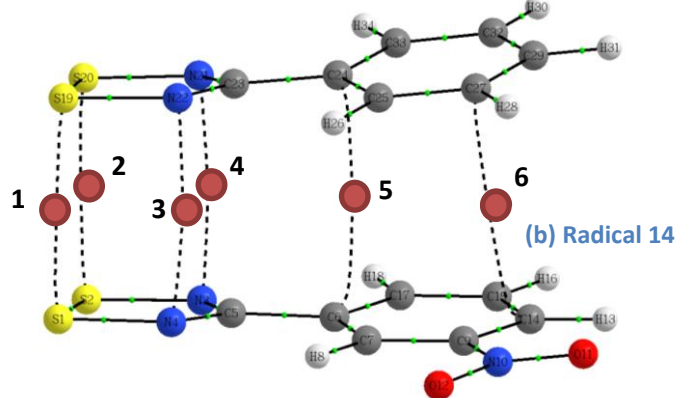


Table b with properties of BCPs (a.u.)

BCP #	Atoms	$\rho(r)$	$\nabla^2\rho$	H
1	S1 - S19	0.0215	0.0421	-0.0003
2	S2 - S20	0.0214	0.0418	-0.0002
3	N4 - N22	0.0085	0.0202	0.0004
4	N3 - N21	0.0084	0.0199	0.0004
5	C6 - C24	0.0061	0.0170	0.0008
6	C14 - C27	0.0049	0.0133	0.0006

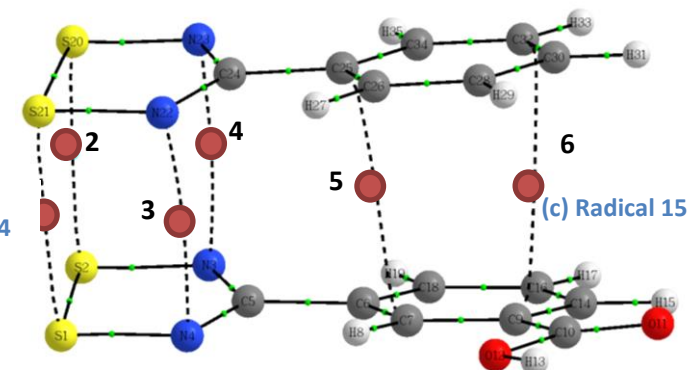


Table c with properties of BCPs (a.u.)

BCP #	Atoms	$\rho(r)$	$\nabla^2\rho$	H
1	S2 - S20	0.0220	0.0427	-0.0003
2	S1 - S21	0.0211	0.0413	-0.0002
3	N4 - N22	0.0085	0.0202	0.0004
4	N3 - N23	0.0080	0.0190	0.0004
5	C7 - C25	0.0066	0.0183	0.0008
6	C9 - C32	0.0052	0.0138	0.0006

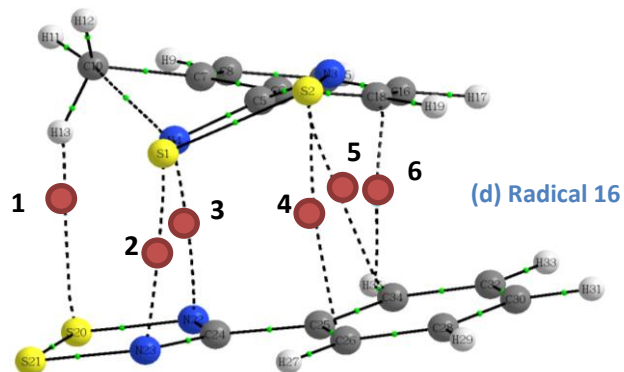


Table d with properties of BCPs (a.u.)

BCP #	Atoms	$\rho(r)$	$\nabla^2\rho$	H
1	H13 - S20	0.0065	0.0182	0.0008
2	S1 - N23	0.0207	0.0491	0.0009
3	N4 - N22	0.0159	0.0468	0.0017
4	S2 - C26	0.0057	0.0171	0.0007
5	N3 - C34	0.0059	0.0168	0.0008
6	C18 - H35	0.0056	0.0180	0.0009

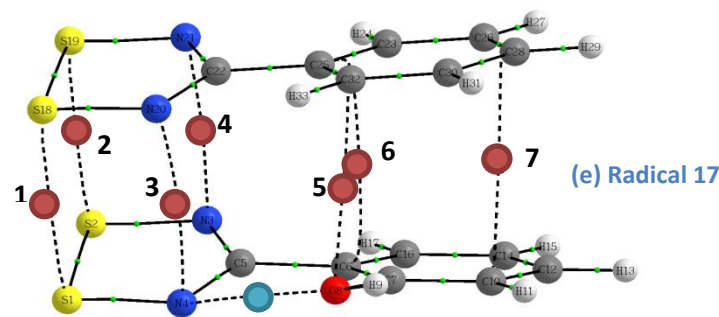


Table e with properties of BCPs (a.u.)

BCP #	Atoms	$\rho(r)$	$\nabla^2\rho$	H
1	S1 - S18	0.0195	0.0388	0.0000
2	S2 - S19	0.0238	0.0454	-0.0006
3	N4 - N20	0.0068	0.0164	0.0003
4	N3 - N21	0.0099	0.0236	0.0005
5	O8 - C32	0.0070	0.0213	0.0007
6	C6 - C25	0.0065	0.0179	0.0008
7	C10 - C28	0.0050	0.0129	0.0005

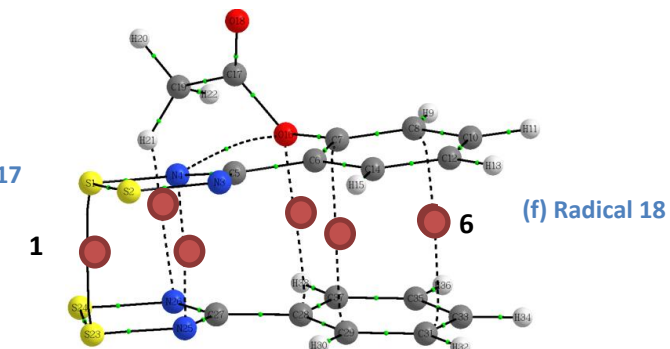


Table f with properties of BCPs (a.u.)

BCP #	Atoms	$\rho(r)$	$\nabla^2\rho$	H
1	S1 - S23	0.0326	0.0566	-0.0019
2	H21 - N26	0.0050	0.0152	0.0005
3	N4 - N25	0.0188	0.0511	0.0013
4	O16 - C28	0.0068	0.0242	0.0010
5	C7 - C29	0.0067	0.0188	0.0009
6	C8 - C31	0.0050	0.0131	0.0006

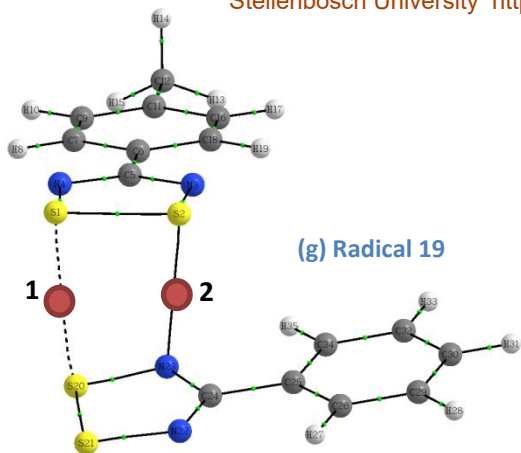


Table g with properties of BCPs (a.u.)

BCP #	Atoms	$\rho(r)$	$\nabla^2\rho$	H
1	S1 - S20	0.0231	0.0450	-0.0003
2	S2 - N23	0.0289	0.0644	0.0000

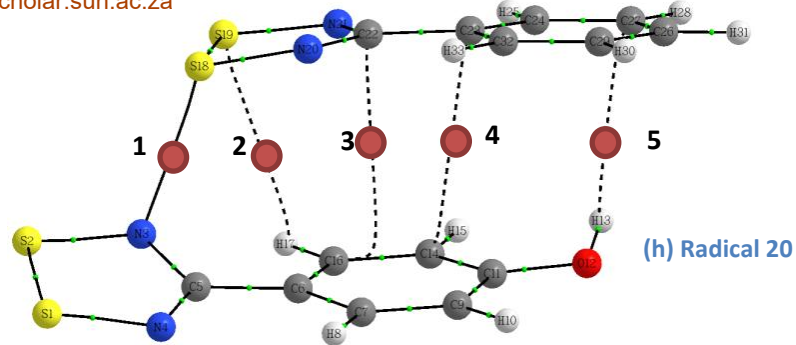


Table h with properties of BCPs (a.u.)

BCP #	Atoms	$\rho(r)$	$\nabla^2\rho$	H
1	N3 - S18	0.0398	0.0844	-0.0009
2	H17 - S19	0.0055	0.0185	0.0009
3	C16 - C22	0.0068	0.0216	0.0011
4	C14 - C23	0.0063	0.0184	0.0008
5	H13 - C27	0.0054	0.0157	0.0007

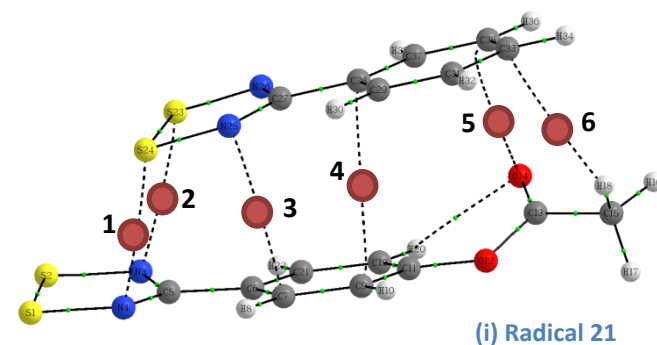


Table i with properties of BCPs (a.u.)

BCP #	Atoms	$\rho(r)$	$\nabla^2\rho$	H
1	N4 - S24	0.0220	0.0518	0.0009
2	N3 - S23	0.0171	0.0420	0.0011
3	C7 - N25	0.0067	0.0200	0.0008
4	C9 - C28	0.0043	0.0120	0.0006
5	O14 - C35	0.0058	0.0186	0.0009
6	H18 - C33	0.0041	0.0110	0.0005

Substituted radicals optimised in the triplet state

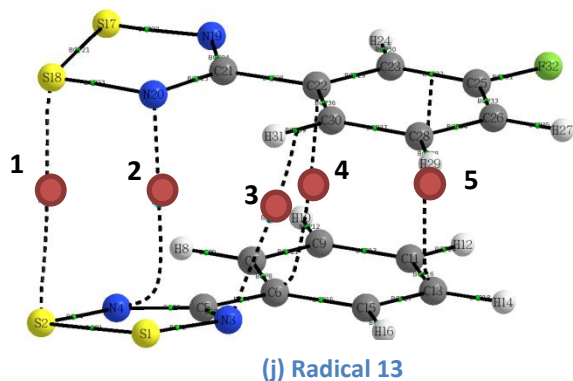


Table j with properties of BCPs (a.u.)

BCP #	Atoms	$\rho(r)$	$\nabla^2\rho$	H
1	S2 - S18	0.0054	0.0190	0.0010
2	N4 - N20	0.0066	0.0208	0.0007
3	N3 - C30	0.0063	0.0204	0.0009
4	C6 - C22	0.0066	0.0188	0.0008
5	C13 - C25	0.0057	0.0152	0.0007

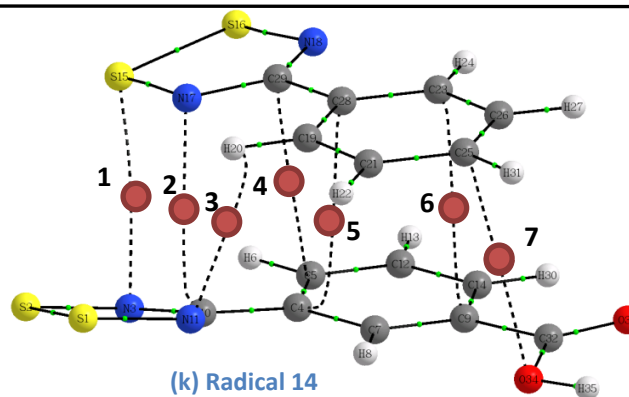


Table k with properties of BCPs (a.u.)

BCP #	Atoms	$\rho(r)$	$\nabla^2\rho$	H
1	N3 - S15	0.0065	0.0215	0.0008
2	C10 - N17	0.0077	0.0254	0.0010
3	N11 - H20	0.0087	0.0283	0.0012
4	C5 - C29	0.0064	0.0207	0.0010
5	C4 - C28	0.0067	0.0188	0.0009
6	C9 - C23	0.0055	0.0147	0.0006
7	C25 - O34	0.0033	0.0103	0.0005

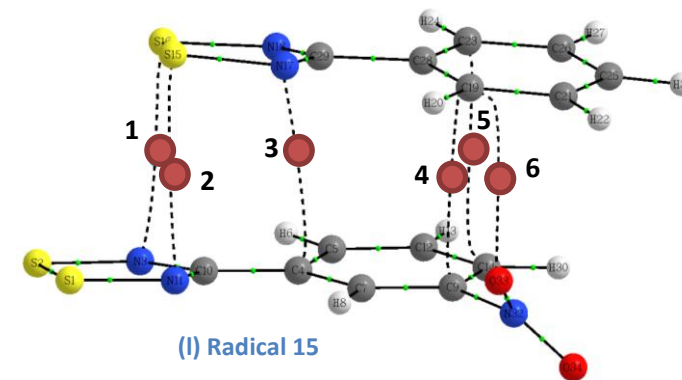


Table l with properties of BCPs (a.u.)

BCP #	Atoms	$\rho(r)$	$\nabla^2\rho$	H
1	N3 - S16	0.0087	0.0258	0.0009
2	N11 - S15	0.0072	0.0225	0.0008
3	C4 - N18	0.0065	0.0190	0.0008
4	C9 - C19	0.0072	0.0209	0.0010
5	C19 - O33	0.0094	0.0326	0.0012
6	C14 - C23	0.0065	0.0179	0.0008

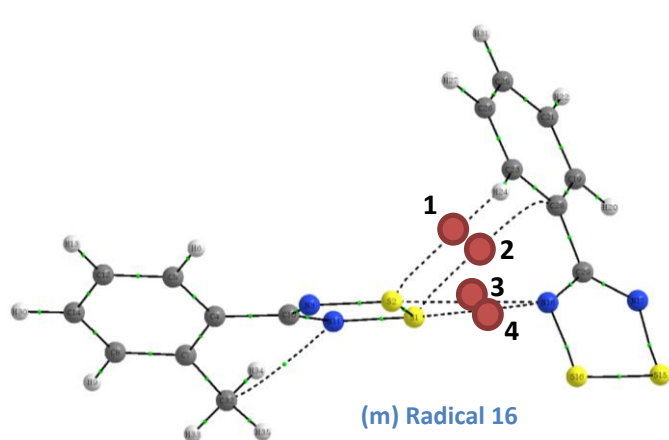


Table m with properties of BCPs (a.u.)

BCP #	Atoms	$\rho(r)$	$\nabla^2\rho$	H
1	S2 - H24	0.0057	0.0189	0.0010
2	S1 - C28	0.0058	0.0181	0.0009
3	S2 - N18	0.0114	0.0364	0.0010
4	S1 - N18	0.0108	0.0357	0.0011

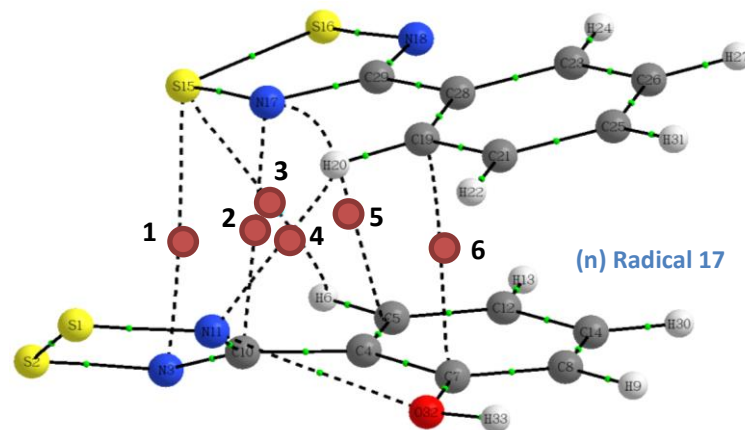


Table n with properties of BCPs (a.u.)

BCP #	Atoms	$\rho(r)$	$\nabla^2\rho$	H
1	N3 - S15	0.0051	0.0158	0.0006
2	C10 - N17	0.0076	0.0264	0.0011
3	H6 - S15	0.0047	0.0165	0.0008
4	N11 - H20	0.0081	0.0241	0.0009
5	C5 - N17	0.0073	0.0228	0.0010
6	C7 - C19	0.0068	0.0201	0.0010

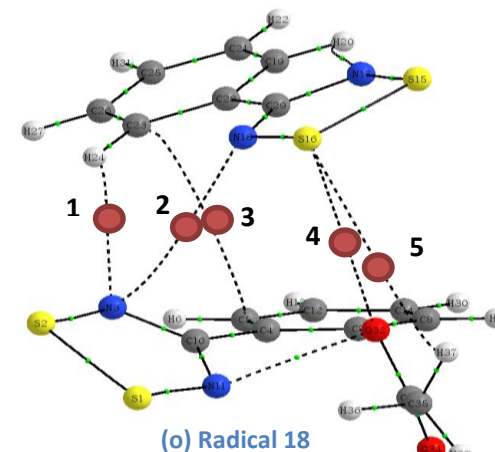


Table o with properties of BCPs (a.u.)

BCP #	Atoms	$\rho(r)$	$\nabla^2\rho$	H
1	N3 - H24	0.0085	0.0259	0.0010
2	N3 - N18	0.0022	0.0076	0.0004
3	C5 - C23	0.0025	0.0066	0.0003
4	S16 - O32	0.0016	0.0065	0.0005
5	S16 - H37	0.0008	0.0024	0.0002

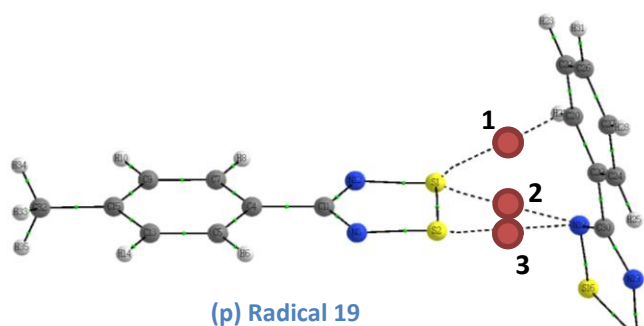


Table p with properties of BCPs (a.u.)

BCP #	Atoms	$\rho(r)$	$\nabla^2\rho$	H
1	S1 - H21	0.0043	0.0145	0.0008
2	S1 - N18	0.0103	0.0329	0.0010
3	S2 - N18	0.0094	0.0301	0.0009

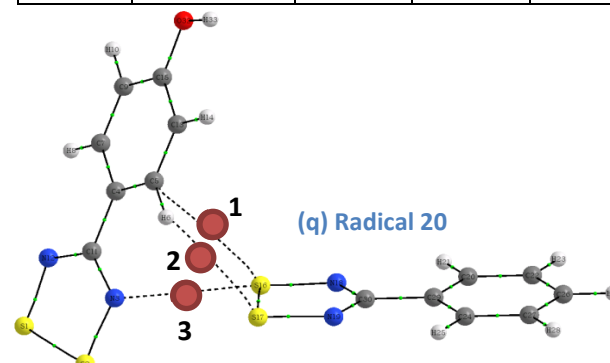


Table q with properties of BCPs (a.u.)

BCP #	Atoms	$\rho(r)$	$\nabla^2\rho$	H
1	C5 - S16	0.0054	0.0171	0.0009
2	H6 - S17	0.0058	0.0180	0.0009
3	N3 - S16	0.0083	0.0263	0.0008

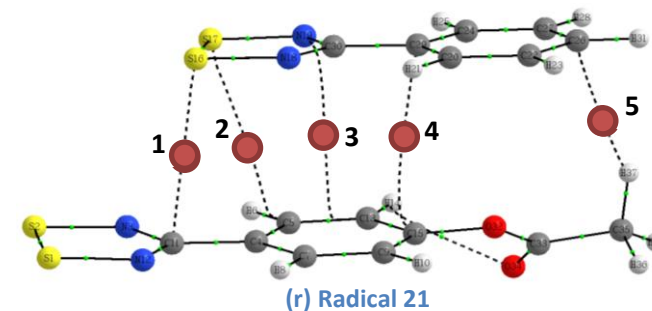


Table r with properties of BCPs (a.u.)

BCP #	Atoms	$\rho(r)$	$\nabla^2\rho$	H
1	C11 - S16	0.0076	0.0246	0.0012
2	C5 - S17	0.0053	0.0178	0.0010
3	C13 - N19	0.0059	0.0175	0.0008
4	C15 - C29	0.0052	0.0152	0.0007
5	C26 - H37	0.0062	0.0164	0.0007

Figure 5.6: AIM plots of radical pairs optimised in the singlet state radicals: 13 (a), 14 (b), 15 (c), 16 (d), 17 (e), 18 (f), 19 (g), 20 (h), 21 (i). AIM plots of radical pairs optimised in the triplet state: 13 (j), 14 (k), 15 (l), 16 (m), 17 (n), 18 (o), 19 (p), 20 (q), 21 (r).

5.3.1 Substituted radicals optimised in the singlet state

The S...S and S...N contacts of the radicals in Figures 5.6a - 5.6i exhibit BCPs with properties similar to those of H-bonds according to the classification of Nakanishi and coworkers (Table 5.3)⁸. These properties also compare well to the properties of the contacts discussed in Chapter 4.

Table 5.3: Classification of different intermolecular contacts with AIM parameters according to Nakanishi and coworkers⁸. Values given in atomic units.

Interaction	$\rho(r)$	$\nabla^2\rho$	H
Van der Waals	$0.00 < \rho(r) < 0.01$	$0.00 < \nabla^2\rho < 0.04$	$0.000 < H < 0.002$
H-bond	$0.01 < \rho(r) < 0.04$	$0.04 < \nabla^2\rho < 0.12$	$-0.004 < H < 0.002$
CT-MC	$0.01 < \rho(r) < 0.03$	$0.02 < \nabla^2\rho < 0.06$	$-0.001 < H < 0.002$
CT-TBP	$0.03 < \rho(r) < 0.12$	$-0.01 < \nabla^2\rho < 0.10$	$-0.060 < H < -0.003$
Weak covalent bonds	$0.05 < \rho(r) < 0.17$	$-0.10 < \nabla^2\rho < 0.07$	$-0.130 < H < -0.030$

Radical pairs **13**, **14**, **15**, **17** (Figure 5.6a – 5.6c, Figure 5.6e) were shown to have stronger interactions when compared to radical pair **1** (Table 5.2). The AIM plots of these radicals exhibit S...S, N...N and C...C contacts that result in a *cisoid* mode of association. The strong interaction between the SOMOs result in short distances between the radical molecules and allows for interaction between the phenyl rings. Radical pair **17** (Figure 5.6e) exhibits a small twist angle between the rings facilitated by the intramolecular interaction between the oxygen and the hydrogen atom, with the BCP indicated by the blue circle. This further suggests that the presence of substituents at the *ortho* position will only result in a large twist angle if there is sufficient steric repulsion.

Radical pairs **16** and **18** (Figures 5.6d and 5.6f) have bulky groups at the *ortho* position that do not allow for strong interactions between the SOMOs, resulting in optimised structures that are no longer *cisoid* dimers. The bulky *o*-CH₃ substituent on radical pair **16** results in less interaction between the SOMOs, which corresponds to the study performed by Beldjoudi and coworkers⁹. Their reported results showed that the steric repulsion of the *o*-CH₃ substituent results in a larger twist angle between the aryl and heterocyclic rings and induces longer S...S contacts. Radical pair **16** (Figure 5.6d) exhibits a mode of association similar to the *twisted* mode of association (See Figure 1.6, section 1.2), with S...N and N...N contacts with BCP properties characteristic of H-bonds. Radical pair **18** (Figure 5.6f) exhibits a short S...S contact (2.89 Å) with a BCP that has properties characteristic of a CT-TBP bond.

All of the *para* substituted radicals were found to exhibit weaker interactions when compared to radical pair **1** (Table 5.1), which is shown by the AIM plots in Figures 5.6g – 5.6i.

Radical pair **19** (Figure 5.6g) exhibits a *twisted* mode of association with the BCPs of the S...S and S...N contacts having properties characteristic of H-bonds. Radical pair **20** (Figure 5.6h) exhibits a mode of association with various contacts between the aryl rings, but only one S...N contact having a BCP that exhibits properties characteristic of a CT-TBP bond. This radical also exhibits a C...H contact, which suggests that a *para* substituent (*p*-OH in **20**) is capable of forming contacts with the aryl ring that result in final structures with decreased interaction between the SOMOs. Radical pair **21** (Figure 5.6i) also exhibits many interactions between the aryl rings in addition to the S...N contacts having BCPs with properties characteristic of H-bonds. This radical also exhibits interactions between the *para* substituents and the aryl ring that result in a final structure with less interaction between the SOMOs.

The origin of the weak interactions observed for radical pairs **18** - **21** in Tables 5.2 can be visualised by their HOMOs, which are illustrated in Figure 5.7. All of the HOMOs only exhibit partial overlap, which results in weak interaction energies for calculations performed in the singlet state, whereas radicals that exhibit a *cisoid* dimeric mode of association result in strong interactions due to the formation of pancake bonding (Figure 5.8).

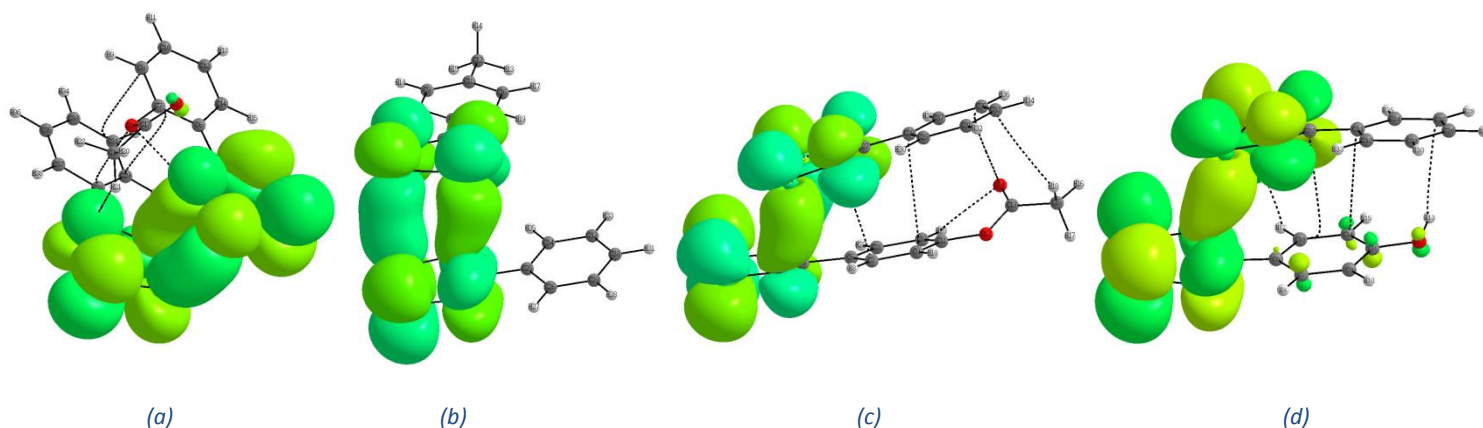


Figure 5.7: HOMOs of radical pairs **18** (a), **19** (b), **20** (c) and **21** (d).

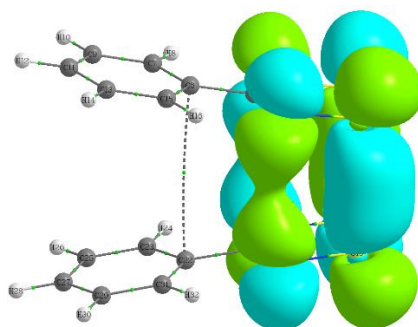


Figure 5.8: The HOMOs of radical pair **1** resulting in pancake bonding.

5.3.2 Substituted radicals optimised in the triplet state

Radical pairs **13** - **15** (Figures 5.6j – 5.6l) exhibit BCPs at the S···N, S···S and other contacts with properties similar to those of van der Waals interactions. The *meta* substituents do not result in large twist angles, but the interactions between aryl rings with each other and the *meta* substituents results in stronger interactions when compared to radical pair **1** (Table 5.2). Radical pair **16** (Figure 5.6m) exhibits a mode of association with S···N contacts similar to the monomeric mode of association observed in radicals **3** and **6** (Chapter 4). The BCPs at the S···N contacts exhibit properties characteristic of van der Waals interactions.

Radical pairs **17** and **18** (Figures 5.6n and 5.6o) do not exhibit any S···S contacts, but several interactions between the aryl rings and with the *ortho* substituents. These interactions result in stronger interactions when compared to radical pair **1**. Additionally, the radical pair **18** exhibits S···O and S···H contacts between the heterocyclic radical ring and the *meta* substituent, where these contacts could be structure-directing contacts that inhibit interaction between SOMOs and hence dimerisation. The BCPs for the S···N, S···O and S···H contacts in *ortho* substituted radicals exhibit properties characteristic of van der Waals interactions.

Radical pairs **19** and **20** (Figures 5.6p and 5.6q) exhibit S···N contacts similar to those observed in the monomeric modes of association in radical **3** and **6**. The BCPs for S···N contacts exhibit properties characteristic of van der Waals interactions.

Radical pair **21** (Figure 5.6r) does not exhibit any S···S or S···N contacts between the heterocyclic radical rings, which results from interactions between the aryl rings and interactions with the *para* substituent. The BCPs at the various contacts exhibit properties characteristic of van der Waals interactions.

In summary, the AIM plots of the substituted radicals that have been optimised in the singlet and triplet states show that *meta* substitution of DTDA radicals results in strong intermolecular interactions that favour a dimeric *cisoid* mode of association. Radical pair **17** also exhibits a dimeric *cisoid* mode of association, resulting from an N···O contact. Radical pairs **16**, **18** - **21** all exhibit geometries that result in decreased interaction between the SOMOs and also exhibit some similarities to the monomeric modes of association in the radicals **3** and **6**. The final structures and intermolecular interactions in these radicals would suggest that the presence of these *ortho* and *para* substituents could reduce the tendency of radicals to dimerise. The sections will focus on studying the intermolecular interactions in these substituted radicals to determine how they result in the different modes of association shown in Figure 5.6.

5.4. EDA analysis of substituted radicals

An EDA analysis was performed on radicals with different substituents at the *ortho*, *meta* and *para* positions that were optimised in the singlet and triplet states. These calculations were carried to investigate which contributions result in strong and weak binding energies (E_{Tot} , Table 5.4), resulting in different modes of association between radicals. Interaction energies (E_{Int}) were also calculated by performing counterpoise-corrected calculations and have been included in Table 5.4. The results in Chapter 4 showed that radicals that exhibit dimeric modes of association have larger ΔE_{orb} contributions due to interaction between the SOMOs, which also results in large repulsive ΔE_{Pauli} contributions from the repulsive interactions between occupied orbitals in close contact. We expect that the final structures of the substituted radicals that a dimeric modes of association will exhibit a similar trend in their contributions to the binding energy.

Radical pairs **13 – 15**, **17** exhibit the strongest binding energies in Table 5.4, which results from the strong ΔE_{disp} , ΔE_{el} and ΔE_{orb} contributions found for radicals that exhibit a dimeric *cisoid* mode of association. The strong ΔE_{disp} and ΔE_{el} contributions result from the various interactions between the heterocyclic and aryl rings of the radical pairs, while the strong ΔE_{orb} contribution results from the strong interaction between the SOMOs.

The weaker binding energies in radical pairs **16**, **18 – 21** exhibit fewer S...S contacts between SOMOs, resulting in smaller ΔE_{disp} contributions as the interactions between sulfur atoms have been shown to contain a large dispersion component¹⁰. Furthermore, these radicals also exhibit fewer S...N contacts, which in combination with fewer S...S contacts results in smaller ΔE_{orb} contributions as there is less interaction between the SOMOs. The presence of bulky groups at the *ortho* position can inhibit interaction between the SOMOs by creating a steric repulsion, which results in a twist of the aryl and heterocyclic ring. The weak binding energies observed for *para* substituted radicals are due to an energy penalty¹¹ required to rotate the *para* substituents and yield the modes of association observed for radical pairs **19 - 21**.

Table 5.4: EDA results for substituted radicals in the singlet and triplet states. Total energy = dispersion + electrostatic + orbital + Pauli. All values are in kcal/mol for binding energies calculated in the singlet state (a) and triplet state (b) energies.

		ΔE_{Tot}	ΔE_{disp}	ΔE_{el}	ΔE_{orb}	ΔE_{Pauli}	
Compound number	E_{Int}	Total	Dispersion	Electrostatic	Orbital	Pauli	
(a)	13	-6.09	-14.26	-18.72	-16.87	-17.79	39.11
	14	-7.24	-15.75	-20.44	-18.00	-18.13	40.83
	15	-6.91	-15.03	-19.08	-17.06	-17.96	39.08
	16	1.06	-4.19	-17.10	-13.91	-4.57	31.39
	17	-6.27	-14.33	-19.29	-17.24	-18.50	40.70
	18	-3.26	-10.45	-18.35	-22.15	-16.88	46.93
	19	0.13	-6.14	-9.65	-18.21	-15.99	37.70
	20	-0.78	-6.57	-16.21	-23.53	-14.16	47.32
	21	-3.00	-9.51	-19.62	-16.37	-9.48	35.96
	1	-2.45	-21.29	-7.17	-11.78	-26.98	24.64
(b)	13	-9.05	-14.14	-16.02	-7.33	-5.87	15.08
	14	-10.22	-15.28	-17.73	-7.99	-6.23	16.68
	15	-10.31	-15.50	-17.49	-8.11	-6.12	16.28
	16	-5.80	-9.94	-7.03	-6.05	-5.85	9.00
	17	-9.41	-14.23	-16.34	-7.46	-6.18	15.75
	18	-10.21	-15.46	-18.36	-8.40	-6.48	17.78
	19	-5.77	-9.85	-7.01	-5.91	-5.87	8.94
	20	-6.09	-10.30	-6.97	-6.82	-6.18	9.67
	21	-9.25	-14.14	-15.88	-6.82	-6.10	14.66
	1	-7.76	-14.68	-9.87	-5.68	-9.67	10.53

The substituted radicals in Table 5.4 all exhibit similar electrostatic ΔE_{el} and ΔE_{orb} contributions to the binding energy if calculations are performed in the triplet state, while some differences are observed for the ΔE_{disp} and ΔE_{Pauli} contributions. Larger ΔE_{disp} and ΔE_{Pauli} contributions are observed for radical pairs **13** – **15**, **17**, **18** and **21** as they exhibit a combination of S...S, N...N, S...N and various other contacts between the radicals. Radical pairs **16**, **19** and **20** exhibit smaller ΔE_{disp} and ΔE_{Pauli} contributions, which results from the orthogonal-like mode of association observed for these radicals that are similar to those observed for radicals **3** and **6**. These small contributions result from these modes of association allowing for fewer interactions between the heterocyclic and aryl rings.

In summary, the EDA analysis of radical pairs optimised in the singlet and triplet states showed that the binding energies of substituted radicals are strongly influenced by S...S, N...N and S...N contacts between the heterocyclic radical rings. It was found that all radicals with EWGs placed at the *meta* position exhibit strong binding energies for calculations performed in both

the singlet and triplet states, resulting from the large ΔE_{orb} contributions from strong interactions between the SOMOs.

Calculations performed in the singlet state showed that the *ortho* and *para* substituted radical pairs exhibit weaker binding energies due to decreased interaction between the SOMOs. Radical pairs **16**, **18** and **19 – 20** were found to exhibit the weakest binding energies when compared to the other substituted radical pairs, resulting from modes of association that allow for fewer interaction between the SOMOs and aryl rings. This results in smaller ΔE_{disp} , ΔE_{el} and ΔE_{orb} contributions to the binding energy and suggests that these radicals have a reduced tendency to dimerise.

Calculations performed in the triplet state showed that radical pairs **16**, **19** and **20** exhibit slightly weaker binding energies when compared to those obtained for other substituted radicals, resulting from orthogonal-like monomeric modes of association similar to that of the radicals **3** and **6** and suggest that these radicals have a reduced tendency to dimerise. These calculations show that small changes to substituents can determine whether radicals prefer a monomeric or dimeric mode of association, which corresponds to a study by Lee and coworkers, where it was found that both EDGs and EWGs could increase or decrease the overall energy of a system due to a subtle interplay between electronic terms contributing to the total interaction energy¹².

5.5 Halogen substitution on the phenyl ring

The calculations in this chapter confirmed two major factors that reduce the tendency of DTDA radicals to dimerise. Firstly, placing substituents at the *ortho* position can result in a large twist angle, which inhibits interaction between the SOMOs. Secondly, the nature of the *para* substituent allows for the formation of other strong intermolecular interactions that could inhibit dimerisation. The *para* group should consist of electronegative groups that are capable of interacting with the area of positive charge between the sulfur atoms or form contacts similar to those observed in radicals **3** and **6**.

Both of these factors contribute to the packing arrangement of these radicals in the solid state, which should allow for communication between the unpaired electrons, resulting in magnetic ordering¹³. Predicting the solid-state packing arrangement of radicals is a non-trivial task, but calculations in the gas phase could provide some information about which geometries and contacts will be favourable in different radicals.

Small changes to known monomeric radicals could result in radicals with similar magnetic properties and even though some of radicals investigated in this work are not synthetically accessible, the results obtained could provide some information regarding how the increased steric effect and potential to form halogen bonds will change once different halogen groups are introduced. In order to test this idea, the fluorine groups on crystal structures of three known monomeric radicals **2**, **3** and **4** were replaced with chlorine (-Cl), bromine (-Br) and iodine (-I) atoms as illustrated in Figure 5.9. The chemical name and corresponding compound number of each substituted radical pair is given in Table 5.5.

Table 5.5: The chemical name and code of each substituted radical.

Chemical Name	Compound number
4-(4'-cyano-2',3',5',6'-tetrafluorophenyl)-1,2,3,5-dithiadiazolyl	2
4-(4'-cyano-2',3',5',6'-tetrachlorophenyl)-1,2,3,5-dithiadiazolyl	22
4-(4'-cyano-2',3',5',6'-tetrabromophenyl)-1,2,3,5-dithiadiazolyl	23
4-(4'-cyano-2',3',5',6'-tetraiodophenyl)-1,2,3,5-dithiadiazolyl	24
4-(4'-bromo-2',3',5',6'-tetrafluorophenyl)-1,2,3,5-dithiadiazolyl	3
4-(4'-bromo-2',3',5',6'-tetrachlorophenyl)-1,2,3,5-dithiadiazolyl	25
4-(4'-bromo-2',3',5',6'-tetrabromophenyl)-1,2,3,5-dithiadiazolyl	26
4-(4'-bromo-2',3',5',6'-tetraiodophenyl)-1,2,3,5-dithiadiazolyl	27
4-(4'-nitro-2',3',5',6'-tetrafluorophenyl)-1,2,3,5-dithiadiazolyl	4
4-(4'-nitro-2',3',5',6'-tetrachlorophenyl)-1,2,3,5-dithiadiazolyl	28
4-(4'-nitro-2',3',5',6'-tetrabromophenyl)-1,2,3,5-dithiadiazolyl	29
4-(4'-nitro-2',3',5',6'-tetraiodophenyl)-1,2,3,5-dithiadiazolyl	30

Geometry optimisation calculations were then performed on the substituted radicals with the starting geometry of radicals **2**, **3** and **4** in both the singlet and triplet states at the UB3LYP-D3/6-311++G(d,p) level of theory. An effective core potential (ECP) was employed for all radicals containing iodine atoms. An ECP reduces the cost of calculations on heavy atoms by replacing the core electrons with a potential, which is constructed by parameterising a pseudopotential against calculations performed at a high level of theory all-electron results. This study employed the Stuttgart ECP¹⁴. Frequency calculations were performed to determine if the minimum energy conformation has been obtained.

Single point counterpoise-corrected energies were then calculated at UB3LYP-D3/6-311++G(d,p) level of theory in both the singlet and the triplet state, which are summarised in Table 5.6.

X = Br, NC, NO₂

Y = F, Br, Cl, I

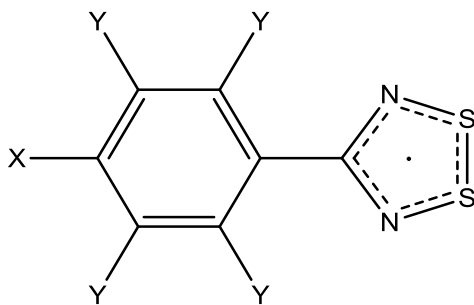


Figure 5.9: The radicals investigated in this study with different groups at the X and Y position on the phenyl ring.

Table 5.6: The counterpoise-corrected interaction energies (kcal/mol) performed at the UB3LYP-D3/6-311++G(d,p) level of theory for radical pairs 22 - 33 optimised in the singlet and triplet states.

Compound number	Singlet	Triplet
2	18.74	-5.14
22	17.64	-5.35
23	17.47	-5.49
24	16.70	-5.66
3	0.85	-8.81
25	0.65	-7.71
26	0.42	-7.50
27	-2.66	-5.08
4	19.16	-4.17
28	19.01	-4.19
29	18.74	-4.36
30	18.08	-4.72

5.5.1 Radical pairs 2, 22 - 24

The radicals containing the CN X-group exhibit repulsive interactions for all calculations performed in the singlet state (Table 5.6). The optimised geometries exhibit a linear mode of association for calculations that have been performed in the singlet and triplet states. This corresponds to results given in Chapter 4, where it was shown that the linear mode of association is very stable and geometry optimisations performed in the singlet and triplet states yield very similar final structures. The energies obtained with singlet state calculations becomes slightly less repulsive if larger halogen atoms are placed at the X positions, while triplet state calculation yield slightly stronger attractive energies occur for radicals with heavier halogen atoms. The stronger energies observed in radicals with larger halogen atoms result

from shorter CN \cdots S contacts as shown in Figure 5.10. The stronger interactions possibly result from larger twist angles, resulting from more steric repulsion between the larger halogen atoms and the nitrogen atom on the heterocyclic radical ring.

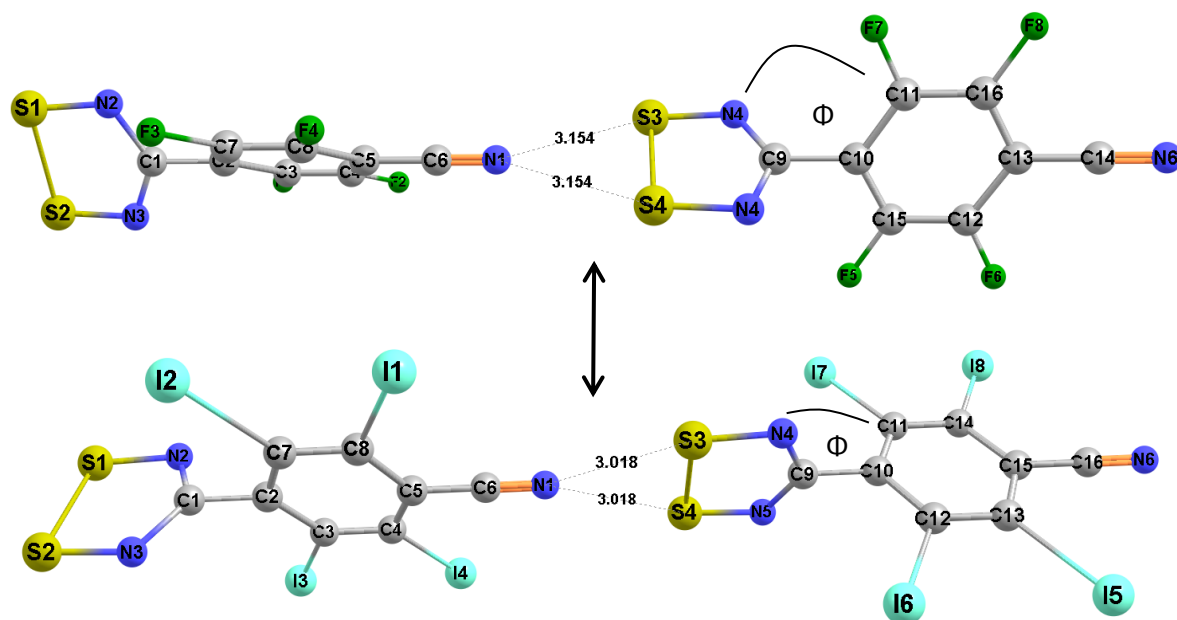


Figure 5.10: The optimised geometry of radical pairs 2 (top) and 24 (bottom) in the triplet state. Twist angles (Φ) between atoms N4-C9-C10-C11 = 58.86° (top) and -89.82° (bottom).

5.5.2 Radical pairs 3, 25 – 27

The interaction energies calculated in the singlet state range from weakly repulsive to weakly attractive as the fluorine atoms are replaced by heavier halogen atoms in radical pairs 3, 25 – 27. The final geometry of the radical with iodine atoms at the Y positions exhibits S \cdots S contacts and overlap between the HOMOs, as illustrated in Figure 5.11. Furthermore, I \cdots I and I \cdots Br halogen bonds are observed in Figure 5.11, which provide additional stabilisation to the final structure that exhibits an attractive energy. The short S \cdots S contacts and interaction between the HOMOs results in a transoid mode of association (Figure 5.11), resulting in an attractive energy of -2.66 kcal/mol.

The radicals optimised in the triplet state exhibit attractive energies, which decreases in strength if larger halogen atoms are placed at Y. The optimised geometries show that the final structures of radical pairs 3, 25 – 27 do not exhibit a linear mode of association as observed for radical pairs with nitro (-NO₂) and cyano (-CN) groups placed at position X, but rather the orthogonal-like mode of association when fluorine atoms are at position Y that exhibits S \cdots N

contacts within the sum of van der Waals radii (Figure 5.12). The larger halogen atoms no longer allow for this orthogonal-like mode of association, but rather the mode of association shown in Figure 5.12 that no longer contains any $S\cdots N$ or $S\cdots S$ contacts within the sum of the van der Waals radii, but rather an $I\cdots S$ contact within the sum of van der Waals radii. Fewer $S\cdots N$ contacts between the radical molecules as larger halogen atoms are introduced to the system could explain the weaker interaction energies observed in Table 5.6 for calculations performed in the triplet state.

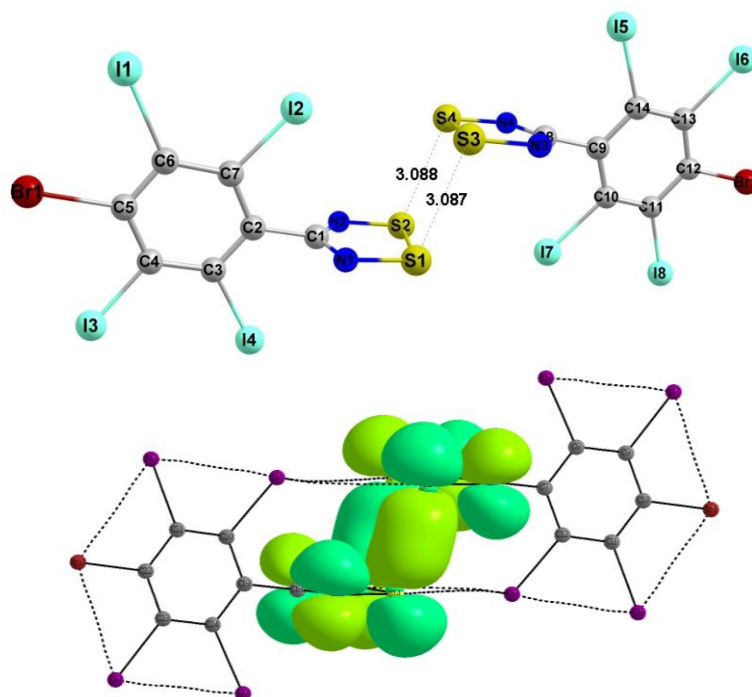


Figure 5.11: The $S\cdots S$ contacts (top) and the HOMOs overlap (bottom) for radical pair 27.

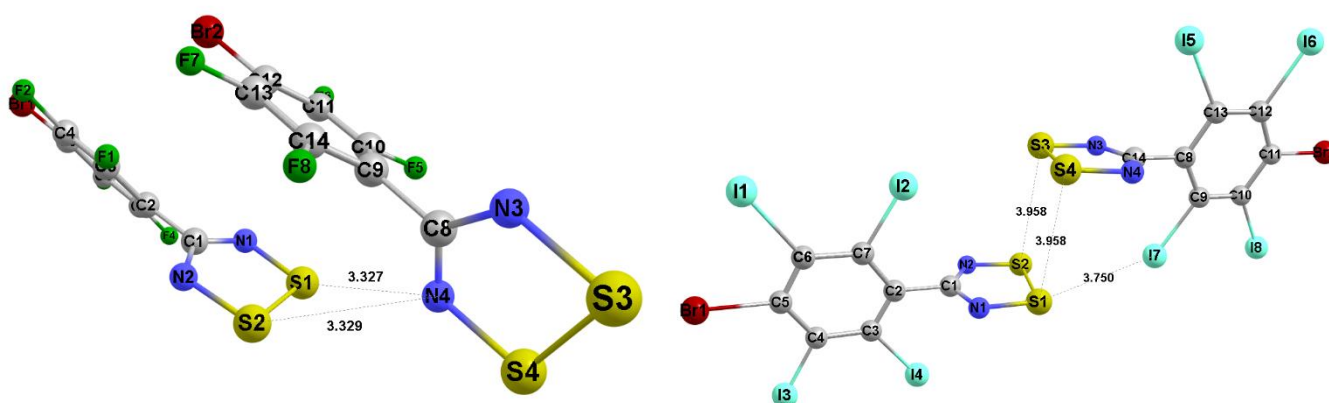


Figure 5.12: The $S\cdots N$ contacts in the radical pair 3 (left) and the $S\cdots S$ and $S\cdots I$ contacts in radical pair 27 (right).

5.5.3 Radical pairs 4, 28 - 30

The radicals containing an NO₂ X-group exhibit repulsive interactions for all calculations performed in the singlet state (Table 5.6). The energies becomes slightly less repulsive if larger halogen atoms are placed at the X positions, which can be explained by looking at the optimised geometries in Figure 5.12. An increase in size of the halogen group will result in changes to twist angle and the overall mode of association as shown Figure 5.13. The formation of the I··I contact in radical **30** results in a final structure that no longer exhibit a linear mode of association (Figure 5.13). Attractive energies are observed for all calculations that have been performed in the triplet state, with a small increase in energy if larger halogen atoms are placed at Y, resulting from an additional I··I contact. All of the optimised geometries exhibit a linear mode of association, where the increase in energy results from larger dispersion components present for halogen groups with more electrons.

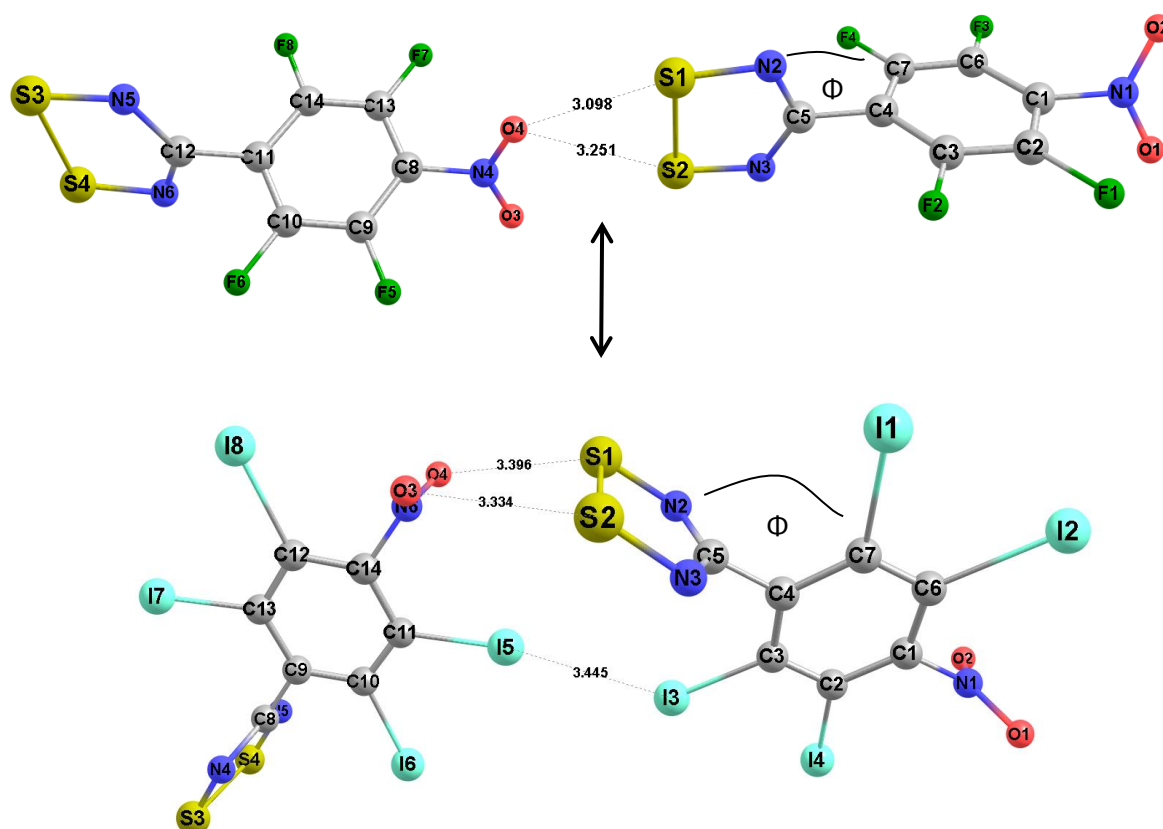


Figure 5.13: The optimised geometry of radical pairs 4 (top) and 30 (bottom) in the triplet state. The twist angle (Φ) between atoms N2-C5-C4-C3 = -87.94° (top) and 86.68° (bottom).

In summary, the calculations have shown that replacing the fluorine atoms with heavier halogen atoms will result in stronger attractive energies for radicals with NO₂ and CN groups at position X. Radicals with heavier halogen atoms could therefore be ideal candidates for attempting to synthesise novel radicals that exhibit a monomeric mode of association.

Conclusions

Calculations on substituted radicals showed that the *meta*-substituted radicals will exhibit strong interaction and binding energies that result in a dimeric *cisoid* mode of association. The *ortho*- and *para*-substituted radicals were found to exhibit fewer S···S and S···N contacts between the heterocyclic radicals rings. Radical pairs **16**, **18**, **19** – **21** were found to exhibit the weakest binding energies for calculations performed in the singlet state, resulting from smaller ΔE_{disp} , ΔE_{el} and ΔE_{orb} contributions to the binding energy as these radicals do not favour interaction between the SOMOs.

Radicals pairs **16**, **19** and **20** were found to exhibit weak binding energies for calculations performed in the triplet state, as they exhibit an orthogonal-like monomeric modes of association similar to that of radicals **3** and **6**, which suggests that these radicals have a reduced tendency to dimerise.

Replacing the fluorine atoms with heavier halogen atoms resulted in stronger interaction energies for radicals with NO₂ and CN groups at the *para* position. These results suggest that replacing the fluorine atoms of radicals **2** and **4** with heavier halogens could yield novel DTDA radicals that exhibit a monomeric mode of association.

The results obtained in this chapter have shown that small changes to the substituents on the aryl ring can significantly affect the preferred mode of association in DTDA radicals. The results obtained from a series of calculations performed on radicals that have not yet been synthesised are reported in the next chapter. These results were used to predict which mode of association will be preferred in the solid state.

References

- (1) Campbell, J.; Klapstein, D.; Bernath, P. F.; Davis, W. M.; Oakley, R. T.; Goddard, J. D. *Inorganic Chemistry* **1996**, *35*, 4264.
- (2) Haynes, D. A. *CrystEngComm* **2011**, *13*, 4793.
- (3) Bhavaraju, M.; Gwaltney, S. R. *International Journal of Quantum Chemistry* **2013**, *113*, 1171.
- (4) Constantinides, C. P.; Eisler, D. J.; Alberola, A.; Carter, E.; Murphy, D. M.; Rawson, J. M.
- (5) Melen, R. L.; Less, R. J.; Pask, C. M.; Rawson, J. M. *Inorganic Chemistry* **2016**, *55*, 11747.
- (6) Domagala, S.; Haynes, D. A. *CrystEngComm* **2016**, *18*, 7116.
- (7) Bader, R. F. W. *Accounts of Chemical Research* **1985**, *18*, 9.
- (8) Nakanishi, W.; Hayashi, S.; Narahara, K. *The Journal of Physical Chemistry A* **2008**, *112*, 13593.
- (9) Beldjoudi, Y.; Haynes, D. A.; Hayward, J. J.; Manning, W. J.; Pratt, D. R.; Rawson, J. M. *CrystEngComm* **2013**, *15*, 1107.
- (10) Tsuzuki, S.; Orita, H.; Sato, N. *The Journal of Chemical Physics* **2016**, *145*, 174503.
- (11) Rakitin, A. R.; Pack, G. R. *Langmuir* **2004**, *21*, 837.
- (12) Lee, E. C.; Kim, D.; Jurečka, P.; Tarakeshwar, P.; Hobza, P.; Kim, K. S. *The Journal of Physical Chemistry A* **2007**, *111*, 3446.
- (13) Luzon, J.; Campo, J.; Palacio, F.; McIntyre, G. J.; Rawson, J. M.; Less, R. J.; Pask, C. M.; Alberola, A.; Farley, R. D.; Murphy, D. M.; Goeta, A. E. *Physical Review B* **2010**, *81*, 144429.
- (14) Igel-Mann, G.; Stoll, H.; Preuss, H. *Molecular Physics* **1988**, *65*, 1321.

6 Predicting the mode of association in 1,2,3,5-dithiadiazolyl radicals

Introduction

The results from the previous chapters showed that the tendency of DTDA radicals to dimerise or remain monomeric in the solid state is largely dependent on their molecular structure and the formation of various intermolecular interactions. The results in Chapter 3 showed that radicals have the potential to exist in different polymorphs or co-crystals that exhibit different monomeric and dimeric modes of association. The results in Chapter 4 showed that some monomeric radicals would prefer to exhibit a linear mode of association for geometry optimisation calculations performed in both the singlet and triplet states, which indicates that this mode is energetically stable. Energy calculations showed that optimising dimeric radicals will yield attractive energies if the geometry optimisation and single-point calculations are performed in the same state, whereas monomeric radicals yield attractive energies for single-point calculations performed in the triplet state, irrespective of whether the geometry optimisation was performed in the singlet or triplet state. A series of calculations were performed on substituted radical pairs in Chapter 5, for which the final geometries and interaction energies showed that *ortho* and *para* substituents can reduce the tendency of radicals to dimerise.

The results obtained from all these theoretical will be utilised to predict the preferred mode of association (or configuration) of radicals that have not yet been synthesised (unknown radicals). A series of gas-phase calculations will be carried out on several DTDA radicals, and the results compared to what was observed for known DTDA radicals. Gas-phase calculations do not consider any additional effects present in the solid-state architecture and are limited to intermolecular interactions between two radical molecules. The work described in Chapters 4 and 5 has shown that gas phase calculations can be used to predict the preferred mode of association a particular DTDA radical will exhibit in the solid state. To extend this work, the results from gas phase calculations will be used to predict the preferred configuration of unknown radicals.

The initial aim was to determine what the preferred modes of association would be between unknown radicals by performing a series of geometry calculations on each unknown radical that has been arranged in eight different monomeric and dimeric modes of association. The geometries used as a basis for these calculations were determined by performing a series of Potential Energy Surface (PES) scans. A 2D plot of each PES scan was used to identify where the strongest intermolecular interactions occur in each mode of association, and these geometries were used for further optimisation calculations. The ability of the calculations to predict the mode of association could be verified by synthesising the unknown radicals and, if possible, obtaining crystals that can be characterised using single crystal X-ray diffraction. The

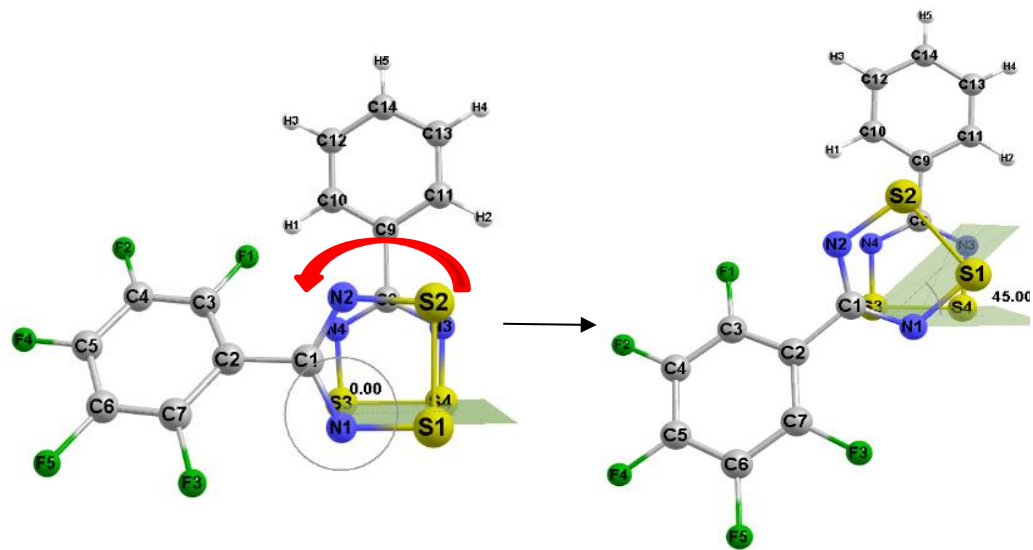
mode of association of the radicals in the crystal structures was then compared to calculated results to determine if the prediction proved successful.

6.1 PES scans on different modes of association

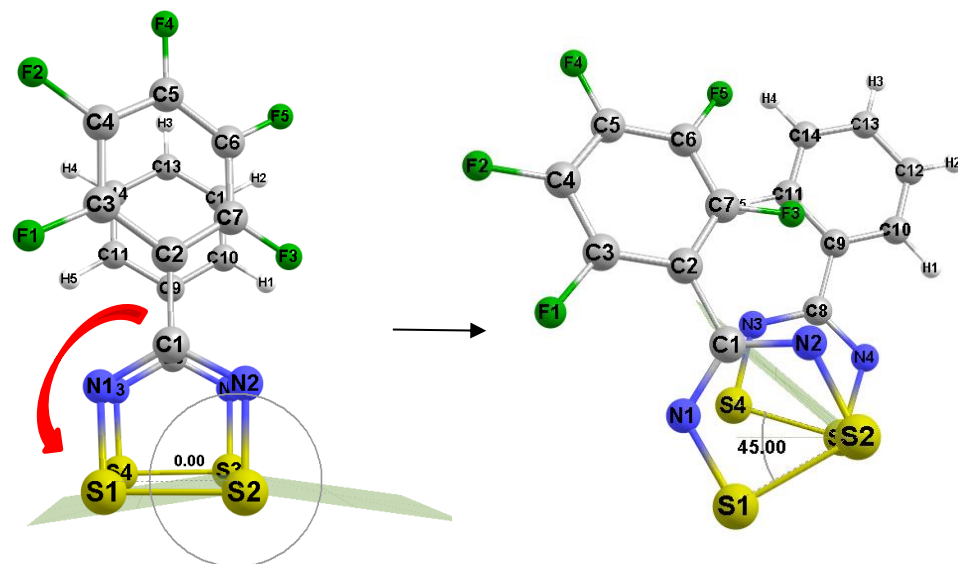
It was noted in previous chapters that radicals prefer to dimerise in five different modes of association^{1,2}, whereas monomeric radicals prefer a linear mode of association, as well as the unique modes observed for radicals **2**, **3** and **4**. The intermolecular interactions present in these monomeric and dimeric modes of association were investigated by performing a series of PES scans on a dimeric and monomeric radical. For dimeric radicals, the co-crystal **11** was arranged in the five dimeric modes of association. Radical **11** was selected to study how changes to the system will affect the fluorinated and non-fluorinated aryl rings. PES scans were used to determine how changes will affect the intermolecular interaction energy.

Constrained geometry optimisation calculations were performed at the UB3LYP-D3/6-311++G(d,p) level of theory by only optimising the distances, angles and torsion angles involved in the S...S and S...N contacts of dimeric radicals that were arranged in the *twisted*, *cisoid*, *transoid*, *trans-cofacial* and *orthogonal* modes of association. Please note that constraints were applied to ensure that the modes of association are maintained; if no restraints were specified, all geometry optimisation calculation converge to the same final structure. This was followed by PES scans on the final structures of these optimisation calculations. For monomeric radicals, PES scans could be performed on the optimised geometries of radical **2**, **3** and **4** reported in Chapter 4 (section 4.2). The torsion angles varied for each radical were selected as they strongly influence the strength of the intermolecular interactions in each mode of association. Changes to the torsion angle for each mode of association are illustrated in Figures 6.1a – 6.1g. The X1 and X2 atoms shown in Figures 6.1f and 6.1e are dummy atoms, which do not contain any electrons, but merely serve as placeholder atoms that simplify the process of varying a torsion angle.

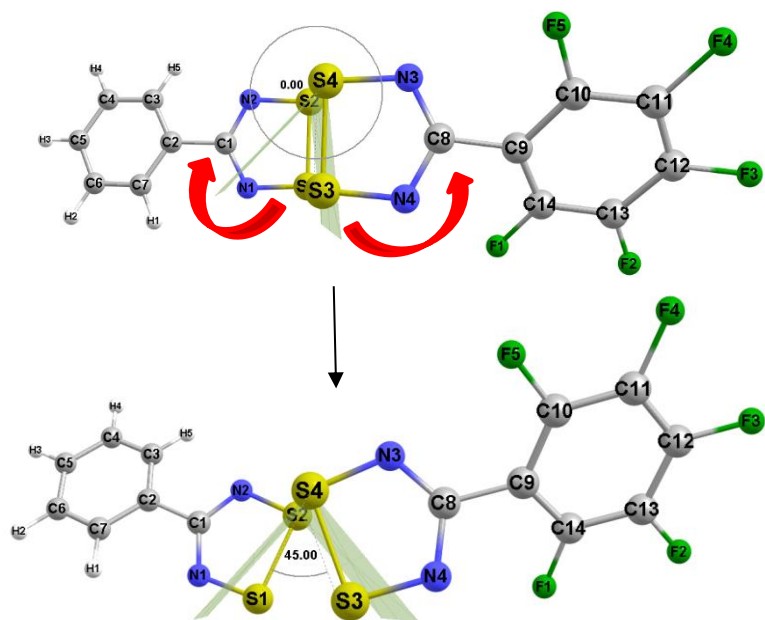
A 2D plot could be generated for each PES scan by varying the torsion angle between -180° and 180° and performing counterpoise-corrected single point calculations at incremental steps of 10° at the UB3LYPD3/6-311++G(d,p) level of theory. All calculations for dimeric radicals were performed in the singlet state, while the triplet state was used for all calculations performed on the monomeric radicals. The 2D plots for each mode of association are shown in Figures 6.2a – 6.2g, where each was truncated to show at which torsion angle the strongest interactions are identified. These geometries are illustrated in Figure 6.3a – 6.3h. Tables (a – h) are included in Figures 6.3, which include the torsion angle and interatomic distances involved in contacts within each radical pair. These geometries were used as a basis for further calculations described in the next section.



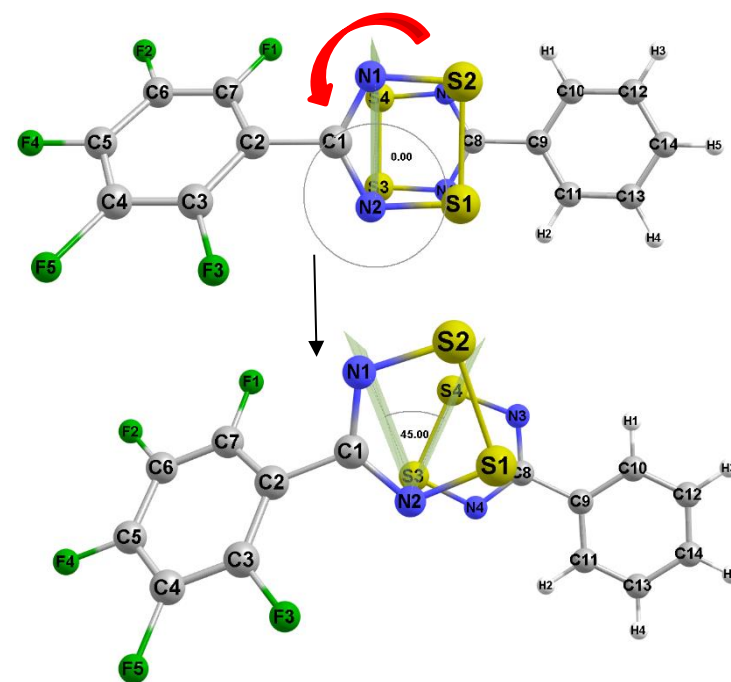
twisted (a)



cisoid (b)



transoid (c)



trans-cofacial (d)

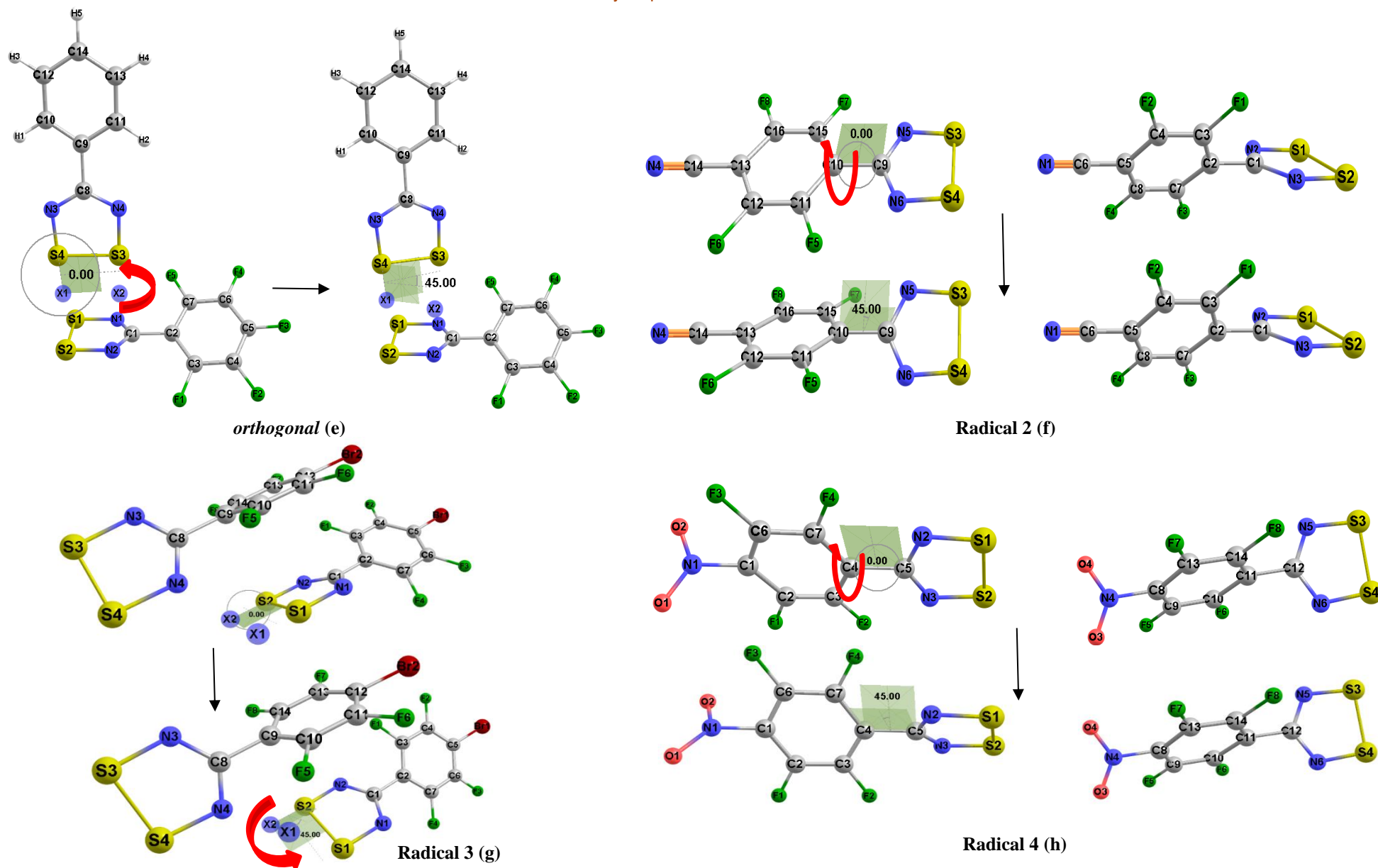


Figure 6.1: The different modes of associations for both dimeric and monomeric. The torsion angles ($^{\circ}$) and radicals are shown for each mode of association: *twisted (a)*, *cisoid (b)*, *transoid (c)*, *trans-cofacial (d)*, *orthogonal (e)*, Radical 2 (f), Radical 3 (g) and Radical 4 (h). X1 and X2 are dummy atoms used as placeholder atoms to easily define torsion angles.

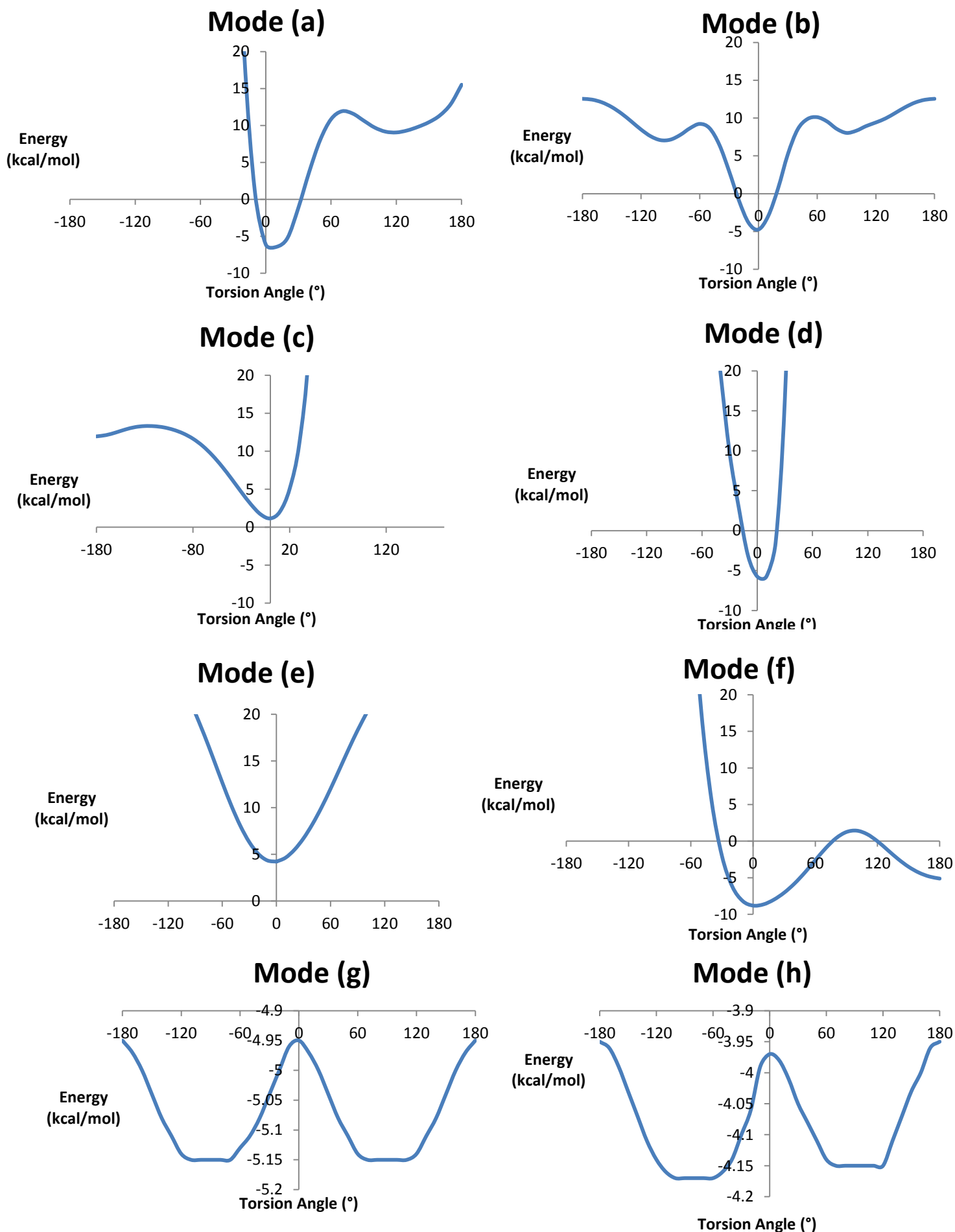


Figure 6.2: PES plots from radicals in *twisted* (a), *cisoid* (b), *transoid* (c), *trans-cofacial* (d), *orthogonal* (e), Radical 2 (f), Radical 3 (g) and Radical 4 (h) modes of association.

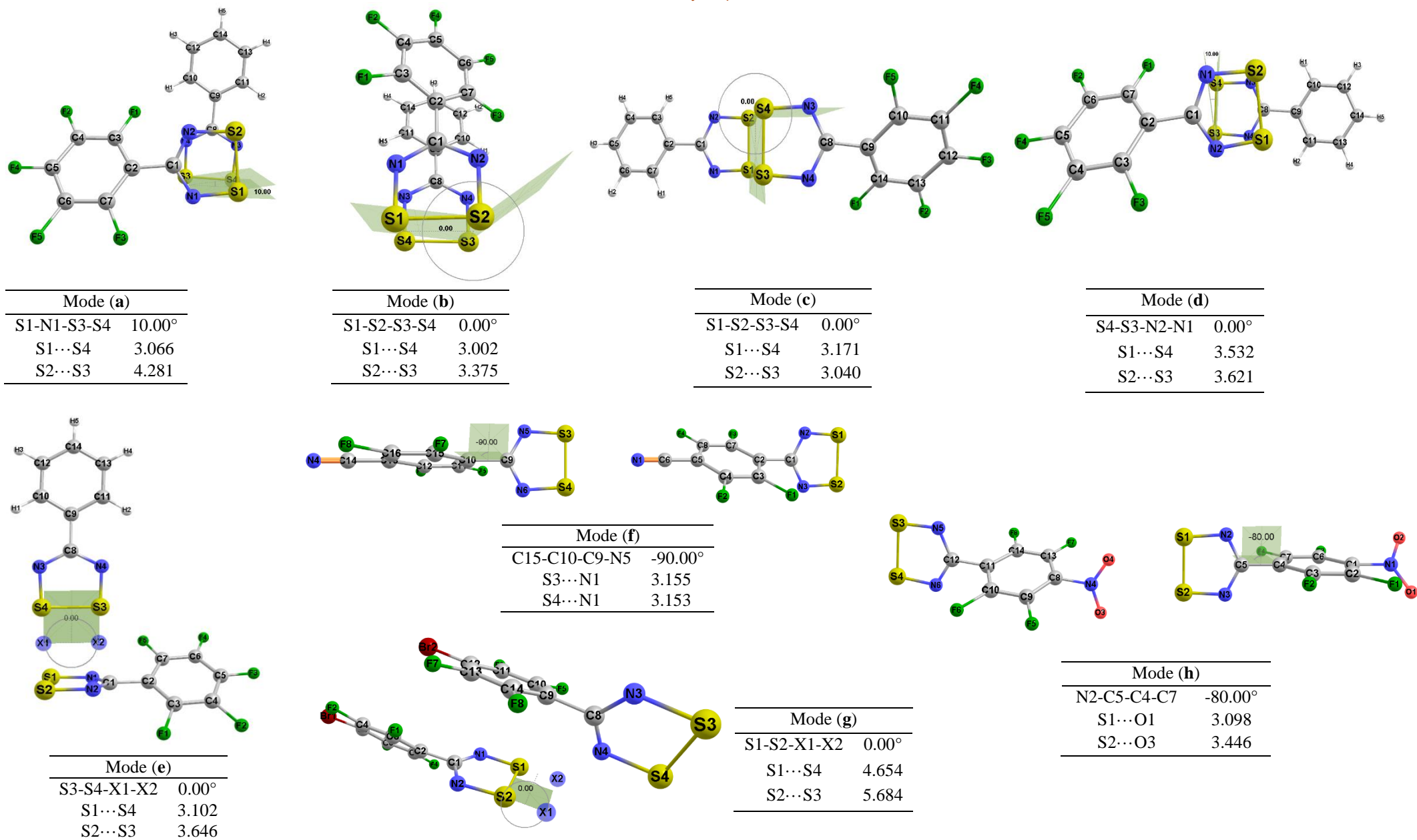


Figure 6.3: The torsion angle and (°) interatomic distances (Å) obtained where the strongest interactions can be identified in PES plots of modes a – h.

6.2 Calculations on unknown radicals

A series of calculations were performed on a set of seven unknown radicals that have not yet been synthesised and therefore their modes of association in the solid state are unknown. All of the unknown radicals were chosen to have -F, -Cl, and -CF₃ groups at the *ortho* position, as large bulky or halogenated groups could possibly result in large twist angles, which can inhibit dimerisation^{2,3}. One radical with a -CF₃ group placed at the *meta* position was also included as the results reported in chapter 5 showed that groups placed at the *meta* position encourage the formation of strong intermolecular interactions that result in dimerisation. Some radicals also contain the -Br, -NO₂, -CN and -CF₃ groups at the *para* position (relative to heterocyclic ring) that have the potential to form structure-directing contacts that could inhibit dimerisation⁴.

The majority of the radicals were also selected according to the availability of their starting material, so that the radical could be synthesised to verify the predictions. The monomeric radicals **2**, **3** and **4** were included in this study for comparative purposes as their modes of association have been determined from their crystal structures.

The chemical names and compound numbers of all radicals studied are given in Table 6.1. All the radicals were arranged in each of the geometries determined for all eight different modes of association (Figure 6.3a – 6.3h). This was followed by geometry optimisation calculations in the singlet and triplet states at the UB3LYP-D3/6-311++G(d,p) level of theory. Frequency calculations were performed to confirm that minimum energy conformation were obtained.

Table 6.1: Chemical and shorthand name of each unknown (a) and monomeric radical pair (b).

	Chemical name	Compound number
	4-(2'-fluoro-4'-(trifluoromethyl)phenyl)-1,2,3,5-dithiadiazolyl	31
	4-(4'-fluoro-2'-(trifluoromethyl)phenyl)-1,2,3,5-dithiadiazolyl	32
	4-(4'-bromophenyl)-1,2,3,5-dithiadiazolyl	33
(a)	4-(4'-cyano-2',3',5',6'-tetrachlorophenyl)-1,2,3,5-dithiadiazolyl	34
	4-(4'-nitro-2'-(trifluoromethyl)phenyl)-1,2,3,5-dithiadiazolyl	35
	4-(4'-nitro-3'-(trifluoromethyl)phenyl)-1,2,3,5-dithiadiazolyl	36
	4-(4'-bromo-2',3',5',6'-tetrachlorophenyl)-1,2,3,5-dithiadiazolyl	37
	4-(4'-cyano-2',3',5',6'-tetrafluorophenyl)-1,2,3,5-dithiadiazolyl	2
(b)	4-(4'-bromo-2',3',5',6'-tetrafluorophenyl)-1,2,3,5-dithiadiazolyl	3
	4-(2',3',5',6'-tetrafluoro-4'-nitrophenyl)-1,2,3,5-dithiadiazolyl	4

If the lowest energy conformations of the unknown radicals are similar to geometries of the known monomeric radicals, this could indicate that these unknown radicals will prefer a monomeric mode of association. Similarly, if the lowest energy conformation exhibits a dimer mode of association, this could indicate that the radicals will prefer a dimeric mode of

association. The radicals could also exist as multiple polymorphs that exhibit monomeric or dimeric modes of association.

6.3 Interaction energies of unknown and known monomeric radicals

Counterpoise-corrected single point calculations were performed at the UB3LYP-D3/6-311++G(d,p) level of theory in the singlet and triplet states on radicals that had been optimised in the singlet and the triplet states. The calculated interaction energies of each radicals are summarised in Tables 6.2, 6.3, 6.5 and 6.6 for the eight modes of association (**a - h**). The values in each table were used to determine whether the unknown radicals prefer a monomeric or dimeric mode of association, which is indicated in the 'Prediction' column. Repulsive energies obtained for calculations performed in the singlet state indicate that interaction between the SOMOs are not favoured, whereas attractive energies suggest that interaction between the SOMOs will lead to dimerisation. In contrast, attractive energies obtained for calculations performed in the triplet state suggest that the radical will remain monomeric, whereas repulsive energies indicate interaction between the SOMOs is favourable. The energies obtained for radicals that have been optimised in the singlet and triplet states will be discussed in two separate sections.

6.3.1 Energies of radicals optimised in the singlet state

The interaction energies from the counterpoise-corrected single point calculations on radicals optimised in the singlet state are summarised in Table 6.2. The known monomeric radicals exhibit attractive energies for modes **a**, **b**, **c**, **d** and **f**, while repulsive energies are shown for modes **e**, **g** and **h**. Inspection of the known monomeric radicals optimised in modes **e**, **g** and **h** exhibit distances longer that do not allow for interaction between the SOMOs. In contrast, known monomeric radicals optimised in modes **a**, **b**, **c**, **d** and **f** exhibit short distances between the heterocyclic radical rings, which allows for favourable interaction between the SOMOs. To confirm this, the HOMOs were calculated for the known monomeric radicals optimised in modes **e** and **f** and are illustrated in Figure 6.5, where the HOMOs shown correspond to the interaction between the SOMOs residing on the two heterocyclic rings.

Table 6.2: Interaction energies obtained from counterpoise-corrected single point (kcal/mol) calculations performed in the singlet state on radicals optimised in the singlet state. Results are shown for *twisted (a)*, *cisoid (b)*, *transoid (c)*, *trans-cofacial (d)*, *orthogonal (e)*, Radical 2 (*f*), Radical 3 (*g*) and Radical 4 (*h*) modes of association. The prediction column shows which mode of association has been predicted of each radical.

Compound number	a	b	c	d	e	f	g	h	Prediction
31	-1.91	-7.48	-8.29	-6.64	-1.87	-0.36	0.56	0.46	Dim
32	5.83	-4.73	-2.26	-8.48	-8.45	19.14	13.67	0.06	Dim
33	-2.00	-7.24	-7.35	-7.27	-2.00	-0.43	8.90	8.92	Dim
34	-6.23	-5.27	-5.25	-0.37	0.42	-0.34	17.36	17.62	Mon
35	-0.84	-7.63	-8.90	-6.64	-2.39	-0.05	17.24	17.30	Mon
36	0.15	-6.73	-8.22	8.42	0.93	53.01	18.37	18.36	Mon
37	-5.61	-8.14	-1.73	-0.8	0.06	-0.75	-4.46	9.09	Dim/Mon
2	-7.12	-4.98	-7.11	-4.30	1.78	-4.31	17.72	17.99	-
3	-7.15	-6.67	-3.14	-4.88	1.42	-4.86	10.99	11.50	-
4	-6.95	-5.32	-7.11	-4.23	1.81	-4.23	18.94	18.99	-

The HOMOs show overlap of only two orbital lobes for radicals that have been optimised in mode **e**, whereas the radicals optimised in mode **f** show the overlap of four orbital lobes due to the S···N contacts between the heterocyclic radical rings. The calculations reveal that attractive energies will only be obtained there is significant orbital overlap between the SOMOs, which is facilitated by the strong S···N contacts shown in Figure 6.4. Inspection of the optimised geometries that yielded attractive energies (modes **a**, **b**, **c**, **d**) revealed similar S···N contacts to those observed in Figure 6.5. The optimised geometries of radicals that yield repulsive energies (modes **g** and **h**) exhibit linear modes of association that do not allow any interaction between the SOMOs.

The optimised geometries and energies were compared to those obtained for known monomeric radicals to determine if radicals **31** - **37** would prefer a monomeric or dimeric mode of association. The sections will be restricted to a discussion of final geometries and energies of unknown radicals that strongly suggest which mode of association they will prefer.

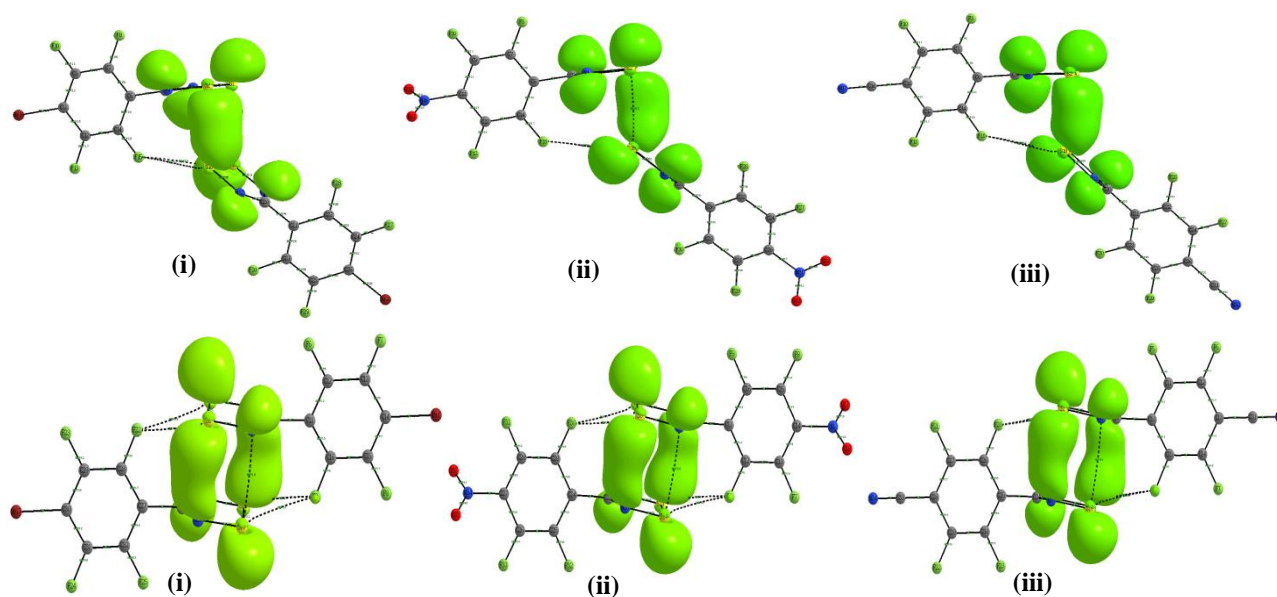


Figure 6.4: HOMOs calculated for radicals that have been optimised the e (top) and f (bottom) modes of association for the known monomeric radicals.

Radical pair **32** exhibits two of the strongest attractive interaction energies when optimised in modes **d** and **e**. The optimised geometries are given in Figure 6.5, with both radical pairs shown to exhibit a *trans-cofacial* mode of association. Very small differences in the S··S and S··N contacts show that both geometry optimisations converged towards the same final structure, which indicates that the *trans-cofacial* is the lowest energy conformations. The strong attractive interactions and optimised geometries that exhibit a dimeric mode of association show that radical pair **32** will prefer a dimeric mode of association in the solid state. Radical pair **31** exhibits attractive energies when optimised in modes **a** – **f**, whereas repulsive energies are obtained when this radical pair was optimised in the linear modes of association, **g** and **h**. This radical also exhibits one of the strongest attractive energies when optimised in mode **c**. The final structure of radical pair **31** optimised in mode **c** is illustrated in Figure 6.6 and shows S··S and S··N contacts within the sum of the van der Waals radii.

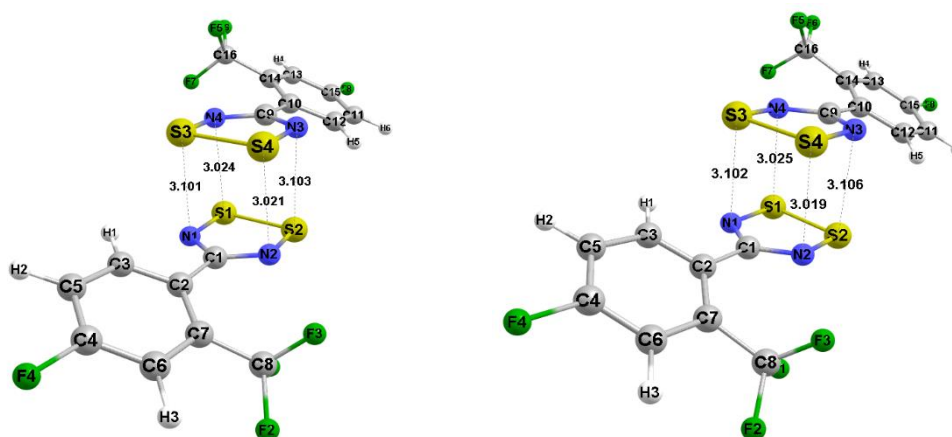


Figure 6.5: The final geometries of radical pair 32 optimised in the d (left) and the e (right) mode of association.

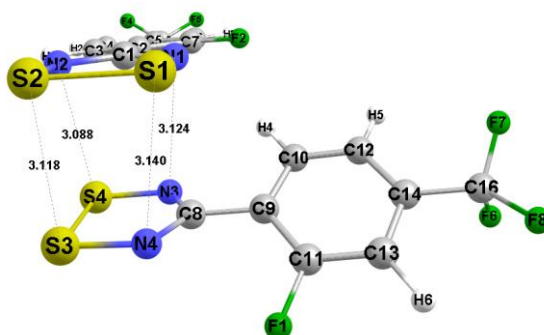


Figure 6.6: The final geometry of the 31 optimised in mode c.

The strong attractive interaction and favourable overlap between the SOMOs strongly suggest that this radical will exhibit a dimeric mode of association in the solid state.

Repulsive energies were obtained for radical pair 36 optimised in modes **a**, **d**, **e**, **f**, **g** and **h**. The optimised geometries of this radical shows that the presence of the bulky CF_3 substituent at the *ortho* position inhibits interaction between the SOMOs in comparison to the other unknown radicals that were optimised in mode **a** (Figure 6.7). The figure shows one $\text{S}\cdots\text{N}$ contact present for the radical optimised in mode **a**, whereas four $\text{S}\cdots\text{S}$ and $\text{S}\cdots\text{N}$ contacts within the sum of van der Waals radii are observed for the radical that has been optimised in mode **c**. Attractive energies were calculated for the radicals optimised in modes **b** and **c**. This radical exhibits the strongest repulsive interaction when geometry optimisation calculations were performed in the singlet state, which suggests that it does not favour interactions between the SOMOs and therefore has the potential to exhibit a monomeric mode of association in the solid state.

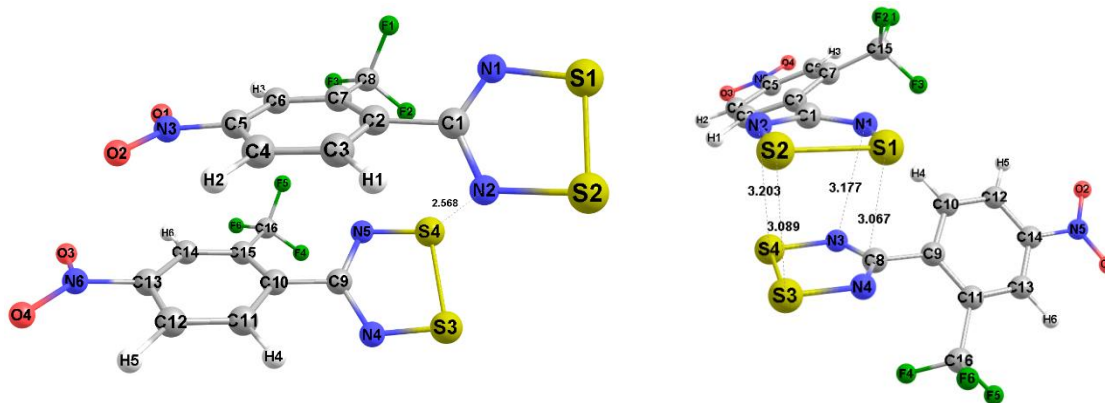


Figure 6.7: The final geometries of radical pair 36 optimised in the a (right) and the c (left) mode of association.

Radical pair **34** is the only unknown radical that exhibits similar attractive and repulsive energies for the same modes of association as the known monomeric radicals. Furthermore, when radical pair **34** is optimised in modes **g** and **h**, it exhibits linear modes of association with short CN...S contacts and large twist angles similar to those observed for the known monomeric radical pair **2** (Figure 6.8).

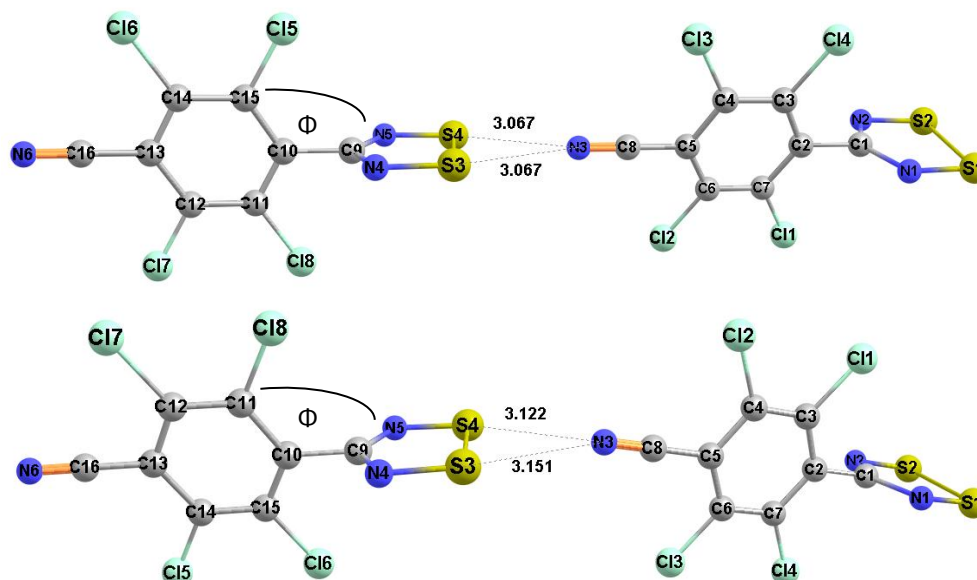


Figure 6.8: The final geometries of radical pair 34 optimised in the g (top) and the h (bottom) mode of association. The twist angles (Φ) are -89.97° (top) and -90.27° (bottom).

Table 6.3 contains the energies from counterpoise-corrected single point calculations performed in the triplet state on radicals that have been optimised in the singlet state. Repulsive energies were calculated for the known monomeric radicals optimised in modes **a** – **f**, whereas attractive energies were calculated for the linear modes of association, **g** and **h**. This is similar to what was reported in Chapter 4, where it was found that the linear mode of association is very stable,

such that geometry optimisation calculations yield final structures with linear modes of association, irrespective of whether the calculations are performed in the singlet or triplet state.

Table 6.3: Interaction energies obtained from counterpoise-corrected single point (kcal/mol) calculations performed in the triplet state on radicals optimised in the singlet state. Results are shown for twisted (a), cisoid (b), transoid (c), trans-cofacial (d), orthogonal (e), Radical 2 (f), Radical 3 (g) and Radical 4 (h) modes of association. The prediction column shows which mode of association has been predicted of each radical.

Compound number	a	b	c	d	e	f	g	h	Prediction
31	-1.1	5.37	4.22	3.93	-1.47	7.50	-4.11	-3.99	Dim
32	-5.28	2.03	3.33	3.67	2.09	-2.50	-8.15	3.08	Dim
33	59.20	4.67	4.59	55.83	59.18	7.24	-11.29	-11.28	Dim
34	36.35	38.82	38.85	3.45	47.87	3.45	-5.26	-5.34	Mon
35	-4.99	4.99	1.91	3.85	-2.56	6.82	-5.25	-5.22	Mon
36	-1.3	32.5	4.03	-9.31	4.49	-12.54	33.56	33.59	Mon
37	-0.54	36.34	5.32	3.26	8.30	3.22	-3.95	-12.8	Dim/Mon
2	3.88	43.09	10.81	4.52	8.55	4.49	-5.08	-5.13	-
3	3.79	42.08	8.43	4.19	8.14	4.19	-10.6	-10.66	-
4	3.97	4.41	3.89	4.64	8.59	4.72	-4.07	-4.15	-

Radical pairs **33** and **4** exhibit similar behaviour with respect to attractive and repulsive energies for the known monomeric radicals. Attractive energies are observed for the two linear modes **g** and **h**. The similarities between the interaction energies in Tables 6.2 – 6.3 and the optimised geometries (singlet state) of radical pair **4** to those of known monomeric radicals suggest that it will prefer a linear mode of association in the solid state. Radical pair **33** optimised in modes **g** and **h** exhibits final geometries unlike any of the known monomeric modes of association (Figure 6.9). The presence of small twist angles and the absence of structure-directing interactions suggest that radical pair **33** will dimerise in the solid state.

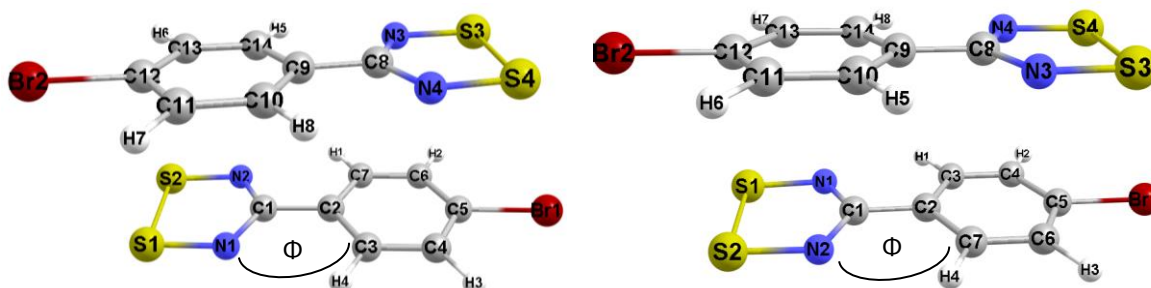


Figure 6.9: The final geometries of radical pair 33 optimised in the g (left) and the h (right) modes of association. The twist angles (Φ) are -0.37° (left) and -1.21° (right).

Studies have reported that some radicals have the potential to exist as multiple polymorphs or exhibit different modes of association within the same crystal structure^{4,5}. Therefore, the

optimised geometries and energies could provide information about the potential of a radical to exist in both monomeric and dimeric modes of association in different polymorphs or within the same crystal. One such example is radical pair **37**. This radical exhibits a weakly attractive energy close to 0 kcal/mol when optimised in mode **a**. Otherwise, this radical exhibits attractive energies when optimised in modes **b – f** and repulsive energies when optimised in modes **g** and **h**, which is similar to what is observed for the known monomeric radicals in Table 6.3. The HOMO of radical pair **37** optimised in mode **a** (Figure 6.10) show significant orbital overlap between the SOMOs on the two heterocyclic radical rings. The favourable interaction between the SOMOs bring the phenyl rings close together leading to $\pi - \pi$ interactions and an interaction between the two bromine atoms (blue sphere). The structure of radical pair **37** optimised in mode **h** exhibits the strongest attractive interaction energy (Table 6.3) and S \cdots N contacts very similar to those observed for radical **3** in the conformation found in the crystal structure (Figure 6.11). The favourable interaction between the SOMOs (mode **a**) and strong attractive interaction energies (mode **h**) suggest that radical pair **37** is analogous to radical **3** and has the potential to exist in two different polymorphs that exhibit either a monomeric or a dimeric modes of association.

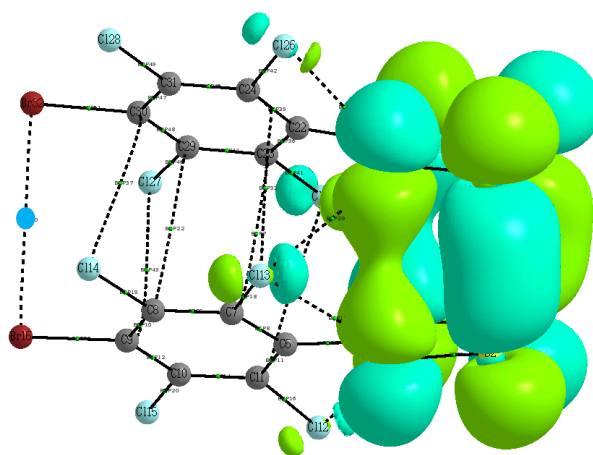


Figure 6.10: HOMO of radical pair **37** optimised in modes **a**. The BCP at the interaction between bromine atoms is indicated by a blue sphere.

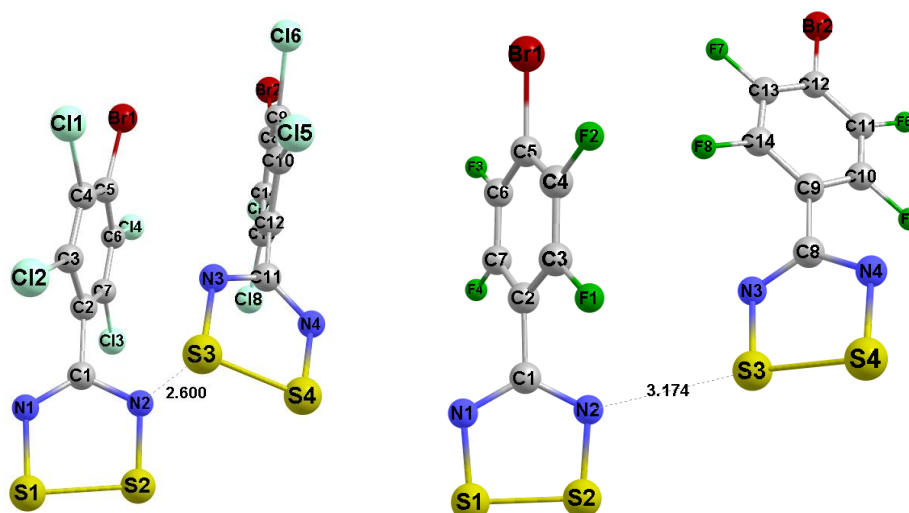


Figure 6.11: The final geometries of radical pairs of **37** optimised in mode **h** (left) and **3** (right, crystal structure).

6.3.2 EDA analysis of unknown radicals optimised in the mode of association of radical **4** (mode **g**) in the singlet state

An energy decomposition analysis (EDA) was performed in the singlet and triplet states to explain why the unknown radicals exhibit very different interaction energies in Tables 6.2 and 6.3 when optimised in mode **g**. In particular, radical pair **37** is the only unknown radical that exhibits an attractive energy for mode **g** in Table 6.2, while the radical pair **31** exhibits a weak repulsive energy (close to 0 kcal/mol) compared to the strong repulsive interaction energies observed for the other unknown radicals that have been optimised in mode **g**. Radical pair **36** exhibits the only repulsive energy in Table 6.3 when optimised in mode **g**, with attractive interaction energies obtained for all other radicals.

Attractive binding energies were obtained for radical pair **31** and **37** for calculations performed in the singlet state. Both radicals exhibit large ΔE_{el} contributions and the only attractive ΔE_{orb} contributions. The origin of the attractive ΔE_{orb} contribution for radical pair **37** can be seen in the HOMO, which shows orbital overlap between the SOMOs, as compared to the HOMO of radical pair **36**, which does not exhibit overlap between the SOMOs, thus yielding the repulsive ΔE_{orb} contribution as shown in Table 6.4.

The favourable orbital interactions between the heterocyclic radical rings also allows for intermolecular interactions between the fluorinated aryl rings, which results in the larger ΔE_{el} contribution shown for radical pairs **31** and **37**.

The EDA calculations performed in the triplet state (Table 6.4) exhibit attractive binding energies for all the unknown radicals. In particular, the ΔE_{orb} contributions to the binding

energy are attractive, which results from favourable interaction between the SOMOs as well as the contributions by other interactions between chlorine atoms as shown in Figure 6.12.

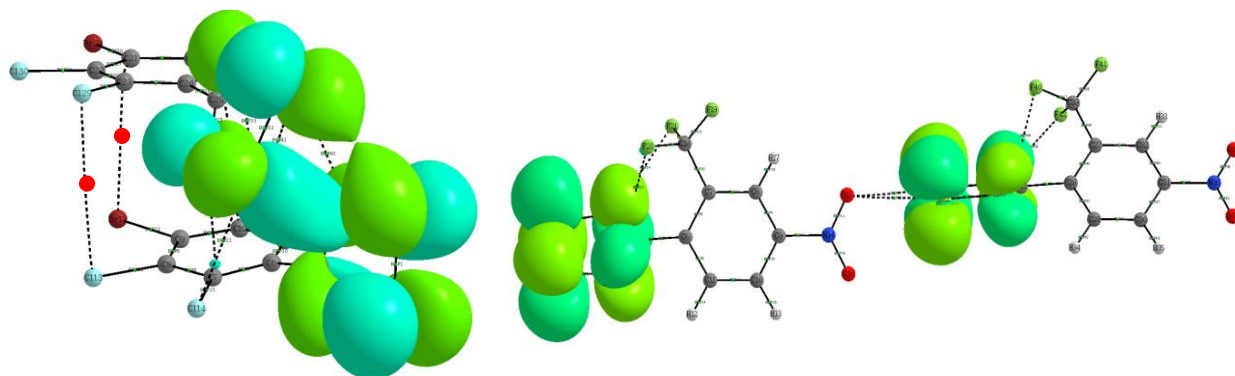


Figure 6.12: HOMOs of radical pairs **37** (left) and the **36** (right) radicals optimised in mode of association **g** in the singlet state.

The unknown radicals that exhibit a linear mode of association when optimised in mode **g** in the singlet state show small ΔE_{disp} , ΔE_{el} and ΔE_{Pauli} contributions to the bonding energy. The optimised geometries of radical pairs **31** and **37** are the only two unknown radicals that do not exhibit a linear mode of association. They exhibit more attractive ΔE_{disp} and ΔE_{el} contributions than the other unknown radicals, but strongly repulsive ΔE_{Pauli} contributions. The contributions show that radical pairs **31** and **37** will exhibit attractive bonding energies even if allowed to optimise in a linear mode of association, as the interactions in the dimeric mode of association are more favourable. Therefore, these two radicals are likely to exhibit a dimeric mode of association in the solid state.

The binding energies in Table 6.4 correspond to the results in Chapter 4, which showed that attractive binding energies are largely dependent on the ΔE_{disp} and ΔE_{el} contributions. Radicals will therefore only exhibit attractive bonding energies for calculations performed in the singlet state if there are favourable interactions between the SOMOs and other intermolecular interactions between the radicals that result in large ΔE_{disp} and ΔE_{el} contributions.

Table 6.4: EDA of bonding energy performed for unknown radicals in the singlet (a) and triplet state (b). Total energy = dispersion + electrostatic + orbital + Pauli (kcal/mol).

Compound number	ΔE_{Tot}	ΔE_{disp}	ΔE_{el}	ΔE_{orb}	ΔE_{Pauli}	
	Total	Dispersion	Electrostatic	Orbital	Pauli	
(a)	31	-4.94	-17.99	-13.84	-2.95	29.84
	32	9.28	-13.28	-6.72	15.92	13.36
	33	3.97	-19.19	-8.38	13.96	17.58
	34	13.94	-2.48	-7.27	17.25	6.43
	35	13.90	-3.22	-5.70	17.55	5.26
	36	15.19	-2.63	-5.45	18.28	4.99
	37	-11.69	-24.27	-25.05	-12.68	50.31
(b)	31	-9.83	-17.99	-13.84	-7.84	29.84
	32	-12.39	-13.28	-6.72	-5.75	13.36
	33	-16.27	-19.19	-8.38	-6.28	17.58
	34	-8.78	-2.48	-7.27	-5.48	6.43
	35	-8.74	-3.22	-5.70	-5.09	5.26
	36	-7.89	-2.63	-5.45	-4.80	4.99
	37	-11.22	-24.27	-25.05	-12.22	50.31

6.3.3 Energies of radicals optimised in the triplet state

Table 6.5 contains interaction energies that were calculated on the singlet state on radicals that have been optimised in the triplet state. Performing a geometry optimisation in the triplet state will yield final structures that do not favour interaction between the unpaired electrons, resulting in optimised geometries that have drifted apart and do not allow for interactions between the SOMOs. Performing interaction energy calculations in the singlet state will therefore yield repulsive energies, as the optimised geometry does not favour paired electrons.

AIM plots for the unknown radicals optimised in mode **a** (Figures 6.13a – 6.13g) show few S···S, N···N or S···N contacts between the heterocyclic radical rings, therefore showing by interactions between the SOMOs are not favourable and repulsive interaction energies will be obtained for calculations performed in the singlet state.

The unknown radicals that exhibit the strongest repulsive interaction energies (Table 6.5), namely radical pairs **34**, **35** and **36**, were optimised in modes **g** and **h** with a linear mode of association. Less repulsion occurs for the unknown radicals that exhibit S···N contacts similar to those observed for the known monomeric radical pair **3**, which indicates that these radicals undergo some favourable interactions between the unpaired electrons. The final geometries of radicals that exhibit weak and strong repulsive interaction energies are illustrated in Figure 6.14. The monomeric mode of association and strong repulsive interaction energies observed for

radical pairs **34**, **35** and **36** indicated that these radicals could prefer a monomeric mode of association in the solid state.

Table 6.5: Interaction energies obtained from counterpoise-corrected single point (kcal/mol) calculations performed in the singlet state on radicals optimised in the triplet state. Results are shown for *twisted* (a), *cisoid* (b), *transoid* (c), *trans-cofacial* (d), *orthogonal* (e), Radical 2 (f), Radical 3 (g) and Radical 4 (h) modes of association. The prediction column shows which mode of association has been predicted of each radical.

Compound number	a	b	c	d	e	f	g	h	Prediction
31	7.21	4.25	4.29	6.50	3.89	10.62	9.27	10.44	Dim
32	8.89	8.73	8.79	8.60	3.57	7.45	8.66	19.97	Dim
33	7.70	6.41	5.80	6.42	6.45	7.68	13.98	9.02	Dim
34	8.40	7.41	7.07	7.17	6.84	10.27	17.62	17.62	Mon
35	6.97	8.49	8.28	8.55	8.05	8.14	17.24	17.30	Mon
36	10.06	7.85	7.83	8.04	9.09	6.42	18.37	18.36	Mon
37	7.49	7.32	7.17	7.41	6.33	10.74	10.74	9.09	Dim/Mon
2	10.60	9.79	10.03	10.53	7.45	6.81	17.99	17.99	-
3	10.91	8.46	10.91	10.9	6.99	9.46	10.88	11.50	-
4	8.48	7.54	10.71	8.54	7.39	5.98	19.00	18.99	-

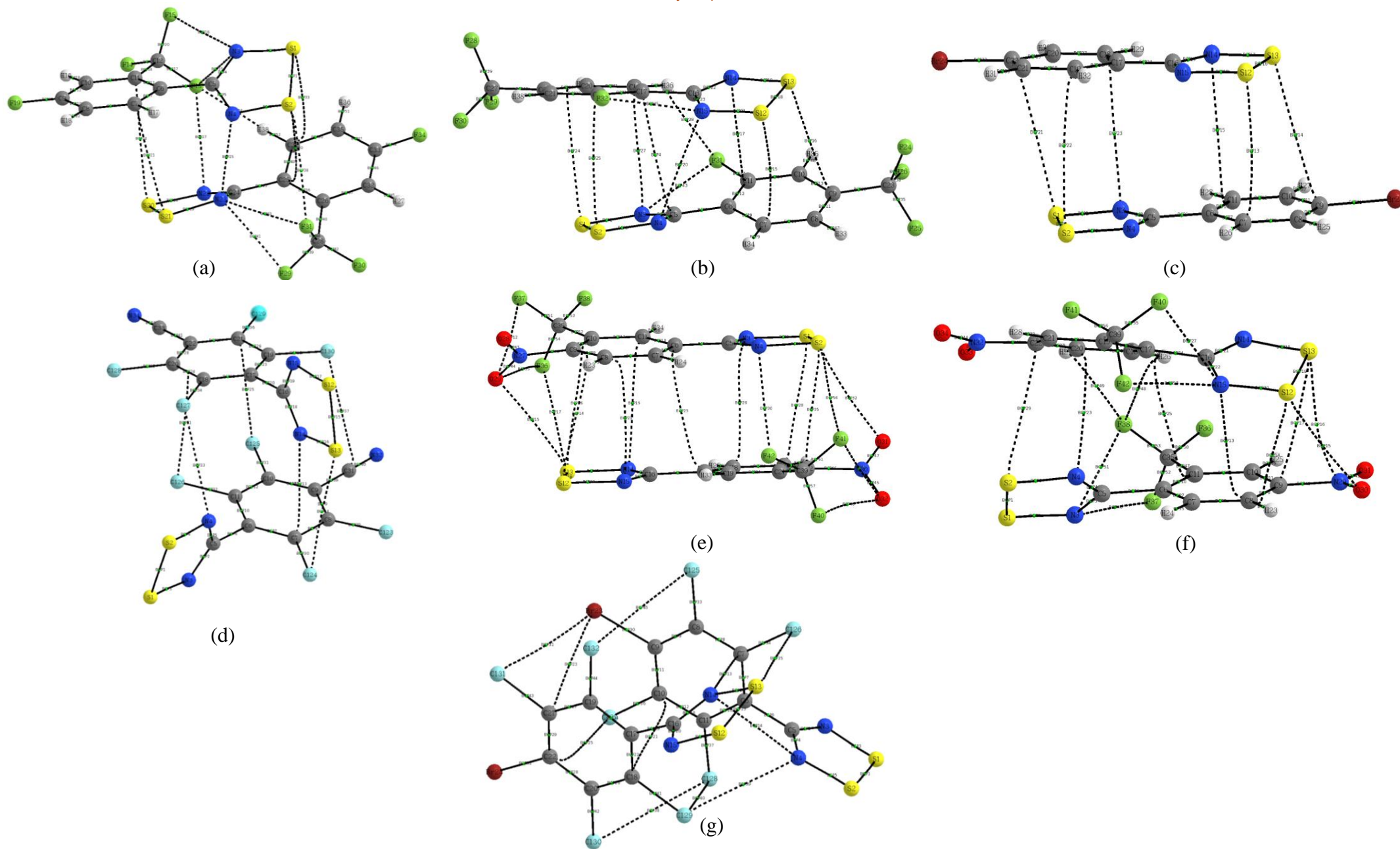


Figure 6.13: AIM plots of radical pairs 31 (a), 32 (b), 33 (c), 34 (d), 35 (e), 36 (f) and 37 (g) radicals that have been optimised in mode a (twisted).

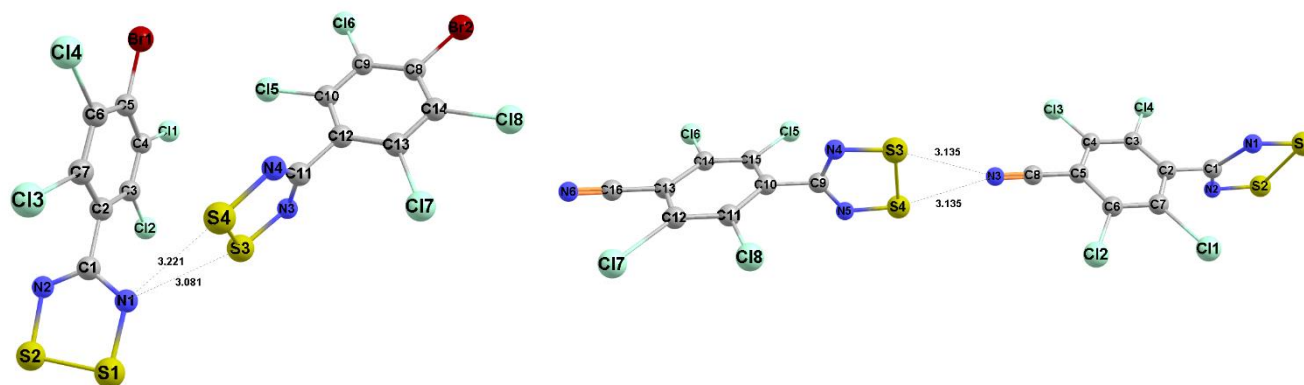


Figure 6.14: A weak repulsive energy is observed for radical pair **37** (left), while a strong repulsive interaction energy is observed for radical pair **34** (right). Both radicals were optimised in the *g* mode of association.

Table 6.6 contains interaction energies calculated in the triplet state for radicals with the same geometries used to generate Table 6.5. All radicals show attractive interaction energies, which results from the geometry optimisation calculations performed in the triplet state not favouring interaction between the unpaired electrons. The strongest attractive interaction energies were calculated for unknown radicals optimised in modes **a** – **e**, whereas weaker attractive energies were calculated for unknown radicals optimised in modes **f** – **h**.

Table 6.6: Interaction energies obtained from counterpoise-corrected single point (kcal/mol) calculations performed in the triplet state on radicals optimised in the triplet state. Results are shown for *twisted* (a), *cisoid* (b), *transoid* (c), *trans-cofacial* (d), *orthogonal* (e), Radical 2 (f), Radical 3 (g) and Radical 4 (h) modes of association. The prediction column shows which mode of association has been predicted of each radical.

Compound number	a	b	c	d	e	f	g	h	Prediction
31	-10.49	-11.52	-11.33	-11.67	-11.68	-11.32	-11.27	-11.07	Dim
32	-9.99	-9.97	-9.98	-10.08	-11.81	-10.26	-7.36	-2.94	Dim
33	-9.78	-10.64	-10.64	-10.65	-10.65	-9.78	-5.71	-11.28	Dim
34	-12.00	-12.65	-12.65	-12.68	-10.00	-7.33	-5.32	-5.34	Mon
35	-12.96	-10.58	-10.58	-10.58	-10.52	-12.73	-5.25	-5.21	Mon
36	-11.87	-11.12	-11.12	-11.12	-11.30	-12.01	-4.64	-4.60	Mon
37	-12.89	-12.86	-12.86	-12.86	-10.08	-7.73	-10.09	-12.82	Dim/Mon
2	-11.12	-10.89	-8.75	-11.17	-6.36	-9.10	-5.14	-5.13	-
3	-10.64	-11.58	-10.64	-10.63	-6.84	-10.82	-10.67	-10.68	-
4	-11.25	-10.08	-10.54	-11.29	-6.35	-9.61	-4.17	-4.15	-

Radical pair **37** exhibits strong attractive interaction energies when optimised in modes **a**, **b**, **c**, **d** and **h**. The weakest attractive interaction energy was calculated for radical pair **32** optimised in mode **h**. The AIM plots of these two radicals (Figure 6.15) reveal the presence of several more BCPs in radical pairs **37** than observed for radical pair **32**, which explains the stronger attractive energy observed. The presence of interactions between the chlorine and bromine

atoms (red spheres, Figure 6.15) also contribute to the strong attractive energy observed for radical pair **37**.

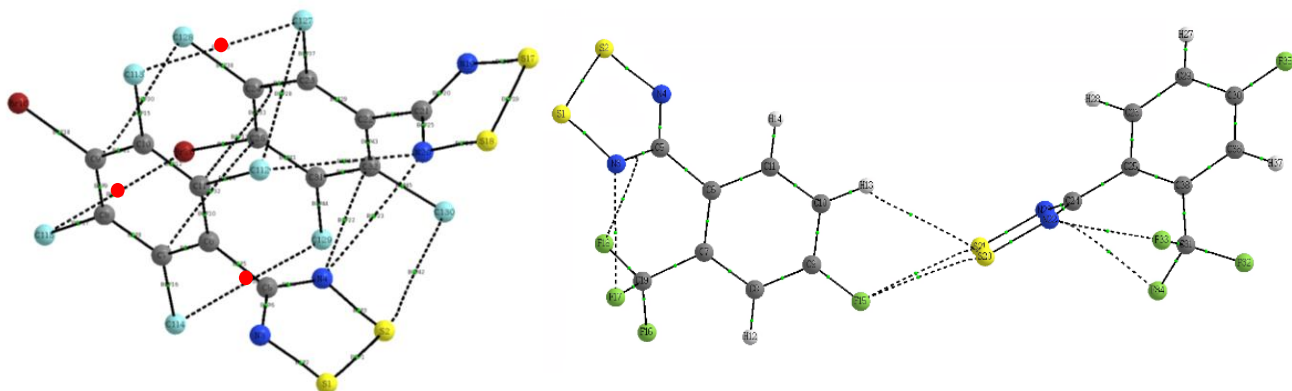


Figure 6.15: AIM plots of radical pair **37** (left) optimised in mode c and radical pair **32** (right) optimised in mode h. Halogen bond BCPs marked by red spheres.

Radical **3** also exhibits structure-directing interactions between the halogen atoms that inhibit dimerisation, which suggests that similar interactions between the halogen atoms present in radical pair **37** could play a similar role.

The optimised geometries and interaction energies were used to determine that radical pairs **31** – **33** are likely to exist in a dimeric mode of association in the solid state, whereas radical pairs **34** - **36** are more likely to exhibit a monomeric mode of association in the solid state. Radical pair **37** could potentially exist as multiple polymorphs with monomeric and dimeric modes of association within one crystal structure or in different polymorphs.

In order to test these predictions, we decided to synthesise radicals **31** – **34** and **36** and structurally characterise them using single-crystal X-ray diffraction. Radicals **35** and **37** could not be synthesised, as the nitrile starting material was not available.

6.4. Synthesis of unknown radicals

The synthesis of radicals **31** – **34** and **36** was performed according to the synthetic procedure⁵ reported in Chapter 2 (section 2.1.1). The details of each procedure is given in Addendum A.

6.5. Analysis of synthesised unknown radicals (31 – 34, 36)

Crystallisation of the unknown radicals proved to be a challenge for many of the unknown radicals, hence Mass Spectrometry (MS) and Electron paramagnetic resonance (EPR) analysis were required to confirm that the desired products had been obtained. The molecular ion peak was identified for each radical; but fragmentation patterns have not been analysed. The product yield where crystals were successfully obtained could not be calculated, which will be explained in the relevant sections. The MS and EPR results of unknown radicals were compared to those of the known monomeric radical **2** (Chapter 3), as the MS and EPR results of radical **2** provided well-defined spectra.

MS analysis was performed utilising an atmospheric solids analysis probe⁶. This probe provides good results for DTDA radicals as it allows for the direct analysis of volatiles and semi-volatiles using an atmospheric pressure ionisation source. The room temperature X-band EPR spectra were recorded for reduced salts to probe whether reduction in fact resulted in radical synthesis. This was performed in both the solid state and in solution (DCM). Studies have reported that a *g*-value close to 2 is indicative of a system containing an organic radical⁷⁻¹⁰. For the purpose of this study, only the solution state *g*-values will be reported for each radical. The hyperfine coupling constant to N, a_N , was also measured for each radical.

6.5.1 Radical 2

The solid- and solution-state EPR spectra of **2** are illustrated in Figure 6.16. The solid-state spectrum shows an isotropic signal. The signal shown in Figure 6.16 is an isotropic signal as all three *g*-tensors are equivalent. The solution-state spectrum shows a 1:2:3:2:1 quintet because of coupling to two nitrogen atoms (¹⁴N). ASAP-MS: *m/z*: (100%) 277.95 (calculated for [C₈F₄N₃S₂]⁺: 278.24). EPR: *g*-value: 2.010, a_N : 4.5 G.

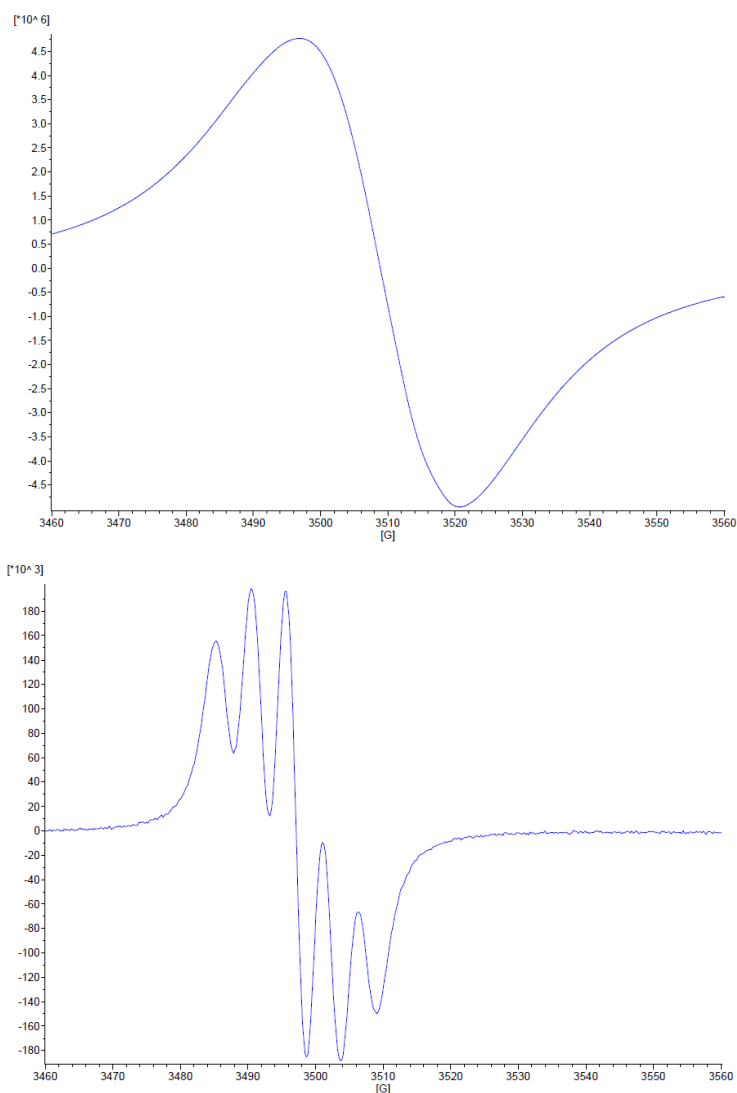


Figure 6.16: The EPR spectra of radical **2** in solid state (top) and solution (bottom).

6.5.2 Radical **31**

The solid-state EPR spectrum of radical pair **31** shows no signal (Figure 6.17). A 1:2:3:2:1 quintet signal is observed in solution, which is similar to the signal observed for radical **2**, confirming synthesis of the DTDA radical. A quintet signal is observed for both dimeric and monomeric radicals in dilute solution, as dissolving a dimeric radical results in monomeric radicals in solution¹¹. A crystal structure is therefore required to determine whether the radical prefers a monomeric or dimeric mode of association in the solid state. ASAP-MS: (72%) m/z : 266.97 (calculated for $[\text{C}_8\text{H}_3\text{F}_4\text{N}_2\text{S}_2]^+$: 266.25). EPR: g -value: 2.010, a_N : 5.0 G.

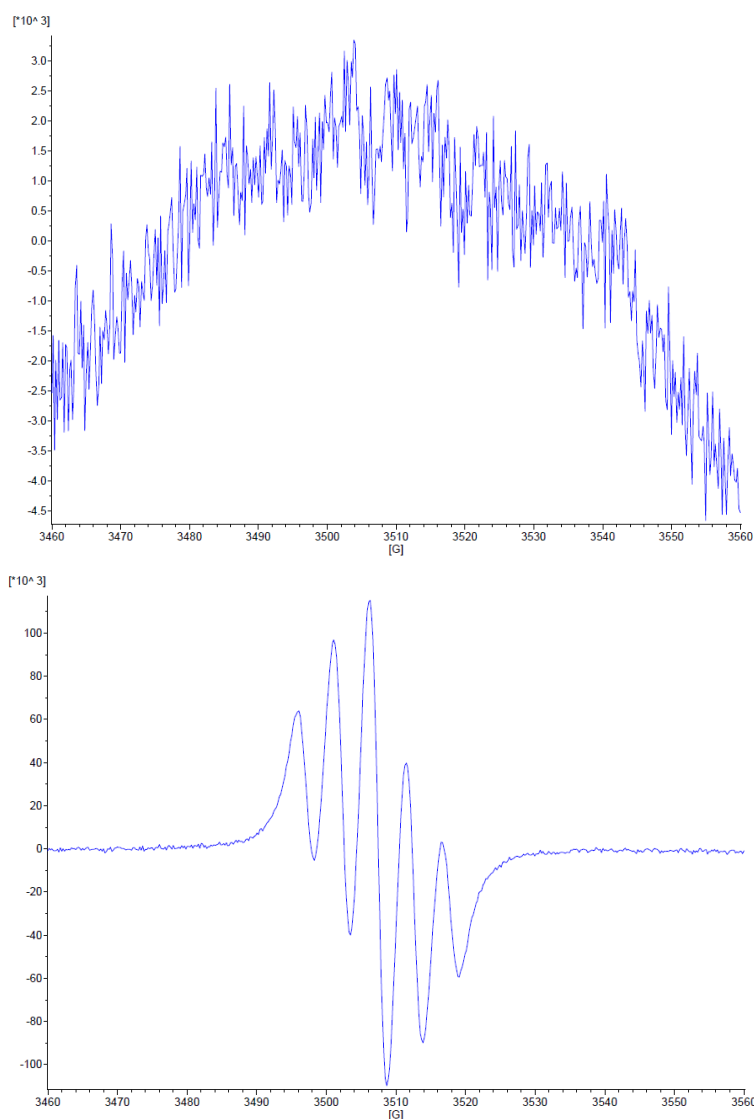


Figure 6.17: The EPR spectra of radical pair **31** in solid state (top) and solution (bottom).

6.5.3 Radical **32**

Radical pair **32** exhibits solid- and solution-state EPR spectra similar to those observed for radical **2** (Figure 6.18). ASAP-MS: m/z : (100%) 266.97 (calculated for $[\text{C}_8\text{H}_3\text{F}_4\text{N}_2\text{S}_2]^+$: 267.25). EPR: g -value: 2.002, a_N : 4.8 G.

Only three rod-shaped pink crystals grew in a small region around the lid of a sealed tube, after reduction of the salt with Ph_3Sb . The small amount of crystals were not weighed to calculate the yield as exposing these crystal to the atmosphere could results in crystal degradation. Purification by sublimation proved unsuccessful. A crystal was analysed by SCD, with the crystallographic information summarised in Table 6.7.

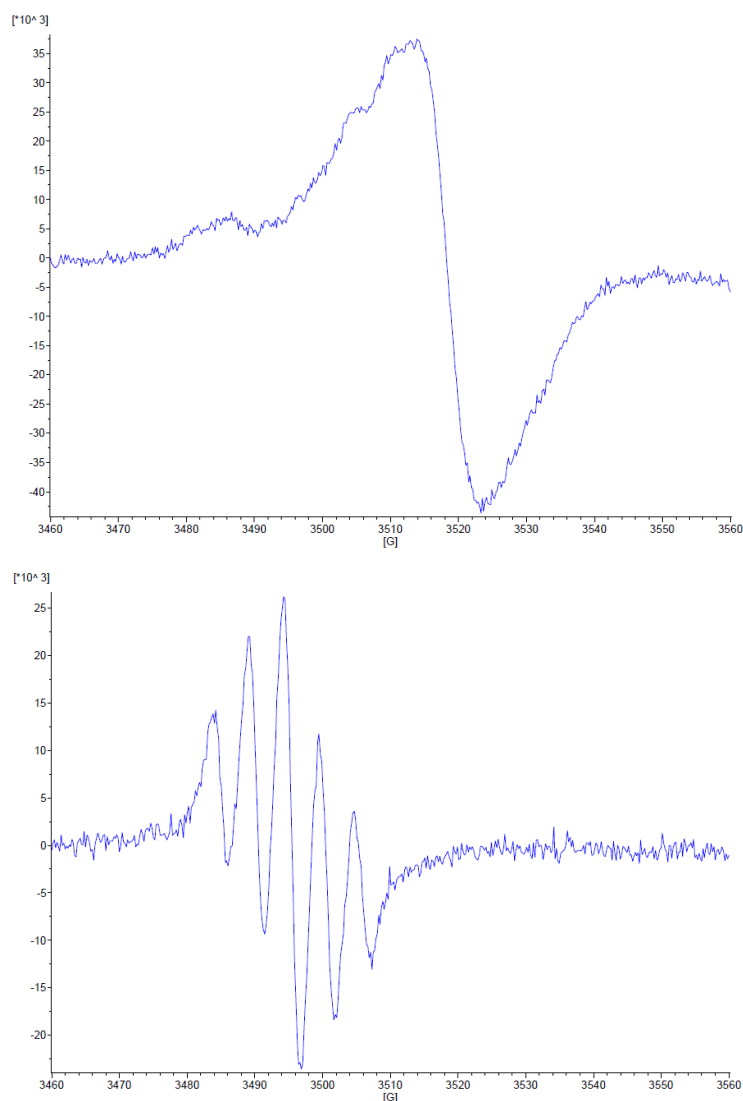


Figure 6.18: The EPR spectra of radical pair **32 in solid state (top) and solution (bottom).**

The crystal structure reveals a dimerised pair of molecules of radical **32** in the *trans-cofacial* mode of association, which results from S \cdots S and S \cdots N contacts within the sum of van der Waals radii (Figure 6.19).

The geometry optimisation of this radical in mode **d** (trans-cofacial) yielded a very similar structure with comparable S \cdots S and S \cdots N contacts and twist angle when compared to the mode of association in the crystal structure (section 6.3.1).

Table 6.7: Crystallographic data and refinement parameters for radical pair **32**.

Radical 32	
Empirical formula	C ₈ N ₂ F ₄ S ₂
Temperature	100 K
Wavelength	0,71073 Å
Crystal system	monoclinic
Space group	<i>P</i> 2 ₁ / <i>c</i>
<i>a</i> (Å)	12.6651 (10)
<i>b</i> (Å)	7.9164 (5)
<i>c</i> (Å)	9.0517 (7)
α (°)	90
β (°)	97.388 (4)
γ (°)	90
<i>V</i> (Å ³)	900.17 (11)
<i>Z</i>	4
Goodness-of-fit on <i>F</i> ²	1.254
R indices (all data)	<i>R</i> 1 = 0.0776 <i>wR</i> 2 = 0.1324

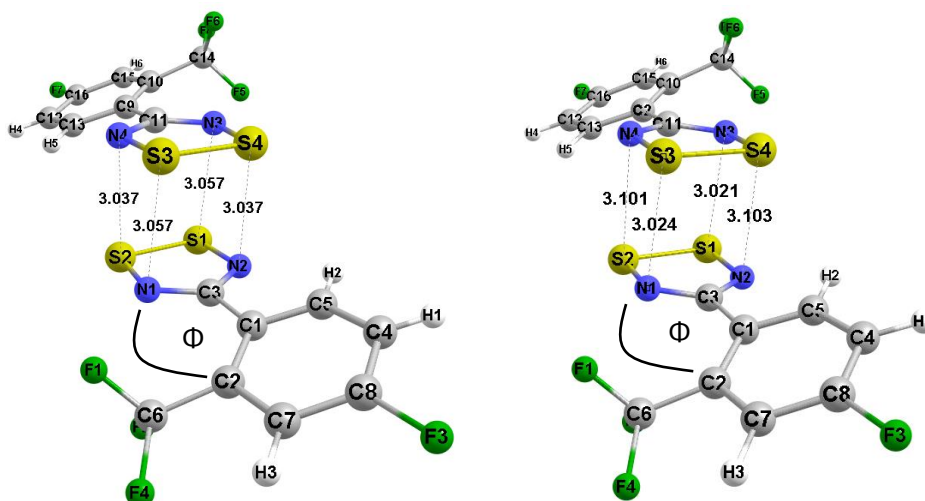


Figure 6.19: The S...S and S...N contacts (Å) in the crystal structure (left) and the geometry optimisation performed in mode **d** (right) of radical **32**. The twist angle between N1-C3-C1-C2 are 22.57° (left) and 29.44(6)° (right). Distances with e.s.d.s for crystal structure (right): 3.101(4) Å, 3.024(4) Å, 3.021(4) Å and 3.103(4) Å.

Furthermore, the values in Table 6.1 show that the optimised geometry of radical pair **32** in mode **d** exhibits the strongest attractive interaction energy calculation when compared to other energies. The calculations therefore successfully predicted that the trans-cofacial mode of association leads to strong attractive energies and would therefore be the more stable and preferred mode of association. The favourable interaction between the SOMOs results from small twist angles and the absence of any contacts that can inhibit dimerisation. The crystal structure exhibits halogen bonds between the fluorine atoms at the *para* position and fluorine atoms of the trifluoromethyl group (Figure 6.20). Additional S...S contacts are present between

neighbouring heterocyclic radical rings. The network of $F\cdots F$, $S\cdots S$ and $S\cdots N$ contacts result in rows of radicals as illustrated in Figure 6.21.

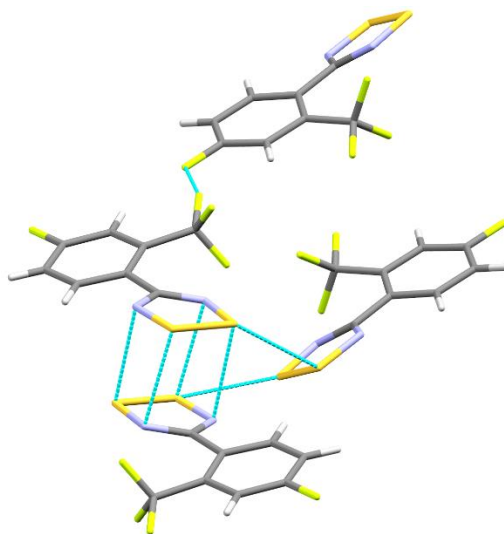


Figure 6.20: The $S\cdots S$, $S\cdots N$ and $F\cdots F$ contacts in the crystal structure of radical **32**.

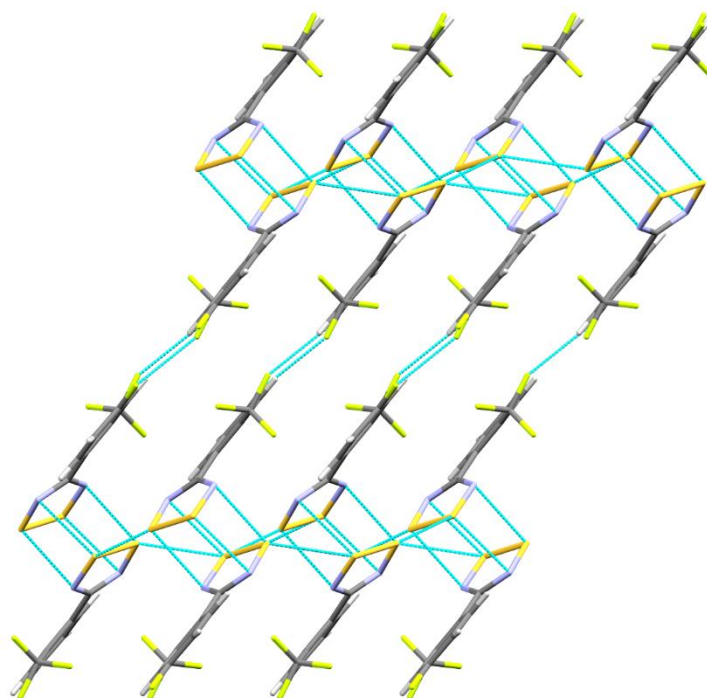


Figure 6.21: Chains of **32** linked by $S\cdots S$, $S\cdots N$ and $F\cdots F$ contacts as viewed down the b axis.

6.5.4 Radical **33**

The synthesis of radical **33** followed the synthetic procedure reported in Chapter 2. It was found that sublimation of the reduced salt with the use of a cold finger did not yield any crystals. The reduced salt was transferred to a larger Schlenk tube, which was heated at 80 °C for approximately two days. This yielded small white Ph_3Sb crystals. The Schlenk tube was heated at 80 °C for an additional week before small block-shaped red crystals grew on the Ph_3Sb

crystals. The growth of crystals in a larger Schlenk tube could indicate that vapour pressure plays an important role in the crystallisation of this radical. Small red crystals were removed from a Ph_3Sb crystal and analysed by XRD, with the crystallographic information summarised in Table 6.9. The solid-state spectrum is anisotropic spectrum owing to different g_{xx} , g_{yy} and g_{zz} components to the g -tensor. The solution-state spectrum shows a well resolved 1:2:3:2:1 quintet (Figure 6.22) that results from coupling to the two ^{14}N nuclei. ASAP-MS: m/z : (100%) 388.99 (calculated for $[\text{C}_{18}\text{H}_{15}\text{SbCl}]^+$: 389.53). EPR: g -value: 2.010, a_N : 4.8 G. MS showed the presence of significant amounts of Ph_3SbCl^+ , which is to be expected based on the unusual method of crystallisation of this radical.

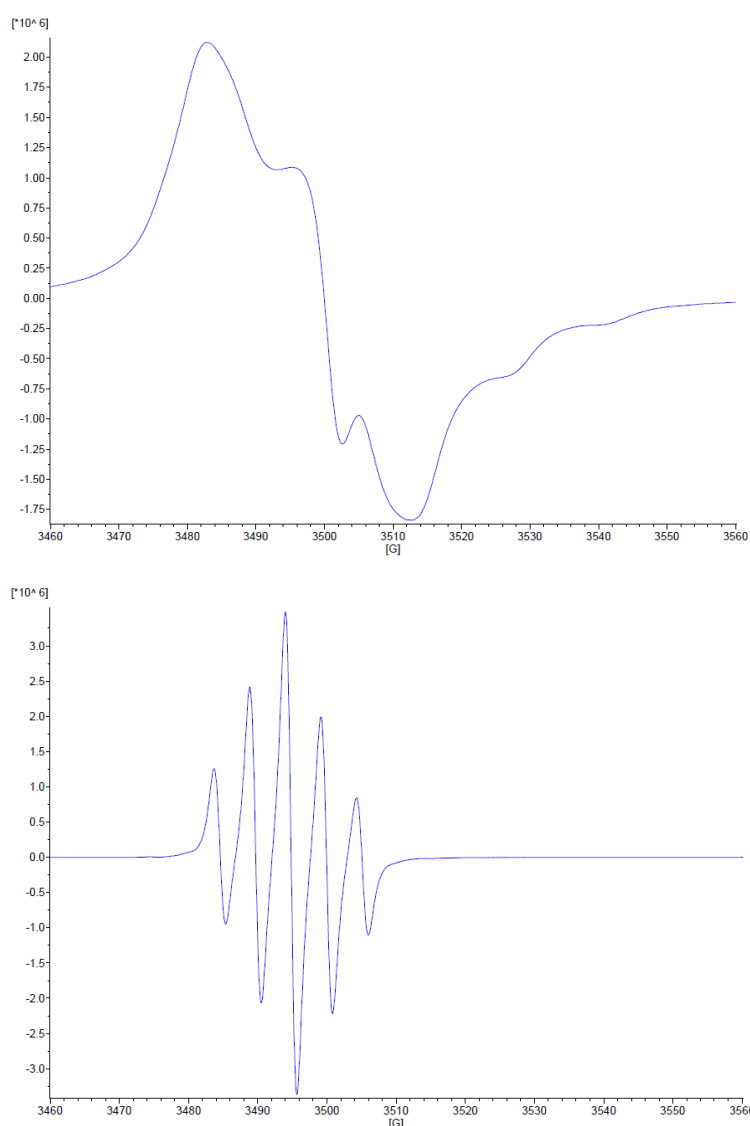
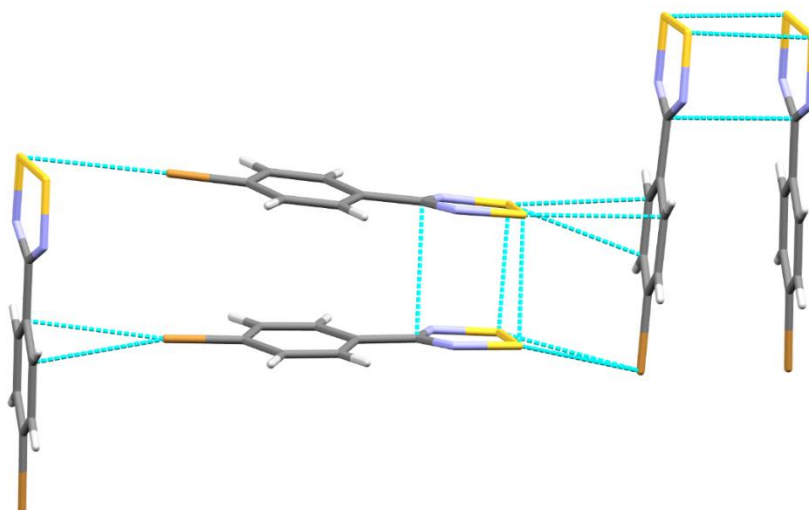


Figure 6.22: The EPR spectra of radical 33 in solid state (top) and solution (bottom).

Table 6.8: Crystallographic data and refinement parameters for radical **33.**

Radical 33	
Empirical formula	C ₈ N ₂ BrS ₂
Temperature	100 K
Wavelength	0.71073 Å
Crystal system	monoclinic
Space group	<i>C2/c</i>
<i>a</i> (Å)	20.9066(17)
<i>b</i> (Å)	10.1072(9)
<i>c</i> (Å)	15.8891(13)
α (°)	90
β (°)	95.412(3)
γ (°)	90
<i>V</i> (Å ³)	3342.5(5)
<i>Z</i>	16
Goodness-of-fit on <i>F</i> ²	1.149
R indices (all data)	<i>R</i> 1 = 0.0246 <i>wR</i> 2 = 0.0441

The crystal structure reveals dimerised pairs of radical **33** molecules in the *cisoid* mode of association (Figure 6.23). Molecules of radical **33** dimerise via S⋯S and N⋯N contacts, while Br⋯S and C⋯S contacts result in a herringbone pattern (Figure 6.24).

**Figure 6.23: The S⋯S, S⋯N, S⋯Br and S⋯C contacts observed in the crystal structure of **33**.**

Radical **33** optimised in mode **b** exhibits very similar S⋯S and S⋯N contacts to the *cisoid* arrangement of radical **33** in the crystal structure (Figure 6.25). The short S⋯S and S⋯N contacts in combination with the small torsion angles are known to result in dimeric modes of association^{1,4}. The calculated energies for the radical pair of **33** (Table 6.2) show that mode **b** is strongly attractive, which indicates that the calculations successfully predicted that a dimerised radical pair would occur in the solid state.

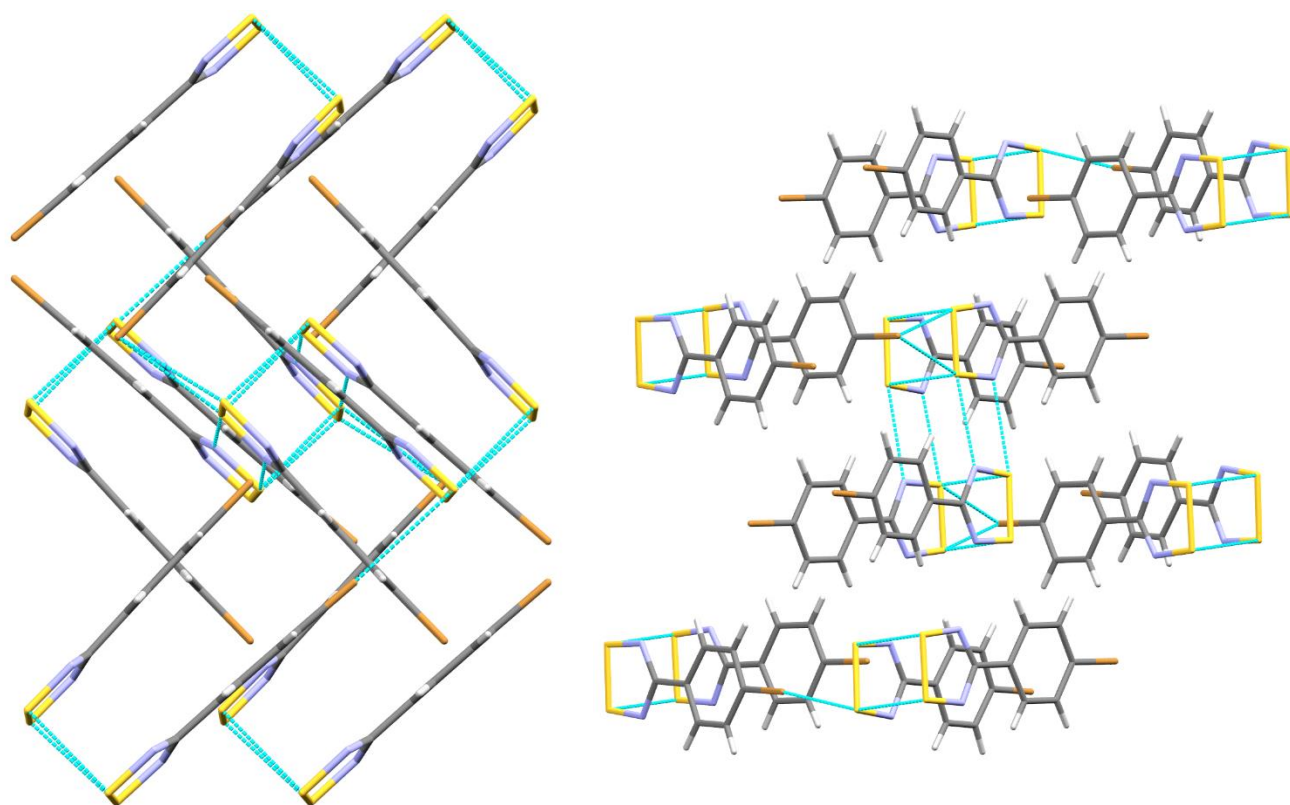


Figure 6.24: Herringbone pattern of radical 33 as viewed down the *a* axis (left) and *b* axis (right).

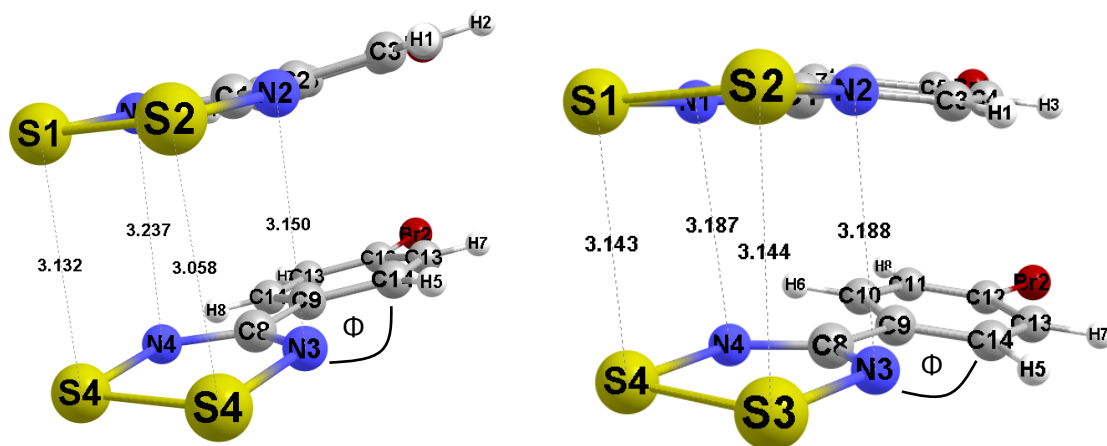


Figure 6.25: The S...S and S...N contacts (Å) for the crystal structure (left) and the geometry optimisation performed in mode b (right) of radical 33. The twist angle between atoms N3-C8-C9-C14 was measured as -6.10° (left) and $9.76(2)^\circ$ (right). Distances with e.s.d.s for crystal structure (right): 3.143(9) Å, 3.144(9) Å, 3.187(3) Å and 3.188(3) Å.

6.5.5 Radical 34

The solid-state spectrum of radical **34** exhibits an anisotropic EPR spectrum, which results from different g_{xx} , g_{yy} and g_{zz} component contributions to the *g*-tensor (Figure 6.26). The solid-state spectrum in Figure 6.26 resembles the solid-state spectrum obtained for the 2,4-dichlorophenyl

DTDA radical, where studies suggest that hyperfine coupling results from the coupling of the two chemically equivalent ^{14}N nuclei ($g_{xx} = 2.002$, $g_{yy} = 2.008$, $g_{zz} = 2.021$)⁴. Constantinides and coworkers explained that the line shape is as a result of kinetic and dynamic processes that result in a triplet paramagnetic state⁴. The spectrum obtained from the solution state experiment once again exhibits the 1:2:3:2:1 quintet. ASAP-MS: m/z: (100%) 345.89 (calculated for $[\text{C}_8\text{Cl}_4\text{N}_3\text{S}_2]^+$: 345.06). EPR: g-value: 2.010, a_N : 4.8 G.

Even though the ERP and MS show that the radical has been successfully synthesised, additional analysis will be required to determine if this radical exhibits a monomeric mode of association in the solid state.

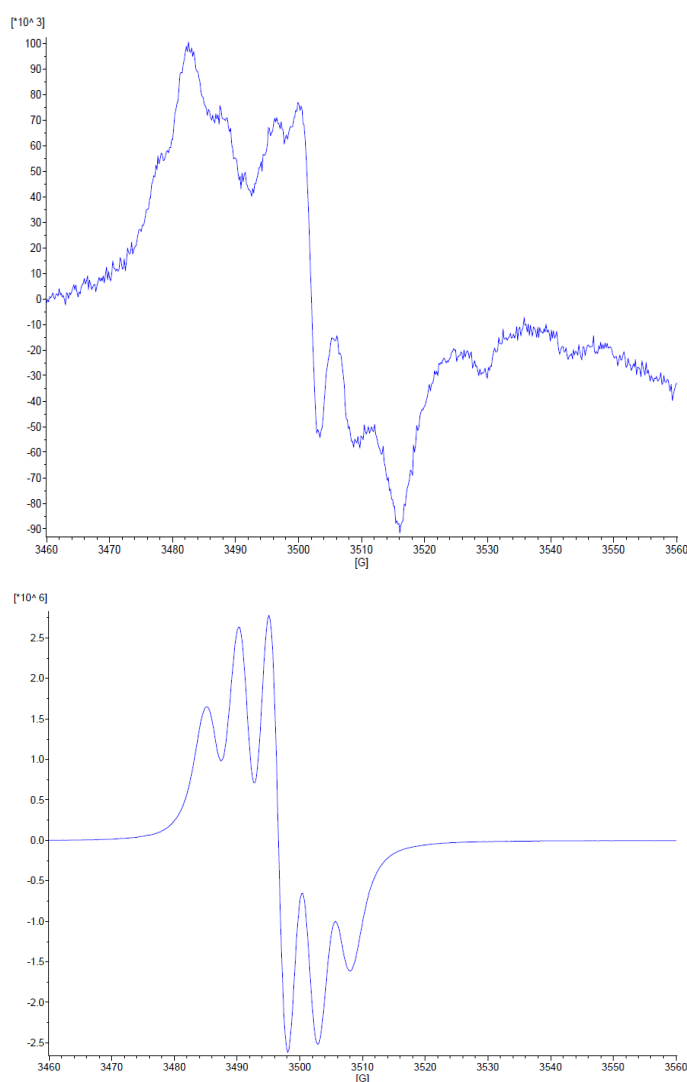


Figure 6.26: The EPR spectra of radical 34 in solid state (top) and solution (bottom).

6.5.6 Radical 36

The solid-state spectrum of radical **36** radical exhibits an anisotropic signal (Figure 6.27). It was found that the solution-state spectrum does not exhibit a well-defined quintet when compared to the spectra of the other unknown radicals (Figure 6.27). The poor definition observed strongly suggests that the radicals decomposes when exposed to solvent¹² or it does not completely dissolve in the solvent. ASAP-MS: m/z: (100%) 388.99 (calculated for $[\text{C}_{18}\text{H}_{15}\text{SbCl}]^+$: 389.53).

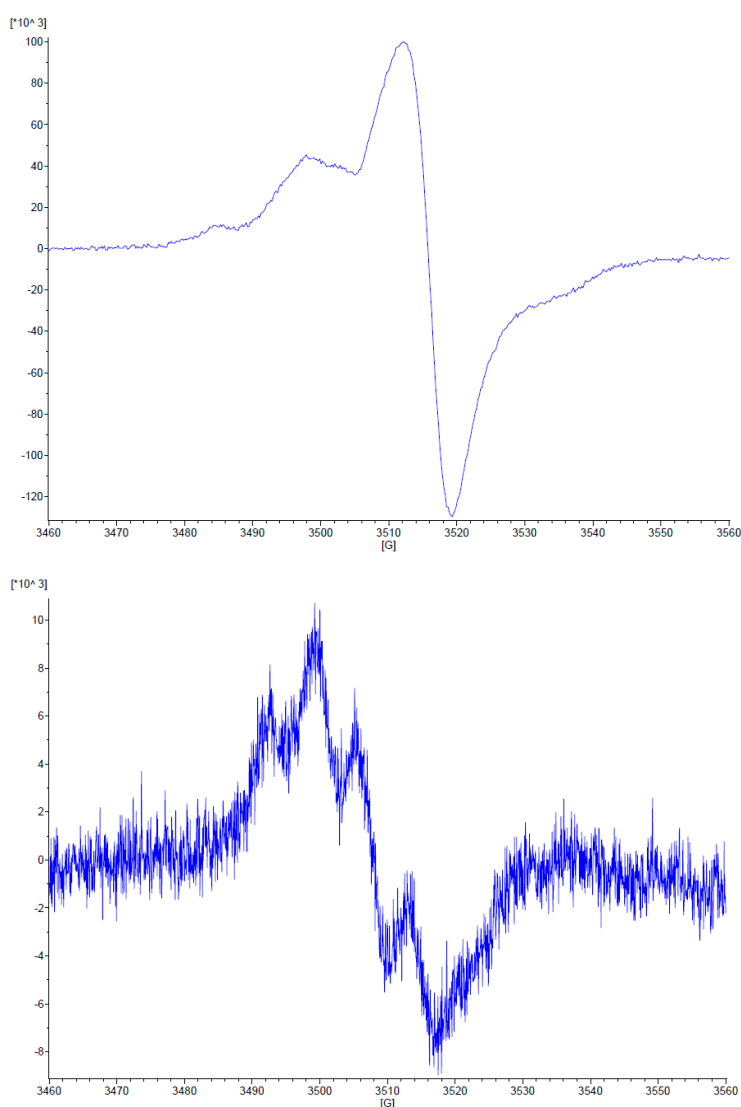


Figure 6.27: The EPR spectra of radical 36 in solid state (top) and solution (bottom).

The MS results and a lack of hyperfine splitting in the solution-state EPR spectra strongly suggest that the desired radical product has not been obtained.

Conclusions

A series of PES scans were performed to identify where the strongest intermolecular interactions occur for eight different modes of association of DTDA radicals (**a** – **h**). Ten known monomeric and unknown radicals were then arranged in the geometries where the strongest intermolecular interactions occur for each mode of association. Full geometry optimisation calculations were performed in the singlet and triplet states. Counterpoise-corrected single-point calculations were then performed in the singlet and triplet states. The interaction energies and optimised geometries were then utilised to identify that radicals **31** - **33** have the potential to yield dimerised radicals in the solid state, whereas radicals **34** - **36** are good candidates to obtain crystals that exhibit monomeric modes of association.

Synthesis yielded the novel crystal structures of radicals **32** and **33**. Calculations successfully predicted that both radicals would dimerise in the solid state. Radical **32** exhibits a *trans-cofacial* mode of association, which was computationally predicted as the most stable mode of association. Radical **33** exhibits a *cisoid* mode of association, which was computationally predicted as one of the most stable modes of association.

The successful prediction of the preferred configuration of radicals **32** and **33** suggest that gas phase calculations can be utilised to predict the preferred configuration of other radicals that have not yet been synthesised. Performing a series of calculations that on average take a few hours can therefore successfully predict the preferred configuration of radicals that have not yet been synthesised, whereas the actual synthesis often requires several weeks. This study highlights the importance of theoretical methods and their ability to utilise fewer resources (time, cost) to produce similar results to experimental methods that would otherwise require significantly more resources.

References

- (1) Haynes, D. A. *CrystEngComm* **2011**, *13*, 4793.
- (2) Alberola, A.; Clarke, C. S.; Haynes, D. A.; Pascu, S. I.; Rawson, J. M. *Chemical Communications* **2005**, 4726.
- (3) Clarke, C. S.; Haynes, D. A.; Smith, J. N. B.; Batsanov, A. S.; Howard, J. A. K.; Pascu, S. I.; Rawson, J. M. *CrystEngComm* **2010**, *12*, 172.
- (4) Constantinides, C. P.; Eisler, D. J.; Alberola, A.; Carter, E.; Murphy, D. M.; Rawson, J. M. *CrystEngComm* **2014**, *16*, 7298.
- (5) Robinson, S. W.; Haynes, D. A.; Rawson, J. M. *CrystEngComm* **2013**, *15*, 10205.
- (6) Bruns, E. A.; Perraud, V.; Greaves, J.; Finlayson-Pitts, B. J. *Analytical Chemistry* **2010**, *82*, 5922.
- (7) Osmanoglu, Y. E.; Sütçü, K. *Journal of Molecular Structure* **2017**, *1145*, 240.
- (8) Luzon, J.; Campo, J.; Palacio, F.; McIntyre, G. J.; Rawson, J. M.; Less, R. J.; Pask, C. M.; Alberola, A.; Farley, R. D.; Murphy, D. M.; Goeta, A. E. *Physical Review B* **2010**, *81*, 144429.
- (9) Pan, Y.; Nilges, M. J. *Reviews in Mineralogy and Geochemistry* **2014**, *78*, 655.
- (10) Chibotaru, L. F.; Ceulemans, A.; Bolvin, H. *Physical Review Letters* **2008**, *101*, 033003.
- (11) Passmore, J.; Sun, X. *Inorganic Chemistry* **1996**, *35*, 1313.
- (12) Ottaviani, M. F.; Geniali, A.; Cangiotti, M.; Mangani, F. *Research on Chemical Intermediates* **2002**, *28*, 117.

7 Summary and concluding remarks

The aim of this work was to perform a series of theoretical and experimental studies to rationalise the solid-state properties of 1,2,3,5-dithiadiazolyl (DTDA) radicals. These radicals are a particular class of thiazyl radicals with unpaired electron density in a low-lying SOMO, which gives rise to their potential application as organic magnets.

Chapter 1 contains a brief overview of the studies that have previously been performed on DTDA radicals. **Chapter 2** contains a detailed discussion of the material and methods used in this work. **Chapter 3** describes the synthesis and properties of four previously-known synthesised DTDA radicals, namely 4-(4-cyano-2,3,5,6-tetrafluorophenyl)-1,2,3,5-dithiadiazolyl (**2**), 4-(4'-bromo-2',3',5',6'-tetrafluorophenyl)-1,2,3,5-dithiadiazolyl, 4-(2,3,5,6-tetrafluoro-4-nitrophenyl)-1,2,3,5-dithiadiazolyl (**4**) and 4-(2,6-difluoro-phenyl)-1,2,3,5-dithiadiazolyl (**7**).

The co-crystallisation of **2** and **7** proved interesting as the preparation produced block-shaped crystals, which were identified by XRD to be the α -phase of **2**, which has previously been found to only grow at temperatures of $-10\text{ }^{\circ}\text{C}$. It was proposed that **7** acts as an additive which provides the necessary stabilisation to promote growth of α -phase crystals. The needle-shaped β -phase crystals of **2** were found to be the first example of DTDA radicals that exhibit flexible properties. EPR results of the bent crystals showed a loss in signal at the bent region. It was proposed that bending the crystals results in rows of **2** that move along the *a*- and *c* axes to yield dimeric pairs of **2**, which results in the observed loss in signal.

Crystallisation in the final step of the synthesis of known monomeric radical **3** yielded a mixture of **3** and a novel co-crystal (**3-cox**). The crystal structure of **3-cox** revealed dimerised pairs of 4-(4'-bromo-2',3',5',6'-tetrafluoro-phenyl)-1,2,3,5-dithiadiazolyls in a *cisoid* mode of association, which co-crystallise with the starting material 4-bromo-2,3,5,6-tetrafluorobenzonitrile. The small twist angles and dimeric mode of association in **3-cox** shows that the network of intermolecular interactions play an important role in the potential of DTDA radicals to dimerise.

The joint refinement of HXRD and PND data of **4** produced a static deformation map, which showed the presence of a sigma hole on the fluorine atoms. The fluorine atoms in known monomeric perfluoroaryl-containing radicals form various intermolecular interactions owing to the presence of this σ -hole, hence preventing dimerisation. In addition, spin density values were calculated with the joint refinement method. These values were found to be in good agreement with experimental data, with the majority of the spin density residing on the sulfur and nitrogen atoms of the heterocyclic radical ring. The interesting properties of monomeric DTDA radicals encouraged a study aimed at understanding the role that intermolecular interactions play in whether the radicals dimerise or remain monomeric in the solid state.

In **Chapter 4**, a series of geometry optimisation and counterpoise-corrected single point calculations were performed in the singlet and triplet states on monomeric and dimeric radicals selected from the CSD. Dimeric radicals were found to yield attractive interactions if the geometry optimisation and single point calculations were performed in the same state, whereas monomeric radicals only yield attractive interactions if single point calculations were performed in the triplet state, irrespective of the geometry optimisation. Radical **3** was found to be the one exception, as this known monomeric radical exhibits a final geometry and attractive interaction similar to those observed for the dimeric radicals. This behaviour was expected as the crystal structure of **3-cox** showed that **3** can exhibit monomeric and dimeric modes of association in the solid state.

A PES scan probed the different dimeric modes of association in a dimeric radical pair. It was found that the *cisoid* mode of association exhibits the strongest attractive interaction. The PES scan of a monomeric radical showed that the most attractive interaction energies occur at large twist angles that minimise the steric repulsion of N...F contacts.

EDA analysis of monomeric and dimeric radicals showed that the orbital interactions do not provide the necessary stabilisation to counter the large repulsive Pauli contribution, and therefore the strong binding energies in dimeric radicals are mainly due to dispersion and electrostatic contributions to the binding energy.

A topological analysis of the dimeric radicals showed that S...S interactions exhibit BCP properties similar to those of H-bonds and contacts in charge transfer molecular complexes. Furthermore, the strong interaction between the SOMOs also allows for interaction between the aryl rings, which further stabilises the dimeric mode of association between radicals. The topological analysis of the monomeric radicals showed the formation of F...F contacts, which confirm that the fluorine atoms in perfluoroaryl radicals play an important role in why these radicals exhibit a monomeric mode of association.

The ESP maps of dimeric radicals showed that the presence of halogenated aryl rings results in an accumulation of negative charge on the nitrogen atoms, which in turn allows for the formation of various contacts that influence the solid-state architecture. The ESP maps of monomeric radicals showed how areas of negative charge on *para* substituents interact with the area of positive charge between the sulfur atoms. These structure-directing contacts play an important role in why these radicals adopt a monomeric mode of association.

In **Chapter 5**, calculations on substituted radicals showed that *meta* substituted radicals exhibit strong S...S and S...N contacts that result in a *cisoid* mode of association. The *ortho* and *para* substituted radicals were shown to form weaker interactions, resulting from fewer S...S and S...N contacts, where radical pairs **16**, **19** and **20** exhibit a mode of association similar to those

observed for radicals **3** and **6**. Replacing the fluorine atoms with heavier halogen atoms was found to result in stronger interactions for radicals with NO₂ and NC groups at the *para* position. These results suggest that replacing the fluorine atoms of radicals **2** and **4** with heavier halogens could yield novel DTDA radicals that exhibit a monomeric mode of association.

In **Chapter 6** the results from the previous chapters were used as a basis for a series of calculations with the aim of predicting what mode of association a set of unknown radicals would prefer in the solid state. Firstly, a series of PES scans were performed to determine where the strongest intermolecular interactions occur for eight monomeric and dimeric modes of association. Ten radicals, consisting of three known monomeric radicals and seven unknown radicals, were then arranged in the calculated geometries where the strongest intermolecular interactions occur for each mode of association. Full geometry optimisation and counterpoise-corrected single point calculations were then performed on all radicals. It was determined from the final structures and interaction energies that radicals **31 - 33** have the potential to prefer a dimeric mode of association, while radicals **34 - 36** are more likely to prefer a monomeric mode of association. The accuracy of these predictions was confirmed by the novel crystal structures of radicals **32** and **33**. Radical **32** exhibits a *trans-cofacial* mode of association, which was computationally predicted as the most stable mode of association, while radical **33** exhibits a *cisoid* mode of association, which was computationally predicted as one of the most stable modes of association.

The results from this study have shown that a combination of theoretical and experimental methods provide a powerful tool for studying DTDA radicals. Theoretical methods were used to understand why radicals prefer different modes of association in the solid state. This knowledge was then used to computationally predict which mode of association radicals will prefer in the solid state. This proved very successful as it accurately predicted the modes of association in radicals **32** and **33**. This method could prove to be invaluable in the design of novel DTDA radicals, as it has the potential to predict the preferred mode of association based on few hours of calculations, whereas a synthetic procedure can sometimes take weeks to produce any crystals.

Addendum A

A.1. Synthesis of 2,3,5,6-tetrafluoro-4-nitrobenzonitrile

The nitrile, 2,3,5,6-tetrafluoro-4-nitrobenzonitrile, was synthesised according to the procedure described by Rawson and coworkers⁵. This nitrile was synthesised in a two-step synthetic procedure as illustrated in Figures A.1 and A.2⁶. All amounts used throughout the synthetic procedure are summarised in Table A.1. An overall yield of 45% was achieved.

A.1.1. Amination of pentafluorobenzonitrile

The amination of pentafluorobenzonitrile was achieved by adding an excess of ammonia (25%) to an oven-dried Schlenk containing the nitrile and heating the mixture to 60 °C for 24 hours. The crude solid was then added to dry ethyl acetate (EtOAc). The mixture was further stirred at room temperature for 8 hours and thin layer chromatography (TLC) was used to confirm when starting material was no longer present. The product was then extracted with ethyl acetate (EtOAc) and washed with 1 M hydrochloric acid (HCl). The organic layer was then dried on MgSO₄, after which the excess solvent was removed under reduced pressure. The product was purified via recrystallisation from a hexane/EtOAc mixture (1:9). Hexane was then added to the solid mixture; small amounts of EtOAc were added until the crude solid had dissolved. Once the mixture cooled, white needle-like crystals precipitated out of solution in a yield of 85%.

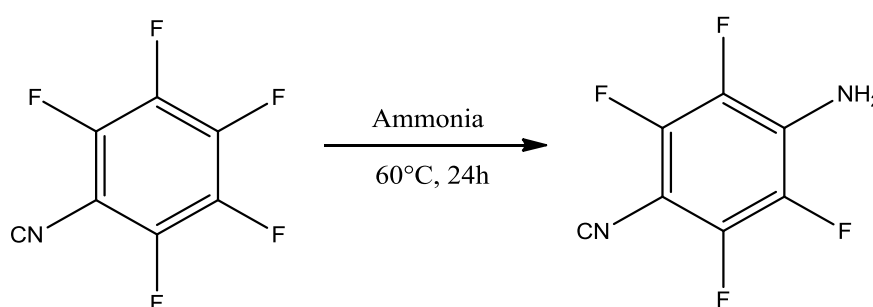


Figure A.1: Amination of pentafluorobenzonitrile

A.1.2. Oxidation of aminotetrafluorobenzonitrile

The oxidation of aminotetrafluorobenzonitrile to nitrotetrafluorobenzonitrile (Figure A.2) was achieved by the addition of aminotetrafluorobenzonitrile and urea hydrogen complex to a round bottom flask containing dry dichloromethane (DCM) (Part 2, Table A.1). The mixture was then stirred at room temperature until the solid had dissolved. Trifluoroacetic anhydride (TFA) was added over 2 hours using an electronic syringe pump. The resulting mixture was refluxed for 16 hours until a visible light green colour was achieved.

The reaction mixture was quenched with water and the subsequently washed with sodium bicarbonate (NaHCO₃) and brine (NaCl + H₂O). The mixture was then dried over MgSO₄ and the excess solvent removed under reduced pressure. The crude product was then purified using column chromatography with a hexane/EtOAc (1:9) solvent system. Tubes containing the product were collected and the solvent removed under reduced pressure. Hexane was added to the crude solid and heated while adding small amounts of EtOAc until all solid had dissolved. Once the flask had cooled, yellow crystals precipitated in a 64% yield.

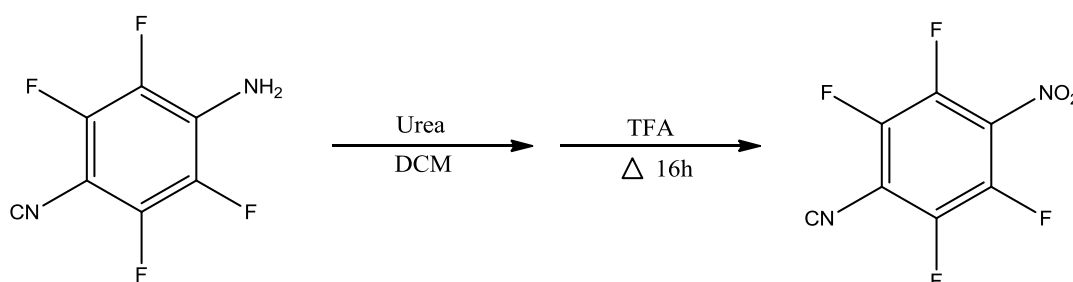


Figure A.2: Oxidation of the amine group to a nitro group

Table A.1: Amounts used for synthesis of 2,3,5,6-tetrafluoro-4-nitrobenzonitrile

Reagent	M _r (g/mol)	Mass/volume	Mol(mmol)	Equivalent
Part 1				
Pentafluorobenzonitrile	193.07	6.53 ml	51.8	1
Ammonia (25 %)	17.00	6.00 mL	-	excess
Aminotetrafluorobenzonitrile	190.02	7.12 g	37.5	1
Part 2				
Urea-Hydrogen complex	94.07	35.25 g	374.7	10
TFA-anhydride (1.47 g/ml)	210.03	25.7 ml	179.8	5

A.2. Synthesis of 4-bromo-2,3,5,6-tetrafluorobenzonitrile

4-Bromo-2,3,5,6-tetrafluorobenzonitrile was synthesised according to the procedure described by Birchall and coworkers⁷. A mixture of pentafluorobenzonitrile, lithium bromide and N-

methyl-2-pyrrolidone was heated under reflux for 30 min. The mixture was allowed to cool and the resulting white solid was washed with H₂O and dried under reduced pressure. Sublimation at 50 °C in combination with recrystallisations from hexane yielded the desired 4-bromo-2,3,5,6-tetrafluorobenzonitrile in a 51% yield. The complete synthesis of this nitrile is summarised in Figure A.3. All amounts used throughout the synthetic procedure are given in Table A.2.

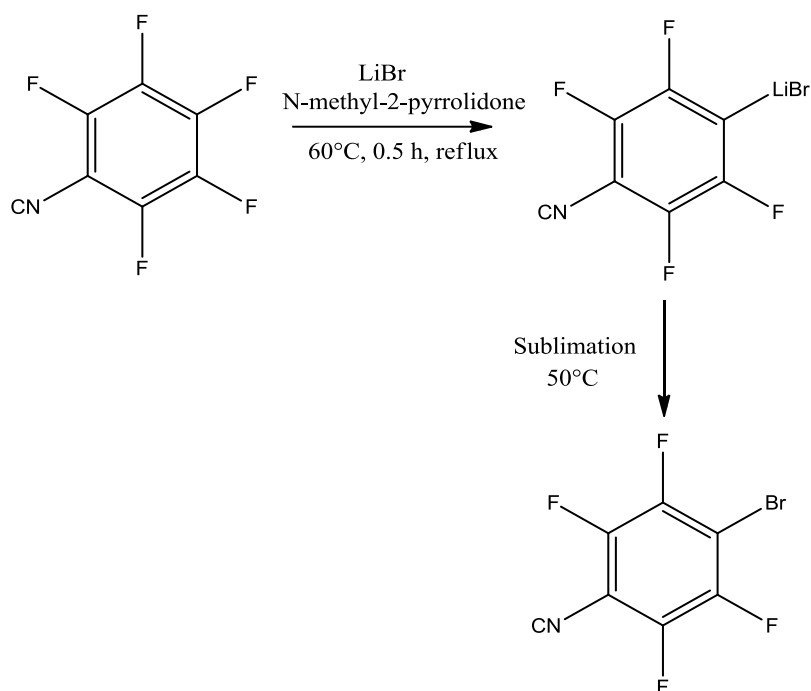


Figure A.3: Synthesis and preparation of 4-bromo-2,3,5,6-tetrafluorobenzonitrile.

Table A.2: Equivalents used for synthesis of 4-bromo-2,3,5,6-tetrafluorobenzonitrile.

Reagent	M _r (g/mol)	Mass/volume	Mol(mmol)	Equivalent
Pentafluorobenzonitrile	193.07	10 ml	80	1
Lithium bromide	86.85	7.0 g	80	1
N-methyl-2-pyrrolidone	99.13	80 mL	80	1

A.3. Synthesis of DTDA radicals.

The amounts used for the synthesis of 4-(4-cyano-2,3,5,6-tetrafluorophenyl)-1,2,3,5-dithiadiazolyl (2), 4-(4'-bromo-2',3',5',6'-tetrafluorophenyl)-1,2,3,5-di-thiadiazolyl (3), 4-(2,3,5,6-tetrafluoro-4-nitrophenyl)-1,2,3,5-dithiadiazolyl (4) and 4-(2,6-difluoro-phenyl)-1,2,3,5-dithiadiazolyl (7) and radicals are given in Tables A.3 – A.6. Addition of SCl₂/S₂Cl₂ resulted in a salt colour that ranges between brown and yellow/orange for the different radicals. A black colour was observed once the salt had been fully reduced. Sublimation of the reduced salt results in the formation of purified crystals.

Table A.3: Amounts used for the synthesis of radical 2, where synthesis generally showed a 28% yield.

Reagent	Mass/Volume	Moles(mmol)
HMDS	1.04 mL	5.0
n-BuLi	3.13 mL	5.0
Nitrile	1.0 g	5.0
S _{Cl} ₂	0.7 mL	11.0
EtO ₂	40 mL	-
EtO ₂ wash	40 mL	-
Salt	1.2 g	3.8
Ph ₃ Sb	0.675 g	1.9

Table A.3: Amounts used for the synthesis of radical 3, where synthesis generally showed a 15% yield.

Reagent	Mass/Volume	Moles(mmol)
HMDS	0.82 mL	4.0
n-BuLi	2.46 mL	4.0
Nitrile	1.0 g	4.0
S _{Cl} ₂	0.64 mL	10
EtO ₂	40 mL	-
EtO ₂ wash	40 mL	-
Salt	1.04 g	3.0
Ph ₃ Sb	0.53 g	1.5

Table A.6: Amounts used for the synthesis of the radical 4, where synthesis generally showed an 18% yield.

Reagent	Mass/Volume	Moles(mmol)
HMDS	0.95 mL	8.8
n-BuLi	2.84 mL	8.8
Nitrile	1.0 g	8.8
S _{Cl} ₂	0.317 mL	22.0
EtO ₂	40	-
EtO ₂ wash	40	-
Salt	0.82 g	2.4
Ph ₃ Sb	0.43 g	1.2

Table A.5: Amounts used for the synthesis of radical 7, where synthesis generally showed a 22% yield.

Reagent	Mass/Volume	Moles(mmol)
HMDS	1.5 mL	7.2
n-BuLi	4.5 mL	7.2
Nitrile	1.0 g	7.2
S _{Cl} ₂	1.15 mL	18
EtO ₂	40 mL	-
EtO ₂ wash	40 mL	-
Salt	1.05 g	4.2
Ph ₃ Sb	0.74 g	2.1

A.4. Synthesis of α -phase of radical 2

Co-crystallisation of the β -phase of radicals **2** and **7** by sublimations at 95 °C was found to result in the formation of α -phase of radical **2** crystals. The quantities of each radical used to obtain α -phase are given in Table A.7.

Table A.7: Equivalents used of each radical in order to obtain α -phase crystals of [Cyano].

Reagent	Mass	Moles (mmoles)
Radical 2	26 mg	0.12
Radical 7	33 mg	0.12

A.5. Synthesis of novel DTDA radicals

The synthesis of 4-(2-fluoro-4-trifluoromethylphenyl)-1,2,3,5-dithiadiazyl (**31**), 4-(4-fluoro-2-trifluoromethylphenyl)-1,2,3,5-dithiadiazyl (**32**), 4-(4-bromophenyl)-1,2,3,5-dithiadiazyl (**33**), 4-(4-cyano-2,3,5,6-tetrachloro-phenyl)-1,2,3,5-dithiadiazolyl (**34**) and 4-(4-nitro-2-trifluoromethylphenyl)-1,2,3,5-dithiadiazolyl (**36**) radicals was performed with the amounts given in Tables A.8 – A.12. The synthetic procedure described in Chapter 2 (Figure 2.1) was followed for each radicals. Addition of $\text{SCl}_2/\text{S}_2\text{Cl}_2$ resulted in a black/brown coloured salt. The conditions used to obtain crystals are included in each table.

**Table A.8: Amounts used for the synthesis of radical 31.
No crystals obtained during sublimation in 60 °C – 200 °C.**

Reagent	Mass/Volume	Moles(mmol)
HMDS	1.11 mL	5.3
n-BuLi	3.31 mL	5.3
Nitrile	1.0 g	5.3
SCl_2	0.84 mL	13.25
EtO ₂	40 mL	-
EtO ₂ wash	40 mL	-
Salt	0.8 g	2.6
Ph ₃ Sb	0.47 g	1.3

**Table A.9: Amounts used for the synthesis of radical 32.
Crystals were obtained during reduction of the salt at 60 °C.**

Reagent	Mass/Volume	Moles(mmol)
HMDS	1.11 mL	5.3
n-BuLi	3.31 mL	5.3
Nitrile	1.0 g	5.3
SCl_2	0.84 mL	13.25
EtO ₂	40 mL	-
EtO ₂ wash	40 mL	-
Salt	0.8 g	2.6
Ph ₃ Sb	0.47 g	1.3

Table A.10: Amounts used for the synthesis of radical 33.
Crystals were obtained by sublimation at 80 °C.

Reagent	Mass/Volume	Moles(mmol)
HMDS	1.15 mL	5.5
n-BuLi	3.44 mL	5.5
Nitrile	1.0 g	5.5
S _{Cl} ₂	0.92 mL	13.75
EtO ₂	40 mL	-
EtO ₂ wash	40 mL	-
Salt	0.9 g	3.4
Ph ₃ Sb	0.6 g	1.7

Table A.11: Amounts used for the synthesis of radical 34.
No crystals obtained during sublimation in 60 °C – 200 °C.

Reagent	Mass/Volume	Moles(mmol)
HMDS	0.78 mL	3.8
n-BuLi	2.35 mL	3.8
Nitrile	1.0 g	3.8
S _{Cl} ₂	0.60	9.5
EtO ₂	40 mL	-
EtO ₂ wash	40 mL	-
Salt	0.9 g	2.37
Ph ₃ Sb	0.42 g	1.19

Table A.12: Amounts used for the synthesis of radical 36.
No crystals obtained during sublimation in 60 °C – 200 °C.

Reagent	Mass/Volume	Moles(mmol)
HMDS	0.96 mL	4.6
n-BuLi	2.88 mL	4.6
Nitrile	1.0 g	4.6
S _{Cl} ₂	0.73 mL	11.5
EtO ₂	40 mL	-
EtO ₂ wash	40 mL	-
Salt	0.7 g	2.12
Ph ₃ Sb	0.37 g	1.06

Appendix

A CD containing the supporting files provides the following:

Chapter 3:

CIF files and CheckCIF report

Log (*.log) files of fully optimised structures.

Chapter 4:

Log (*.log) files of fully optimised structures.

Chapter 5:

Log (*.log) files of fully optimised structures.

Chapter 6:

CIF files and CheckCIF report

Log (*.log) files of fully optimised structures.

EPR and MS spectra of unknown radicals